THE UNIVERSITY *of* EDINBURGH

The Affinity Of Ediacaran Skeletal Fauna And Their Environmental Context

Amy J. Shore

Thesis submitted for the degree of Doctor of Philosophy

The University of Edinburgh

2021

Author Declaration

I, Amy Shore, declare that the research presented in this thesis is the work of myself, unless stated otherwise. There is no part of this thesis which has been previously submitted for a professional qualification, such as a degree, at the University of Edinburgh or at other universities.

Amy J. Shore

Abstract

The Ediacaran-Cambrian boundary (~541 million years ago (Ma)) signifies the start of the 'Cambrian Explosion' of animals, and by 520 Ma most major phyla had emerged. However, characteristics associated with the Cambrian Explosion, such as motile behaviours and biomineralisation, originated during the Ediacaran. It is thought that oxygenation is the key driver of the rise of metabolically costly forms of life. Yet, the drivers behind the oxygenation of Ediacaran basins are not well known. This thesis contributes to the understanding of the drivers behind the rise of skeletal animals during the Ediacaran as well as offering insight into their morphology, affinity and mode of life.

New phosphorus speciation data were collected from siliciclastic samples of the terminal Ediacaran-Cambrian Nama Group, Namibia (ca. 550-538 Ma), from shelf transects of the two subbasins in order to determine regional nutrient cycling. This was achieved by combining redox, nutrient cycling, and biotic distribution and diversity data to understand the controls behind oxygenation through time. Limited phosphorus cycling, prior to 547 Ma, may have supported the ferruginous conditions, with possible influence from upwelling from the deep ocean. However, the reduction in continental run off caused the Nama Basin to transition from unstable redox conditions to more stable oxic conditions at ~547 Ma with full oxic conditions across the basin by ~542 Ma. The decrease in recycling of bioavailable phosphorus into the water column allowed for the development of more stable oxic conditions. This in turn allowed for the radiation of mobile taxa and biomineralising taxa, both metabolically costly forms a life, allowing them to inhabit deeper areas of the Nama Basin.

The changing redox conditions determined the availability of habitable areas along the shelf of the Nama Basin. In oxygenated, or transiently-oxygenated, areas of the shelf *Cloudina* was able to form reef-frameworks, often in association with microbial mats. Coeval *Cloudina* across the Zaris Subbasin share similar features, such as *Cloudina*-associated

cements and paired lamina, implying calcification was biologically-controlled where laminae acted as part of the 'biomineralisation toolkit'. *Cloudina*-associated cements may have formed during life as they form prior to breakage, transportation, and abiotic cement formation. However, the mineralisation of *Cloudina* must have been environmentally controlled as evidenced by the variation of paired lamina thickness and *Cloudina* wall thickness across the shelf. The variation in thickness may have been due to physical factors, such as hydrodynamic energy, or chemical factors, such as seaswater pH.

The affinity of Ediacaran fauna are greatly contested due to the general absence of preserved diagnostic features and soft tissue. However, this thesis presents new findings of polytomous branching in cloudinomorphs within the Omkyk Member of the Nama Group. Polytomous branching is a feature attributed to non-bilaterian taxa and so could suggest that these cloudinomorphs are of cnidarian origin and are part of a potentially polyphyletic group. In addition, the discovery of a Lagerstätte within the Omkyk Member shows soft-tissue preservation of *in-situ Namacalathus* where a combination of features, such as a U-shaped gut and organic-rich pores within the skeleton, could suggest a lophotrochazoan affinity. Although molecular phylogenies predict an older origin, lophotrochozoan fossils were previously known only from the Early Cambrian and so this discovery provides a potential link between the Ediacaran and Cambrian biotas.

Lay Summary

The Cambrian Explosion started around 541 million years ago and it is at this time where the major groups of the animal kingdom started to appear, and lasted for around 20 million years. Body plans which we see today originated during this time as well as other features such as movement and the ability to produce minerals through biological processes, termed biomineralisation. This sudden appearance of complex life puzzled Charles Darwin, and is termed ‘Darwin’s Dilemma’. However, more recently evidence of biomineralisation and mobile animals have been found prior to the Cambrian Explosion, in a time period known as the Ediacaran (635 to 541 million years ago). The reason for the explosion of life and the complexity of ecologies at this time is thought to be due to an increase in oxygen in the marine water column. Though, the control behind the increase in oxygen at this time are still unknown.

This thesis presents nutrient cycling data, from a method known as phosphorus speciation, which were collected from sedimentary rocks of the Ediacaran Nama Basin in Namibia. Phosphorus, a limiting nutrient which is vital for life, behaves differently depending on whether the water column is oxygenated or is anoxic. During anoxic times in the Nama Basin small amounts of phosphorus were being released into the water column from the sediment whilst during oxic conditions the phosphorus was retained within the sediment so the water column contained a lower concentration of phosphorus. However, it is unlikely that the phosphorus cycling was a driver of stable oxygenated conditions within the basin due to the limited amount of phosphorus being released. Yet, during this time there was a decrease in continental runoff which reduced the nutrient supply into the basin. During times of increased runoff ocean productivity increases which uses the free oxygen within the water column and so causes anoxic conditions. However, the reduction of continental weathering through time reduced productivity in the oceans and so the Nama Basin gained more stable oxic conditions at around 547 million years ago, which was aided by the retainment of

phosphorus in the sediment. The increase of oxygenated areas in the basin allowed for organisms, with complex behaviours like biomineralisation and mobility, to move into deeper parts of the basin.

Biomineralising organisms that lived within the Nama Basin include: the tube-like *Cloudina*, the goblet-shaped *Namacalathus*, and *Namapoikia* which looks similar to a sponge, all having a carbonate skeleton. These organisms inhabited oxygenated areas along the shelf where *Cloudina* were able to form reef-frameworks on top of microbial mats, which were very common during this time period. The *Cloudina*-reefs formed through attachment of one tube to another through the formation of very early calcium carbonate cements. As these cements, and other cements associated with the *Cloudina*, formed early and are found across the shelf of the basin it can be assumed that these cements formed through biomineralisation. However, the cements are expressed differently between sites causing variation in the thickness of *Cloudina* walls could suggest that the biomineralisation was environmentally controlled and so the organism did not have the biological processes needed to form a consistent shell across different environments.

New data presented in this thesis also shed light on what groups of animals these Ediacaran taxa belong as this is difficult to determine due to the lack of preservation of characteristic structures and soft tissue. However, the findings of preserved soft-tissue in *Namacalathus* highlight features which signify that the organism could have been a lophotrocozoan, a large animal group which includes worms and molluscs. This link between the Ediacaran and Cambrian could suggest that the Cambrian Explosion may not have been a short-lived event as previously thought but had roots in the Ediacaran.

Acknowledgements

It has been a privilege to be given the opportunity to be able to study such a fascinating period of time in an amazing city. There are so many people I need to thank for helping me along the way and I hope I am able to pay you back one day, but these words could be a start.

First and foremost I would like to thank my supervisor Rachel Wood, for her never-ending help and enthusiasm which has pushed me along through this process, even through times when my motivation was lacking. Thank you for all the insightful discussions which have led to many lightbulb moments. Also, I can't thank you enough for the opportunity to go to Namibia, but more on that later.

I'd also like to thank my other members of my supervisory and advisory team: Alex Thomas, Fabio Nudelman and Steve Brusatte. Especially thank you to Alex for your discussions over coffee time when I had questions about a particular method. I am also incredibly grateful for the conversations with Andrey Zhuravlev on all things Ediacaran, especially *Namacalathus*, and cheese. Fred Bowyer has been an amazing help for all things geochemical, thank you for pointing me in the right direction and giving feedback on my work.

Fieldwork in Namibia was a definite highlight over the past few years. So a big thanks go to "Team Namibia 2018": Rachel Wood, Andrew Curtis, Fred Bowyer, Geoff Wood, Shona Curtis-Walcott and Ali Curtis-Walcott. Thank you all for fantastic scientific discussions over breakfast and evening campfires, expert hammering, fantastic photography, efficient tyre replacing, chopping onions, pizza oven construction, and the garlic bread. I will never forget observing the Milky Way by firelight or seeing elephants without barriers, I can't help but smile every time I think about these thing.

I have had so much technical help which has helped me throughout this entire process. I have to give thanks to: Mike Hall, John Craven, Nicola Cayzer, Alison MacDonald, Chris

Hayward, Clare Peters and Ian Butler of the University of Edinburgh. Your training and, in some cases, data collection have made this project possible. Another big thank you goes to Simon Poulton, Lewis Alcott and Andrew Hobson of the Cohen Labs at the University of Leeds for their help during my two weeks there. Your exceptional training and advice through the two weeks was extremenly useful and I learnt so much.

I am also grateful for having received funding from the School of Geosciences and the International Centre for Carbonate Reservoirs. Without this funding this project would not have been carried out.

The 'Carbonate Crew' have been a big help throughout the Lockdown times. Thank you all for listening to and discussing my work at great length, this has been so helpful through these difficult times and has spurred me on. It has also been extremely refreshing to here your work and have discussions on all things carbonate. Keep up the good work!

I am so happy to have been able to share an office with such wonderful people as those found in the Grant Attic. A massive thanks goes to Hannah and Julia for being two thirds of the Aspall Girls and for the many pub trips to John Leslie's, 2 for 1 nachos, and meals where we would discuss everything and nothing. I am hugely indebted to Isla and Davide for their countless walkies, immeasurable amount of tortellini and fish and chip picnics (for which I should really thank Salvatore). And to my Booth 4 buddies, it has been an a pleasure working with you and we truly are the best booth. Sophie, thank you for the Strictly chat and the re-introduction to netball. Also, I am thankful to Jonny for drinks, games and seal watching.

Lastly, a big thank you goes to my family. You have been there for me constantly and you keep me grounded. Thank you for the care packages and many video/phone calls as you always know what to say. Thank you for all the cups of tea, the delicious food and all the good times. You might not realise it but you have given me the skills I needed to do this, so thank you. Mum, thank you! Dad, thank you! Emma, thank you! Stuart, thank you! Nan, thank you!

Table of Contents

Chapter 2: Phosphorus Cycling and Oxygenation in the Nama Group, Namibia

Chapter 3: Multiple Branching and Attachment Structures in Mat-dwelling *Cloudina*, Nama Group, Namibia

List of Figures

List of Tables

Chapter 1: Oxygenation and Biomineralisation of Ediacaran Organisms

1.1 Background

The Cambrian Radiation, which began ~541 Million years ago (Ma), marks the first appearance of the major groups of metazoan phyla and widespread bioturbation. This is known as 'Darwin's Dilemma' as the appearance of complex life occurred so abruptly in the Cambrian geological record and appears to contradict the gradual processes of evolution. However, more recent discoveries show that multicellular organisms, including probable metazoans, lived during the Ediacaran (635-541 Ma).

The Tonian (1000 – 720 Ma) to early Cambrian was an interval of dynamic earth processes. This saw the disassembly of the supercontinent Rodinia (900 Ma to ≥750 Ma (Li et al., 2008)) and the later break-up of the low-latitude short-lived supercontinent of Pannotia at ~550 Ma formed the continents of Gondwana and Laurentia, and the formation of the Siberia (Scotese, 2009; Young, 2013). The later break-up phases occurred after a series of near-global glaciations where atmospheric oxygen levels were probably low (Hoffman et al., 1998; Knoll and Sperling, 2014).

The fossil record of the Ediacaran consists of generally low-diversity assemblages which feature high-disparity, i.e. morphological differences, which have been assigned to varied affinities including Protista, 'Venobionta' and Metazoa (Seilacher, 1992; Seilacher et al., 2003). Precursors of bioturbation, biomineralisation, macropredation, and ecological tiering are all present in the Ediacaran even though these innovations are more often attributed to the Cambrian (Bengtson and Zhao, 1992; Jensen et al., 2000; Laflamme et al., 2013; Droser

and Gehling, 2015). The rise and stabilisation in oxygen has been attributed to these biological innovations within the macrofauna. However, there is still considerable debate as to whether, and how, these factors are inter-linked (Figure 1.1). Pulses of oxygenation have been noted to correlate with carbon isotope excursions (Wood et al., 2019) which could suggest a potential cause or coupling (Figure 1.1).

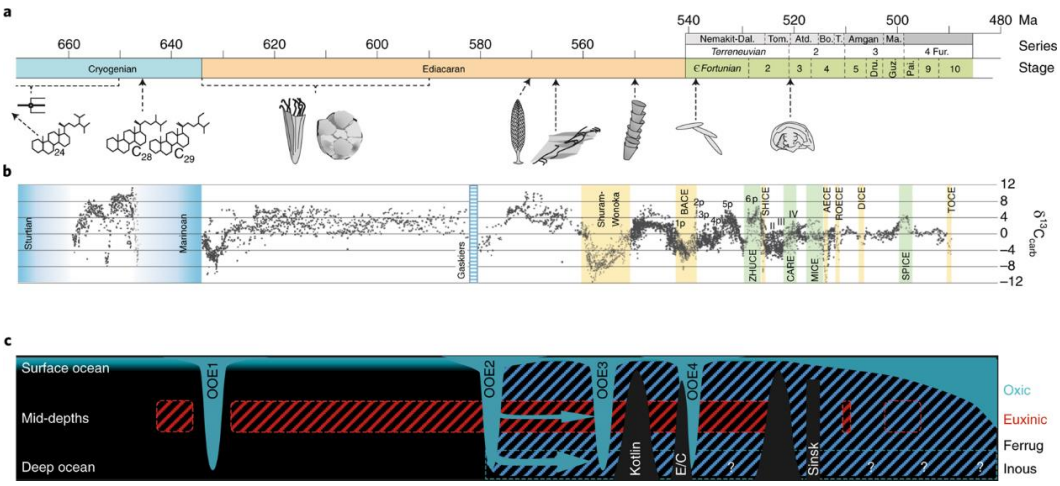

Figure 1.1*: Integrated geochemical and biotic record of the Cryogenian to End Cambrian.* ***A****: The biological timescale signifying biological innovations, such as the minimum age of planktonic algae (~659-645 Ma, possible stem-group Cnidarian* Lantianella laevis *and the first fossil embryos (635-590 Ma),* Charnia masoni *(~570.9 Ma), the first potential locomotive trace fossil (~565 Ma), the earliest skeletal macrofauna (*Cloudina *at ~550 Ma), first appearance of* Treptichnus pedum*, and earliest trilobite (*Profallotapis jakutensis*).* ***B****: Ediacaran carbon isotope record compilation.* ***C****: a schematic of ocean redox conditions through time, compiled through Fe speciation data, highlighting oxygenation and anoxic events. Modified from Wood et al. (2019).*

This thesis is based on field and analytical work on samples from the terminal Ediacaran Nama Group, Namibia. The research contributes to the understanding of the affinity and growth form of the Ediacaran skeletal metazoans, *Cloudina* and *Namacalathus*, and explores the potential controls behind a transition to more oxic conditions in the terminal Ediacaran via consideration of the phosphorus cycle using a newly developed method previously untested on sedimentary rocks of this age.

1.2 Carbon Cycle Perturbations In The Ediacaran

Throughout the Neoproterozoic, there have been multiple carbon isotope excursions which all feature $\delta^{13}C$ values that reach below -5‰, potentially due to negative rates of carbon burial (Shields et al., 2019) (Figure 1.1). These excursions include the Gravellach (~720 Ma), the Trezona (~650 Ma), and the Shuram/Wonoka/DOUNCE (~560 Ma) (Fairchild et al., 2018; McKirdy et al., 2001; Rose et al., 2012; Fike et al., 2006; Lu et al., 2013). The $\delta^{13}C_{carb}$ values remained constant after the recovery of the Shuram excursion in the last 10 million years of the Ediacaran, but the values decreased once again at the start of the Cambrian, with the basal Cambrian carbon isotope excursion (BACE) (Figure 1.1). The BACE has been noted to coincide with the demise of soft-tissue Ediacaran biota but there is a lack of datable beds across this time period (Wood et al., 2019), meaning it is difficult to correlate these two events.

During the mid-Ediacaran the largest negative $\delta^{13}C_{carb}$ excursion, known as the Shuram-Wonoka isotope excursion (Burns and Matter, 1993; Grotzinger et al., 2011) (Figure 1.1). The isotopic values reached -12‰, with values reaching to -6‰ within the Buschmannklippe Formation of the Witvlei Group, Namibia (Kaufman et al., 1991). The causes behind this is still contested, but hypotheses include the build-up of light carbon, mantle-derived carbon in the atmosphere and oceans during Snowball Earths during the Cryogenian (Hoffman et al., 1998), the overturning of a stratified ocean (Grotzinger and Knoll, 1995), the release of methane clathrate reserves, which is a light carbon reservoir (Dickens et al., 1995; Schrag et al., 2002), and changes in the style of post-depositional processes (Derry, 2010). While the latter could explain the covariation of $\delta^{13}C$ and the $\delta^{18}O$, this process would not support the apparent global feature of the Shuram-Wonoka excursion as the effects of diagenetic fluids might indicate more local processes (Grotztinger et al., 2011).

A further potential cause of the Shuram-Wonoka excursion is the large-scale precipitation of ^{13}C-depleted authigenic carbonates which occurred below the water-sediment interface due to the anaerobic microbial metabolism and microbial sulphate reduction within

the sediment (Cui et al., 2017). Cui et al (2017) showed that samples from the Doushantuo Formation are composed of authigenic carbonate that are methane-derived, with negative ^{13}C values between -5 and -37‰. Husson et al. (2020) also agrees with this hypothesis and show that there is a gradient along a shelf to basin transect within the Australian Wonoka succession with deeper marine carbonates showing higher $\delta^{13}C$ values. Cao et al. (2020) suggest that the formation of this depleted authigenic carbonate in a diagenetic event that occurred globally at the sediment-water interface due to a steep redox gradient, evidenced by high uranium isotope ($\delta^{238}U$) values that coincide with the peak of the excursion in the Doushantuo Formation. A similar shift in $\delta^{238}U$ values has been found within the Sonora Succession, Mexico, but occurred ~0.8 million years after the isotope excursion (Li et al., 2020). Li et al. (2020) suggest that oxygenation was a two-step process, with the initial oxidation of dissolved organic carbon (DOC) shifting $\delta^{13}C_{carb}$ to more negative values and the oxidation of methane shifting $\delta^{13}C_{carb}$ values up to -12‰, linked with the increasing $\delta^{238}U$ values suggesting oxygenation of the oceans.

Another possible source of such low ^{13}C values may be the organic carbon oxidation of a large carbon sink, leading to a ^{13}C depleted dissolved inorganic carbon (DIC) sink (Rothman et al., 2003; Fike et al., 2006; McFadden et al., 2008). Rothman et al. (2003) suggests that for such negative values of $\delta^{13}C_{carb}$ a large dissolved organic carbon pool (DOC) which is 100 to 1000 times larger than those in the modern oceans would have to be remineralised. The excursion lasted for between 25 and 50 Myr, suggesting the reservoirs were oxidised during this time (Fike et al., 2006). This time scale does not correspond with the oxidant repletion rate as this would suggest a DOC reservoir of this magnitude would have been exhausted after 800,000 years (Bristow and Kennedy, 2008), suggesting that this model could not explain the magnitude and length of such of an excursion. However, Shields et al. (2019) propose that weathering of evaporate deposits and the reburial of sulphur as pyrite is an additional oxidant source that would allow the excursion to last for tens of millions of years. It has recently been suggested, however, that the excursion too place between 574.0 ± 4.7 and

567.3 ± 3.0 Ma years ago (Rooney et al., 2020) and so did not last as long as previous estimates but a feedback loop must have been present to sustain the excursion. Canfield et al. (2020) have also attempted to date the excursion suggest that the Shuram event lasted between 571 Ma to 562.50 Ma, so the timing of the excursion is still up for debate.

The BACE occurred before the first appearance of *Treptichnus pedum* (Zhu et al., 2001; Smith et al., 2016; Hodgin et al., 2021) where the excursion has been dated at 541.00 ± 0.13 Ma (Bowring et al., 2007), with more recent estimates suggesting between 538.58 ± 0.19 and 538.99 ± 0.21 Ma (Xiao and Narbonne, 2020)

It has been suggested that the BACE occurred in response to the appearance of anoxia across multiple shallow marine environments (Kimura and Watanabe, 2001; Willie et al., 2008). However, Hodgin et al. (2021) propose that the BACE dated from Sonora, Mexico, is ~1.5 Myr younger (539.40 ± 0.23 Ma). The samples collected from the Ara Group, Oman, were deposited in an evaporitic basin which potentially underwent depositional hiatus and so may not give accurate depositional dates (Zhu et al., 2019). The bed dated from the La Ciénega Formation, Mexico, is associated with basaltic rocks which are derived from the mantle and flood basalts formed from rift-related volcanism which occurred on the Caborca block and southwestern Oklahoma (Stewart et al., 1984; Barrón-Díaz et al., 2019; Hogdin et al., 2021) and could have acted as a cause of the BACE.

1.3 Ediacaran Redox Conditions

The rise of complex life has been attributed to the increase in atmospheric oxygen. Oxygen levels increased above a threshold value for organisms to evolve (Nursall, 1959); however, this is difficult to quantify. The demosponge *Halichondrea panacea* can tolerate 0.5% PAL which is below the minimum oxygen level of 1% PAL suggested by Berkner and Marshall (1965). Hammalund (2020) suggests that the acquisition of internalised hypoxic

conditions allowed organisms to move to environments where oxygen concentrations were unstable or fluctuating.

Multiple studies have been undertaken in order to understand oxygenation through this time interval, which include a variety of proxies including iron (Fe) speciation, cerium anomalies, uranium and molybdenum isotopes, trace metals, rare earth elements (REE) and sulphur isotopes.

Uranium isotopes ($\delta^{238}U$), a global redox proxy, indicate that the Ediacaran oceans had pulses of short-lived oxygenation in a mostly anoxic ocean (Sahoo et al., 2016; Tostevin et al., 2019) (Figure 1.2). These findings correlate with Fe speciation studies that highlight anoxia at depth during the Neoproterozoic (Canfield et al., 2008). A study of the Nama Group shows a decrease in the $\delta^{238}U$ isotope ratios at around 550 to 547 Ma indicating that approximately one third of the sea floor was anoxic (Tostevin et al., 2019) (Figure 1.2). The appearance of biomineralisers in the Nama Group occurred in the Mara Member which predates the minimum values of $\delta^{238}U$ indicating that global anoxia did not cause a biological turnover, i.e. the transition from the White Sea Assemblage to the Nama Assemblage, or the

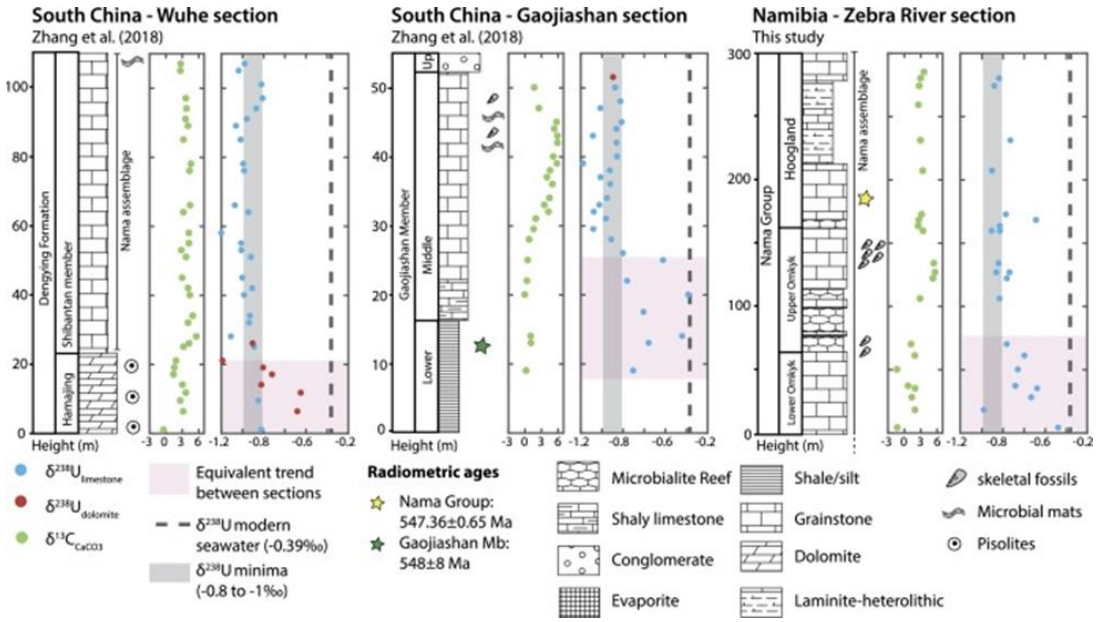

***Figure 1.2**: $\delta^{13}C$ and $\delta^{238}U$ values from the carbonate successions of the Dengying Formation (Wuhe and Gaojiashan) (from Zhang et al., 2018) and from the Nama Group, Namibia with stratigraphic logs and fossil appearances. Modern $\delta^{238}U$ values are indicated by the black dashed line. A shift towards low values (the grey line) is seen in the three sections. From Tostevin et al. (2019).*

general decline of Ediacaran fauna (Germs, 1983; Tostevin et al., 2019) (Figure 1.2). This suggests that shallow shelf communities must have had different redox histories to that of the deep open ocean, highlighting the need to study Ediacaran basins individually to understand redox state in association with the rise of metazoans. However, this is under the assumption that the correlation between the Witputs and Zaris Subbasins of the Nama Group and other Ediacaran basins are correct.

Local redox proxies indicate whether the water column was anoxic or oxic within a single basin. Fe speciation can also differentiate the different types of anoxia, i.e. whether the waters were euxinic (free H_2S) or ferruginous (free Fe^{2+}) (Poulton and Canfield, 2005). Canfield et al. (2007) propose that there was a transition to oxic conditions in the deep ocean at ~580 Ma determined from Fe speciation data from the Avalon Peninsula, Newfoundland. However, as Fe speciation is a local redox proxy, the varied redox signals between basins suggest that the Ediacaran oceans were spatially and temporally heterogenous. Ferruginous conditions were most common in Ediacaran oceans but some successions are suggestive of euxinia as evidenced by the deposition of pyrite and Fe speciation data, such as the Yangtze Platform in China (Cui et al., 2016; Och et al., 2016).

Cerium anomalies are another redox proxy which allow for further classification of redox states as oxia can be classified as fully-oxic or poorly-oxygenated manganous waters, which has been highlighted in the Nama Group where a manganous zone is situated between well-oxygenated surface waters and deep ferruginous waters (Tostevin et al., 2016a; Tostevin et al., 2016b, Tostevin et al., 2021). These low-oxygen waters were not able to support metazoan communities suggesting that there is a correlation between metazoans and oxygenation and potentially gives further insight to the oxygen requirements of these organisms (Tostevin et al., 2016b).

Tostevin and Mills (2020) suggest that the Neoproterozoic Oxygenation Event (NOE) should be named as a ‘Neoproterozoic Oxygenation Window” with pulses of oxia occurring during a time where oxygen levels were increasing gradually, as deciphered from a

compilation of geochemical proxies and modelling (Figure 1.3). Stable oxic conditions did not occur until the Palaeozoic Oxygenation Event (Tostevin and Mills, 2020) (Figure 1.3). Recently, Planavsky et al. (2020) implies that the reason for differing conclusions of redox conditions in Ediacaran oceans could be due to the heterogenous and dynamic nature of oxygenation at that time, as discussed above, or researchers potentially using samples which have undergone differing alteration during diagenesis. This highlights the need for multi-proxy studies and screening of samples used for geochemical analysis.

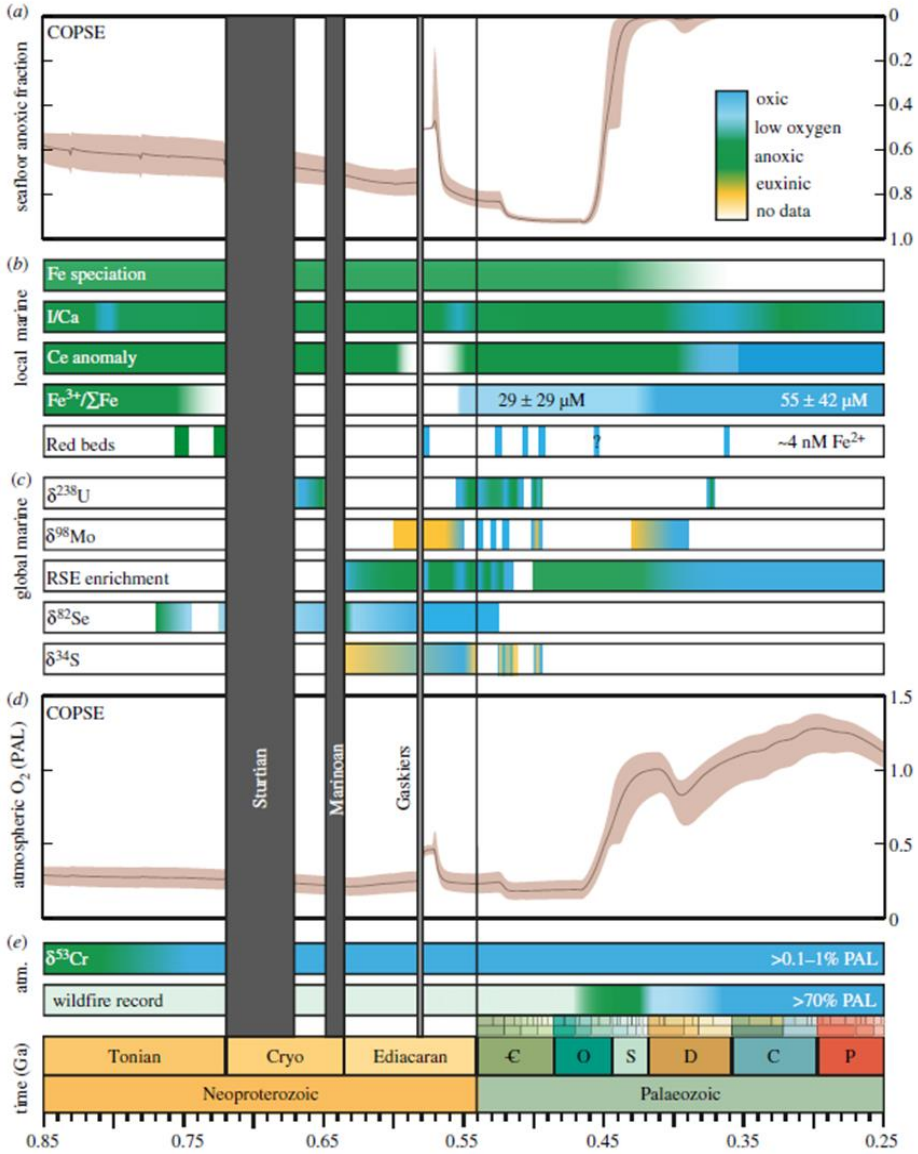

Figure 1.3*: Geochemical atmospheric and marine redox proxies highlighting changes in redox conditions throughout the Neoproterozoic and Palaeozoic, in association with the COPSE model.* ***A****: Modelled seafloor anoxia.* ***B****: Local marine redox proxies.* ***C****: Global marine redox proxies.* ***D****: Model of atmospheric O2 (PAL).* ***E****: Proxies for atmospheric O_2. From Tostevin and Mills (2020).*

1.4 The role of phosphorus

Phosphorus is a structural component for all organisms as the element is found in DNA (deoxyribonucleic acid) and RNA (ribonucleic acid); used in the transmission of chemical energy through adenosine triphosphate (ATP) molecules, which are important in the production of nucleic acids; and is the principal component of apatite, the main mineral of vertebrate bone production.

Phosphorus is thought to be one of the limiting nutrients (Redfield, 1958), with nitrogen being considered as the other limiting nutrient. Riverine input is the main form of phosphorus delivery into oceans and once in the oceans has a long residence time of between 10,000 and 20,000 years (Froelich et al., 1982; Filippelli and Delaney, 1996) (Figure 1.4). Upwelling from the deep ocean and vertical diffusivity are processes which can circulate phosphorus to shallower waters (Berner, 1990; Filippelli and Delaney, 1996).

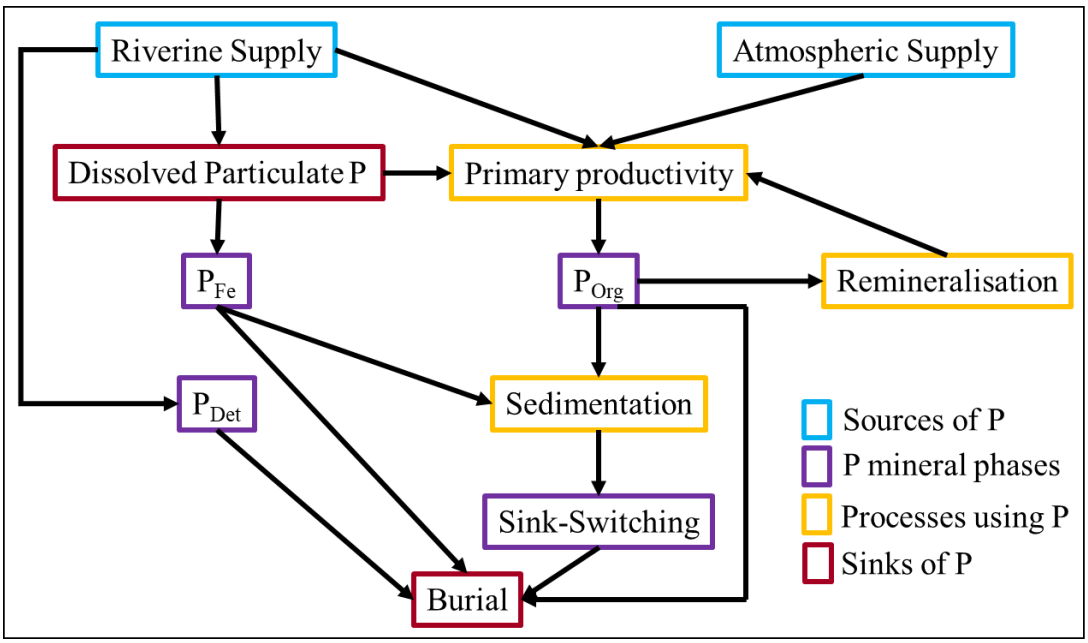

***Figure 1.4**: Simplified flow diagram of the marine phosphorus cycle. Modified from Doyle (2018).*

1.4.1 The phosphorus cycle and productivity

Phosphorus is mainly brought into the ocean system via rivers, and can be transported in particulate form, as particulate inorganic phosphorus or particulate organic phosphorus (PIP and POP, respectively), or dissolved form, as dissolved inorganic phosphorus or dissolved organic phosphorus (DIP and DOP, respectively) (Figure 1.4). Phosphorus bound to ferric (oxyhydr)oxides and phosphorus as apatite are usually forms of PIP.

There are two main sinks for phosphorus: iron (oxyhydr)oxides and organic matter (Figures 1.4 and 1.5). A large source of Fe(II) into the marine system are hydrothermal vents. At these sites, Fe(II) with the fluids ejected from the vent system produce ferric (oxyhydr)oxides (Wheat et al., 2003). Phosphorus can adsorb onto these ferric minerals around the vents which are deposited away from the vents as hydrothermal plume fallout (Poulton and Canfield, 2006). The adsorption of phosphorus to iron (oxyhydr)oxides can also occur at the chemocline, as well as in the sediment (Berner, 1973; Jones et al., 2015). Organic matter is the dominant sink of phosphorus at the sediment-water interface (Tyrrell, 1999; Filippelli, 2008).

Phosphorus cycling varies depending on the redox conditions, with processes occurring mostly in the sediment. Unstable organically bound phosphorus (P_{org}) can be released into the water column under anoxic and oxic conditions due to microbial respiration (Ruttenberg and Berner, 1993; Ruttenberg, 2003) which can cause for the release of phosphate which can be adsorbed by Fe (oxyhydr)oxides within the sediment (Slomp et al., 1996). The release of adsorbed phosphate from ferric minerals can also occur due to a reaction with dissolved sulphides (Poulton et al., 2004). In the case where sulphidic conditions cause the dissolution of iron-bound phosphorus the iron can be retained in the sediment through the formation of iron-sulphide minerals, such as pyrite (Colman and Holland, 2000; Kraal and Slomp, 2014). During times of oxia, when the oxic-anoxic boundary is within the sediment, the Fe (oxyhydr)oxides in the oxic layer act as a barrier to halt any phosphorus from being released back into the overlying water column (Slomp et al., 1996; Lenton and Watson, 2000;

Algeo and Ingall, 2007). The free phosphate can then be scavenged by (oxyhydr)oxides and retained within the sediment (Slomp et al., 1996).

Phosphorus can be retained within the sediment in authigenic phases (Figures 1.4 and 1.5). Under oxic conditions, phosphorus associated with organic matter can undergo "sink-switching" to authigenic phosphorus, such as carbonate fluorapatite (CFA), which can lead to phosphorite deposits (Ruttenberg and Berner, 1993). Phosphorite formation can be linked to oceanic anoxic events; high primary production, increasing organic matter burial; and sea level changes (Ruttenberg, 2003). Authigenic iron phosphate minerals form when conditions, such as high sedimentation rates, allow for the burial of iron (oxyhydr)oxide minerals to avoid surficial diagenetic processes (Marz et al., 2008). The authigenic iron phosphate minerals include vivianite and form from the dissolution of iron (oxyhydr)oxides by the anaerobic oxidation of methane which generates free HS^- (Egger et al., 2015; Marz et al., 2018).

Phytoplankton use phosphorus, and other elements such as nitrogen and carbon, during primary production (Figure 1.5). The Redfield Ratio (C:N:P 106:16:1; Redfield (1958)) aids in the understanding of phosphorus cycling under different redox conditions, especially the organic carbon to phosphorus ratios (Ingall and Van Cappellen, 1990; Ingall et al., 1993; Anderson et al., 2001; Faul et al., 2005; Algeo and Ingall, 2007; Jilbert et al., 2011). So, during periods of anoxia where remineralisation of organic matter leads to an elevated C_{org}:P_{org} ratio within the sediment (Van Cappellen and Ingall, 1996). However, Reinhard et al. (2016) suggest that the Redfield Ratio might be different to that found in ancient oceans, potentially due to cyanobactieria ability to occupy nutrient limiting environments unlike today. Different redox states, as explained above, and sedimentation rates affect phosphorus cycling. With the release of phosphorus, in most cases promoted by anoxia especially euxinic conditions, promotes primary productivity (Ingall et al., 1993; Slomp et al., 2004; Marz et al., 2008; Poulton et al., 2015).

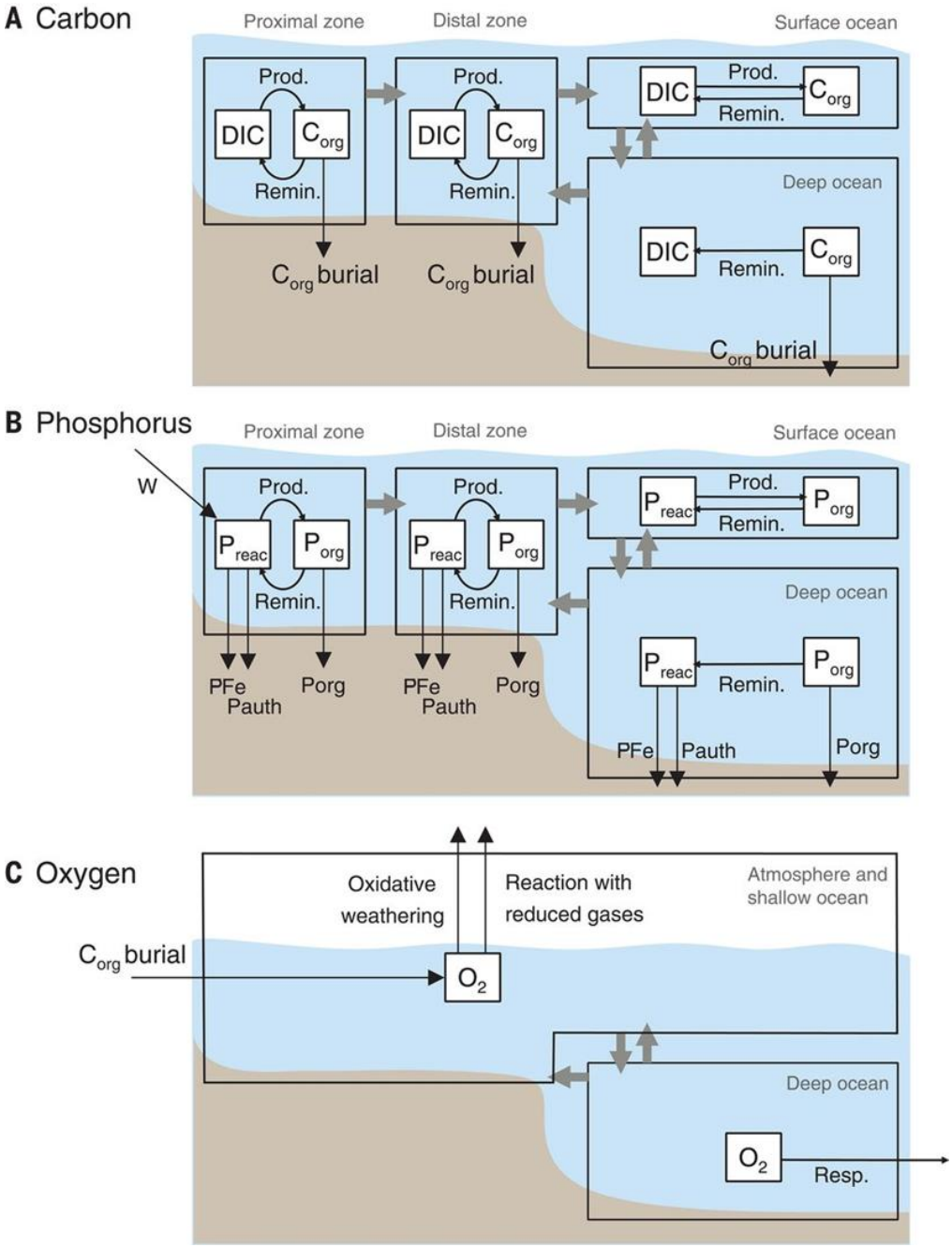

***Figure 1.5**: Carbon, phosphorus, and oxygen cycling. Atmospheric (no background) and oceanic (blue background) box models of elemental sinks. Grey arrows signify the mixing between the different oceanic reservoirs. A: The carbon cycle where carbon exists as dissolved inorganic carbon (DIC), or organic carbon (C_{org}) which is cycled through primary productivity (Prod.) and remineralisation (Remin.). B: The phosphorus cycle where phosphorus is present as reactive phosphorus (P_{reac}) and organic phosphorus (P_{org}) and is brought into the system via weathering (W). C: The oxygen cycle where oxygen can be exchanged from the ocean to the atmosphere and can be taken out of the system through respiration (Resp.). From Alcott et al. (2019).*

1.5 Record of Metazoan fossils through the Ediacaran

Until recently, the first possible evidence for the oldest metazoans are phosphatised animal embryos found in the Doushantuo Formation (Figure 1.1), suggested to be a possible Cnidarian (Xiao et al., 1998), with recent findings of external moulds of nuclei in such embryos (Sun et al., 2020), but there is some debate as to whether these are animal embryos (Bailey et al., 2007; Huldtgren et al., 2011). The Lantian Biota are preserved as carbonaceous compressions and are thought to be older than the typical Ediacaran Biota and are dated between 580 and 635 Ma (Yuan et al., 2011). These biota consist of algae with a fan-shaped morphology and possible tentacled metazoans (Yuan et al., 2013). The distinction between the Lantian and Ediacaran Biotas could suggest that the diversification of macroscopic eukaryotes could have occurred after the Marinoan glaciation in the early stages of the Ediacaran (Yuan et al., 2013).

The first evidence of large body fossils known as the Ediacaran biota were found to be ~579 to 575 Ma in age, from the Avalon Assemblage which include soft-bodied Rangeomorphs (Laflamme et al., 2013). There have also been recent findings of *Palaeopascichnus linearis* stratigraphically below diamicties deposited during the Gaskiers glaciation (580 Ma in age) (Liu and Tindal, 2020) The White Sea Assemblage contains the earliest dickinsonoamorphs, erniettamorphs, bilateralmorphs and kimberellamorphs from sections in Siberia and Australia, with the Lower Shibantan Member of the Yangtze Block, South China, also housing this assemblage (Fedonkin et al., 2007; Zhu et al., 2008; Gehling and Droser; 2009) (Figure 1.6). There have also been recent findings of potential *Dickinsonia* in India (Retallack et al., 2021). The Nama Assemblage houses the lowest diversity of fauna and can be found in the Nama Group, Namibia; Dengying Formation, South China; Wood Canyon, USA; Miette Group, British Columbia; Khatyspyt, Siberia and Chamokamen, Russia (Narbonne et al., 1997; Corsetti and Hagadorn, 2000; Hofmann and Mountjoy, 2001; Chen et al., 2014; Grazhdankin, 2014) (Figure 1.6). These assemblages are thought to be divided

biogeographically and stratigraphically; however, it has been suggested that fossils of both the Avalonian and White Sea Assemblage lived coevally, likely during the transition between the two assemblages (Boag et al., 2016).

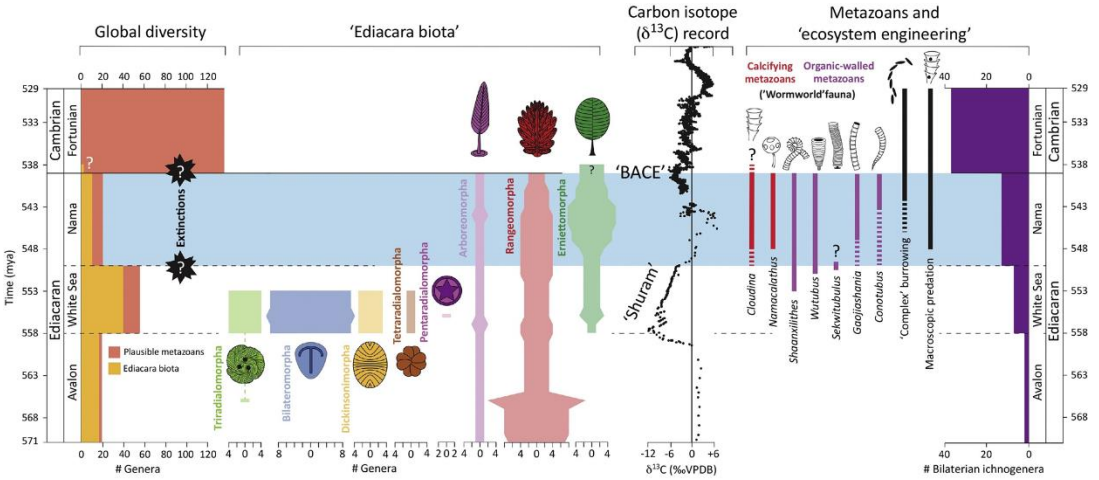

***Figure 1.6**: Diversity of the Ediacaran biota in relation with the carbon cycle. Modified from Darroch et al. (2018).*

The emergence of motile behaviours allowed shallow bioturbation to occur in the sediment during the Ediacaran, which affected chemical and physical mixing of upper sedimentary layers (Figure 1.6). *Kimberella quadrata* was thought to be the oldest mobile bilaterian from the Ediacara Member of South Australia and the White Sea Area in Russia evidenced by scratches in the sediment termed *Radulichnus* (Martin et al., 2000; Fedonkin et al., 2007). However, two recent studies have discovered motile bilaterians with their associated trace fossils. Chen et al. (2019) discovered a trace fossil, evidenced by lateral grooves and some with a chevron like morphology, and associated organism, *Yilingia spiciformis*, which is a segmented bilaterian and is evidence of motility was found in the Shibantan Member of the Dengying Formation (~551-539 Ma; Condon et al., 2005; Okada et al., 2014). *Y. spiciformis* has been attributed to arthropods as the lateral lobes of the organism resemble that of these groups (Chen et al., 2019). There is a correlation between the evolution of segments and motility in bilaterians suggesting that this morphology could have initiated the major overturing of the sediment column during the Cambrian (Couso, 2009; Chen et al., 2019).

Evans et al. (2020) discovered *Ikaria wariootia* with associated trace fossil *Helminthoidichnities* suggesting mobility in the sediment. *I. wariootia* has been proposed to be the oldest bilaterian found in South Australia. This title recently belonged to *Kimberella*, but *I. wariooti* is found stratigraphically lower in the Ediacara Member in Australia (Evans et al., 2020). The fossils of the White Sea Assemblage in the Ediacara Member have been dated between 560 to 551 Ma (Waggoner, 2003; Grazhdankin, 2014).

Bioturbation in the Precambrian was dominated by horizontal burrows which lacked complexity, unlike the evidence of motile behaviour found in Cambrian substrate revolution and the appearance of more complex behaviours, such as traces like *Treptichnus pedum* (Brasier et al., 1994; Droser et al., 1999; Landing, 1994; Bottjer, 2010). However, traces such as *Lamonte trevallis* from the Dengying Formation which, when studied through petrographic sectioning, display features attributed to complex burrowing behaviours which even target and penetrate and mine microbial mats (Chen et al., 2013; Meyer et al., 2014; Xiao et al., 2021), so resembling complex Cambrian traces more than those from the Ediacaran (Darroch et al., 2018). *Lamonte trevallis* has also recently been observed in the Wood Canyon Formation, California (O'Neil et al., 2020). The comparison to Cambrian traces has also been made with other trace fossils of the Deep Spring Formation in Nevada, where complex structures have been found 500 m below the Ediacaran-Cambrian boundary (Tarhan et al., 2020). These complex features of the terminal Ediacaran biota, such as complex microbial behaviour, point toward the notion that the 'Cambrian Explosion' did not occur over a short period of time but, in fact, had roots in the Ediacaran.

The terminal Ediacaran and the early Cambrian saw a wide diversity of animal skeletons, mostly in the form of small shelly fossils, which had not been seen in in older successions in the geological record and is linked to rapid diversification in metazoan body plans (Bengtson, 2004, Smith and Harper, 2013; Zhu et al., 2017). The first skeletal metazoans, *Cloudina* and *Namacalathus*, appear at around 550 Ma and are part of the Nama Assemblage (Grant, 1990) (Figure 1.6).

1.6 Biomineralisation and ecology of metazoans in the Ediacaran

Biomineralisation is the process by which organisms produce minerals, termed biominerals (Lowenstam and Weiner, 1989; Weiner and Dove, 2003). Biominerals are compound materials consisting of both mineral and organic constituents with different attributes in their inorganic equals, such as differences in crystal habits and compositions (Weiner and Dove, 2003). The formation of biominerals provides multiple advantages including protection and structural support.

1.6.1 Biologically-induced vs. biologically-controlled biomineralisation

The passive formation of minerals caused by the interaction between the biological system and the surrounding environment is termed biologically-induced mineralisation (Weiner and Dove, 2003). The lack of biological control is due to the absence of specialised mechanisms, as well as the process of mineral formation takes place in an open environment within the cell which has not been evolved for this function (Lowenstam and Weiner, 1989) (Figure 1.7). As the mineral production is not under biological control, the minerals produced are randomly oriented and vary in size (Weiner and Dove, 2003). However, the metabolic processes of the organism within its environment mediates the composition of the biomineral produced causing a variation in biomineral composition with environment (Frankel and Bazylinski, 2003).

During biologically-controlled biomineralisation, the biological system of the organism has greater control over the biomineralisation process and its environment (Weiner and Dove, 2003). Cellular activities are able to nucleate, grow, and control the morphology and the location where the mineral is deposited (Weiner and Dove, 2003). The formation of biominerals is performed in an area of the cell closed off by a barrier which ions are unable to diffuse through, such as the cell wall membrane or a vesicle (Lowenstam and Weiner, 1989) (Figure 1.7). As biomineralisation is separated from the external environment and the

organism can control the ions extracted, unlike in biologically-induced biomineralisation, mineral composition will be consistent across the whole taxa (Lowenstam and Weiner, 1989).

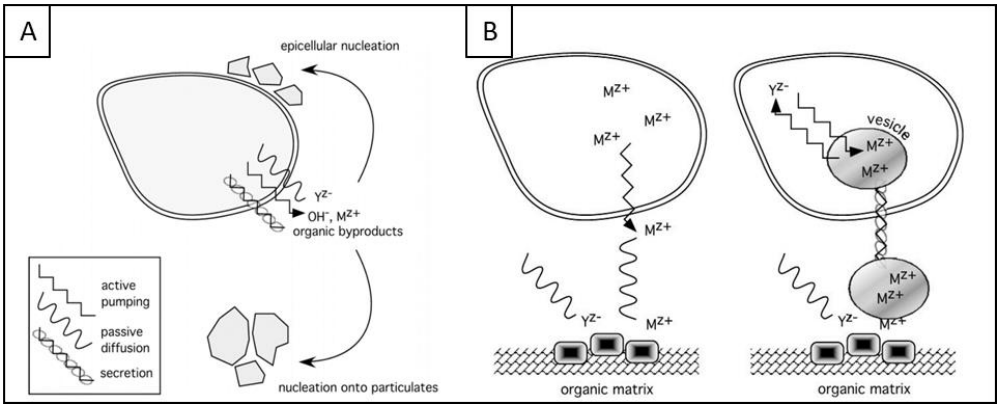

Figure 1.7*: Illustrations of biomineralisation processes.* ***A****: biologically induced biomineralisation caused by metabolic functions without biological control.* ***B****: Extracellular biologically controlled biomineralisation where cations are moved to the nucleation site through extracellular fluid or the cations can be concentrated within the cell and transported to the organic matrix. From Weiner and Dove (2003).*

1.6.2 *Cloudina*

Of the Nama fauna, *Cloudina* is the most studied due to its widespread geographic range making it an excellent index fossil (Grant, 1990). *Cloudina* is a biomineraliser that have a sinuous tube-like morphology (Germs, 1972) formed of nested funnels that lack transverse cross-walls (Hua et al. 2005) (Figure 1.8A and B). *Cloudina* and other similar tubular fossils from this time period, whether skeletal or organic, are informally known as 'cloudinids', a term used to refer to the Cloudinidae family, and 'cloudinomorphs', a term describing a group of form-taxa (Selly et al, 2020). At least seven genera have been attributed to cloudinomorphs (Yang et al., 2020), with the group being transitional across the Ediacaran-Cambrian boundary. Recent work has highlighted a potential new cloudinomorph to add to the groups with *Shaanxilithes* discovered in North China have a nested-funnel tube which was housed within an organic outer tube which could also have an index fossil status, much like *Cloudina* (Pang et al., 2021; Wang et al., 2021).

Cloudina has a smooth inner wall, in which the organism lived, and an outer wall showing annular ridges (Germs, 1972) (Figures 1.8A and B). "Crumpling" (Brain, 2001) and

"irregular folding" (Feng et al, 2003) of the skeletal walls cause layers of the wall to be discordant providing evidence of flexibility potentially pointing towards a possible organic component of the shells (Grant, 1990). Raman point spectra and EDS mapping data from *Cloudina* collected from the Tamengo Formation, Brazil, confirm that the shells have a high concentration of organic matter interpreted as organic sheets that acted as an interface between the biomineral laminae (Becker-Kerber et al., 2017).

Dichotomous branching has been observed in a few cases in *Cloudina* (Hua et al., 2005; Penny et al, 2014) and budding of daughter tubes between two adjacent tubes (Cortijo et al., 2010), both suggestive of asexual reproduction (Figure 1.8C).

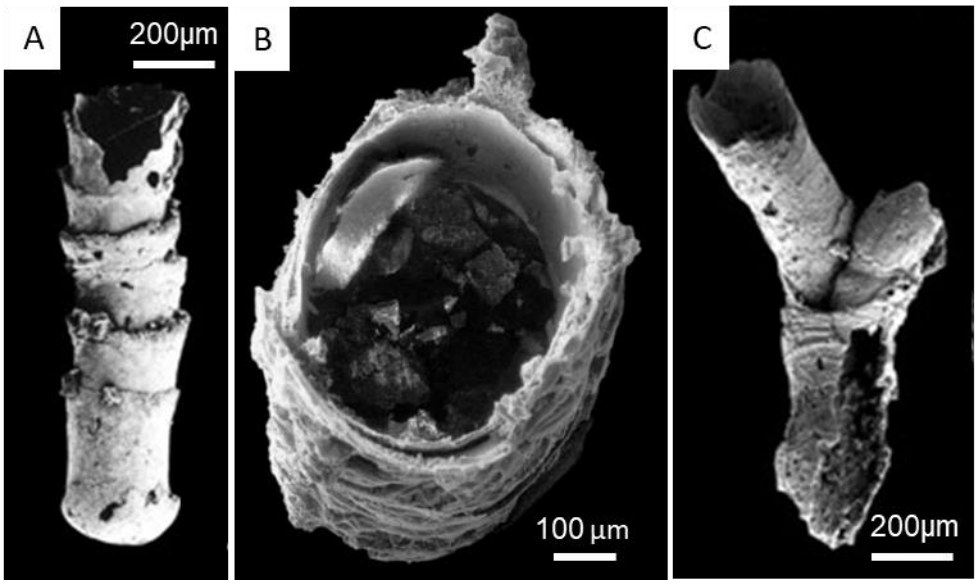

***Figure 1.8**: Cloudina morphology and form of branching. **A**: Longitudinal view of* Cloudina hartmannae *from the Dengying Formation, from Hua et al. (2005) highlighting the funnel-in-funnel structure. **B**: Cross sectional view of* Cloudina riemkeae *nested funnels from the Siberian Platform, featuring a smooth inner wall, from Zhuravlev et al. (2012). **C**: Dichotomous branching in* Cloudina hartmannae *from the Dengying Formation. Daughter tubes bifurcate at the aperture of the parent tube. From Hua et al. (2005).*

1.6.2.1 Ultrastructure and biomineralisation

Zhuravlev et al. (2012) described the microstructure of *Cloudina* tubes as made of thin primary layers (8 to 12 µm) equal to the size of an individual crystal, which fuse together to form secondary laminae (up to 60 µm) (Figure 1.9). While Feng et al. (2003) described the microstructure to be crypto-micrograined with irregularly arranged <1 µm crystals.

The original biomineral composition of *Cloudina* has been assumed to have been aragonite or high-Mg calcite (Morris et al., 1990; Hua et al., 2003, Wood et al., 2011; Zhuravlev et al., 2012; Becker-Kerber et al., 2017). Pruss et al. (2018) suggest *Cloudina* were aragonitic in composition by analysing the $\delta^{44/40}$Ca of *Cloudina* shells collected from the Omkyk Member, Namibia. However, these biominerals have been diagenetically altered depending on fossil location; specimens from Namibia and Oman noted to be dolomitised (Grant et al., 1990; Morris et al., 1990; Wood et al., 2018), while *Cloudina* from China and Spain have been phosphatised (Feng et al., 2003; Zhuravlev et al., 2012). Silicified *Cloudina carinata* are found within the Ibor Group, Spain (Cortijo et al., 2010). Regardless of the differences in preservation and mineralogy, all *Cloudina* shells supposedly have a similar microstructure (Zhuravlev et al., 2012).

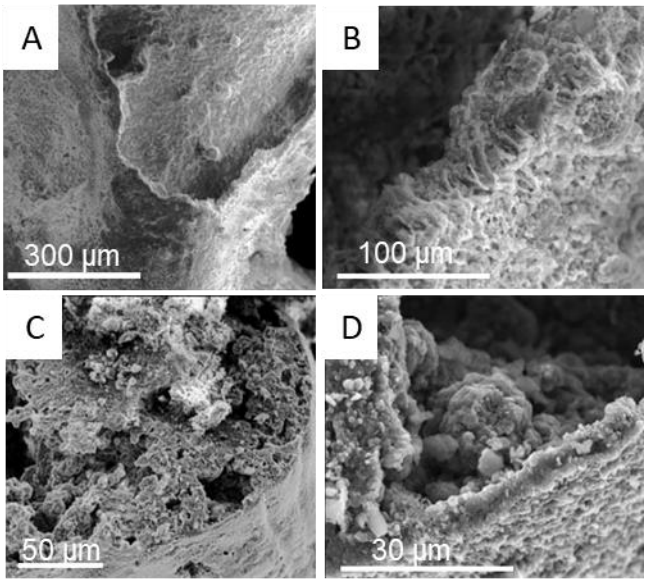

Figure 1.9*: SEM images of* Cloudina *collected from the Siberian Platform highlighting ultrastructure.* ***A****: Fragmented* Cloudina *wall.* ***B****: Higher magnification image of* ***A*** *highlighting microstructure.* ***C****: Fragmented* Cloudina *wall.* ***D****: Higher magnification image of* ***C*** *highlighting microstructure. From Zhuravlev et al. (2012).*

There is speculation as to how *Cloudina* biomineralised. Grant (1990) argues that biomineralisation in *Cloudina* was under minor biological control as there did not seem to be a specialised region where the shell growth took place. Wood et al. (2017) also suggest that biomineralisation was under minimal biological control. However, Zhuravlev et al. (2012)

suggested a two-stage tube formation process where the organism was able to control the formation of a primary layer, which then acted as a template for mineralisation of the interlayer space. This two stage biomineralisation process could also be evidenced where secondary inorganic calcite was precipitated between the funnels after the initial biominerals formed the funnels and fused the funnels through time (Grant et al., 1990; Cortijo et al., 2010). While, even with the evidence of a flexible skeleton, Hua et al. (2005) argue that because the *Cloudina* skeletons lack a radial fibrous ultrastructure this suggests that nucleation and growth of crystals was little influenced by an organic sheet implying that biomineralisation was under minimal biological control. However, SEM analysis of the nanoparticle fabric of phosphatised *Cloudina* shells of the Dengjing Formation indicates biomineralisation in *Cloudina* occurred through the attachment of anhydrous calcium carbonate (ACC) (Gilbert et al. 2019). The nanoparticle fabric is comparable to modern echinoderms, molluscs and cnidarian, and so can be assumed that these clades share the same biominerlisation processes (Gilbert et al. 2019).

However, Yang et al. (2020) recently argued that the presence of the organic lamellae, deduced through Raman spectroscopy, and plastic deformation suggests a primarily organic composition of chitin or collagen, where calcification was entirely post-mortem and diagenetically-mediated.

1.6.2.2 Affinity

Cloudina had been described previously as an alga with similar attributes to that of *Praulopora rarissima*, an early Cambrian calcareous algae (Beurlen and Sommer, 1957; Terleev et al. 2004). However, Grant (1990) suggests, due to the gregarious and filter feeding nature of these organisms and the observation of asexual budding, that *Cloudina* were metazoans.

There are two main schools of thought on the metazoan affinity of *Cloudina*. A cnidarian, especially anthozoan affinity, has been proposed due to the form of reproduction

being similar, with features such as the rapid diameter increase of the daughter tube after branching and a similar diameter of the daughter tubes, but smaller than the parent tube (Vinn and Zaton, 2012). The microgranular ultrastructure of *Cloudina* also resembles that of cnidarians (Vinn and Zaton, 2012).

An annelid affinity is also suggested for *Cloudina*. Hua et al. (2005) note that the morphology, skeletogenesis and asexual reproductions of *Cloudina* are similar to that of serpulid annelids, even though the serpulid walls are thicker and do not consist of nested funnels. Even though dichotomous branching has been linked with a cnidarian affinity, annelids also show evidence of dichotomous budding (Hua et al., 2005). The morphology structure and the ontogeny of *Cloudina* has also been attributed to siboglinid worms, as well as similarities in the environments in which they lived, with *Cloudina* often attached to microbial surfaces and siboglinids to hydrothermal seepage vents (Reitner and Wörheide, 2002). Yang et al. (2020) also concluded that the cloudinid *Zuunia chimidtserent*, of the Zuun-Arts Formation on Mongolia, was of annelid affinity due to a shared ultrastructure and tube construction with siboglinid annellids.

Due to the lack of soft-tissue preservation it has been difficult to determine an affinity for *Cloudina*. Recently, the discovery of pyritised cylindrical structures found within cloudinomorph tubes, *Saarina hagadorni*, from the Wood Canyon Formation, Nevada, USA, have been interpreted as the earliest digestive tracts discovered in the geological record (Schiffbauer et al., 2020). The presence of a through-gut could suggest an annelid affinity rather than cnidarian, as the latter have a two-way digestive system with a coelenteron. Murdock (2020) suggests that if an annelid affinity for cloudinomorphs was true this would represent a further, independent origin of biomineralisation within the annelids.

1.6.3 *Namacalathus hermanastes*

Namacalathus hermanastes, the only species of the genus, is relatively widespread and can be found in multiple Ediacaran localities associated with thrombolitic reefs, including the Nama Group, Namibia (Figure 1.10); the Miette Group, Canada; the Ara Group, Oman; and the Itapucumi Group, Paraguay (Grotzinger et al., 2000, Hofmann and Mountjoy, 2001, Amthor et al., 2003, Warren et al., 2017). *Namacalathus* have also been reported in West and South Siberia (Terleev et al., 2011; Grazhdankin et al., 2015). However, these fossils have a phosphatic skeleton and are far smaller to their calcified counterparts found elsewhere, however size differences have been noted in *Namacalathus* of the Nama Group (Penny et al., 2017). They are also known to have randomly distributed lumens and so may not be part of the *Namacalathus* genus (Penny et al., 2017).

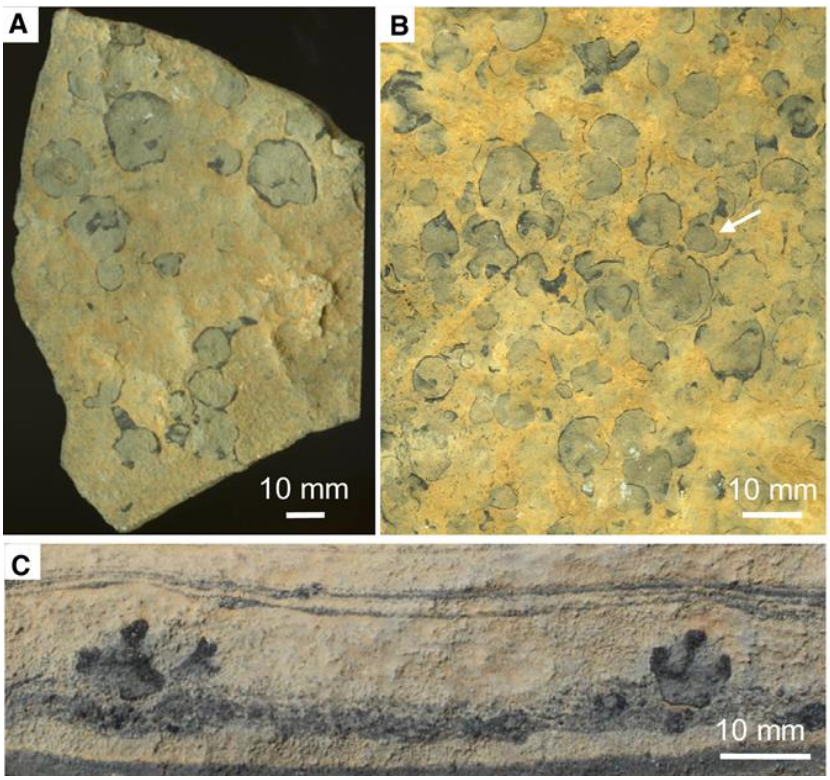

***Figure 1.10**: Bedding plane images of* Namacalathus hermanastes *of the Omkyk Member, Nama Group.* ***A**: Bedding plane view of* Namacalathus, *potentially* in-situ, *with some showing longitudinal sections.* ***B**: An in-situ aggregation of* Namacalathus *on the bedding surface, arrowed cup highlighting budding. The cups are deformed where* Namacalathus *are situated close together.* ***C**:* Namacalathus *with stems anchored on undulating laminae. From Penny et al. (2016).*

The goblet-like morphology of *Namacalathus* is formed of a hollow stem that expands into a cup (3 mm to 35 cm in diameter) with a top opening which curls towards the centre (Grotzinger et al., 2000; Hoffman and Mountjoy., 2001; Penny et al., 2017) (Figures 1.10 and 1.11). Each cup has six or seven regularly arranged holes, called lumen, giving the organism a hexagonal symmetry (Grotzinger et al., 2000).

Like *Cloudina*, *Namacalathus* show evidence of deforming flexibly during compaction, potentially indicating the presence of an organic template on which biominerals precipitated or calcification was relatively light (Grotzinger et al., 2000) (Figure 1.10). Spines have been noted on the outer wall of *Namacalathus* from specimens from the Nama Group, but are rare (Penny et al., 2017). Due to the sharp contrast between sediments found within the cup and surrounding the cup, in terms of texture and colour, it has been suggested that the lumens were not present during life and early deposition indicating a diagenetic feature or that material once covered these holes, such as tentacles, which are now degraded (Grotzinger et al., 2000) (Figure 1.10). Some *Namacalathus* show individuals are sharing cavities, signifying potential asexual internal budding (Wood and Curtis, 2015, Zhuravlev et al., 2015) (Figures 1.10 and 1.11).

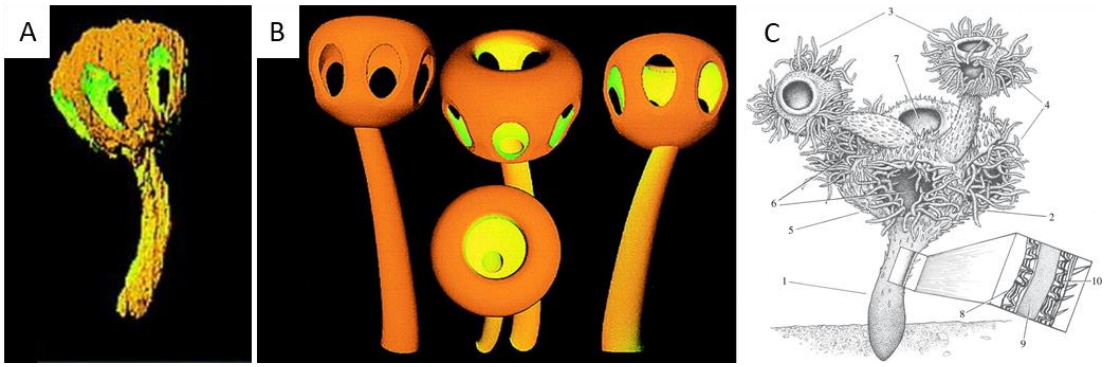

Figure 1.11*: Reconstructions of* Namacalathus hermanastes. ***A****: Tomographic reconstructions of* Namacalathus. ***B****: Mathamatical models, based on serial sectioning of* Namacalathus *from the Nama Group. Both from Grotzinger et al. (2000).* ***C****: Reconstruction of* Namacalathus *from observations made of the fossil, from Zhuravlev et al. (2015).*

1.6.3.1 Biomineralisation

Previously studied *Namacalathus hermanastes*, of the Nama Group, indicate a calcite or high-magnesium calcite skeleton (Grotzinger et al., 2000, Zhuravlev and Wood, 2008, Warren et al., 2017), with the shells being replaced by sparry calcite, but there is evidence of a foliated skeletal structure (Hofmann and Mountjoy, 2001, Zhuravlev et al., 2015). Much like *Cloudina* of the Omkyk Member, Namibia, $\delta^{44/40}$Ca data suggests that the skeleton of *Namacalathus* was of aragonitic composition (Pruss et al., 2018). However, possible *Namacalathus* of Siberia have been noted to have a phosphatic shell (Grazhdankin et al., 2015).

SEM analysis on the ultrastructure of *Namacalathus*, collected from the Nama Group, shows that the skeleton has a tripartite structure of an internal space in between two thin layers (Figure 1.12; Zhuravlev et al., 2012, 2015). This internal space was infilled by randomly orientated rod-like crystals with the external layers having a platy structure (Zhuravlev et al., 2015). An organic matrix has also been inferred due to the organised structure of the skeleton (Zhuravlev et al., 2012).

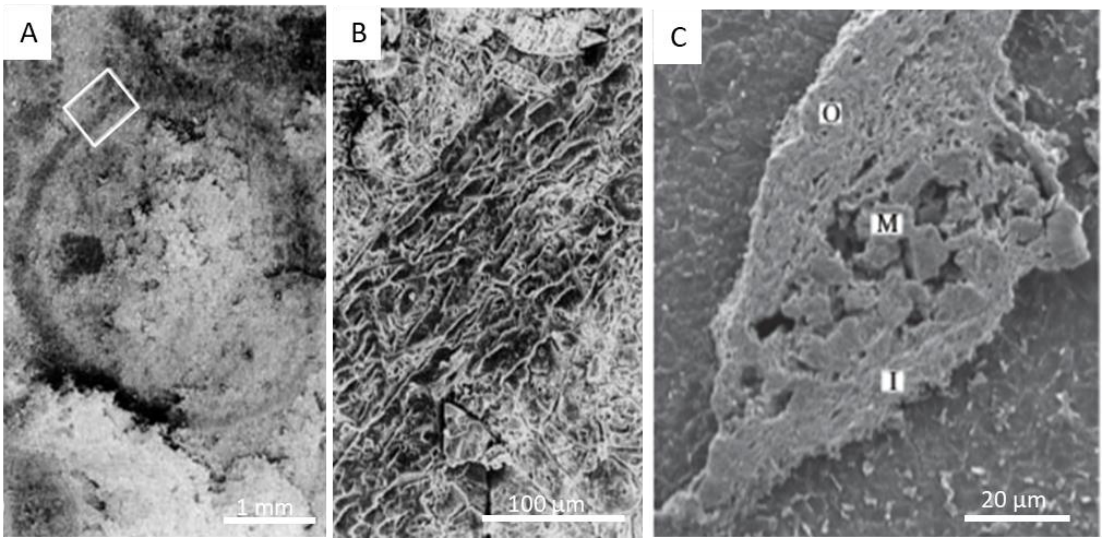

Figure 1.12*: SEM images of* Namacalathus hermanastes *of the Nama Group highlighting the ultrastructure.* ***A****: Cross section of stem.* ***B****: Inset of* ***A****, highlighting elongate, parallel crystals of calcite. From Zhuravlev et al. (2012).* ***C****: Transverse section of the skeletal wall ultrastructure highlighting a tripartite structure a central layer of microdolomite rod-like crystals (M) and a foliated inner (I) and outer (O) layer. From Zhuravlev et al. (2015).*

1.6.3.2 Affinity

The affinity of *Namacalathus* has not been fully resolved. *Namacalathus* has been assigned a protozoan due the lack of accretionary growth and the small size of the organism (Seilacher et al., 2003). However, the goblet-like morphology and hexaradial morphology, due to the presence of lumens, are common in *Namacalathus* is also attributed to cnidarians (Grotzinger et al., 2000). A lophophorate affinity has also been suggested for *Namacalathus* due to the presence of bilaterally symmetrical budding and a tripartite skeletal ultrastructure (Zhuravlev et al., 2015). More recently, a ctenophore affinity has been proposed for *Namacalathus* through phylogenetic analyses and general similarities in morphology with Cambrian dinomischids and scleroctenophores (Zhao et al., 2019).

1.6.4 *Namapoikia rietoogensis*

Namapoikia reitoogensis is a domal organism which amalgamated to form a sheet that could grow up to 1 m in width and 0.25 m in height (Wood et al., 2002) (Figure 1.13). The sheets consist of many adjoined tubules which can reach 5 mm in diameter which show annular features (0.5 to 2.5 mm) (Wood et al., 2002). Transverse structures formed between the tubules linking the vertical structures forming an intricate labyrinth of tubules with voids within the

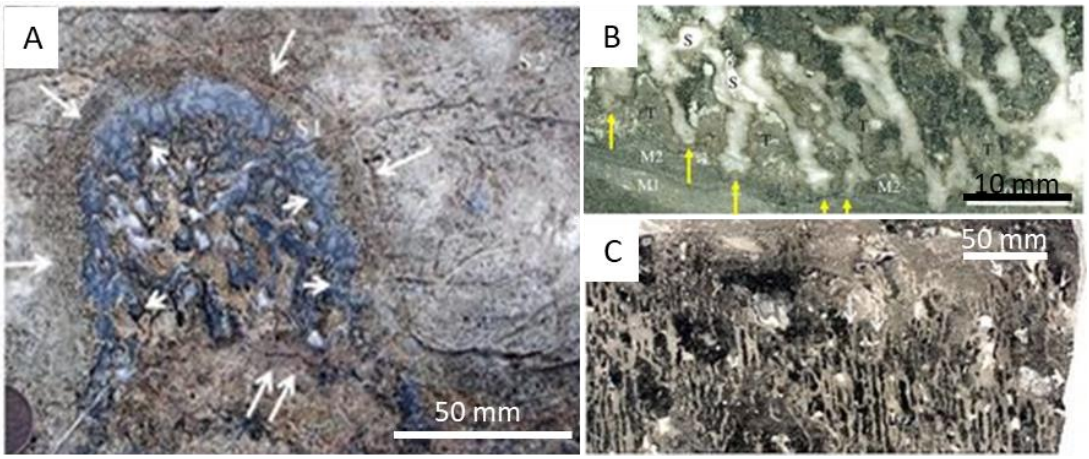

Figure 1.13*: Bedding plane and polished sections of* Namapoikia rietoogensis *of the Omkyk Member, Nama Group.* ***A****: Outcrop photograph of* Namapokia *encrusted on microbialite fissure wall.* ***B****: Longitudinal polished surface of* Namapoikia *showing encrusting onto first generation microbialite (M1) with further generations of microbialite filling pore spaces as* Namapoikia *grows.* ***C****: Longitudinal section of* Namapoikia *highlighting tubules, with possible branching tubules arrowed. From Wood and Penny (2018).*

skeleton (Wood and Penny, 2018) (Figure 1.13C). The spaces between the skeletal tubules consist of aragonitic cement botryoids while the pore space outside the skeleton consists of microbialite or later formed sparry calcite cement (Wood and Penny, 2018). The skeletal microstructure of *Namapoikia* contains coarse sparry calcite, indicating the recrystallisation of the original structure, with an aragonitic original composition suggested (Wood et al., 2002, Zhuravlev et al., 2012) (Figure 1.13).

Namapoikia was an encrusting organism which habited lithified thrombolite and unlithified microbialite and can be found within fractures within microbialite structures (Wood and Penny, 2018). Evidence of repeated encrustation on multiple generations of the microbialite and the interfingering texture of the microbialite and skeletal material suggests growth for each structure occurred simultaneously showing the organisms grew with the microbialite (Wood and Penny, 2018) (Figure 1.13B).

1.6.4.1 Biomineralisation

The lack of an original microstructure of *Namapoikia* causes difficulty in determining how this organism biomineralised. However, an organic matrix may have been present before biomineralisation took place due to the rapid formation of skeletal material as well as the evidence of septum-like structures in younger areas of the skeleton, and biomineralisation occurred due to the formation and thickening of the organic component which calcified with time (Wood and Penny, 2018).

1.6.4.2 Affinity

Antcliffe et al. (2014) suggest that the morphology of *Namapokia* could potentially show the calcification of a microbial colony, with others suggesting a protozoan affinity (Seilacher et al., 2003). Even with the primitive morphology of these organisms, the affinity of microbial colony or skeletal protozoan has been discounted due to the elements of the

skeletal structure being free-standing (Wood and Penny, 2018). However, the cross-linked walls resemble that of tabulate corals and poriferans. The tubules of *Namapoikia* show lateral branching and longitudinal fission, which is a feature attributed to porifera (Scrutton, 1987; Wood and Penny, 2018). Living poriferans also have an organic scaffold in which biomineralisation can occur and is inferred for this taxon (Wood and Penny, 2018). These features have led to the claim that *Namapoikia* is a poriferan. If a sponge affinity for *Namapoikia* is correct it could show the earliest evidence for the co-option of the 'biomineralisation toolkit' which was inherited from the last common ancestor of metazoan biomineralisation (Germer et al., 2015; Wood and Penny, 2018; Murdock 2020). According to molecular clocks data, poriferans originated during the Cryogenian and the appearance of evidence, such as biomarkers and fossil evidence, of poriferans predate the Ediacaran suggesting the poriferan affinity is possible (Antcliffe et al., 2014).

Recently, Mehra et al. (2020) suggests that the septal and inter-septal thicknesses of *Namapoikia* is large for a calcified demosponge and these thicknesses are highly variable. *Namapoikia* has been attributed to a microbially mediated sedimentary construction due the lack of tabulae, according to the 3D models produced, with tubule elements which branch and produce the labyrinth structure with septa found within thrombolite communities, as well as the void areas (Mehra et al., 2020). However, only two specimen were sectioned and so the features described by Wood and Penny (2018) may not have been captured due to the small sample size. Despite this, 3D models are useful for in understanding the morphology of these organisms but understanding the biomineralisation style might be the key in interpreting the affinity of *Namapoikia*.

1.6.5 Ecology of Ediacaran skeletal metazoans

Skeletal Ediacaran organisms are sessile creatures and are known to have been attached to stromatolitic and thrombolitic biostromes (Grotzinger, Watters, and Knoll 2000;

Warren et al. 2011; Becker-Kerber et al., 2017; Wood et al. 2017a) (Figure 1.14). This may be due to the microbial mat communities providing oxygen oases during the day which lowered the metabolic cost of biomineralisation (Sahoo et al., 2016; Xiao et al., 2019).

The living habit of *Cloudina* was complex as they inhabited a range of different carbonate substrates including microbial mats, thrombolites and reefs (Cai et al., 2014; Penny et al, 2014; Becker-Kerber et al., 2017; Wood et al., 2017, Álvaro et al., 2019) (Figure 1.14). Honeycomb-shaped imprints from Ediacaran deposits of South China, interpreted as moulds of *Cloudina*, potentially give evidence of vertical growth (Cai, et al., 2014). Becker-Kerber et al. (2017) describe a horizontal living habit for *Cloudina* in the Tamengo Formation, interpreted as being *in-situ* due to the presence of fine features (such a planges) and evidence of microbialite-*Cloudina* interactions indicating no transport.

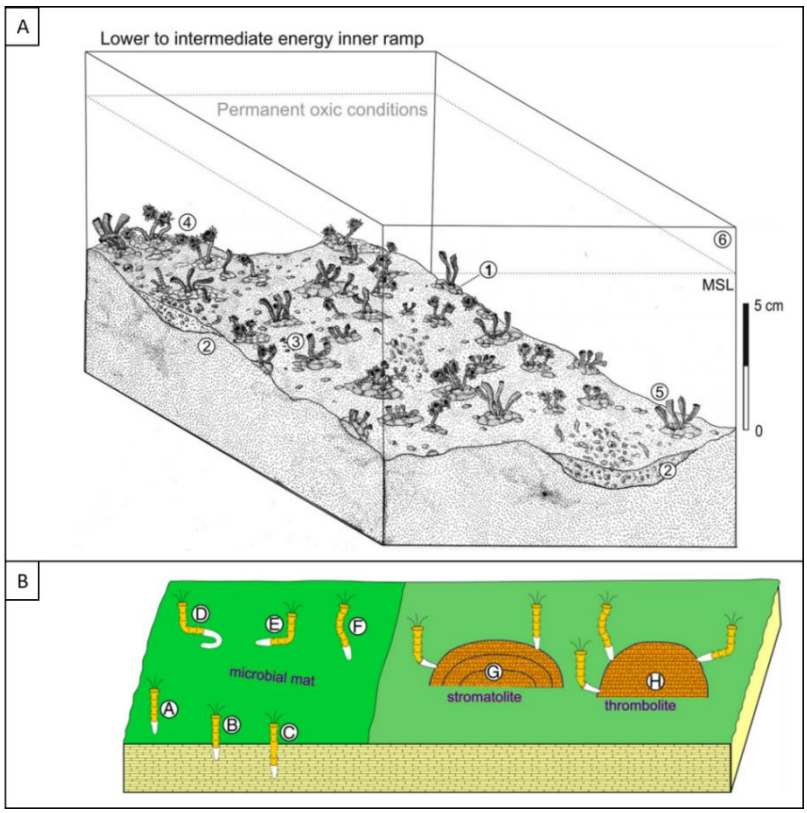

Figure 1.14*: Examples of* Cloudina-Namacalathus-Corumbella *ecological associations and different life modes of* Cloudina *with interactions with microbial mats and biostromes/bioherms.* ***A****: Reconstruction of ecology and mode of life of* Cloudina, Namacalathus *and* Corumbella *indicating attachment to microbial mats. From Warren et al. (2017). 1 – thrombolites, 2 – shell beds, 3 –* Cloudina, *4 –* Namacalathus, *5 –* Corumbella. ***B****: Reconstruction* Cloudina *life positions. From Cai et al. (2014).*

Namacalathus are also known to inhabit the same microbial environments as *Cloudina* (Figure 1.14A). However, size variation of *Namacalathus* have also been noted in the Nama Group where larger forms are found in low energy inner ramp environments and outer ramp environments housed smaller forms. External factors, such as water depth, substrates and hydrodynamic conditions, could have an influence on their size (Penny et al., 2017). *Namapoikia* are only found within neptunian dyke complexes within Ediacaran reef structures (Wood et al., 2002; Wood and Penny, 2018) (Figure 1.15).

It was previously thought that the diversity of these terminal Ediacaran reefs was low, but field evidence from Namibia show that reefs were diverse and complex (Wood et al., 2002; Wood and Curtis, 2015) (Figure 1.15). Tiering is found within these reef systems with *Namacalathus* and *Cloudina* living within and on the surface of reef mounds, and *Namapoikia* within crypts and fractures within the microbialite reefs (Wood et al., 2002; Penny et al., 2014) (Figure 1.15).

Ediacaran microbial-metazoan reefs in Namibia are found within the Omkyk Member of the Nama Group within a carbonate succession housing microbial reefs at Driedoornvlakte Farm, in the Zaris Subbasin (Penny et al., 2014). The reef consists of amalgamated *Cloudina* attached by a meniscus-like cements to form a *Cloudina* supported reef framework (Penny et al., 2014). These cements are interpreted as skeletal and were produced by the *Cloudina* as they formed before the early forming aragonitic botryoids which nucleate from or abut against the meniscus cements and the *Cloudina* tubes (Penny et al., 2014). However, these cements have also been described as inorganic in origin (Grant et al., 1990, Cortijo et al., 2010).

Mehra and Maloof (2018) argue that the reefs are not built or supported by *Cloudina*, rather these structures are aggregates of transported shells due to the lack of *Cloudina* ornamentation, absence of basal apical ends and the spread of orientation of the *Cloudina* shells suggest deposition. However, the *Cloudina* reef hypothesis is supported by field observations described by Penny et al. (2014) and Wood and Curtis (2015) including the meniscus like cements amalgamating the *Cloudina* as well as early botryoidal cements infilling

primary cavities. Also, *Cloudina* supported reefs have been found in other locations, such as the Villarate Formation of the Ibor Group, Spain (Álvaro et al., 2020). Here, *Cloudina* tubes are preserved in an upright position which have been enveloped in a microbialite which suggests *Cloudina* acted as a pioneer frame-building taxa (Álvaro et al., 2020).

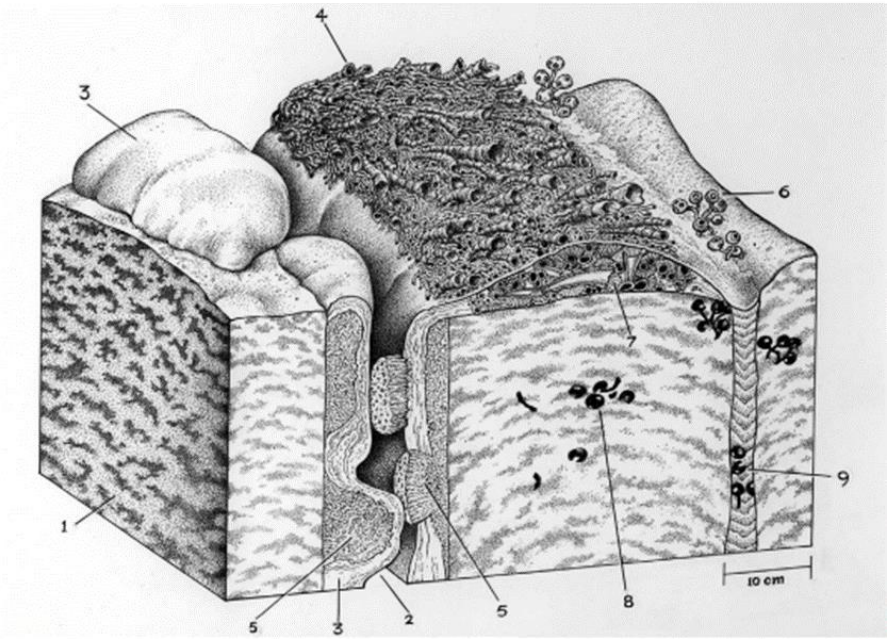

Figure 1.15*: Reconstruction of* Cloudina*-supported reef of the Nama Group, Namibia and associated features. 1 – thrombolite; 2 – neptunian dyke; 3 – stromatolite; 4 –* Cloudina*; 5 –* Namapoikia*; 6 –* Namacalathus*; 7 – aragonitic botryoids; 8 - entrapped* Namacalathus*; 9 – sediment. From Penny et al. (2014).*

1.7 Triggers of biomineralisation during the Ediacaran

Groups of biomineralising organisms have close relatives which do not biomineralise and so point towards convergent or parallel evolution at a phylum level (Murdock and Donoghue, 2011). The 'biomineralisation toolkit' was thought to be a group of genes which were co-opted from a common suite of genes or it represents the inheritance of a biomineralising gene regulatory network from a common ancestor which biomineralised (Livingston et al., 2006; Jackson et al., 2007; Murdock and Donoghue, 2011). A study by Murdock (2020) where the distribution of skeletons was plotted against a phylogeny of metazoans and an ancestral state reconstruction adds to this hypothesis. The data suggest that

there were multiple instances of biomineralisation evolution through gaining the ability to produce an organic skeleton and the genetic toolkit; this then led to the acquisition of skeletal tissues that through time came under increasing biological control (Murdock and Donoghue, 2011; Murdock, 2020) (Figure 1.16A).

It is suggested that the Ediacaran biomineralisers were under limited biological control. *Sinotubulites* is thought to produce aragonitic biominerals where *Cloudina* formed either aragonitic or high-Mg calcite (Chen et al, 2008; Wood, 2011; Pruss et al., 2018). However, Cambrian groups, such as brachiopods and molluscs, have more complex biomineralisation patterns. Within the lophotrochozoan group biomineralisation was acquired independently but all have features such as pores, an organic-rich shell, and a periostracum (an outer layer of the shell which protects the biominerals from dissolution) (Vendrasco et al., 2011). Biomineralising lophotrochozoans also have a soft-bodied ancestor and a common ancestor which allowed for the inheritance of a chitinous scaffold which became mineralised with different biominerals in different lineages (Vendrasco et al., 2010; Murdock 2020).

The skeletal forms of earlier metazoans are less consistent than more recent forms of biomineralisation, i.e. the early animal skeletons had an organic scaffold inherited from a common ancestor with biomineralisation under minimal control but through time the skeletal form has become more complex (Wood, 2011, Murdock, 2020). As biologically-controlled biomineralisation produces biominerals in areas isolated from the surrounding seawater, the sea water chemistry is not thought to have a direct influence on biomineral mineralogy (Weiner and Dover, 2003). However, the production of biominerals which are not favoured by the seawater chemistry have a greater metabolic cost and so biominerals were produced with similar compositions to the surrounding seawater, the composition of which remained throughout the taxa in the case of carbonate minerals (Stanley and Hardie, 1998; Porter, 2007) (Figure 1.16B). This could suggest that the origin of biomineralisation may have been influenced by both biological and environmental factors as the ‘biomineralisation toolkit’

provided the scaffold and processes needed to produce biominerals, but environmental factors influenced the composition of the biominerals.

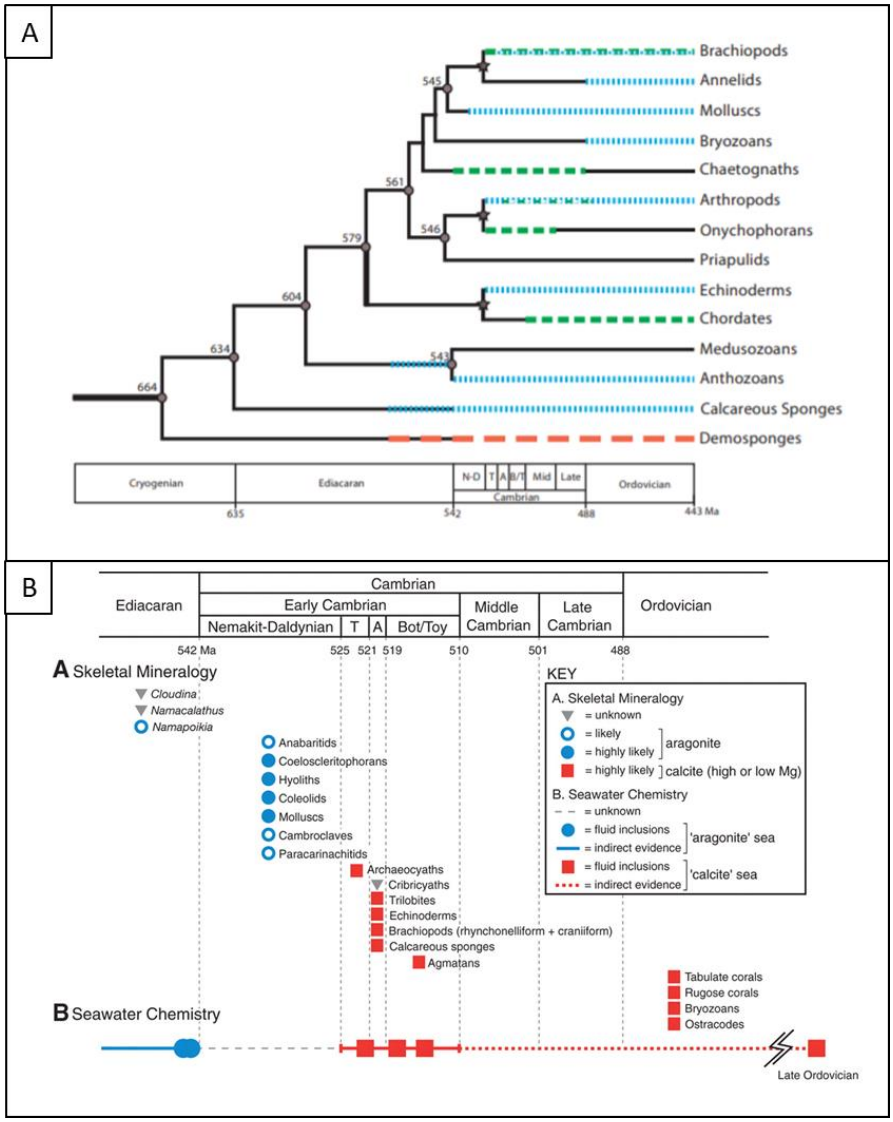

***Figure 1.16**: Distribution of biomineralisation through time and phyla. **A**: The origination points of animal skeletons and mineralogy from the Precambrian to Ordovician. Coloured lines correspond to different composition of skeletons: green dashed lines signify calcium phosphate whilst blue dashed lines and red dashed lines show calcium carbonate and silica compositions, respectively. From Murdock and Donoghue (2011). **B**: First appearance of calcium carbonate skeleton in association with seawater chemistry through time, where there is a correlation between the composition of the skeletons produced and the seawater. From Porter (2007).*

1.7.1 Biological trigger

Predation has been suggested as a biological trigger for biomineralisation as the formation of biominerals can act as a form of protection. Supposed borings have been noted in *Cloudina* in the Dengying Formation, China (Hua et al., 2003) and the Tamengo Formation in Brazil (Becker-Kerber et al., 2017) and have been attributed to the oldest form of predation and prey selectivity, as these holes are only found in *Cloudina* (Bengtson and Zhao, 1992; Hua et al., 2003; Chen et al., 2008) (Figure 1.17). The predatory borings in the *Cloudina* skeleton range from perfectly to irregularly circular in shape and have a positive correlation with the width of the *Cloudina* shell (Bengston and Zhao et al, 1992).

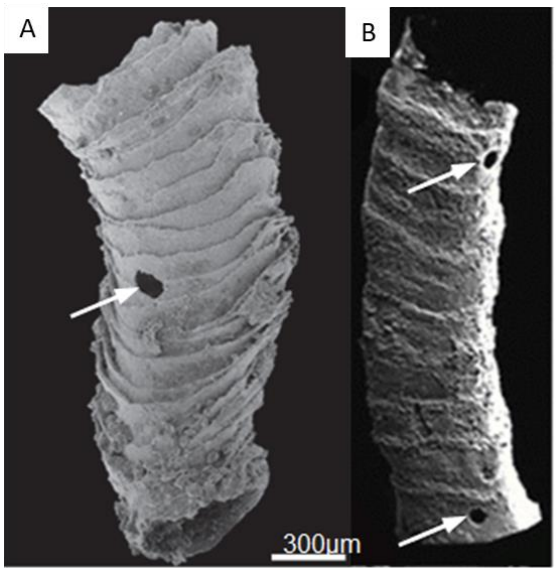

Figure 1.17: *Examples of* Cloudina *with small, circular holes of potential borings penetrating the annulated outer wall (arrowed). From* ***A****: Bengston and Zhao (1992);* ***B****: Hua et al. (2003).*

However, these holes may have been misinterpreted and were not formed by predation. It has been suggested by Debrenne and Zhuravlev (1997) that these holes formed due to the dissolution of microdolomite, but this forms a more quadrangular outline, and does not account for the circular shape of the holes (Zhuravlev et al., 2012). The attachment of ectoparasites have also been suggested for the formation of these holes but fixation scars are not present (Kowalewski and Kelley, 2002; Becker-Kerber et al., 2017). Nevertheless, the shape and lack of perforations around these holes may be due to weathering and

recrystallisation. However, these holes are found at consistent distances from the open end of the *Cloudina* tube (Bengston and Zhao, 1992). This feature could suggest the potential predator targeted areas where there would be living tissue and not areas where the organism may have potentially abandoned, but far enough away from the open end in order to avoid any defence from the *Cloudina* organism.

Even though the rough, annulated outer surface of *Cloudina* is thought to have acted as a defence to the organism living inside the biomineralising tube (Bicknell and Paterson, 2017), predation is an unlikely promoter of biomineralisation as the borings are still seen to penetrate the shell. Biomineralisation originated in microorganisms between 812-717 Ma, with the formation of supposed phosphatic skeletons in algae (Cohen et al., 2011). The appearance of biomineralisation at this time indicates that the epigenetic pathways for biomineral production was present before this first evidence of macropredation (Cohen, 2005) and potentially suggests a genomic cause for biomineralisation. It is due to this that predation is an unlikely trigger for, but it may have acted as a contributing factor to, the formation of skeletons and the rapid diversification of the Cambrian Explosion (Bengston and Zhao, 1992; Murdock, 2020).

1.7.2 Environmental trigger

Changes in seawater chemistry may have encouraged biomineralisation in macrofauna in the terminal Ediacaran. The decrease in ocean Mg/Ca ratios allowed for the formation on "aragonitic seas" at around 545 Ma, (Wood et al., 2017b). The change from the "dolomitic seas", which were mostly ferruginous anoxic, favoured biomineralisation due to the slow kinetics of dolomite which makes it an unsuitable mineral to produce biominerals (Wood et al., 2017b). Wood et al. (2017b) suggested that the change to "aragonitic seas", as evidenced by data collected on the Siberian Platform, was due to the increase in continental weathering which increased the input of calcium into the seawater which lowered the Mg/Ca ratio.

The production of biominerals has a great metabolic cost, but the oxygenation of the water column throughout the Ediacaran would lower the metabolic cost of forming structural collagen and skeletal structures (Towe, 1970; Wood et al., 2017b). Oxygenation is not a cause of biomineralisation but it removed or lessened the biological barriers present, i.e., reducing the metabolic cost of producing biominerals, especially in areas of high alkalinity (Knoll and Carroll, 1999; Brennan et al., 2004; Wood et al., 2017b). As previously stated, the major biomineralising taxa are likely unrelated and the biomineralisation process is acquired at the same time suggesting that there must have been an external factor to trigger biomineralisation in macrofauna, whether environmental or predational. However, Ediacaran biomineralised fauna are found mainly within carbonate successions, with the soft-bodied equivalents found in clastic units, such as *Conotubus* and *Corumbella* (Wood et al., 2017b). Also, skeletal taxa are not recorded in Ediacaran rocks which were deposited in low-oxygen, manganous water conditions (Tostevin et al., 2016b; Wood et al., 2017b). These observations act as possible evidence that seawater chemistry, particularly calcium and oxygen concentrations in the seawater, influenced biomineralisation (Wood et al., 2017b).

1.8 Thesis aims and hypotheses

This thesis contributes to the understanding of the potential controls behind a transition to more oxic conditions in the terminal Ediacaran using a method previously untested on sedimentary rocks of this age, phosphorus speciation. The integration of these data and previously collected Fe speciation data as well as palaeontological diversity allows for a multi-proxy approach to this problem from a 4D transect of the Nama Basin

The affinity of the skeletal Ediacaran taxa, such as *Cloudina* and *Namacalathus*, are still unresolved. Due to the lack of soft tissue and specific diagnostic features preserved in Ediacaran assemblages, it has been difficult to determine the affinity of skeletal organisms that lived during this time.

Overall, this thesis aims to:

Chapter 2: Present new phosphorus speciation data from clastic sediments from multiple sites in the Nama Group to understand phosphorus and nutrient cycling in the Nama Basin in the terminal Ediacaran. These data will be compared with previously collected redox data in order to determine a trigger behind the transition to more stable oxic conditions in the Nama Basin after 545 Ma.

Hypothesis: Changes in nutrient cycling, particularly phosphorus, controlled the rise and stabilisation of oxygen within the water column of the Nama Basin which influenced the radiation of more metabolically costly modes of life of Ediacaran organisms in the basin.

Chapter 3: Present new observations of *in-situ* cloudinomorphs associated with microbial mats within the Upper Omkyk Member of the Nama Basin using serial sectioning and 3D modelling.

Hypothesis: Cloudinomorphs can have multiple branching sites

Chapter 4: Present new data on cloudinomorphs from different localities from the Nama Group, of the same age, to further understand biomineralisation in cloudinomorphs and the diagenetic history of each site.

Hypothesis: The type and extent of mineralisation and morphology of *Cloudina* was controlled environmentally.

Chapter 5: Present new findings of a taphonomically unique Lagerstätte where *Namacalathus* are pyritised and preserved in 3D collected from the Omkyk Member, Nama Group.

Hypothesis: Pyritisation of *Namacalathus* has preserved soft tissue features not previously recognised, which in turn are suggestive of a lophotrochozoan affinity.

1.9. Geological Setting: Nama Group, Namibia

The Nama Group (ca. 550 – 541 Ma) is a ~3000 m thick fossiliferous succession deposited in two subbasins, the Zaris and the Witputs Subbasins (Germs, 1983) (Figure 1.18). The sedimentary succession consists of carbonates and clastic sediments which document a marine shelf and fluvial environments which infill the foreland basin on the Kalahari Craton which formed during the collision along the Damara and Gariep orogenic belts to the north and west, respectively (Saylor et al., 1995; Saylor and Grotzinger., 1996). The base of the Nama Group is an unconformity which can be traced for around 1000 km (Germs and Gresse, 1991). Ash bed dates and inferred sedimentation rates suggest the basal Nama unconformity is ca. 550–553 Ma (Saylor et al., 1998). The top of the Schwarzrand Group is younger than at least 539.64 ± 0.19 Ma, determined from ash beds collected from the Spitskop Member (Linnemann et al., 2019).

The Kuibis Subgroup is overlain by the Schwarzrand Group within both subbasins which are separated by the Osis Arch (Germs et al., 1983; Saylor et al., 1995) (Figure 1.18B). Due to the arch stratigraphic units thicken the more distal the sediments are (Germs, 1983). The sediments of both subbasins have been correlated using sequence stratigraphy and chemostratigraphy, such as inorganic ^{13}C values in Nama Group carbonates (Kaufman et al., 1991; Saylor et al., 1995).

In general, the Nama Basin became more oxygenated throughout deposition during the Ediacaran. During the deposition of the Kuibis Subbgroup, there was redox stratification within the water column (Wood et al., 2015). A marine transgression, which occurred during the deposition of the Lower Kuibis Sediments (the Lower Omkyk Member of the Zaris Subbasin and the Mara and Kilpoek Members of the Witputts Subbasin) caused the shallowing of the chemocline and so these waters were dominantly anoxic ferruginous (Wood et al., 2015; Tostevin et al., 2016b). Oxygenation follows in the upper Kuibis Subbgroup and into the lower Schwarzrand Subgroup in basinal and inner-shelf environments, but there were short periods

of anoxia within the mid-ramp environments (Wood et al., 2015, Bowyer et al., 2020). Oxygenation continues into the Upper Schwarzrand Subgroup (Wood et al., 2015; Bowyer et al., 2020). This is also evidenced by the appearance of trace makers within the Nudaus Formation, within he Lower Schwarzrand Subgroup of the Zaris Subbasin, which suggest a stable oxygenated environment (Bowyer et al., 2020).

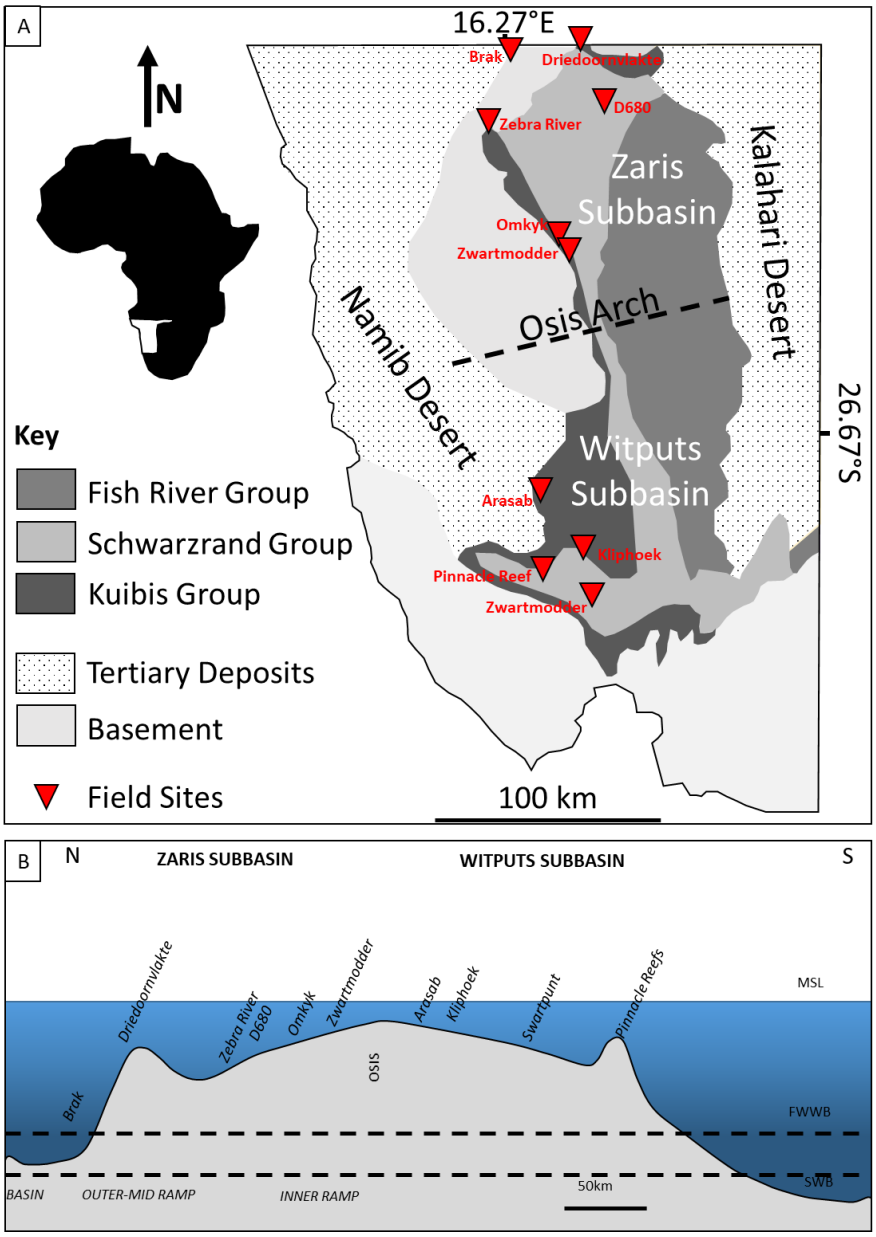

***Figure 1.18**: Geological map with cross section of thew Nama Basin to show location of field sites. **A**: Geological map with field site location. Modified from Grotzinger and Miller (2008). **B**: Schematic of the Nama Basin with field site location. Modified from Wood et al. (2015).*

1.9.1 Sampling localities

The position and co-ordinates of all sample localities are given in Fig. 1.18 and Table 1.1, and the geological setting for each is detailed below.

Table 1.1: co-ordinates of sampled localities from the Nama Group, Namibia, split by subbasin.

Subbasin	Location	Latitude	Longitude
Zaris	Zwartmodder	24°53'41.00"S	16°19'31.00"E
	Omkyk	24°48'19.00"S	16°13'45.00"E
	Zebra River	24° 30' 49.38" S	16° 12'13.24" E
	Driedoornvlakte	23° 51' 36.83" S	16° 39' 50.57" E
	Brak	23°58'17.00"S	16° 8'6.50"E
	D860	24°05.5922"S	016°59.801"E
Witputs	Arasab	26°53'15.00"S	16°24'47.00"E
	Farm Kliphoek	27°17.088"S	016°46.793"E
	Pinnacle Reefs	27°27’52.70"S	16°3’40.60"E
	Swartpunt	27°28'29.00"S	16°41'33.00"E

1.9.1.1 Driedoornvlakte (Kuibis Subgroup)

The succession at Driedoornvlakte consists of ~47 m of the Kaines member and is overlain by the Lower Omkyk Member (~60 m thick) and the Upper Omkyk Member (~380 m thick) (Wood et al., 2015). The Lower Omkyk Member (OS1) consists of mostly carbonate grainstones with the Upper Omkyk Member (OS2) is dominated by microbial reefs, mostly stromatolites and thrombolites (Grotzinger et al., 2000) (Figure 1.19).

The reef complex is located in OS2 and consists of thrombolitic limestones and grainstones (Wood et al., 2015) (Figure 1.19). The carbonate platform of OS2 experienced three accommodation cycles. The first cycle is a coarsening upward sequence topped by massive dolostones which overly stromatolities and thrombolites and produced a flat-topped platform (Adams et al., 2004). The second cycle formed a ‘bucket-shaped geometry’ which contains thrombolite mounds with columnar stromatolites are more common on the platform interior (Adams et al., 2004). The third cycle led to the drowning of the interior, but the mid-

ramp platform was able to keep up with the rising sea level forming a pinnacle reef consisting of thrombolites flanked by shale (Adams et al., 2005; Wood et al., 2015). The pinnacle reefs were later drowned and covered by the Urikos Member, which consists of shales (Wood et al., 2015).

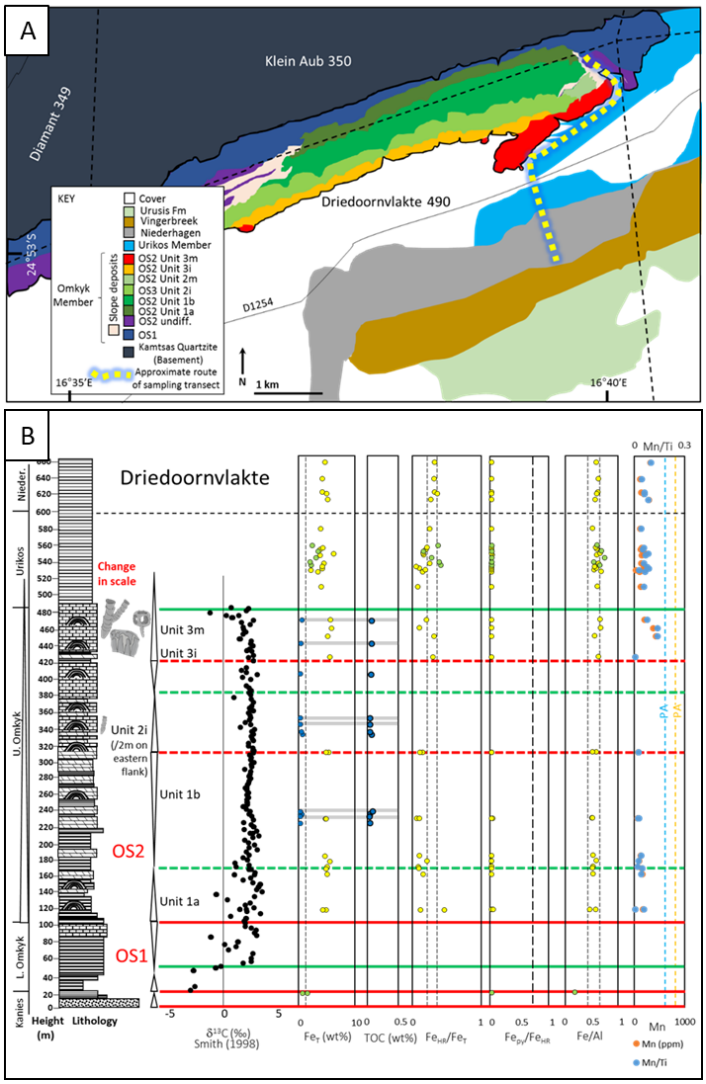

***Figure 1.19**: Geological setting, sedimentary log and geochemical data of Driedoornvlakte. From Bowyer et al. (2020). **A**: Geological map of the Driedoornvlakte field site including the reef, map is redrawn after Adams et al. (2004) and 1:250000 map of Rehoboth area, Geological Survey of Namibia, Ministry of Mines and Energy. **B**: Stratigraphic log and geochemical data, including occurrences of fossil data, section redrawn after Wood et al. (2015).*

Multiple biomineralising Ediacaran fauna are found at this locality. *Cloudina hartmanae* have also been noted to produce a free-standing reef framework without an internal microbial component (Penny et al., 2014). *Cloudina riemkeae* and *Namacalathus* form reefs, up to 20 m in height and width, at this site in association with microbialites and thrombolites

and have also been noted in a cryptic setting (Wood and Curtis, 2015). The *Namacalathus* aggregations are monospecific that proceed the *Cloudina riemkeae* accumulation (Wood and Curtis, 2015). *Namapoikia* are also found at Driedoornvlakte within synsedimentary neptunian dykes (Wood et al. 2002).

Carbon isotope values at Driedoornvlakte range between -3.5‰ and 2‰ from the base of the Kanies Member and through to the reef, respectively (Smith, 1988; Wood et al., 2015) (Figure 1.19). Fe speciation, TOC values and Fe_T data indicate predominant oxic conditions throughout the deposition of the succession (Wood et al., 2015; Bowyer et al., 2020) (Figure 1.19).

1.9.1.2 Zebra River (Kuibis Subgroup)

The Omkyk and Hoogland Members crop out at Zebra River. OS1 (dominated by grainstones) and OS2 (dominated by microbial mat facies with grainstones and shales) can both be sampled at this site (Johnson and Grotzinger et al., 2006; Wood et al., 2015) (Figure 1.20). The thrombolite-stromatolite reefs form continuous biostrome layers in up-dip areas, which form patch-reefs, down-dip, in other areas of the Zebra River Valley (Grotzinger et al., 2000). A large biostrome at the top of OS2 is found within a highstand system tract which potentially corresponds with the reef complex found at Driedoornvlakte (Smith, 1999; Grotzinger et al., 2005). The sheet-like continuous biostromes are different to that of the pinnacles at Driedoornvlakte due to accommodation space differences, with patch-like biostromes down-dip (Grotzinger et al., 2000; Grotzinger et al., 2005). The form of biostrome between the two sites vary with domal thrombolites being absent from Zebra River, unlike at Driedoornvlakte (Grotzinger et al., 2005).

Grotzinger et al. (2005) noted that the biostromes had varying microbial fabrics, ranging from stromatolities to thrombolites which featured columnar stromatolites at Zebra River. *Cloudina reimkeae*, *Cloudina hartmannae* and *Namacalathus* have been observed

within the inter-column infill with micrite or dolomitised micrite, with *Namacalathus* also found on top of the thrombolite columns (Grotzinger et al., 2000; Grotzinger et al., 2005) (Figure 1.20).

The Hoogland Member overlies the Omkyk Member and comprises of storm-dominated interbedded limestone laminites which shallows up to a grainstone facies (the Lower Hoogland Member) and limestone laminites (the Upper Hoogland Member) (Wood et al., 2015) (Figure 1.20).

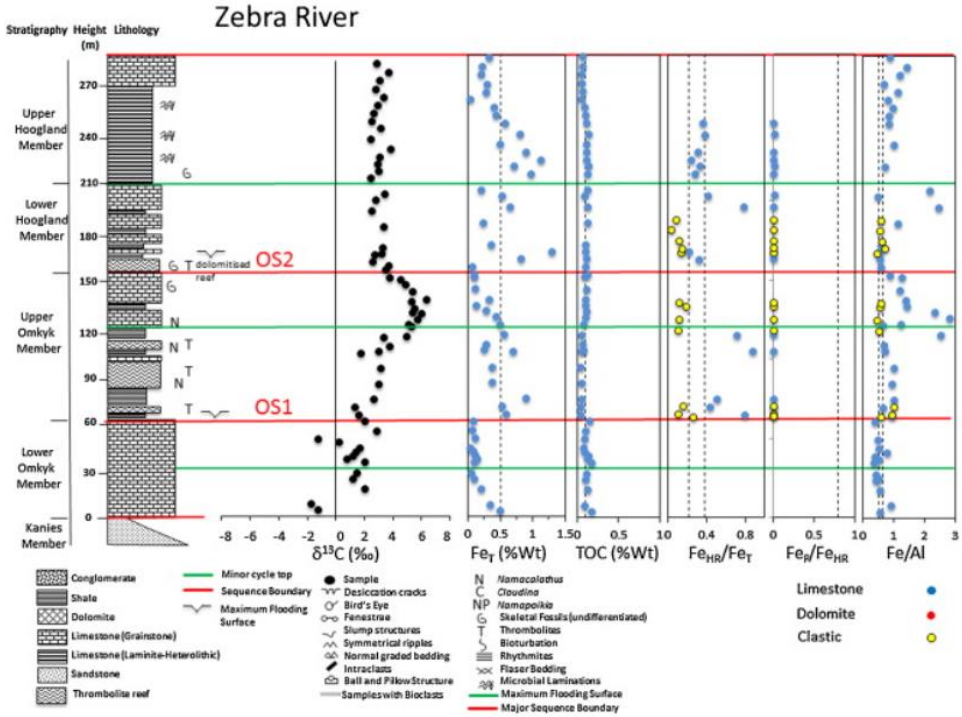

Figure 1.20*: Stratigraphic column of Zebra River field site with geochemical data. From Wood et al. (2015).*

There is an increase in carbon isotope values in the Zebra River Section from -1.75‰ to 6.3‰ between the Lower Omkyk Member and the Upper Omkyk Member (Wood et al., 2015) (Figure 1.20). The carbon isotope signature becomes stable at ~3‰ in the Lower and Upper Hoogland Members (Wood et al., 2015) (Figure 1.20). The Fe_T values within this sequence vary at stratigraphic boundaries, ranging between 0.03 and 1.28 wt% (Wood et al. 2015) (Figure 1.20). Fe speciation data indicate oxic signals in the Upper Omkyk Member with overlying sequences indicating anoxic conditions (Wood et al., 2015) (Figure 1.20).

1.9.1.3 Omkyk Farm (Kuibis Subgroup)

~73 m of the Lower Omkyk Member and 30 m of the Upper Omkyk Member is located at the Omkyk Farm site and is part of the mid-shelf environment and typifies a low energy, potentially lagoonal setting (Wood et al., 2015). Thinly laminated micrite, which has been dolomitised, crops out at Omkyk Farm with evidence of potential microbial mats with associated skeletal metazoans (Wood et al., 2015) (Figure 1.21).

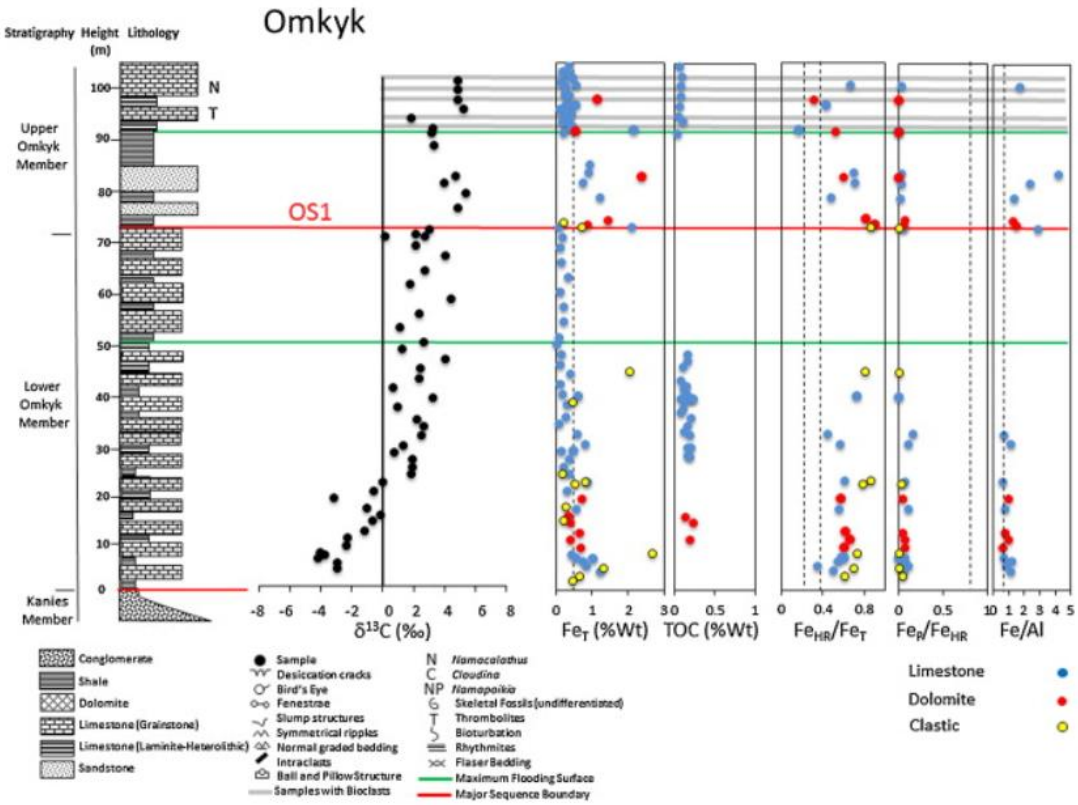

***Figure 1.21**: Stratigraphic column of Omkyk Farm field site with geochemical data. From Wood et al. (2015).*

The carbon isotope values at Omkyk Farm show a generally increasing trend throughout the section from -0.20‰ in the Lower Omkyk Member to 4.80‰ in the Upper Omkyk Member, with a peak in the Upper Omkyk Member (Wood et al., 2015) (Figure 1.21). The Fe_T values in this section vary between 0.02 and 2.66 wt% with the Fe speciation data suggesting mostly anoxic signals (Wood et al., 2015) (Figure 1.21).

1.9.1.4 Zwartmodder Farm (Kuibis Subgroup)

The Zwartmodder site houses the Kaines Member (~18 m) which is overlain by the Lower Omkyk Member (~22 m) and the Upper Omkyk Member (~75 m) and the Hoogland Member (~30 m) (Wood et al., 2015). The Lower Omkyk Member consists of mainly dolostones at its base and grades to dominantly limestone laminites and packstones and grainstones at the top of the sequence (Wood et al., 2015) (Figure 1.22). *Cloudina hartmannae* and *Namacalathus* are abundant in the Upper Omkyk Member and Hoogland Member at this site (Wood et al., 2015) (Figure 1.22). The Upper Omkyk Member features thrombolites and was deposited a highstand system tracts up to a transgressive system tract of the Hoogland Member (Wood et al., 2015) (Figure 1.22).

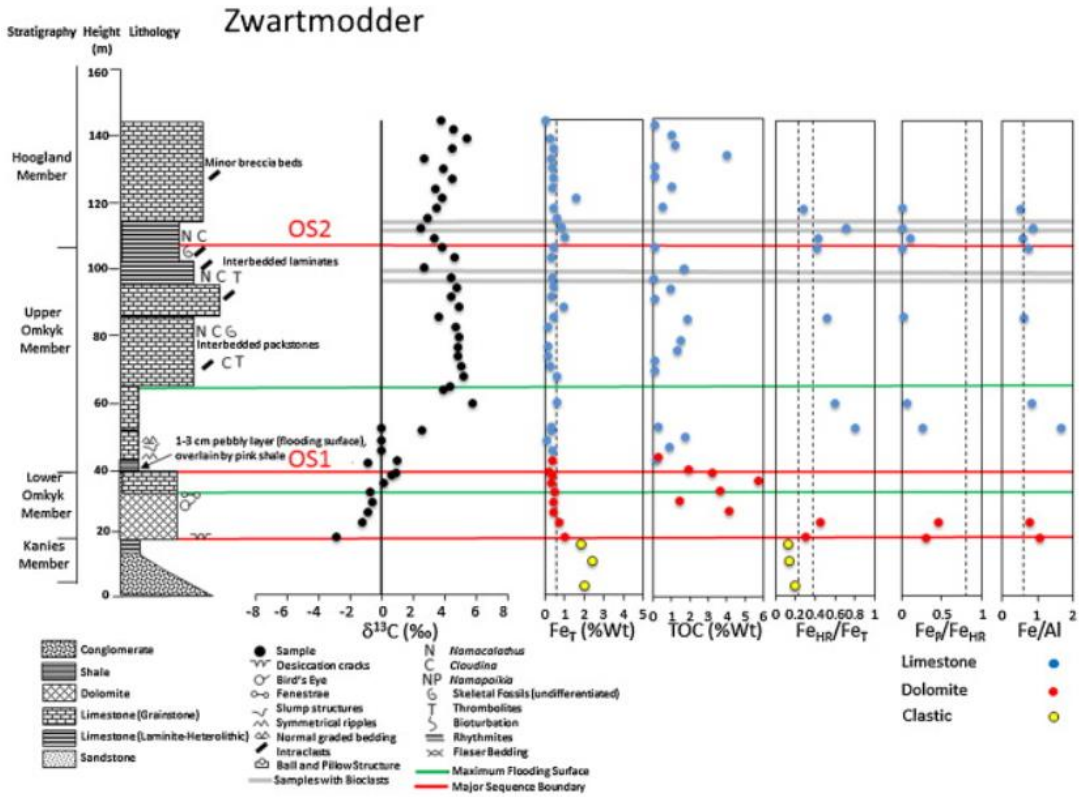

Figure 1.22*: Stratigraphic column of the Zwartmodder field site with geochemical data. From Wood et al. (2015).*

Carbon isotope values at Zwartmodder increase from -2.93 to -0.07‰ in the lower 30 m of the section and range between 5.66 to 2.34‰ for the rest of the sequence (Wood et al., 2015) (Figure 1.22). Fe_T varies between 0 and ~2 wt% at this site with TOC ranging between 0.04 to 5.66 wt%, where both these values equal <0.5 wt% have been interpreted as possible

oxygenated layers (Wood et al., 2015) (Figure 1.22). Potential oxic settings are found in clastic sediments in the Kanies Member, but carbonate samples show mostly anoxic settings throughout the rest of the sequence (Wood et al., 2015) (Figure 1.22).

1.9.1.5 Swartpunt (Schwarzrand Subgroup)

500 m of the Spitzkopf Member, Urusis Formation, is exposed at Swartpunt, with the top of the exposure terminating at the Ediacaran-Cambrian boundary/unconformity (Wood et al., 2015). The inner ramp succession contains highstand system tract carbonate rocks (including carbonate microbialites and micritic beds) and transgressive system tract siliciclastics (including quartzite and shales) and records a generally shallowing up sequence (Grotzinger el al., 1995; Narbonne et al., 1997; Wood et al., 2015) (Figure 1.23).

In the lower carbonate facies the units are metre scale cycles capped with karsts and contain bioclastic material, such as *Namacalathus*, and have been suggested to have been deposited in an high energy, inner-ramp environment (Wood et al., 2015) (Figure 1.23). The deeper ramp siliciclastic succession (~22 m) overlying these carbonates are coarsening-upward packages of mudstones to ripple-laminated and planar-laminated or cross-bedded sandstones (Wood et al., 2015) (Figure 1.23). Above these beds are mudstones and sandstones containing soft-bodied Ediacaran fauna, such as *Swartpuntia* and *Pteridinium*, and complex trace fossils, such as *Strepichnus narbonnei* (Narbonne et al., 1997; Jensen and Runnegar, 2005). The carbonates overlying this section are thinly bedded dolomites and limestones with a microbial component, mostly thrombolites, with flat-pebble and intraclastic breccias indicative of a shallow to deep subtidal ramp environment (Wood et al., 2015). Overlying this, just below the Ediacaran-Cambrian unconformity, flaggy limestones are deposited which house *in-situ Cloudina riemkeae* in association with thrombolites (Wood et al., 2015).

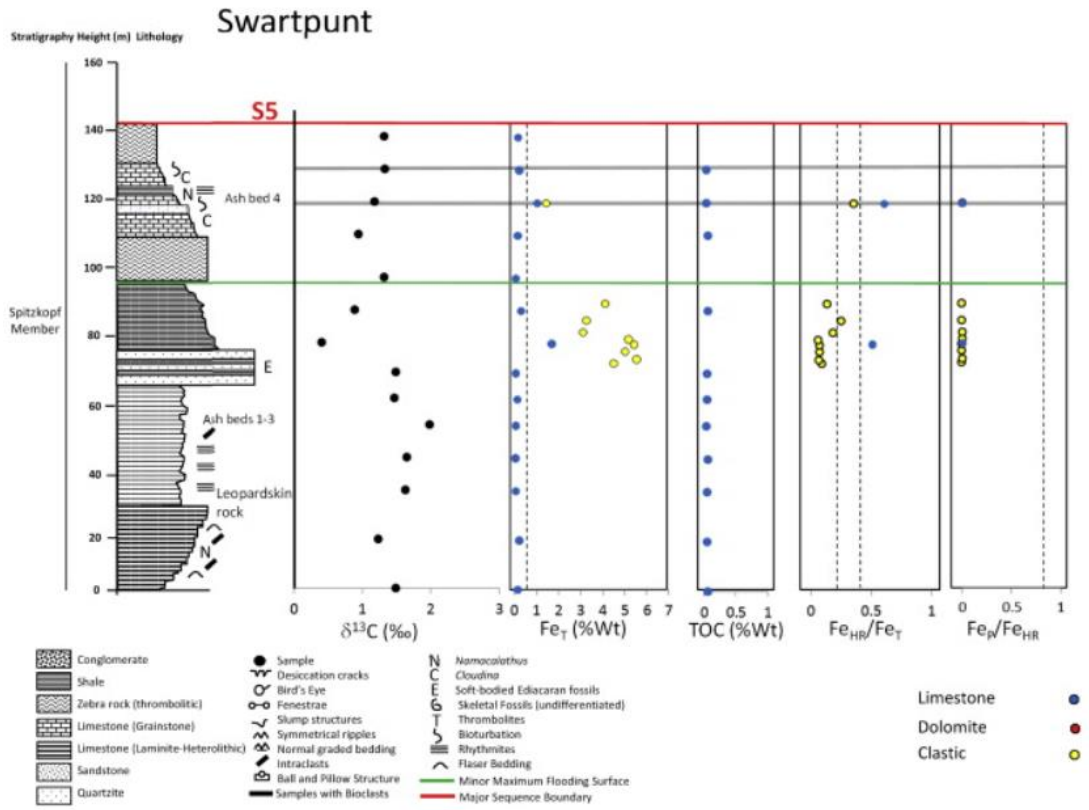

***Figure 1.23**: Stratigraphic column of the Swartpunt field site with geochemical data. From Wood et al. (2015).*

The carbon isotope values at Swartpunt are variable between 0.5‰ and increasing to 2‰ mid-section (Wood et al., 2015) (Figure 1.23). The isotope values decrease to 0‰ but continue to steadily rise again throughout the section to 1.5‰ (Wood et al., 2015) (Figure 1.23). Fe_T and TOC vales are low throughout the section at <0.5 wt% and 0.04 to 0.07 wt%, respectively (Wood et al., 2015) (Figure 1.23). Fe speciation data show a predominantly oxic signature in clastics unlike carbonate samples located up to 50 m below the Ediacaran-Cambrian boundary which indicate anoxia suggesting that the water column was mostly anoxic with brief periods of anoxia (Wood et al., 2015) (Figure 1.23).

1.10 Sampling, material and methods

1.10.1 Sampling and geochemical sample preparation

Fieldwork took place over two weeks during the summer in 2018 in the Nama Basin of southern Namibia. Throughout multiple fieldwork sites, including Driedoornvlakte Farm, Omkyk Farm, Zwartmodder Farm and Swartpunt, palaeoecological data and geochemical sample collection took place which contributed to this thesis. Siliciclastic samples for geochemical analyses have been collected from previous field expeditions led by Rachel Wood.

For geochemical analyses, as stated below, weathered surfaces and veining were removed from the samples which were divided into two, with one half for powdering and the other half as a record. Each sample for analysis was washed and dried which were then ground by a tungsten carbide jaw crusher and disc mill at the University of Edinburgh.

1.10.2 Bulk rock digestion: major elements (Fe, Al, Mn, P)

50-80 mg of sediment was transferred into porcelain crucibles. Two standards and two duplicates were used for this analysis. The samples were ashed overnight at ~550°C. The ashed samples were transferred to teflon beakers using 5 1 ml HNO_3 to rinse out the crucibles of the sediment. 2 ml of concentrated (40%) hydrofluoric (HF) acid and 2 or 3 drops of concentrated $HClO_4$ were added and placed on a 70°C hotplate until dry (overnight). 2 ml solution of a 50 g/L boric acid was added to neutralise the HF, and to prevent the formation of aluminium complexes, and left of the 70°C hotplate.

50% hydrochloric acid (HCl) was added to the solution in 5 1 ml increments to bring the samples back into solutions and were transferred to 100 ml volumetric flasks with Milli-Q and the teflon pot was further rinsed with Milli-Q to ensure all the sample was transferred. The flasks were rotated once filled to volume and 15 ml were transferred into a centrifuge tube. The major element concentrations were then measured by the use of Thermo Fisher iCAP

7400 Radial Inductively Coupled Plasma Optical Emission Spectrometry (ICP-OES) at the University of Leeds.

1.10.3 Total organic carbon (TOC)

TOC measurements were carried out at the University of Leeds on the from the same ground samples used in phosphorus speciation and bulk rock digestion. Small amounts of HCl were added to each sample (1 to 5 g, record as $m_{initial}$), within centrifuge tubes (weighed as m_{tube}), to dissolve the carbonate within the sample in order to leave organic carbon, add until the reaction ceases. Each sample undergoes washes with distilled water for three rinses or until at pH of the leachate is <4. The sample are left to dry in an over at 60°C overnight. The samples were weighed to determine the mass change of the samples ($m_{lost} = (m_{initial} - m_{tube}) - (m_{final} - m_{tube})$. The samples underwent a series of washes with distilled water and were measured in the LECO carbon/sulphur analyser at the University of Leeds.

1.10.4 Phosphorus speciation

Each sample was broken into rock chips by means of tungsten carbide jaw crusher, and powdered using a tungsten carbide rotary mill, housed at the University of Edinburgh. 0.15 – 0.19 g of each sample was weighed out and transferred into a 15 ml centrifuge tube. Two duplicates and two standards were used for this investigation. Phosphorus speciation was carried out at the University of Leeds.

1.10.4.1 Extraction

The steps involved for the extraction of phosphorus in this method are highlighted in Figure 1.24. 10 mL of each reagent, according to phase of phosphorus needed to be extracted (Figure 1.24), was added to each sample and was shaken until the sediment was suspended in solutions. The rack of samples was placed on the shaker table at ~100 rpm at room temperature

for the allotted time for each reagent and phosphorus phase (Figure 1.24). The samples were then centrifuged at 4000 rpm for 4 minutes. Once each sample had been centrifuged, 8 mL of the supernatant fluid was subsampled into another centrifuge tube (15 mL). Following P_{Fe1}, P_{auth}, P_{mag}, and P_{Fe2} washes are carried out in order to ensure all phosphorus of each phase has been extracted. P_{Fe1}, P_{mag}, and P_{Fe2} undergo one $MgCl_2$ wash, whilst the P_{auth} phase undergoes an $MgCl_2$ wash and if the absorbance of the supernatant liquid is higher than 0.1 a further $MgCl_2$ wash proceeded by a Milli-Q wash is undertaken. The sodium citrate/-dithionite/acetic acid (CDA) reagent, used for the extraction of P_{Fe2}, and sodium citrate/-bicarbonate/-dithionite (CBD) reagent, used for the extraction of P_{Fe1}, were prepared on the day of use due to the oxidative behaviour of dithionite.

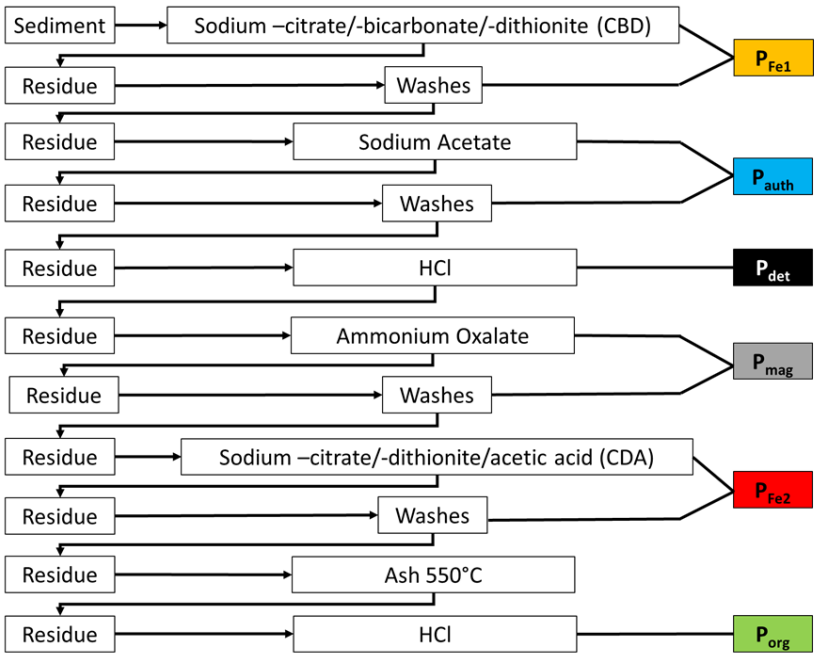

***Figure 1.24**: Flow chart of the modified SEDEX phosphorus speciation method. From Thompson et al. (2019).*

Before extraction could take place for the final phase, P_{org}, samples were transferred into porcelain crucibles using 4 to 6 ml of Milli-Q and were dried in an oven at 100°C and then ashed for 2 hours at 550°C. The samples were then transferred back to the centrifuge tubes using a spatula with any sample left in the crucible was washed by 5 2 ml of 10% HCl. The samples were shaken for 16 hours at 100 rpm at room temperature.

1.10.4.2 Spectrophotometer

Multiple phases of the extraction are measured via spectrophotometry using molybdate blue, where formation of phospomolybdate in the presence of phosphorus. The concentration of the phosphmolybdate is measured in the spectrophotometer at a specific wavelength (880 nm) allowing for the concentration of phosphorus in the solution to be determined. To ensure the pH remains constant over a given time period, aliquots of acid were tested on standards prior to measuring P_{auth}, P_{det}, and P_{org} absorbances, with the volume of acid determined by the amount which shows the least amount of change over the time period set.

1 ml of sample supernatant following an extraction process was pipetted into a microtube, if diluted the fluid would have to equal 1 ml (e.g. 10 times dilution equates to 100 µl of sample supernatant and 900 µl of Milli-Q). 200 µl of molybdate blue was added to the solution. 15 minutes after molybdate blue was added to the first sample each sample was poured into a 2 ml cuvette, if bubbles were present in the tube once the solution was added the cuvette was tapped until the bubble dispersed. Before the first sample was analysed, standards of known concentrations were measured to produce a calibration line which aids in the calculation of phosphorus concentration in the sample. All samples needed to be analysed within 30 mins of the addition to molybdate blue to the sample otherwise it would not give a correct reading.

1.10.4.3 ICP-OES

The P_{Fe1}, P_{mag}, and P_{Fe2} phases were measured using ICP-OES. For ICP-OES analysis the supernatant was diluted by 20x (500 µl of sample, 9500 µl MQ). 4.9 ml of each sample with 0.1 ml of Co internal standard was used for ICP analysis. The following calibration was performed before each new analysis: 0, 0.5 ppm, 1 ppm, 2 ppm, 5 ppm P. A quality check (QC) of 0 and 2 ppm P was run every 10 samples to ensure the machine was not drifting

throughout the analysis. Standards used for the calibration were prepared using a different standard solution to the QC for a more accurate test of instrument drifting.

1.10.5 Cathodoluminescence microscopy (CL)

Highly polished thin sections of cloudinomorphs and *Namacalathus* of the Nama Group were studied using transmitted and cathodoluminescence microscopy, highly polished sections of *Namacalathus* were also analysed. The Cathodoluminescence Cold Cathode CITL 8200 MK3A, which is attached to a Nikon optiphot microscope was used at the University of Edinburgh. In order not to damage the thin sections used the working current ranges between 900 and 1000 µA, and the voltage is maintained between 29 and 30 kV. Also, the thin sections were not analysed for long periods of time under cathodoluminescence to prevent any damage to the sample.

1.10.6 Electron microprobe analysis (EMPA)

Highly polished thin sections, which were used for cathodoluminescence microscopy, were carbon coated. Sites of interest were targeted manually with the Cameca SX100 Electron Microprobe with a 6 µm beam diameter, 35 nA beam current and 15 kV accelerating voltage. This work was carried out at the University of Edinburgh by Christopher Hayward.

1.10.7 Serial sectioning, image processing and 3D model reconstruction

In cases where it was not possible to undertake micro-CT scanning (µCT), due to the lack of contrast between the calcium carbonate skeletal fossil and the surrounding calcium carbonate sediment/matrix, samples had to undergo serial sectioning. This is a destructive and time-consuming method but is the only way to produce 3D models of these specimens.

To produce a 3D model through serial sectioning the sample must be serially ground at regular increments (this differed depending on the model) which were be imaged after each

sectioning. Two methods of serial sectioning have been used, the first is using polishing paper and the seconds is using a Buehler Petrothin thin sectioning system. After each polishing/grind, before imaging, the sample was coated in a thin layer of emulsion oil to reduce the appearance of scratching of the sample surfaces.

Two imaging techniques have been used during serial sectioning throughout the undertaking of this thesis: binocular microscope and flatbed scanning. These images stacked, aligned, and then segmented or binarised depending on the contrast of the image. During image processing there is constant reference with the original image in order to ensure the model will reflect the sample.

The processed images were imported as a virtual stack into Avizo 9 software to create 3D models and were smoothed. Smoothing thresholds were used to reduce noise within the model by constant reference to features in the original scans as to not remove key features such as branches or attachments.

1.10.8 Micro CT scanning and 3D model reconstruction

Cored *Namacalathus* individuals were scanned via micro CT scanning (µCT) due to the high contrast of the fossils with the matrix as evidenced by an initial radiograph of the sample. Scanning was at 120 kV and 824 images were collected. The contrast was enhanced by applying the stretch histogram option in ImageJ, while not affecting the original data. A 3D model of the scans was rendered using Avizo 9 software. Voxel size of reconstructions equates to 20.7 µm. The pre-defined colour map ‘physics.icol’ was applied to the model to aid in visualisation of the features of the fossil, but the false colours are not quantitatively correlated to any property of the object. The colour thresholds of the colour map were altered in Avizo (255-65535) in order to reduce the noise of the surrounding calcium carbonate sediment in order to produce a model of the whole individual.

1.11 Thesis overview

Chapter 2: Multiple studies have been carried out on Ediacaran sediments in order to understand changes in redox during this time period. However, these studies do not provide a mechanism for oxygenation of the shallow shelf environments. The modified SEDEX phosphorus speciation method was used on siliciclastic sediments of the Nama Group. Shelf to basin transects, of the Zaris and Witputs Subbasins, provide a reconstruction of nutrient cycling within the Nama Group. These data are combined with the local redox data and palaeontological data to understand the potential link between diversification and changing redox of the Nama Group.

Published as: Bowyer, F.T., Shore, A.J., Wood, R.A., Alcott, L.J., Thomas, A.L., Butler, I.B., Curtis, A., Hainanan, S., Curtis-Walcott, S., Penny, A.M. and Poulton, S.W., 2020. Regional nutrient decrease drove redox stabilisation and metazoan diversification in the late Ediacaran Nama Group, Namibia. *Scientific Reports*, 10(1), pp.1-11.

Chapter 3: *Cloudina* and other cloudinomorphs are well studied, but the affinity of these organisms is still contested. Serial sectioning and the production of a 3D model highlight the presence of polytomous branching through external within a cloudinomorphs collected from the Omkyk Member of the Nama Group. This evidence, along with a fast growth rate after initial branching, suggests a non-bilaterian affinity, potentially a cnidarian affinity. However, evidence of an inferred gut from cloudinomorphs of Nevada would suggest an annelid affinity, and so the stacked-funnel morphology of cloudinomorphs is a convergent morphology.

Published as: Shore, A., Wood, R., Curtis, A. and Bowyer, F., 2020. Multiple branching and attachment structures in cloudinomorphs, Nama Group, Namibia. *Geology*, *48*(9), pp.877-881.

Chapter 4: *Cloudina* show the first evidence of macrofaunal biomineralisation at ~550 Ma. However, recently there has been debate as to whether these organisms could biomineralise due to the presence of organic laminae and the suggestion these organisms' mineralised post-mortem. Observations of cloudinomorph associated cements from multiple sites within the Omkyk Member of the Zaris Subbasin show that these cements formed before the formation of early inorganic cements and before any syn-sedimentary diagenetic processes and are independent of the diagenetic environment. These observations imply cloudinomorphs of the Nama Group biomineralised. Measurements made of laminae thickness are consistent between sites in which they are present and so suggest that these features were under biological control. Published as: Shore, A. and Wood, R., 2021. Environmental and diagenetic controls on the morphology and calcification of the Ediacaran metazoan *Cloudina*. *Scientific reports*, 11(1), pp.1-13.

Chapter 5: The lack of soft-tissue preservation makes determining the phylogenetic affinity very difficult within Ediacaran taxa, especially the biomineralising Ediacaran biota as the hard parts are only preserved. This means that the features needed to determine affinity have been lost through fossilisation. The chapter presents the first three-dimensional soft-tissue preservation of *Namacalathus hermanastes*. This provides an evolutionary link between the Late Ediacaran and Cambrian taxa.

Published as: Shore, A.J, Wood, R.A, Butler, I.B., Zhuravlev, A., McMahon, S., Curtis, A., and Bowyer, F.T., 2021, Ediacaran metazoan reveals lophotrochozoan affinity and deepens root of the Cambrian Explosion: *Science Advances*, v. 7, no.1.

Chapter 6: Conclusions and Discussion.

Chapter 2: Phosphorus Cycling and Oxygenation in the Nama Group, Namibia

The data presented in Chapter 2 have been published as: Bowyer, F.T., Shore, A.J., Wood, R.A., Alcott, L.J., Thomas, A.L., Butler, I.B., Curtis, A., Hainanan, S., Curtis-Walcott, S., Penny, A.M. and Poulton, S.W., 2020. Regional nutrient decrease drove redox stabilisation and metazoan diversification in the late Ediacaran Nama Group, Namibia. Scientific Reports, 10(1), pp.1-11. The text in the following chapter is adapted from this paper, with the published paper given in Appendix 1.1.

Amy Shore carried out phosphorus speciation as well as total organic carbon and bulk total element analysis on the samples used for phosphorus speciation, trained by Lewis Alcott and Andrew Hobson at the University of Leeds. Fred Bowyer, Rachel Wood, and Simon Poulton conceived the study. Fred Bowyer, Rachel Wood, Amelia Penny, S Hainanan, Andrew Curtis and Shona Curtis-Walcott collected the sample material. Fred Bowyer carried out iron speciation and total organic carbon analyses, with the help of Alex Thomas and Ian Butler. All samples used for phosphorus speciation have undergone Fe speciation analysis.

2.1 Introduction

Uranium isotope data suggest that between ~550 to 547 Ma anoxic bottom waters expanded to occupy at least a third of the total sea floor. Yet, Ediacaran taxa, including skeletal taxa, are known to inhabit multiple shallow shelf environments prior to this time, and throughout this interval (Tostevin et al., 2019). This emphasises the importance of local redox studies to understand local redox conditions and biotic distribution. Previous work has focussed mainly on the redox conditions of the Nama Group and how it changed towards the Ediacaran-Cambrian boundary (Wood et al., 2015; Tostevin et al., 2016b). These studies show

a dynamic redox history of the Nama Basin where short-lived oxygenation supported fleeting communities and the ventilation of the mid-shelf environment allowed for the formation of reef systems (Wood et al., 2015). Low oxygen conditions have also been identified in the Nama Basin, between deeper anoxic, and shallow well-oxygenated waters, with skeletal organisms only occupying the well-oxygenated zones (Tostevin et al., 2016b). These studies, however, do not provide a mechanism for a deepening of the chemocline during this time and how long-term redox evolution correlates with the changes to the ecology of the Nama Basin. This is particularly important for understanding the palaeoecological distribution of Ediacaran organisms throughout deposition of the Nama Group.

In this chapter, data are presented for two shelf-to-basin transects to show a 4D reconstruction of spatial and temporal changes to the long-term evolution of the dominant limiting nutrient phosphorus (P) during deposition of the Nama Group. These data are presented in conjunction with previously collected iron (Fe) speciation data, and biotic diversity and distribution data, to understand the link between redox and the diversification of Ediacaran fauna in the Nama Group.

2.2 Methods

2.2.1 Sampling

Phosphorus speciation was carried out on powdered shales and siltstones collected from multiple field excursions to the Nama Group, Namibia (see Appendix 1.1.). Carbonate rocks were avoided due to the fact that the modified phosphorus speciation proxy has not been calibrated for use on carbonate-rich sediments (Thompson et al., 2019).

2.2.2 Phosphorus speciation

Phosphorus speciation extractions were performed at the University of Leeds, Cohen Laboratories. Sequential P extraction and total digest solutions were analysed by Inductively Coupled Plasma Optical Emission Spectrometry (ICP-OES) by Stephen Reid.

Ruttenberg (1992) developed a phosphorus speciation sequential extraction (SEDEX) technique for use on modern sediments to operationally quantify a number of sedimentary reservoirs of phosphorus, including: loosely sorbed phosphorus; authigenic carbonate fluorapatite (CFA); biogenic apatite and calcium carbonate associated phosphorus (P_{auth}); iron-bound phosphorus (P_{Fe}); organic phosphorus (P_{org}); and detrital phosphorus (P_{det}). This protocol has recently been enhanced for use on ancient sediments with the ability to specifically target phosphorus bound in: reactive Fe (oxyhydr)oxide minerals (P_{Fe1}); crystalline Fe (oxyhydr)oxide minerals (P_{Fe2}); and magnetite (P_{mag}).

The phosphorus speciation scheme subjects powdered rock samples to a series of sequential chemical digestions which operationally extract individual phosphorus phases (P_{Fe1}, P_{auth}, P_{det}, P_{mag}, P_{Fe2} and P_{org}) from each powdered rock sample. P in supernatant solutions from the P_{auth}, P_{det} and P_{org} extractions were measured using spectrophotometry after reaction with molybdate blue. P in supernatant solutions from the P_{Fe1}, P_{mag} and P_{Fe2} extractions were measured using ICP-OES.

2.2.3 Major elements analysis (Fe, Al, Mn, P)

Bulk rock digestion was carried out at the University of Leeds Cohen Labs in order to determine the total wt% of Al, Fe, Mn and P. Samples were ashed at 550°C followed by complete dissolution using HF-$HClO_4$-H_3BO_3-HNO_3, and resultant solutions were analysed by Stephen Reid, using ICP-OES at the University of Leeds but Stephen Reid. Andrew Hobson

carried out steps in the method which included hydrofluoric (HF) acid. All samples collected for phosphorus speciation underwent total digestion.

2.2.4 Total organic carbon (TOC)

TOC measurements were carried out at the University of Leeds from the same samples used in phosphorus speciation and bulk rock digestion. Hydrochloric acid (HCl) was added to each sample to dissolve the carbonate within the sample in order to leave organic carbon. The samples were measured in the LECO carbon/sulphur analyser at the University of Leeds.

2.3 Results

2.3.1 Phosphorus speciation

Data collected from phosphorus speciation are assessed herein, based on the palaeoredox interpretation as determined through previously collected Fe speciation data from the same sample (Figure 2.1C and D; Bowyer et al., 2020; see Appendix 1.1 and 1.2.1).

Anoxic sediments (n = 12) yield a greater P_{Fe} mean values of 0.060 wt% (range = 0.001 to 0.008 wt %), compared with sediments deposited under oxic conditions (n = 25) where the P_{Fe} mean equates to 0.001 wt% (range = 0 to 0.016 wt%). Greater mean values are also seen within the P_{org} pool within anoxic sediments with mean values of 0.003 wt% (0 to 0.016 wt %) compared to the oxic counterparts which have a reduced pool in comparison of 0.001 mean values (0 to 0.003 wt%). The greatest proportion of phosphorus in oxic sediments is in the form of P_{auth}, with a mean value of 0.037 wt% (range = 0.005 to 0.067 wt%), compared with a mean value of 0.018 wt% (range = 0 to 0.002 wt%) in anoxic sediments. P_{mag} values from sediments deposited in oxic waters are relatively higher (mean = 0.001 wt%, 0 to 0.001 wt%) compared to those deposited in anoxic settings (mean = 0.0004 wt%, range = 0 to 0.002

wt%). The P_{reac} pool (bioavailable phosphorus including P_{Fe}, P_{org}, P_{auth} and P_{mag}) has a relatively high mean value in oxic sediments (mean = 0.040, range = 0.007 to 0.071). By contrast, the mean concentration of P_{reac} in anoxic sediments is low (mean = 0.025, range = 0.005 to 0.079), which may imply that P_{auth} retention in oxic sediments counteracts the lowering of the P_{Fe} and P_{org} during the transition to oxia.

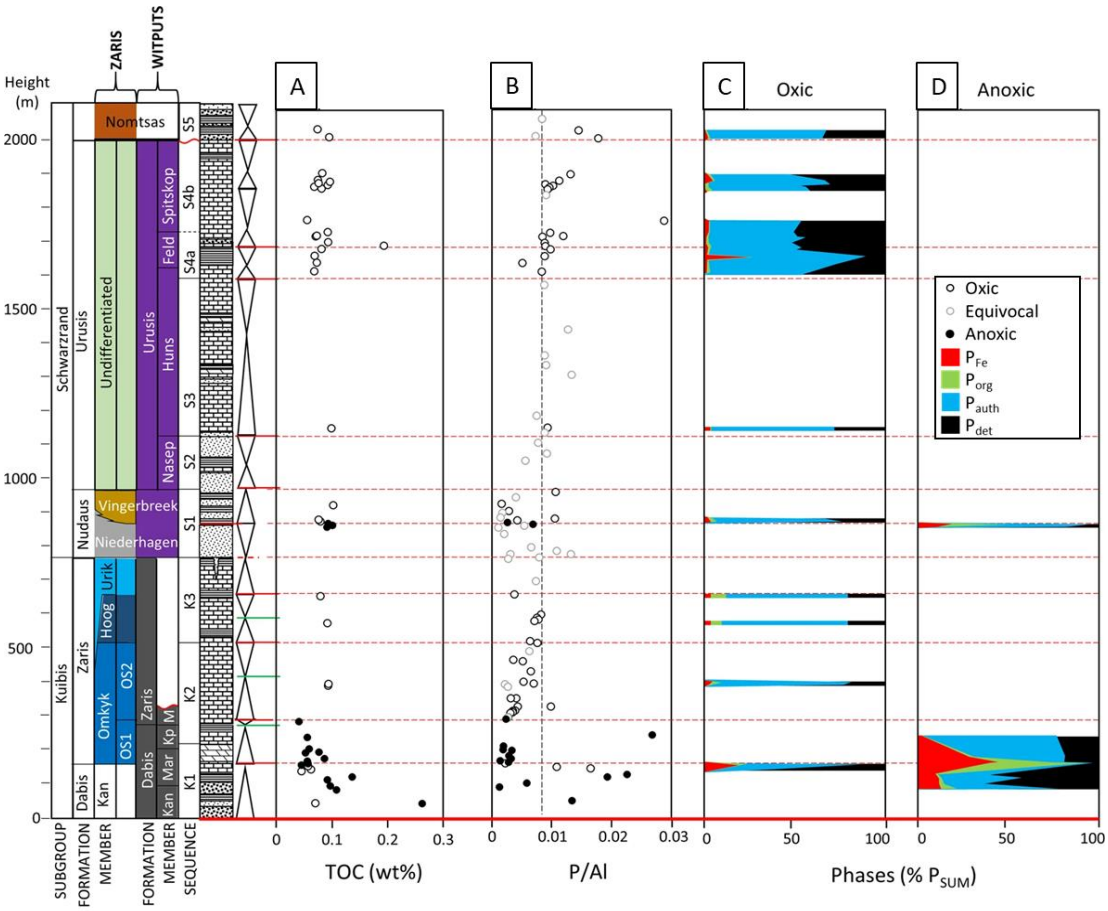

***Figure 2.1**: Elemental and phosphorus speciation data from the Nama Group which has been differentiated between anoxic and oxic samples (determined through Fe-speciation) with stratigraphic column. **A**: TOC. **B**: Ratio between total phosphorus (Ptot) to aluminium (Al). **C**: Phosphorus phase percentage in oxic samples. **D**: Phosphorus phase percentage in anoxic samples. From Bowyer et al. (2020).*

The P_{det} is not a bioavailable species of phosphorus, but this pool also shows a shift between oxic and anoxic settings. The P_{det} pool mean value is 0.011 wt% (ranges = 0 to 0.054 wt%) and are found in anoxic sediments but the change to more stable oxic conditions shows an increase in the P_{det} values (mean = 0.026 wt%, range = 0.001 to 0.048 wt%).

2.3.2 Critical assessment of phosphorus phase extraction

The sequential extraction of phosphorus has limitations as not all phosphorus is extracted producing a lower recovery of phosphorus. An example of this includes the loss of sediment at each stage when decanting the supernatant solution after each extraction. There is also the potential of the incomplete extraction of phosphorus within some of the phases. However, there was minimal loss of P_{Tot} through P speciation where recovery was >70% (mean = 90.8%) (Figure 2.2A). The negative correlation between the recovery of P and Al is a common occurrence in P speciation (Figure 2.2B).

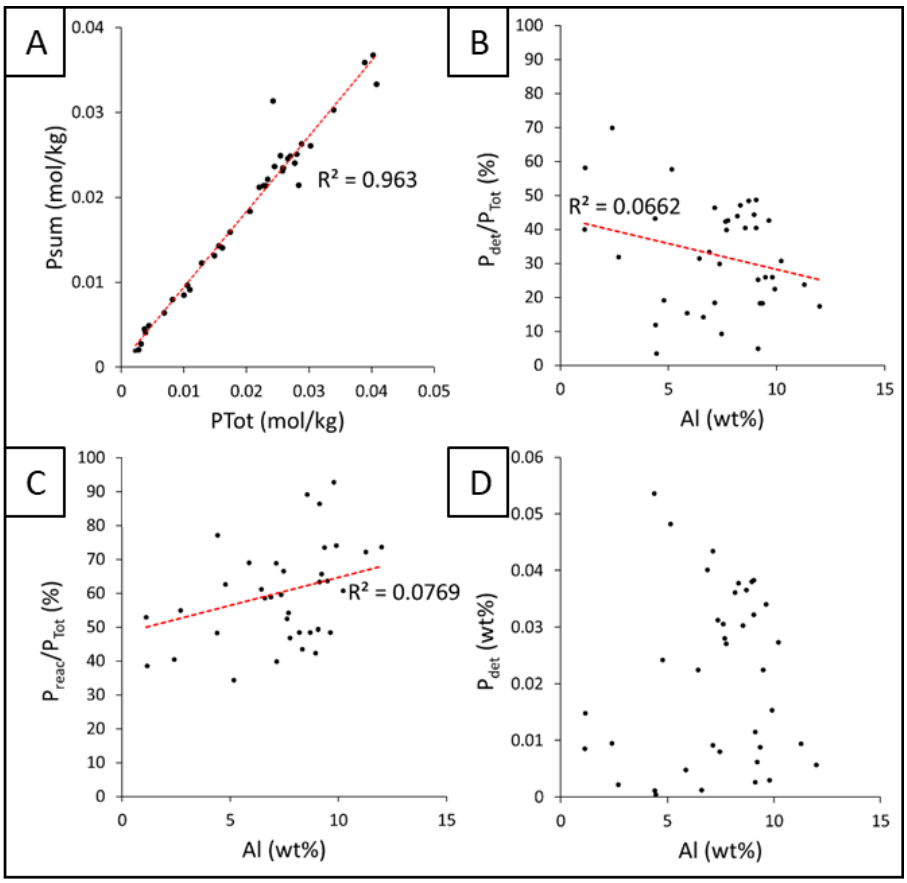

Figure 2.2*: The relationships between extracted P phases and the detrital background (represented by the concentration of Al).* ***A****: Strong positive correlation between P_{sum} and P_{tot}, measured from phosphorus speciation and bulk elemental analysis, respectively.* ***B****: A weak negative correlation between percentage of P_{det} and Al (wt%).* ***C****: Weak correlation between percentage P_{reac} and Al (wt%).* ***D****: No correlation between P_{det} (wt%) and Al (wt%). From Bowyer et al. (2020).*

The transfer of P_{auth} into the P_{det} pool is also a concern within the modified SEDEX method and so it must be noted that the P_{auth} concentrations presented in this chapter represents the minimum values of P_{auth} within the sample due to authigenic apatite recrystallisation, whereas the P_{det} values presented more likely show the maximum values (Marz et al., 2014; Thompson et al., 2019). The P_{auth} extraction occurs before the extraction of P_{det}, meaning that if during burial there was a decrease in the solubility of the primary P_{auth}, it may not be fully extracted and could be transferred into the P_{det} pool. Nama Group samples have a P_{det} phase between 4.2 to 536.4 ppm (mean = 208.7 ppm). The maximum P_{det} value is greater than modern shelf environments P_{det} values (~186 ppm in modern continental margins, and 62 to 310 ppm for oligotrophic settings) (Ruttenberg and Berner, 1993; Slomp et al., 2013; Marz et al., 2014). The high P_{det} value could suggest the burial recrystallisation of initial P_{auth}. However, there is no significant correlation between P_{reac} and Al (r^2 = 0.077) (Figure 2.2C), which may suggest negligible contamination of the P_{auth} phase by P_{det}.

2.3.3 Total organic carbon and bulk element analysis

The TOC content of the sediments is relatively low within the Nama Group with all samples featuring concentrations <0.3 wt% (Figure 2.1A, see Appendix 1.2.2). When comparing TOC data based on redox conditions the mean values are similar. TOC concentrations of sediments deposited in anoxic settings (n = 14) have a marginally lower mean value (mean = 0.082, range = 0.04 – 0.14) compared to their oxic (n = 26) counterparts (mean = 0.083, range = 0.05 – 0.019).

Mean P concentrations are higher in sediments interpreted as oxic from Fe speciation (mean = 721.692 ppm, n = 26) compared to P in sediments deposited under anoxic conditions (mean = 360.500 ppm, n = 14) (see Appendix 1.1 and 1.2.2). However, mean P concentrations are relatively constant between the two redox states, with P concentrations in oxic shales

ranging from 97 to 1204 ppm compared to anoxic sediments with P concentrations in the range 57 to 1263 ppm.

This trend is similar for Al concentrations, whereby oxic sediments yield higher mean Al (mean = 8.231 wt%, range = 4.41 to 11.27 wt%, n = 26%). The mean P/Al mean values (Figure 2.1B), however, are marginally greater in anoxic sediments (mean = 0.010, n = 14) in comparison with oxic sediments (mean = 0.009, n = 26), but these values are relatively consistent throughout the succession. The P/Al values of the Nama Group are scattered above and below the average shale values of 0.009 (Turekian and Wedepohl, 1961) (Figure 2.2B).

2.4 Discussion

2.4.1 Phosphorus cycling in the Nama Basin

The low P/Al values recorded in sediments deposited during anoxic conditions within the Kuibis Subgroup (Figure 2.1B) could suggest the recycling of P back into the water column, but also could be due to low phosphate availability in the overlying water column. This is unexpected, as Reinhard et al. (2017) suggest that anoxia and upwelling could promote adsorption of P to iron minerals which are deposited into the sediments, but this was potentially not representative of the global deep ocean redox state during the Ediacaran. It is under euxinic conditions where recycling of P is more likely (Ingall and Jahnke, 1994), but euxinia is not found in the Nama Group.

Comparing the phosphorus species data between oxic and anoxic sediment aids in the understanding of phosphorus cycling and retention, for example the greater P_{Fe} values in anoxic sediment shows retention of P_{Fe} within the sediment which is common to such conditions (Reinhard et al., 2017). Also, the increase of P_{auth} from anoxic to oxic sediments suggests retention of P as authigenic apatite. However, in order to fully understand phosphorus cycling in the rock record C_{org} and P ratios should be compared with the Redfield ratio (106:1)

(Figure 2.3). In older more ferruginous samples the C_{org}/P_{org} seems to fall around the Redfield ratio. Yet, some of the samples are above the Redfield ratio, which suggests the more effective recycling of phosphorus through anaerobic organic matter remineralisation. C_{org}/P_{reac} ratios fall at or below the Redfield ratio which signifying the retention of phosphorus in the sediment with iron (oxyhydr)oxide minerals.

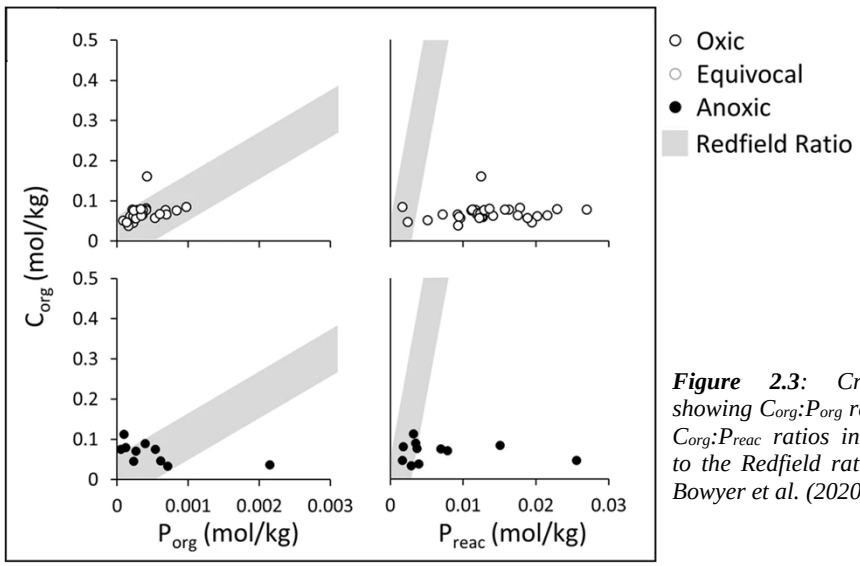

***Figure 2.3**: Cross-plots showing C_{org}:P_{org} ratios and C_{org}:P_{reac} ratios in relation to the Redfield ratio. From Bowyer et al. (2020).*

However, during more oxic conditions, the C_{org}/P_{reac} ratio also fall below the Redfield ratio, but to a greater extent than during ferruginous conditions. This shows the release of phosphorus during anoxic conditions was greater than during oxic conditions meaning that during anoxic times there was the potential of a relative increase in productivity during this time (Reinhard et al, 2017). C_{org}/P_{org} ratios for samples collected in oxic conditions cluster around the Redfield ratio suggesting the limited release of phosphorus from organic matter, which are expected due to the limited anaerobic organic matter remineralisation under low TOC conditions of the Nama Group. These C_{org}/P_{org} and the low C_{org}/P_{reac} (Figure 2.3) values as well as the high proportion of P_{auth} in the oxic samples imply that the phosphorus released from organic matter degradation and the reductive dissolution of iron (oxyhydr)oxides was retained in the sediment through sink-switching - a process by which a phosphorus is released from one pool and forms into another during diagenesis, which occurs between P_{reac} species

usually to form P_{auth} - as there is no evidence of the recycling of phosphorus into the overlying water column. These data suggest that the oxic Nama Basin underwent similar nutrient cycling as seen in modern oxic marine settings and so the limited recycling of phosphorus into the water column during such conditions was likely to have limited primary productivity.

2.4.2 Redox stabilisation in the Nama Group and the role of weathering

During the deposition of the Kuibis Subgroup (~550 to <547 Ma; Bowring et al., 2007) there was extreme water column redox stratification, with anoxic and ferruginous deeper waters indicated by shale deposition with $Fe_{HR}/Fe_T > 0.38$ and $Fe_{py}/Fe_{HR} < 0.7$ (Wood et al., 2015; Bowyer et al., 2020) (Figure 2.4). Shallowing of the redoxcline, possibly due to a marine transgression, is indicated during deposition of the Mara, Kliphoek and lower Omkyk

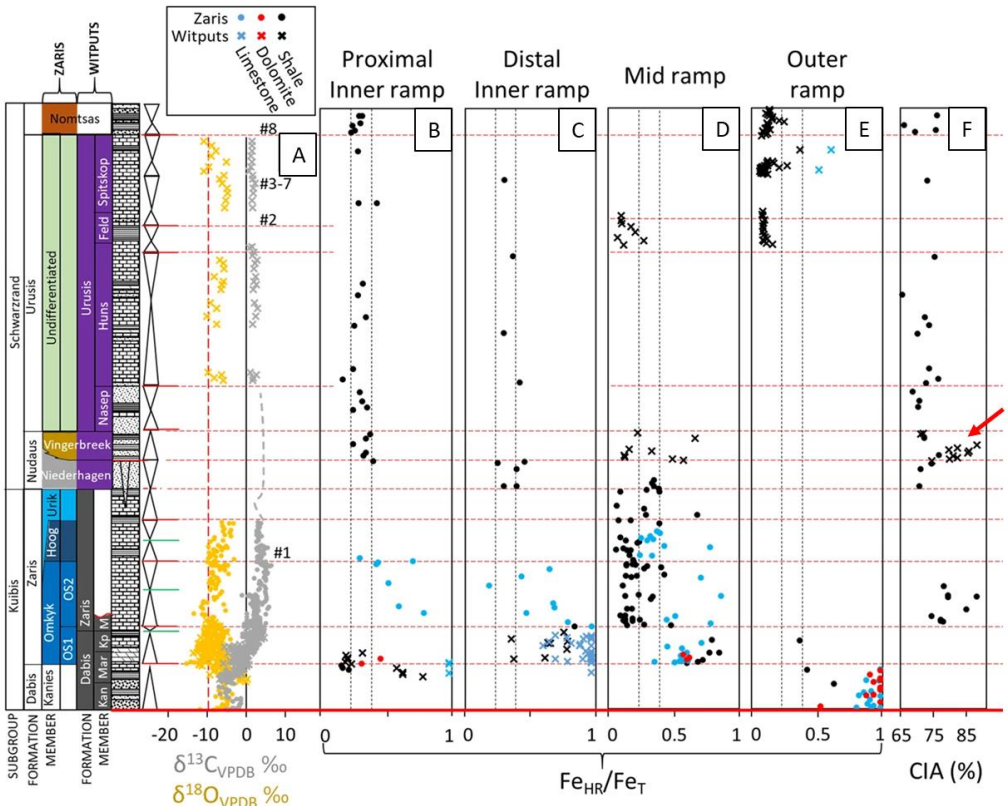

Figure 2.4*: Carbonate C isotope, redox and CIA values in the Nama Group. Red dashed lines indicate ash bed dates: 1: 547.36 ± 0.65 Ma (Bowring et al., 2007); 2: 542.68 ± 2.80 Ma (Grotzinger et al., 1995; Schmitz, 2012); 3–7: 540.095 ± 0.099 Ma to 538.99 ± 0.21 Ma (Linnemann et al., 2019); 8: 538.58 ± 0.19 Ma (Linnemann et al., 2019).* ***A****: $\delta^{13}C_{carb}$ profile.* ***B-E****: compiled Fe-speciation data split between shelf environments. Anoxic signals are indicated by FeHr/FeT > 0.7.* ***F****: chemical index of alteration (CIA), with glaciation even causing a dramatic increase in CIA values (arrowed). Modified from Bowyer et al. (2020).*

Members, but mid-ramp areas were well ventilated (Wood et al., 2015; Bowyer et al., 2020). However, during deposition of the upper Kuibis and the lower Schwarzrand subgroups shallower and deeper water areas transitioned to more oxygenated conditions and the shelf became fully oxygenated during deposition of the upper Schwarzrand Group (~542 to 540 Ma) (Linnemann et al., 2019) (Figure 2.4B-D; 2.5).

Chemical weathering, which is affected by climate and regional tectonic setting, had a major influence on the redox history of the basin as this process influences the nutrient supply and the composition of clays transported into the basin (Nesbitt and Young, 1982). This is measured through the chemical index of alteration (CIA) (see methods in Appendix 1.1 and 1.3; Bowyer et al., 2020), a proxy to determine the degree of chemical weathering (CIA = $[Al_2O_3/(Al_2O_3 + CaO^* + Na_2O + K_2O)] \times 100$). Elevated CIA values indicate a larger degree of weathering due to the preferential weathering of labile elements. Within the Kuibis Subgroup, the average CIA values are relatively high suggesting a large amount of chemical weathering during this time facilitated by the hot and humid climate (Nesbitt and Young, 1982) (Figure 2.4F). However, through continual deposition in the Nama Group, there is a lowering of CIA values. Still, there is a major increase in CIA values within the Vingerbreek Member of the Schwarzrand Subgroup, which is thought to be due to a short, regional glacial episode (Germs and Gaucher, 2012) (Figures 2.4F; 2.5). The influx of sediment from the Kalahari Craton to the east of the Nama Basin coincides with a short period of anoxia within the water column, which is likely due to the increase in nutrient supply. The changes in chemical weathering throughout this time period correspond to the redox history of the basin, it can be assumed that the changes in continental weathering controlled the redox state of the Nama Basin. The high intensity of chemical weathering on the land, as well as the marine transgression, allowed for increased nutrient input into the basin, which would have promoted primary productivity causing anoxia in deeper areas of the basin (Figure 2.5). It is possible that during this time, the basin was also receiving nutrients from deep waters through

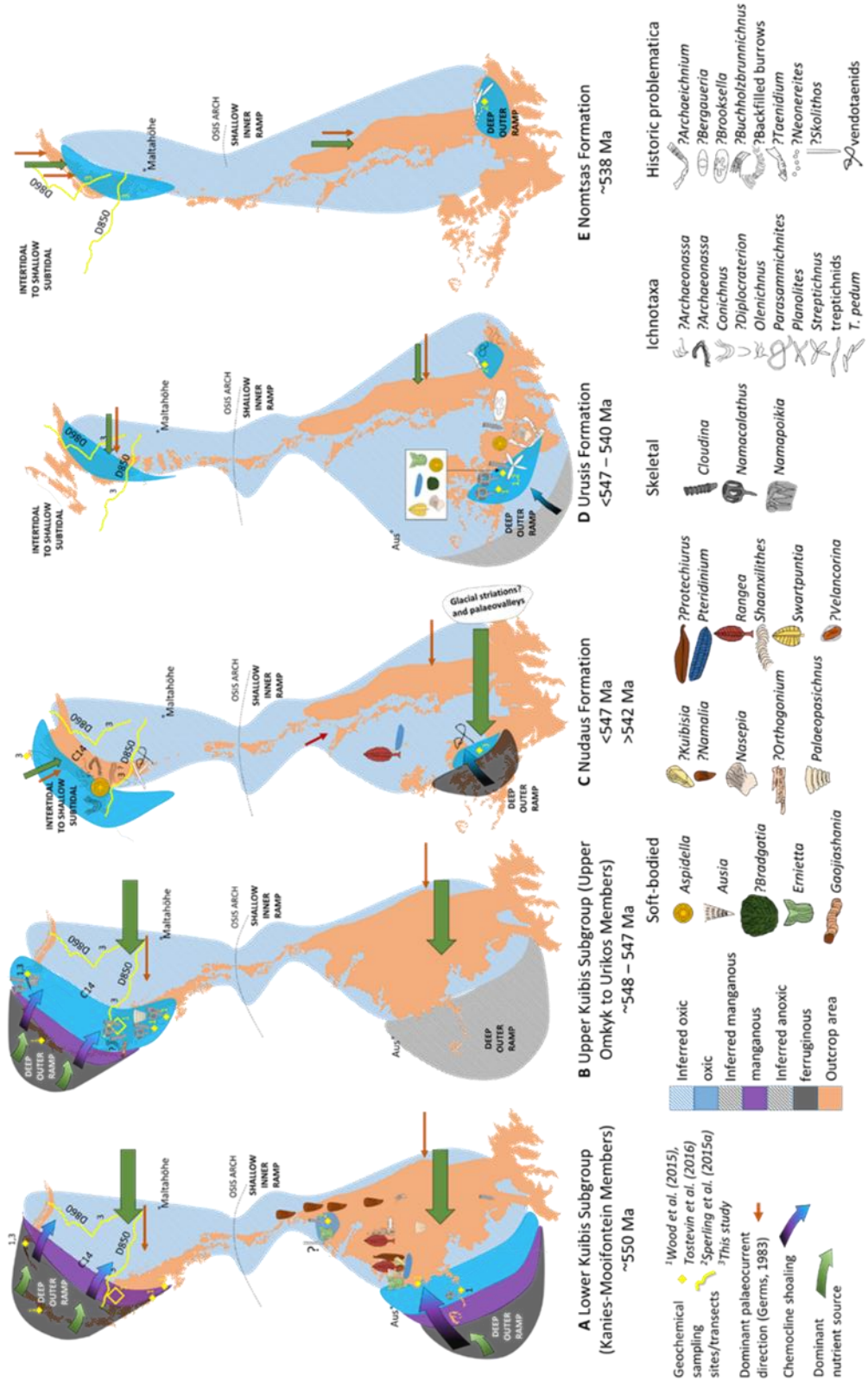
A Lower Kuibis Subgroup (Kanies-Mooifontein Members) ~550 Ma
B Upper Kuibis Subgroup (Upper Omkyk to Urikos Members) ~548 – 547 Ma
C Nudaus Formation <547 Ma >542 Ma
D Urusis Formation <547 – 540 Ma
E Nomtsas Formation ~538 Ma
Maltahöhe
OSIS ARCH
SHALLOW INNER RAMP
DEEP OUTER RAMP
INTERTIDAL TO SHALLOW SUBTIDAL
D860
D850
D580
Glacial striations? and palaeovalleys
Soft-bodied
Aspidella
Ausia
?Bradgatia
Ernietta
Gaojiashania
Skeletal
?Kuibisia
?Namalia
Nasepia
?Orthogonium
Palaeopasichnus
?Protechiurus
Pteridinium
Rangea
Shaanxilithes
Swartpuntia
?Velancorina
Cloudina
Namacalathus
Namapoikia
Ichnotaxa
?Archaeonassa
?Archaeonassa
Conichnus
?Diplocraterion
Olenichnus
Parasammichnites
Planolites
Streptichnus
treptichnids
T. pedum
Historic problematica
?Archaeichnium
?Bergaueria
?Brooksella
?Buchholzbrunnichnus
?Backfilled burrows
?Taenidium
?Neonereites
?Skolithos
vendotaenids
Inferred oxic
oxic
Inferred manganous
manganous
Inferred anoxic
ferruginous
Outcrop area
Geochemical sampling sites/transects
[1]Wood et al. (2015), Tostevin et al. (2016)
[2]Sperling et al. (2015a)
[3]This study
Dominant palaeocurrent direction (Germs, 1983)
Chemocline shoaling
Dominant nutrient source

Figure 2.5

***Figure 2.5 (page 66)**: Schematic plan-view of the redox conditions and biotic distribution of the Nama Group, between 547 and 538 Ma, indicating the stabilisation of oxygen within the water column. From Bowyer et al. (2020).*

upwelling from the Brazilides Ocean, to which the Nama Basin was partially connected (Bowyer et al., 2017). However, the upwelling would be short-lived due to the closure of the Brazilides Ocean (Gaucher et al., 2009), meaning the Nama Basin would have only been supplied from nutrients from the continent. Decrease in the nutrient input from continental weathering during deposition of the Schwarzrand Subgroup resulted in a reduction of primary productivity and promoted oxic conditions. The sink-switching allowed P to be trapped within the sediment as authigenic apatite, meaning there was limited recycling of P back into the water column causing the stabilisation of these oxic conditions.

Uranium isotopes ($\delta^{238}U$), a global redox proxy, suggest a global expansion of anoxic waters at ~547 Ma (Zhang et al., 2018; Tostevin et al., 2019), which contradicts the local redox data of the Nama Group. However, $\delta^{238}U$ also shows that there was a global increase in oxygenation at ~545 to 540 Ma which coincides with the later redox history of the Nama Basin (Zhang et al., 2018; Tostevin et al., 2019; Zhang et al., 2019). This highlights the need for multi-proxy investigations in order to understand redox conditions at this time. It also suggests that the redox state of the global ocean is unlikely to have had an influence on the shallow shelf environments and ecosystems.

2.4.3 Biotic distribution and redox within the Nama Group

The organisms present within the Nama Group are not found in anoxic sediments. However, it has been noted that *Namacalathus* were able to inhabit areas with short-lived oxia during a time where the water column was mostly anoxic (Wood et al., 2015). The fossil distribution of the Nama Group was determined through compiling data from literature of fossil occurrences within the basin (Figure 2.6; Appendix 1.1; Bowyer et al., 2020).

During the deposition of the Kuibis Subgroup organisms inhabited shallower environments (Figure 2.5; 2.6). Within the Witputs Sub-basin, soft-bodied organisms were prevalent in these environments, featuring *Ernietta*, *Pteridinium*, *Rangea* and *Ausia* which area common within the Nama faunal assemblage (Germs, 1973; Bouougri et al., 2011; Hall et al., 2013; Darroch, et al., 2015). However, *Rangea* and *Ernietta* populated in deeper settings, inner-ramp to mid-ramp settings within he Kliphoek Member (Hall et al., 2013; Vickers-Rick et al., 2013). Biomineralisers are also known to have inhabited shallower environments with *Cloudina* of the Mara Member and *Namacalathus* of the Upper Kliphoek Member colonising inner ramp settings (Grotzinger et al., 2000; Wood et al., 2015). Macro-fossils have not been found within the lower Kuibis Subgroup within the Zaris Sub-basin, equivalent to that of the Mara and Kliphoek members of the Witputs Sub-basin. However, within the Upper Kuibis Subgroup, particularly the Omkyk Member, *Cloudina* and *Namacalathus* are found inhabiting inner-ramp and mid-ramp environments, and even forming reefs (Penny et al., 2014).

The Schwarzrand Subgroup of the Wiputs Sub-basin contains a diverse biota, including *Nasepia*, *Swartpuntia*, *Pteridinium*, *Aspidella*, *Cloudina* and *Namacalathus* within the Urusis Formation, which represents a shallow, potentially shoreface environment (Narbonne et al., 1997; Wood et al., 2015; Darroch et al., 2015). However, there are examples of soft-bodied organisms located within the mid- to outer-ramp settings within the upper Spitskop Member (Narbonne et al., 1997; Darroch et al., 2000) and outer-ramp settings contain in-situ *Cloudina* and *Namacalathus* (Wood et al., 2015); settings which were not commonly occupied in comparison to the Kuibis Subgroup.

The Kuibis Subgroup is characterised by small, shallow and simple traces within subtidal to intertidal environments (Germs, 1983; Crimes et al., 1982; Crimes and Fedonkin; 1996). Within the shallower settings of the Witputs Sub-basin there is an increase in bioturbation intensity within the Nudaus Formation and this continues to increase during deposition of the Schwarzrand Subgroup, from 1.94% in the Kliphoek Member to 5.61% in

the Spitskop Member (Cribb et al., 2019), with the earliest treptichnids found within the Urusis Formation of the Witputs Subbasin (Jensen et al., 2000, Jensen and Runnegar, 2005; Wilson et al., 2012). There are, however, potential complex feeding structures found within the Upper Omkyk Member of the Nama Group, but there is debate as to the affinity of these fossils, which may rather represent *Palaeopasichnus*, or even abiotic structures of syn-depositional soft sediment deformation (Jensen, 2003; MacDonald et al., 2014; Smith et al., 2017; Darroch et al., 2020). The increase in bioturbation intensity coincides with the stabilisation of oxic conditions within the basin. The increase in oxygen concentration within the water column would have lowered the metabolic costs for locomotion allowing these motile Ediacaran organisms to utilise microbial mats and nutrients trapped within the sediment. This is also true for calcifying taxa as they require well-oxygenated conditions to produce biominerals (Wood et al., 2015; Tostevin et al., 2016b). The deepening of the redoxcline allowed the Ediacaran taxa to inhabit deeper areas of the shelf. However, skeletal taxa were most abundant during the deposition of the Kuibis Subgroup where the mid-shelf areas were well-ventilated and with nutrient-rich waters. This could imply that there are optimal conditions for skeletal taxa, which includes oxia and higher nutrient input.

Combining biotic distribution data with redox proxies provides evidence that Ediacaran organisms of the Nama Basin inhabited solely fully oxygenated areas (Figure 2.6). The successive expansion and stabilisation of oxygenation in the Nama Group allowed for the increase of habitable areas for Ediacaran organisms enabling them to inhabit and utilise deeper parts of the basin (Figures 2.5; 2.6).

***Figure 2.6 (page 70)**: Nama Group fossil occurrences, separated between subbasins. Violin plots of the bioturbation intensity, after Cribb et al. (2019), which increases throughout the succession. Taxonomic diversity of body fossils split between shelf environment setting where taxa inhabited deeper settings through time. Modified from Bowyer et al. (2020).*

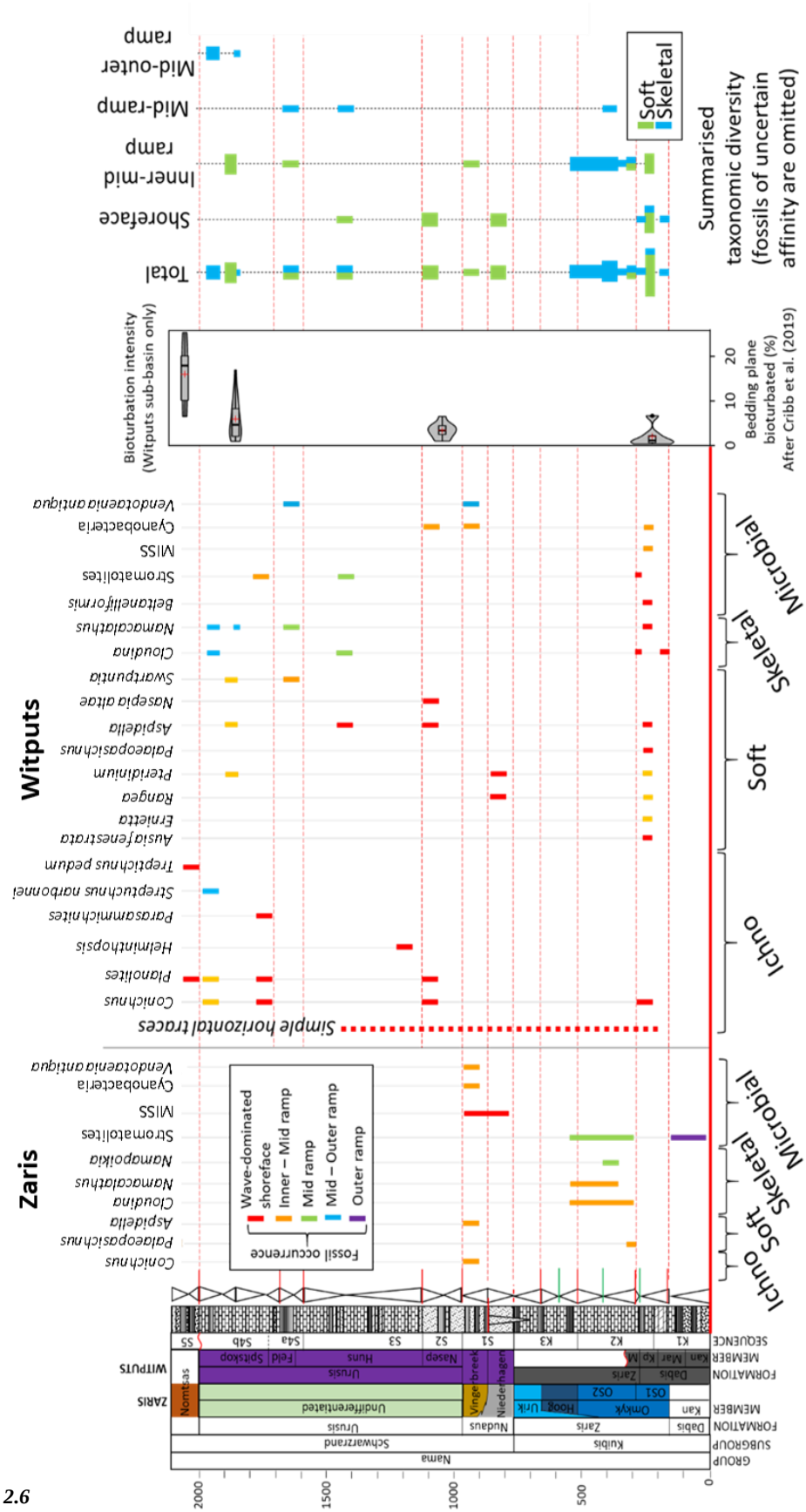
Summarised taxonomic diversity (fossils of uncertain affinity are omitted)
Soft
Skeletal
Total
Shoreface
Inner-mid ramp
Mid-ramp
Mid-outer ramp
Bioturbation intensity (Witputs sub-basin only)
Bedding plane bioturbated (%)
After Cribb et al. (2019)
Witputs
Zaris
Simple horizontal traces
Fossil occurrence
Wave-dominated shoreface
Inner – Mid ramp
Mid ramp
Mid – Outer ramp
Outer ramp
Ichno
Soft
Skeletal
Microbial
Conichnus
Planolites
Helminthopsis
Paragrammichnites
Streptichnus narbonei
Treptichnus pedum
Ausia fenestrata
Enigetta
Rangea
Periditinium
Palaeopascichnus
Aspidella
Nasepia atlae
Swartpuntia
Cloudina
Namacalathus
Beltanelliformis
Stromatolites
MISS
Cyanobacteria
Vendotaenia antigua
Namapoikia
GROUP
SUBGROUP
FORMATION
MEMBER
SEQUENCE
Nama
Schwarrand
Urusis
Nudaus
Kuibis
Zaris
Dabis
Kan
Mar
Kp
M
Omkyk
Hoogk
Urik
OS1
OS2
Vingerbreek
Niederhagen
Undifferentiated
Nomtsas
ZARIS
WITPUTS
Urusis
Huns
Nasep
Feld
Spitskop
S5
S4b
S4a
S3
S2
S1
K3
K2
K1
2000
1500
1000
500
0

Figure 2.6

2.5 Conclusion

Phosphorus speciation data of the Nama Group shows that there were changes in phosphorus cycling throughout the deposition of the succession. During the stratified redox conditions of the Kuibis Subgroup (ca. 550-547 Ma) anoxia prevailed in the deeper settings, which promoted drawdown of bioavailable phosphorus. However, there was limited recycling back into the water column during these anoxic episodes, further promoting primary productivity, which may have been further supplemented from the upwelling of nutrient-rich waters from the deep ocean. From ~547 Ma onwards the redoxcline began to deepen, and the recycling of bioavailable phosphorus back into the water column decreased through the process of sink-switching to authigenic apatite. However, the cycling of phosphorus did not have control over the oxygenation of the Nama Group, as it was likely the decrease is nutrient input from the reduction of chemical weathering from the continent that caused the shift, but the retention of phosphorus within the sediment allowed for the stabilisation of oxia within the Nama Basin. The stable oxic conditions and the deepening of the redoxcline allowed more metabolically costly forms of life to prevail within the Nama Group and to inhabit deeper areas of the basin.

Chapter 3: Multiple Branching and Attachment Structures in Mat-dwelling *Cloudina*, Nama Group, Namibia

The results reported in Chapter 3 are published as: Shore, A., Wood, R., Curtis, A. and Bowyer, F., 2020. Multiple branching and attachment structures in cloudinomorphs, Nama Group, Namibia. Geology, 48(9), pp.877-881. The text in the following chapter is adapted from this paper and the published paper and supplementary materials are given in Appendix 2.1.

Sample collection was carried out by Amy Shore, Rachel Wood, Andrew Curtis and Fred Bowyer. Amy Shore undertook photography of the samples, serial sectioning, 3D reconstruction, photography of thin sections (under PPL, XPL and cathodoluminescence) and measurement of tube dimensions. Amy Shore wrote the first draft of the manuscript.

3.1 Introduction

The affinity of *Cloudina* and other cloudinomorphs, tubular skeletal and organic taxa of similar morphology, is contested (see Chapter 1, Section 1.6.2.2). While different features, such as the ultrastructure, general morphology and soft tissue preservation, have been used to try and understand the affinity of cloudinomorphs (Hua et al., 2005; Vinn and Zaton; 2012; Schiffbauer et al., 2020), there is still much debate.

In this chapter, the first recorded instance of multiple (polytomous) branching and the form of attachment sites in cloudinomorphs is described. Multiple methods were used to acquire data for this study. Serial sectioning and 3D modelling were used to understand the form and structures of cloudinomorphs in 3D and to determine whether the potential branching

cloudinomorphs had a shared cavity. Measurements of tube width in 2D and 3D give insight to the growth rates of cloudinomorphs after budding or attachment. Also, cathodoluminescent imaging of cloudinomorphs is used to visualise generations of cements associated with cloudinomorphs, providing further understanding of potential shared cavities and attachment cements. These observations, such as polytomous branching and initial fast rate of tube growth, add to the debate of the affinity for cloudinomorphs.

3.2 Material and methods

Samples from *in-situ* bedding planes were collected from near the top of the Upper Omkyk Member of the Kuibis Subgroup, at Omkyk Farm and Driedoornvlakte in the Zaris Subbasin of the Nama Group, Namibia (see Chapter 1, section 1.9.1.3 and Appendix 2.1). An ash bed from the overlying Hoogland Member is dated at 547.32 ± 0.65 Ma, suggesting the samples collected are older than this date (Grotzinger et al., 1995; Bowring et al., 2007; Schmitz, 2012). Driedoornvlakte is a shallow reef complex that formed in a mid-ramp setting that contains abundant skeletal taxa, *Cloudina*, *Namacalathus*, and *Namapoikia*. At Omkyk Farm, strata record deposition at an inner ramp position close to the Osis Arch, into increasingly shallow, very low-energy, possible lagoonal settings containing *Cloudina* and *Namacalathus* (Wood et al., 2015). A full geological description of these sites is found in Chapter 1, section 1.9.

Cloudinomorph tubes which appeared to show bifurcation on the bedding surface were selected for serial sectioning. During serial sectioning cloudinomorph specimens were ground in increments of 10 µm, 1.23 mm in total, or 25 µm, 1.25 mm in total using fine sandpaper (1200) or a Buehler Petrothin thin sectioning system, respectively. Three vertical holes were drilled in each sample to aid alignment of the images, which were imaged using a binocular microscope (300 dpi; 19 x 19 to 31 x 31 µm pixel size) or a Canoscan Lide 210

flatbed scanner at (4800 dpi; 53 x 53 to 39 x 39 µm pixel size). Before imaging each sample was ground until flat to ensure the sample was being ground equally across the surface. The aligned images were either segmented manually or through binarising each section with the contrast settings of each scan replicating the original image. Background noise was removed manually. Cloudinomorph walls and the open cavity were manually segmented separately, in the case of one model. The processed images were imported as a virtual stack into Avizo 9 software to create 3D models composed of between 50 to 123 2D images and smoothed to reduce noise. Smoothing thresholds were used to reduce noise within the model by constant reference to features in the original scans as not to remove key features such as branches or attachments. Highly polished thin sections were imaged by standard petrographic and cathodoluminescence microscopy.

ImageJ (Fiji) software (https://imagej.net) was used to measure internal cement thickness within cloudinomorphs from polished sections, and to quantify cloudinomorph specimen dimensions from bedding planes. ImageJ was also used to measure the dimensions of the cloudinomorph tubes in increments on both the bedding surface and in the models. Measurements were taken perpendicular to the central line of the tube at 0.5 mm increments in the model, and 1 mm increments on the bedding plane surface. Only the major axis of each tube was measured in increments in each 3D model, as the necessary removal of material to produce a flat surface rendered minor axes measurements meaningless.

3.3 Results

3.3.1 Microbial metazoan communities

Bedding planes of flaggy, wackestone to packstone grading into friable, dolomitised wackestone to mudstone from Omkyk Farm, 12 to 30 mm thick, show abundant aggregations of sinuous, straight, and apparently branching cloudinomorphs and *Namacalathus* associated with inferred microbial mats (Figures 3.1A and B). Inferred microbial mats are dark or covered in iron oxides and have irregular or patchy edges distinct from the yellow, micritic mudstone with skeletal bioclasts. Mats are usually <1 mm thick and undulating, and occur parallel to bedding at a spacing of 2 to 5 mm.

Few tubular fossils from Omkyk Farm show a distinct annulated outer wall structure (Figure 3.1C) but recrystallisation obscures any internal stacked, funnel organisation. They are therefore attributed to cloudinomorphs. However, material from Driedoornvlakte can be attributed to *Cloudina* (Grant, 1990).

Cloudinomorph individuals range from 1.2 to 21.7 mm in length (mean = 11.2 mm, n = 17), and 0.1 to 2.3 mm in width (mean = 0.6 mm, n = 604) as measured from serial sectioning or on bedding planes respectively (see Appendix 2.21). The cloudinomorphs are inferred to be attached to mats as they are most abundant within these areas and some individuals appear to radiate from them into the surrounding micritic sediment of the inter-mat area (Figure 3.1A). *In-situ Namacalathus* are present as clusters of small individuals within the mats (Figure 3.1A), and as larger individuals outside the mats, which show close aggregation and radiate from a smaller area of attachment with deformation between individuals (0.9 to 10.3 mm, mean = 2.9 mm, n = 91) (Figure 3.1B).

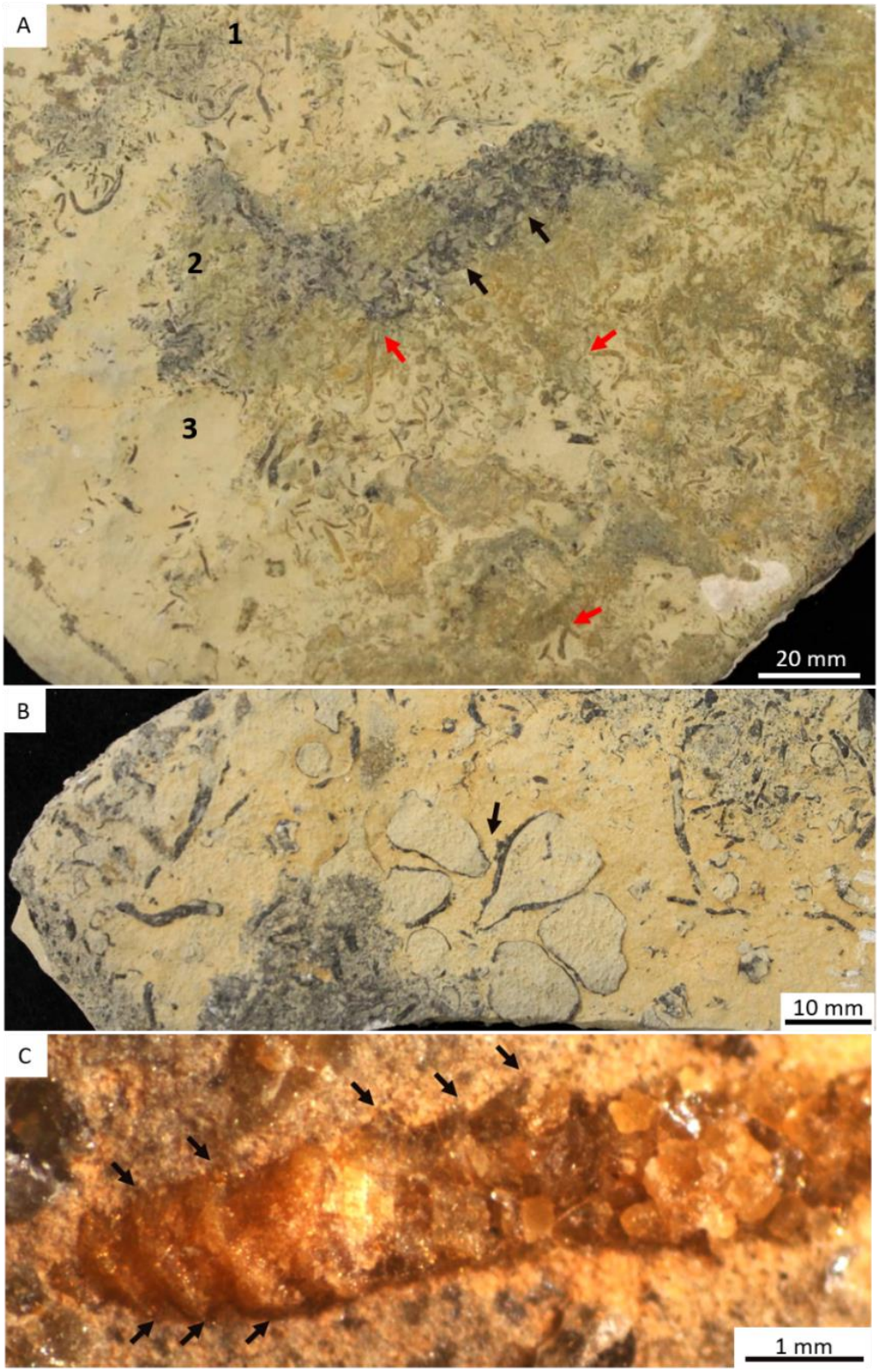

***Figure 3.1**: Bedding surfaces from Upper Omkyk Member, Omkyk Farm, Namibia. **A**:* In-situ *cloudinomorphs and* Namacalathus *(black arrows) on two generations of microbial mat surfaces (1 and 2) with projecting cloudinomorphs (red arrows), and bioclasts in inter-mat mudstone (3). **B**: Cluster of large* Namacalathus *in inter-mat area (arrow). **C**: Cloudinomorph with annulated morphology (funnels arrowed).*

3.3.2 Bedding plane observations and serial sectioning of cloudinomorphs

Bedding plane surfaces of Omkyk Farm have many examples of cloudinimorphs which look as though they are branching at multiple sites along one tube (Figure 3.2). This branching has two forms on the bedding surface where the possible daughter branches are merged with the parent tube (Figure 3.2A to D) or where there is a small gap between the tubes (Figure 3.2E to F). While bedding plane surfaces show examples of potential attachment sites and/or branching cloudinomorphs, evidence for bifurcating tubes can only be proven by the presence of a shared cavity.

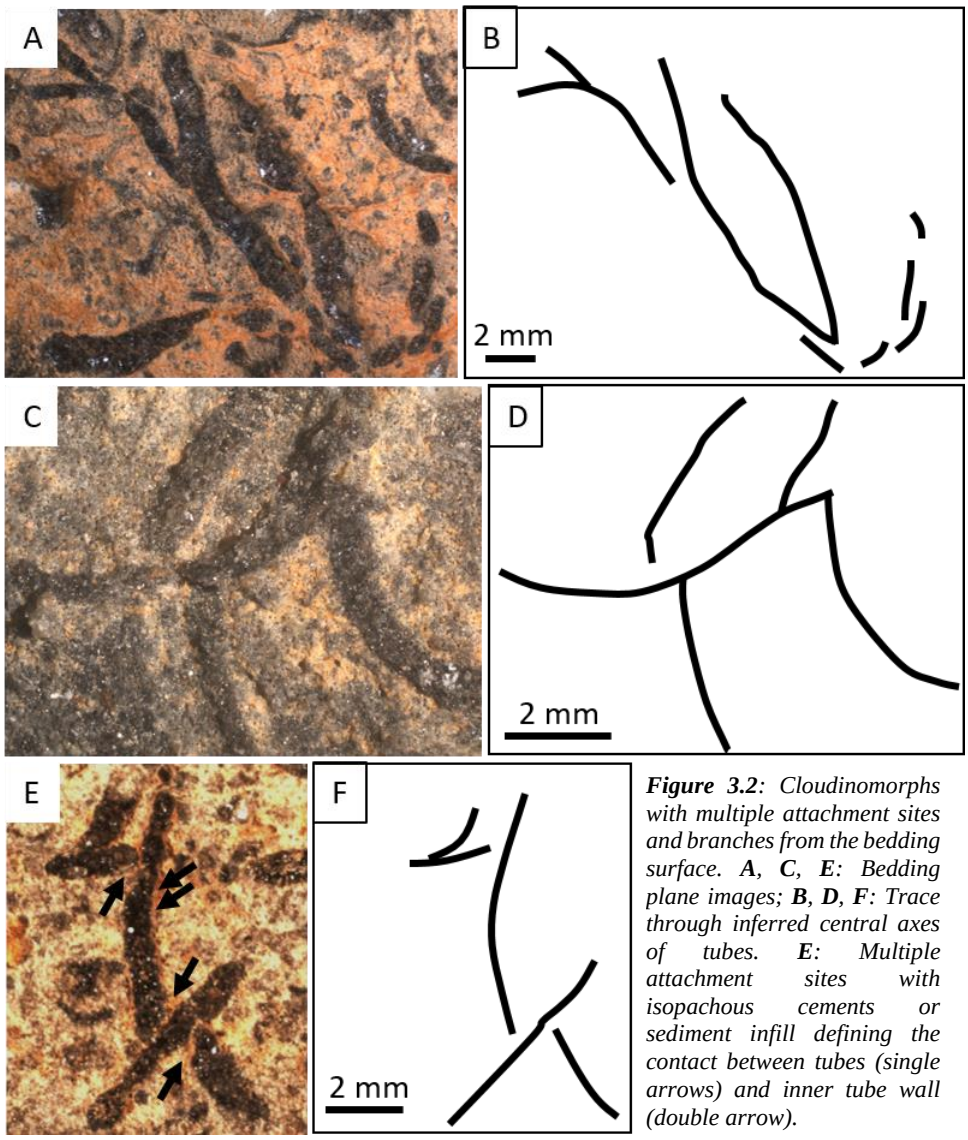

***Figure 3.2**: Cloudinomorphs with multiple attachment sites and branches from the bedding surface. **A**, **C**, **E**: Bedding plane images; **B**, **D**, **F**: Trace through inferred central axes of tubes. **E**: Multiple attachment sites with isopachous cements or sediment infill defining the contact between tubes (single arrows) and inner tube wall (double arrow).*

Polished surfaces reveal that cloudinomorph tubes are infilled first by a cloudy, isopachous cement (21 to 587 µm thick; mean = 110 µm; Figure 3.3), then remaining internal space by sparry calcite (Figure 3.4). The presence of a shared cavity is evidenced by the absence of a wall or any associated skeletal breakage that might imply post-depositional compaction, and also that the isopachous cement crust forms a continuous crust connecting both tubes, as well as continuous sparry calcite cement infill (Figure 3.4 and 3.5A-D). Cathodoluminescence images of a cloudinomorph show variations in morphology between funnel sections (Figure 3.5). In older parts of the tube each stacked funnel is separated from the next by the fine, needle-shaped early cement in which the zoned sparry cement nucleates and grows (Figures 3.5E-G). In younger areas of the tube the stacked funnel system is open with sparry calcite nucleating only from the shell walls into the cavity (Figures 3.5E-G). This morphology may be a primary feature of cloudinomorphs found at this locality, but as these observations were made in thin sections so these attributes may represent the tube undulating through the plane of the sections.

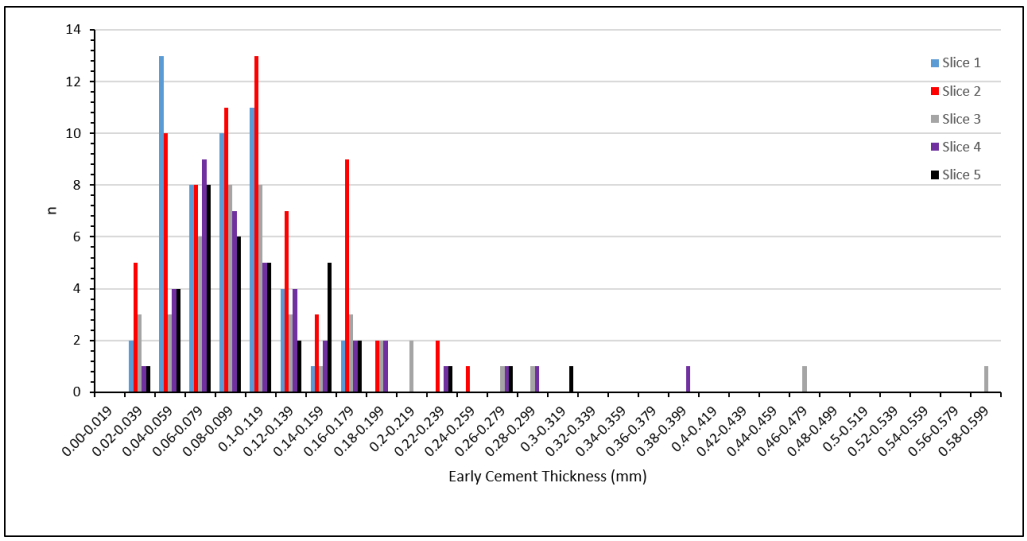

Figure 3.3*: Thickness of the isopachous crust in the parent tubes measured from 5 slices throughout serial sectioning.*

Figure 3.4 (page 80): *Evidence of budding in cloudinomorphs from the Nama Group, through serial sectioning.* ***A****: Potential branching cloudinomorph on bedding surface, with branching highlighted.* ***B****: Polished surface of branching cloudinomorph.* ***C****: Inset of B, with white arrow showing no wall between parent and daughter tube, indicating that they share one cavity. Black arrow indicates isopachous cement.* ***D****: Polished surface of branching cloudinomorph.* ***E****: Inset of D, with white arrow in sparry calcite showing no wall between parent and daughter tube, indicating that they share one cavity.* ***F****: Polished surface of branching cloudinomorph.* ***G****: Inset of F, parent and daughter tube do not share the same cavity as isopachous cements forms against parental wall (red arrow).*

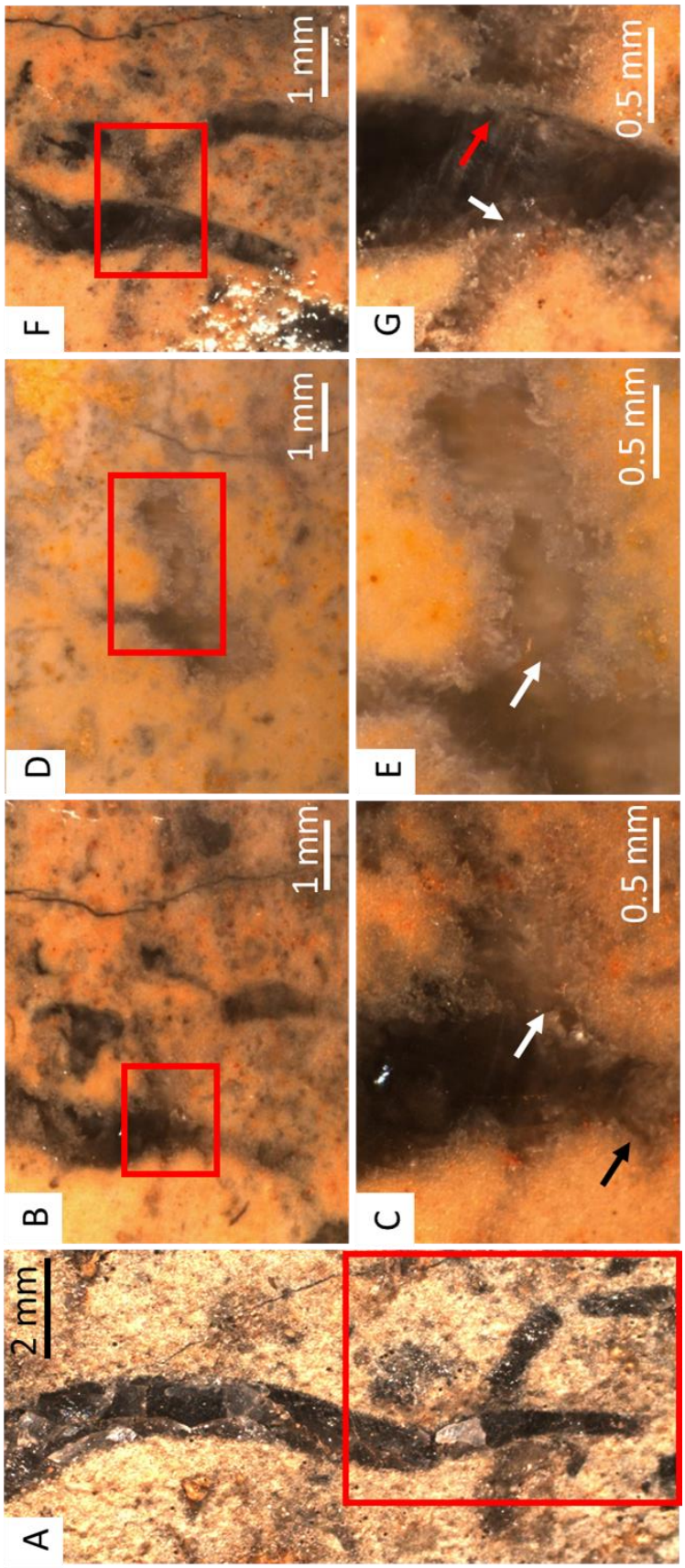

Figure 3.4

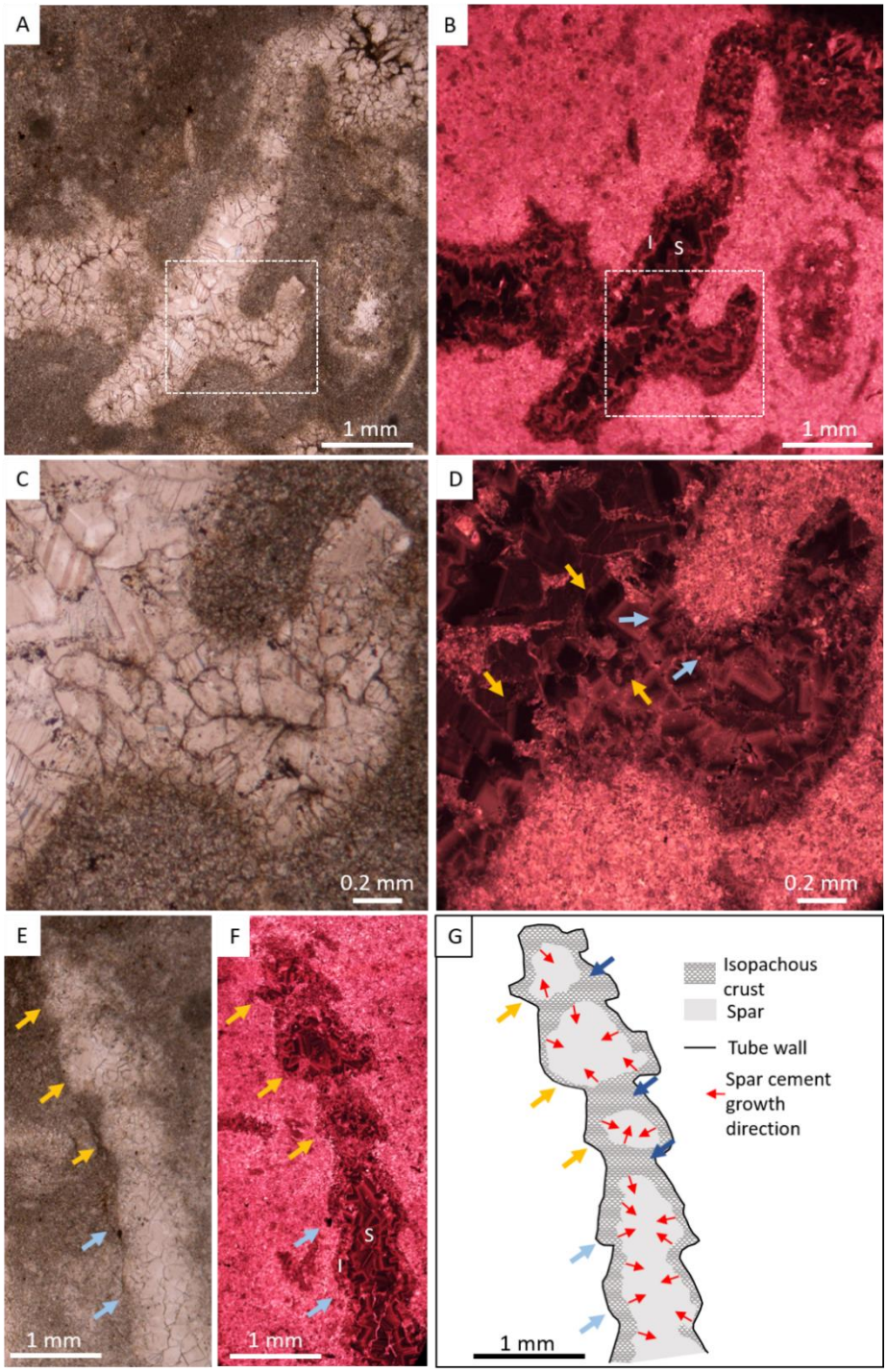

Figure 3.5*: Petrographic and cathodoluminescent images of a branching cloudinomorph and a cloudinimorph with the preserved stacked funnel morphology.* ***A****: PPL photomicrograph and* ***B****: Cathodoluminescent photomicrograph of branching cloudinomorph, showing continuity of isopachous (I) and sparry calcite (S) cements in parent and daughter tubes.* ***C****: Inset of A and* ***D****: Inset of B, showing continuity of isopachous cement between the two tubes (blue arrows) and later sparry cement infilling both (orange arrows).* ***E****: PPL photomicrograph and* ***F****: Cathodoluminescent photomicrograph of cloudinomorph tube where arrows mark successive funnels, with isopachous (I) and sparry calcite (S) cement infill. Older funnels (orange arrow) are sealed off by fine early cements and younger funnels (blue arrows) are connected with zoned sparry calcite infilling the cavity.* ***G****: Schematic of the cloudinomorph and cement generations of F. Early cements close off the older funnels in which sparry calcite grows, direction of growth highlighted by red arrows. Younger funnels are not closed off indicated by the spar cement zones that grow throughout the cavity and not nucleate within the individual funnels. Dark blue arrows highlight the fine cements acting as a barrier between funnels.*

3.3.3 3D reconstruction of a branching cloudinomorph

One 3D model of the cloudinomorph outer wall, highlighted by the micritic envelope or the outer edge of the cavity lining isopachous cement, confirms the presence of multiple branches with differing orientations along one parent tube (Figures 3.6A, B; 3.7). These diverge from the parental tube at angles of 35 to 299° (Table 3.1; Figure 3.8). The plunge angle of the branches and attachment sites are consistently shallow, from 1.4 to 7.1° (Table. 3.1; Figure 3.8). Models of the cavity as defined by the extent of sparry calcite confirms this multiple branching structure (Figures 3.6C, D).

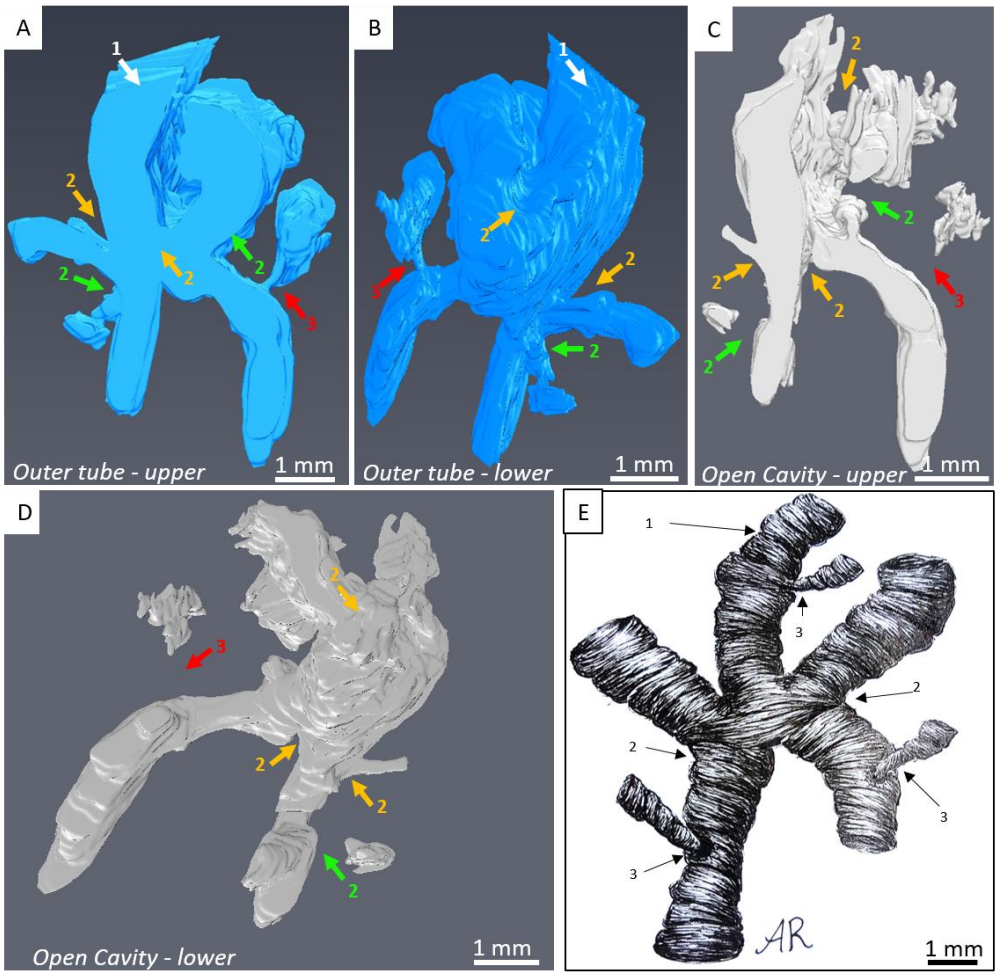

Figure 3.6*: Model and reconstruction of multiple branching cloudinimorph. Multiple branching cloudinomorph with the parent tube (1, white arrow), branching daughter tube (2; shared cavities, orange arrow), indirect evidence of branching where the cavity does not extend to the full tube (green arrow), and attachment sites (3, red arrow).* ***A****: Upper, plan view of 3D model (from bedding surface) of outer tube with 5% smoothing.* ***B****: Lower, rear view of same model.* ***C****: Upper, plan view of 3D model (from bedding surface) of open cavity.* ***D****: Lower, plan view of same model.* ***E****: Reconstruction of multiple branching cloudinomorph (Artist: Astrid Robertsson).*

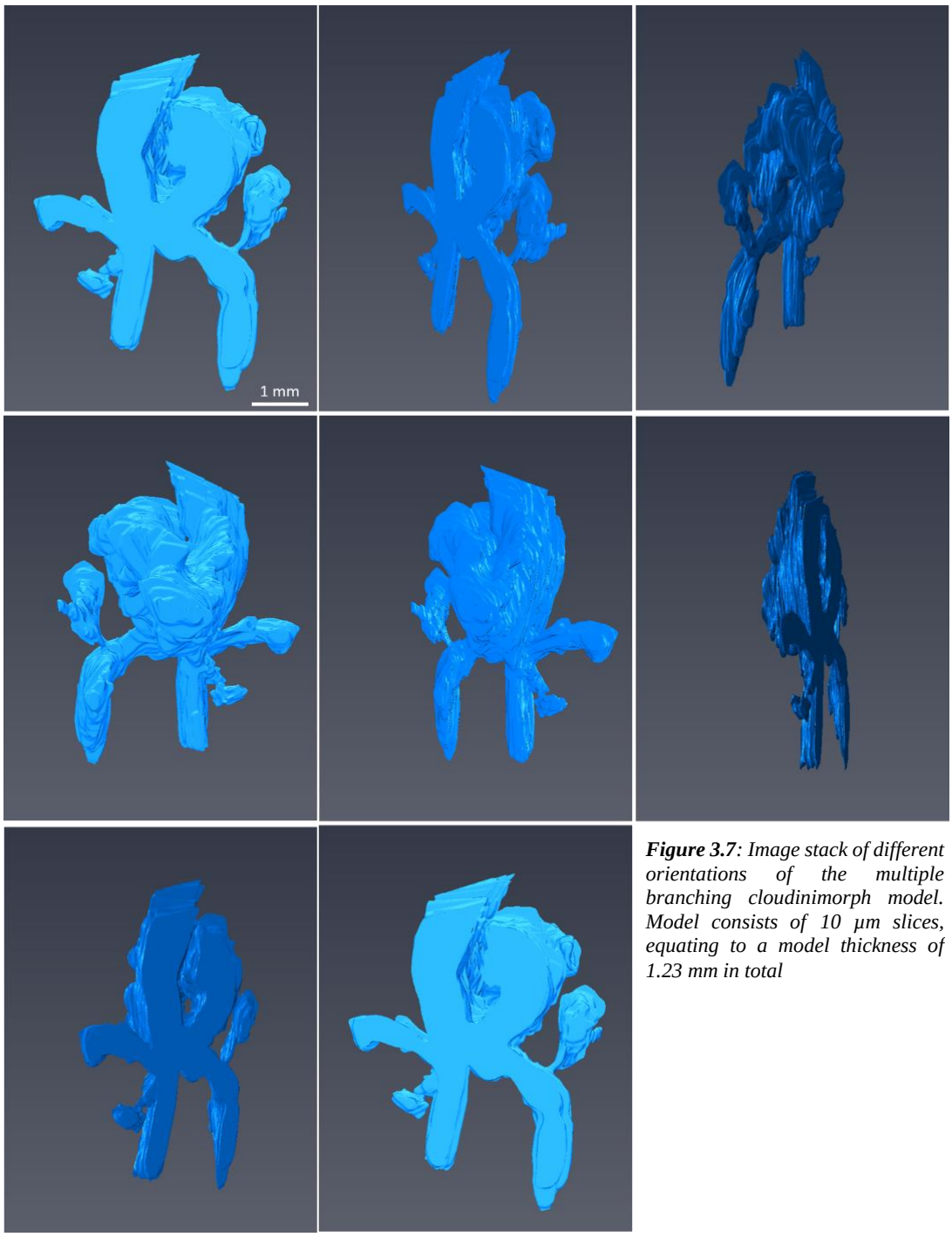

***Figure 3.7**: Image stack of different orientations of the multiple branching cloudinimorph model. Model consists of 10 µm slices, equating to a model thickness of 1.23 mm in total*

***Table 3.1**: Trend and plunge of branches at the attachment in the multiple branching model with branch number corresponding to those given in Figure 3.8.*

Branch/ Attachment	Trend (°)	Plunge (°)
1	35.1	6.0
2	26.6	5.7
3	30.2	9.0
4	131.8	1.7
5	299.1	1.4
6	231.3	7.1

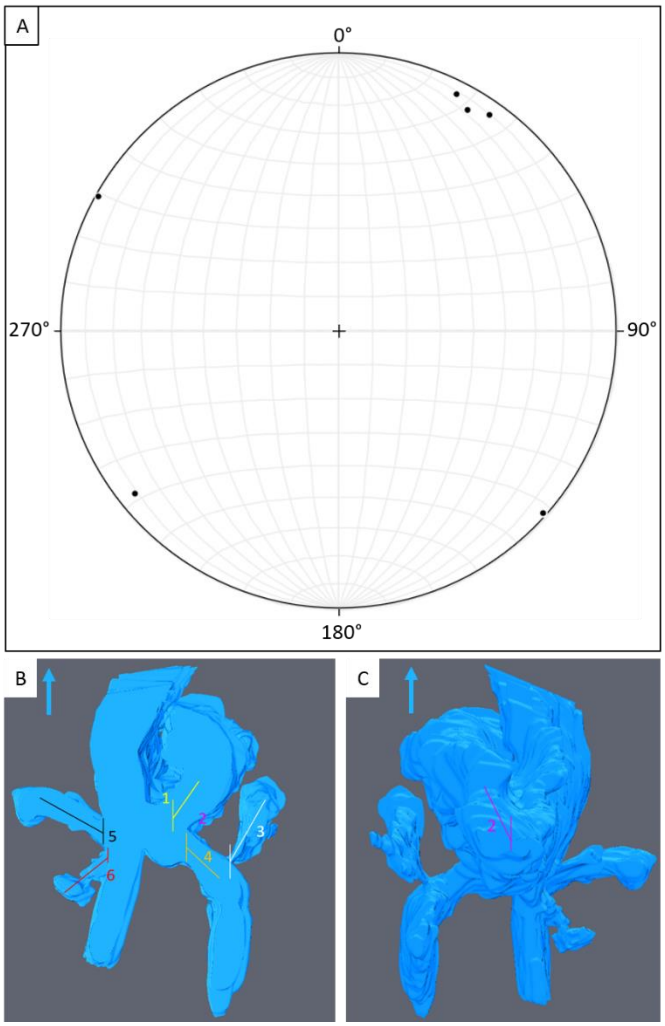

***Figure 3.8**: Trend and plunge of the daughter tubes of the multiple cloudinimorph model from the parent tube. **A**: Stereonet indicating plunge of the branches and attachment from the multiple branching cloudinomorph model with the trend taken from the orientation arrow indicated in B and C, the orientation of the parent tube. Numbers correspond to the branches and attachment site in B and C. **B**: Plan view of model with trend lines for each branch or attachment. **C**: View of underside of the model with trend line for a branch indicated.*

The diameter of cloudinomorph branches measured directly from the 3D models also shows an initial fast rate of inflation within the first 1 mm of growth but constant diameter thereafter (Figure 3.9). This is similar to measurements collected from potential branching cloudinomorphs from the bedding surface, measured in 2D (Figure 3.2, see Appendix 2.2.2)

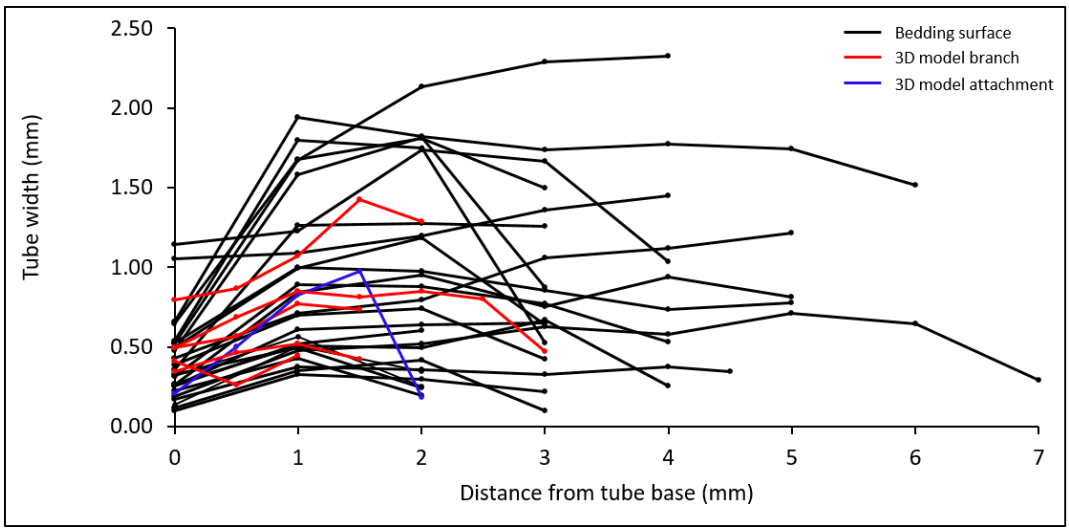

Figure 3.9: *Width of cloudinomorph tubes measured from 2D bedding planes and multiple branching 3D models.*

Branches grow from the outer wall of the parent tube, i.e. with no intra-calar bifurcation (Figures 3.6A-D). Models also reveal attachment sites of small cloudinomorph individuals, as indicated by the presence of the parental tube outer wall and no shared cavity (Figures 3.6; 3.7A, B). The attached tube is often initially more narrow than the width of the tube to which it attaches (Figures 3.6A, B), but the tube inflates also rapidly to form a cavity (Figure 3.9). Individuals can therefore be reconstructed with both multiple branches and attachment sites (Figure 3.6E).

3.3.4 Cloudinomorph attachment structures

Cementation can occur as one tube attached either at the base (attachment) or along the length of the shell (mutual cementation) of another tube (Penny et al., 2014). On the bedding surface, potential cemented/attached tubes are indicated by a gap between apparently branching tubes (Figure 3.2E). This is inferred to represent either the isopachous cement crust or sediment infill between the parent and inflating daughter tube, or two attached tubes which are differently orientated in 3D relative to one another.

Mutual cementation is also observed at both Omkyk Farm and Driedoornvlakte between adjacent or near parallel tubes in close proximity (<0.3 mm) in differing orientations (Figure 3.10A). At Driedoornvlakte, *Cloudina* walls are composed of brown, inclusion-rich dolomite and dolomitised extra-tubular structures, with geopetal dolomitised micrite present within the tube (Figure 3.11A). Under cathodoluminescence, *Cloudina* walls show bright luminescence and neomorphosed calcite with the same bright luminescence is also present between the adjacent tubes suggesting that the *Cloudina* walls and the extra-tubular structure share the same diagenetic signature (Figure 3.11B). This structure predates the formation of a further bluish, dull luminescent neomorphosed calcite with patchy areas of brighter luminescence that forms both adjacent to *Cloudina* walls and within the inner tube (Figure 3.11B). An inclusion rich, non-luminescent sparry calcitic cement and a later clear sparry calcite postdate these cements, which are of organic origin (Figure 3.11B).

Similar mutual cementation is also noted between cloudinomorphs and the outer wall of a fragment of *Namacalathus* (Figure 3.10C), reaching 0.4 mm thickness. Attachment is further confirmed via serial sectioning and 3D modeling (Figure 3.10D-F).

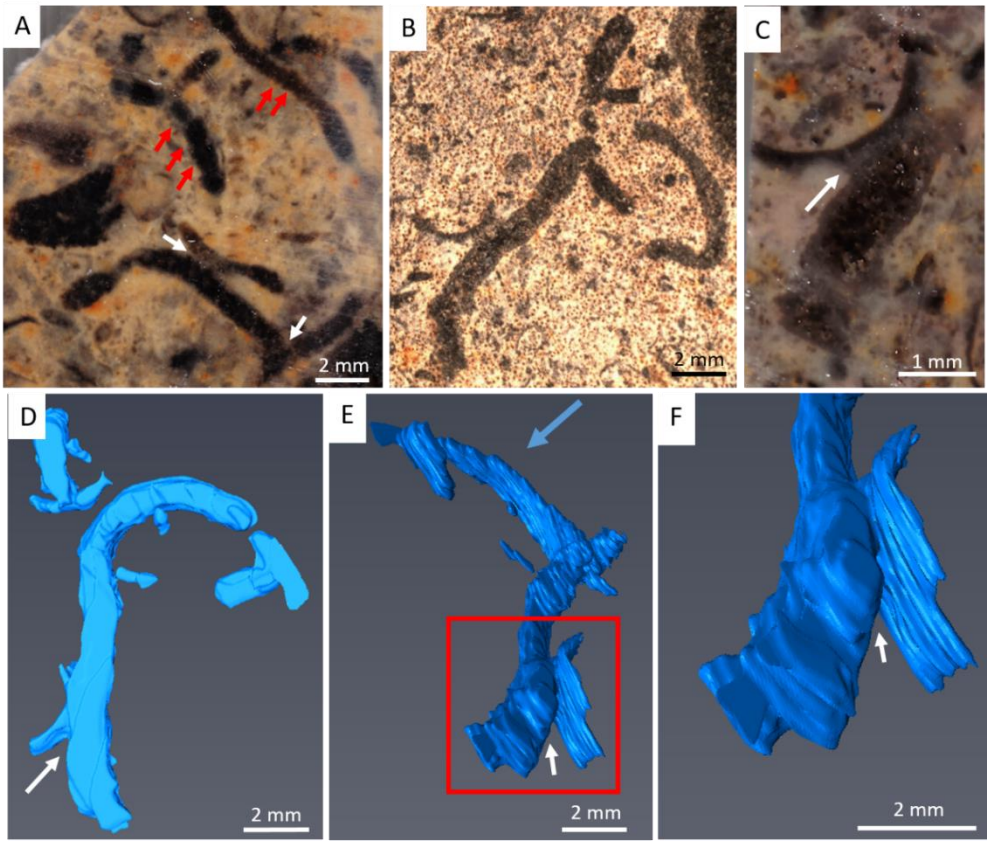

***Figure 3.10**: Cloudinomorph attachment at Omkyk Farm. **A**: Plan view of attached parallel cloudinomorph tubes (white arrow) with stacked funnel morphology (red arrows indicate funnels). **B**: Potential branching cloudinomorph from bedding surface. **C**: Plan view of extra-tubular structure between cloudinomorph tube and* Namacalathus *(white arrow), same sample as B which has been serially ground to reveal attachment. **D**: 3D model of a cloudinomorph attached to* Namacalathus *(11.7 x 7.6 x 1.475 mm). Model consists of 25 µm slices equating to a model 1.25 mm in total. This has a smoothing extent of 3.86%. **E**: Rotated 3D model orientated to cementation surface (white arrow), blue arrow indicating way up. **F**: Inset of E, 3D model of attachment between the cloudinomorph and* Namacalathus *(white arrow).*

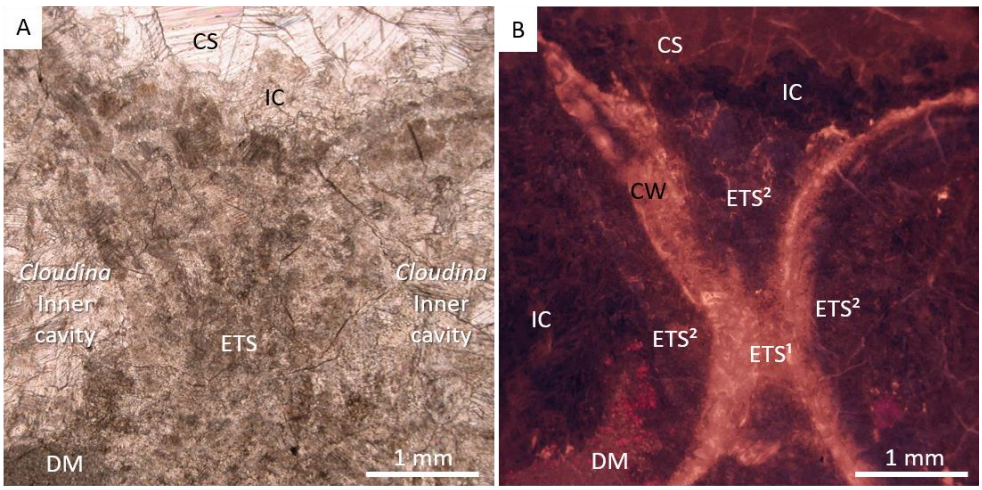

***Figure 3.11**: Attachment at Driedoornvlakte. **A**: PPL photomicrograph of two* Cloudina *tubes from Driedoornvlakte, with inclusion rich extra tubular structure (ETS) between the tubes. Geopetal dolomitic geopetal micrite (DM), and calcitic spar infill (CS). **B**: Cathodoluminescent image of same area as A, showing two generations within the ETS, bright luminescence (ETS^1) then dull luminescence with patches of bright luminescence (ETS^2). Both pre-date the inclusion-rich cement (IC) and latest sparry cements (CS).*

3.4 Discussion

The low energy, inner ramp environment dominated by fine-grained micrite mud of the Upper Omkyk Member at Omkyk Farm has allowed for the preservation of an inferred microbial mat community of delicate, *in-situ* branching or cemented cloudinomorphs and *Namacalathus*. The low-energy setting is potentially why such fine branching structures are not preserved at other sites in the Nama Group.

The presence of a shared cavity in these cloudinomorphs shows that the parent and daughter branches shared the same living space. The continuation of early cement between the parent and daughter tube and the lack of evidence for breakage of the tube walls suggest this is a growth feature and were not due to compaction during diagenesis. The style of branching presented in this study is unlike that previously recorded where the tube splits into two half cylinders within the parent tube, i.e. intra-parietal budding, or dichotomous branching (Hua et al., 2005; Cortijo et al., 2010). There is no evidence of a dividing wall along the midline within the parent tube, suggesting a different form of reproduction, here conforming to external budding.

Multiple examples of apical and longitudinal attachment accompanied by a neomorphosed calcite extra-tubular structure, which aided mutual cloudinomorph attachment, are also present. It is further shown that attachment is possible between cloudinomorphs and *Namacalathus*. These structures pre-date all inorganic cements, including pseudomorphed aragonitic cement botryoids, at the Driedoornvlakte site (Penny et al., 2014).

Given that these structures are only found associated with cloudinomorphs, and also have multiple positions relative to the tubular growth form, it is likely that they have a biological origin. These structures may have formed by extra-tubular secretion, perhaps via extracellular polymeric substances (EPS) or an organic template, which later became calcified. The close proximity of individuals appears to have encouraged mutual cementation allowing for the formation of a horizontal, multi-component, rigid framework structure associated with

microbial mat surfaces (Figure 3.12). This confirms that the ability to gain secure, mutual, attachment was present by the terminal Ediacaran.

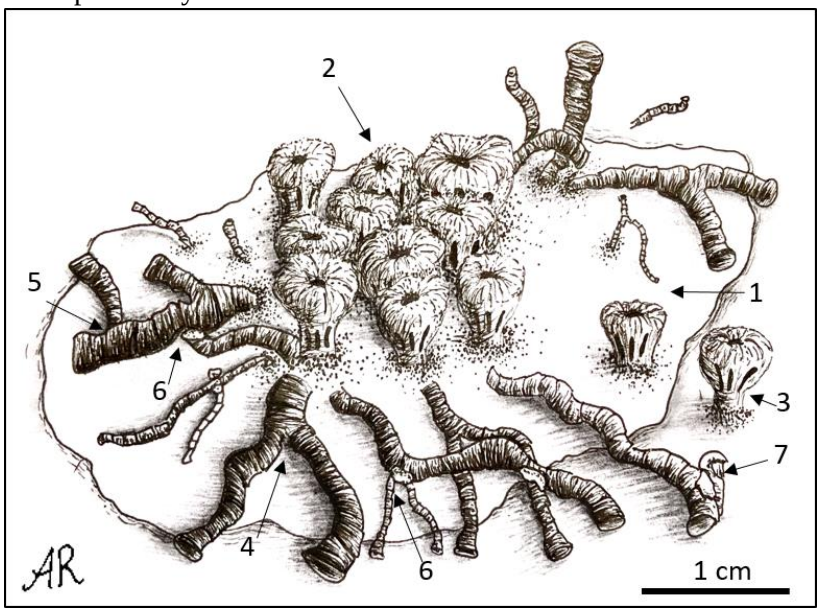

Figure 3.12*: Reconstruction of inferred microbial mat-community with* in-situ *skeletal metazoans (1) Microbial mat; (2)* Namacalathus *cluster; (3) Isolated* Namacalathus *outside microbial mat; (4) Branching cloudinomorph with horizontal habit; (5) Multiple branching cloudinomorph; (6) Mutual attachment of cloudinomorph by extra-tubular structures; (7) Attachment between cloudinomorph and* Namacalathus*. (Artist: Astrid Robertsson).*

The observation of multiple branching in cloudinomorphs at Omkyk suggests a non-bilaterian affinity. Modern cnidarians, in particular hydrozoans, show various forms of asexual reproduction, including longitudinal fission and external budding, rapid daughter branch diameter increase after branching, similar diameters of parent and daughter tubes, and multiple branching (Vinn and Zaton, 2012; Han et al., 2017; Yang et al., 2020). Evidence that the organism inhabited younger sections of the tube also supports the notion of a non-bilaterian affinity (Reitner et al., 1997). However, this has been contested by the finding of soft-tissue preservation throughout cloudinomorph tubes of Wood Canyon, Nevada, USA (Schiffbauer et al., 2020). Such a non-bilaterian affinity would also counter the annelid affinity suggested by the interpretation of this soft tissue as a gut (Schiffbauer et al., 2020), as well as the organised, lamellar microstructure of organic-walled cloudinomorphs from Mongolia (Yang et al., 2020). This apparent contradiction therefore raises the possibility that the common

Ediacaran-Cambrian tubular and stacked, funnel morphology is convergent, and that cloudinomorphs may, in fact, represent taxa of diverse affinity.

3.5 Conclusions

Polytomous branching found in a cloudinomorph of the Nama Group and the observation of mutual cementation at multiple sites suggests that multi-component rigid structures were able to form on microbial mats during the Ediacaran. These structures were able to form both between adjacent cloudinimorphs, and between cloudinomorphs and *Namacalathus*.

The multiple branching cloudinomorph observed from this site adds to the debate of cloudinomorph affinity. This evidence, along with soft-tissue preservation of a potential gut of a cloudinimorph from Nevada (Schiffbauer et al., 2020), suggests cloudinomorphs may be a polyphyletic group with convergent morphology.

Chapter 4: Environmental and Diagenetic Controls on the Morphology and Calcification in *Cloudina* of the Nama Group, Namibia

The results reported in Chapter 4 are published as Shore, A. and Wood, R., 2021. Environmental and diagenetic controls on the morphology and calcification of the Ediacaran metazoan Cloudina. *Scientific reports, 11(1), pp.1-13. The text in the following chapter is adapted from this paper with the published paper given in Appendix 3.1.*

Amy Shore and Rachel Wood conceived this study. Amy Shore conducted the research, including photography of the bedding surface, measuring all dimensions and photography under plane polarised light and cathodoluminescence. Chris Hayward, of the University of Edinburgh, carried out electron microprobe analysis on selected sample, through Amy Shore's instruction. Amy Shore and Rachel Wood wrote the final manuscript.

4.1 Introduction

Cloudina and cloudinomorphs are thought to be the first macrofaunal biomineralisers, as evidenced by the fracturing of the tube and internal tube cements, and are thought to have had either an aragonitic or high-Mg calcite mineralogy (Germs, 1972; Grant, 1990; Tucker and Wright, 2009; Pruss et al., 2018). However, other studies have shown evidence of both brittle and ductile deformation of *Cloudina* (Grant, 1990; Feng et al., 2003) raising doubts as to whether *Cloudina* biomineralised during life.

Cloudina is proposed to have biomineralised via calcification of pre-existing organic laminae as revealed by Raman spectroscopy, which are 1-10 μm in thickness. These are often paired, with up to eight laminae within a wall (Becker-Kerber er al., 2017; Yang et al., 2020).

The walls of *Cloudina* show a granular, micritic microstructure (crystal size ca.1 µm), even in phosphatised specimens (Feng et al., 2003). The calcification may have occurred through the growth of initial amorphous calcium carbonate (ACC) nanoparticles, a process also found in modern echinoderms, molluscs and cnidarians (Gilbert et al., 2019).

However, it has been argued that the presence of delamination structures in *Zuunia*, and the common occurrence of plastic deformation in other cloudinomorphs generally, suggests a skeleton of primarily organic composition, where calcification took place post-mortem and was under the control of the surrounding diagenetic conditions (Yang et al., 2020). The presence of sparry calcite crystals that incorporate multiple laminae and infill *Cloudina* tubes from the Mooifontein Member in the Witputs Basin of the Nama Group has been used to further support the hypothesis that *Cloudina* tube walls consist of abiotic calcite (Yang et al., 2020). However, it has long been known that acicular, pseudomorphed aragonitic cements are present between *Cloudina* laminae which are often neomorphosed to a fibrous or sparry calcite (Grant, 1990), and similar cements have been found to be organic-rich in specimens from Brazil (Becker-Kerber, 2017).

Identifying biologically controlled vs. biologically induced calcification (Lowenstam, 1981) is difficult and problematic as the degree of biological control can vary. Limited or considerable biological control can still be demonstrated even where most aspects of calcification vary with environmental parameters (Enmar et al., 2000; Wizemann et al., 2014). Conversely, apparently organised microstructures may not result from biological control but may reflect interactions among otherwise disorganised crystals (Cartwright and Checa, 2007).

In this chapter, the hypothesis that the type and extent of calcification and morphology in *Cloudina* was controlled environmentally is tested, by considering coeval assemblages from the Upper Omkyk Member of the Nama Group, Namibia, from diverse water depth and hydrodynamic settings along an inner shelf to reef transect from the Zaris Subbasin. Potential ecophenotypic responses of the *Cloudina* tube are quantified by comparing whole tube

sinuosity (the degree of curvature), and individual lamina thickness and overall tube wall thickness distributions are used to test whether these are variable across the transect. Variability would suggest these features are controlled environmentally, or invariant and so are under strong biological control. The sinuosity of *Cloudina* tubes, for example, is noticeably variable throughout the Nama Group, and this may reflect some aspect of ambient hydrodynamics or feeding efficiency. The control of differing early diagenetic style on the preservation of *Cloudina* skeletal material is also considered, as the inner ramp settings are prone to meteoric diagenesis but the more energetic mid-ramp reef settings to high carbonate supersaturation and marine phreatic diagenesis. Features found consistently across all diagenetic settings might be considered more likely to have a biological, rather than diagenetic, origin.

Different forms of data are used for this study. Descriptive and quantitative data derived from reef surfaces, and bedding planes, using petrographic and cathodoluminescence (CL) microscopy, and electron microprobe analysis (EMPA) of Sr concentrations, which can indicate differences in original carbonate mineralogy, and Mg/Ca which may also vary according to diagenetic phase or with biological fractionation.

4.2 Materials and methods

Cloudina and cloudinomorphs within the Omkyk Member of the Zaris Subbasin were collected from multiple sites along the inner-shelf to reef transect (Figure 4.1). *Cloudina* from each site were documented using digital photography in the field or samples were taken and photographs were taken from bedding surfaces.

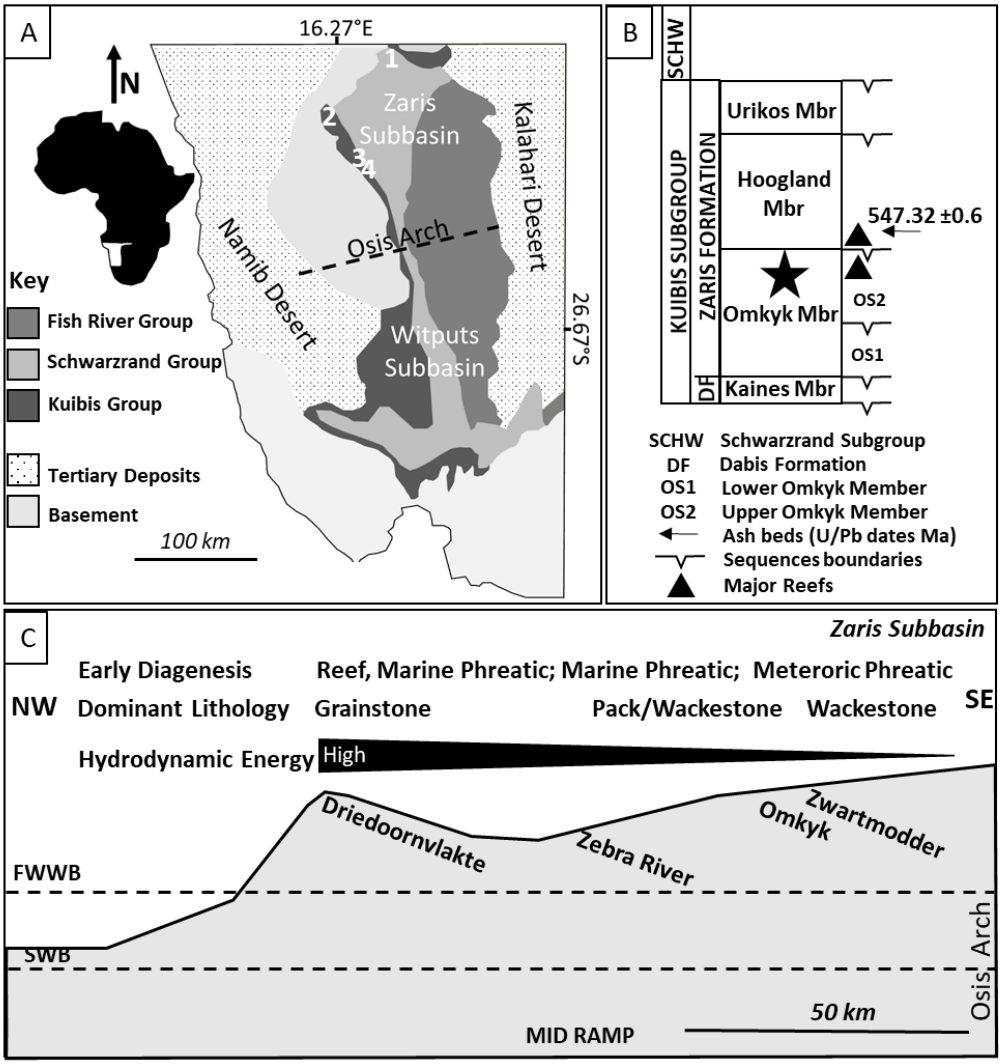

Figure 4.1 *Geological map and study site locations (1: Driedoornvlakte; 2: Zebra River; 3: Omkyk Farm; 4: Zwartmodder) within the Nama Group, Namibia.* ***A****: Localities, modified from Grotzinger and Miller (2008).* ***B****: Stratigraphy of the Nama Group with the Upper Omkyk Member highlighted by a star, modified from Wood et al. (2015).* ***C****: Schematic of the Zaris Subbasin with relative position of localities, and dominant hydrodynamic regime and lithologies, and early diagenetic setting. Modified from Wood et al. (2015).*

ImageJ (Fiji) software (https://imagej.net) was used to quantify the size of *Cloudina* features from photographs, hand specimens, and thin sections. Sinuosity, a term mostly associated with river morphology and describes as the degree of curvature, of the tubes and wall thickness from bedding surface images was also determined using ImageJ. Sinuosity is defined by dividing the length of an object by the length of the straight-line distance from bedding plane surfaces (Figure 4.2). Values of <1.1 indicate straight linear objects with higher values indicating increasing sinuosity. Percentage shortening is the amount of shortening of the tube in comparison to the original and assumed straight *Cloudina* tube length that is calculated as a percentage ((straight line distance/ midline distance)*100/midline distance). A large number of measurements were obtained to overcome any systematic bias due to use of 2D measurements.

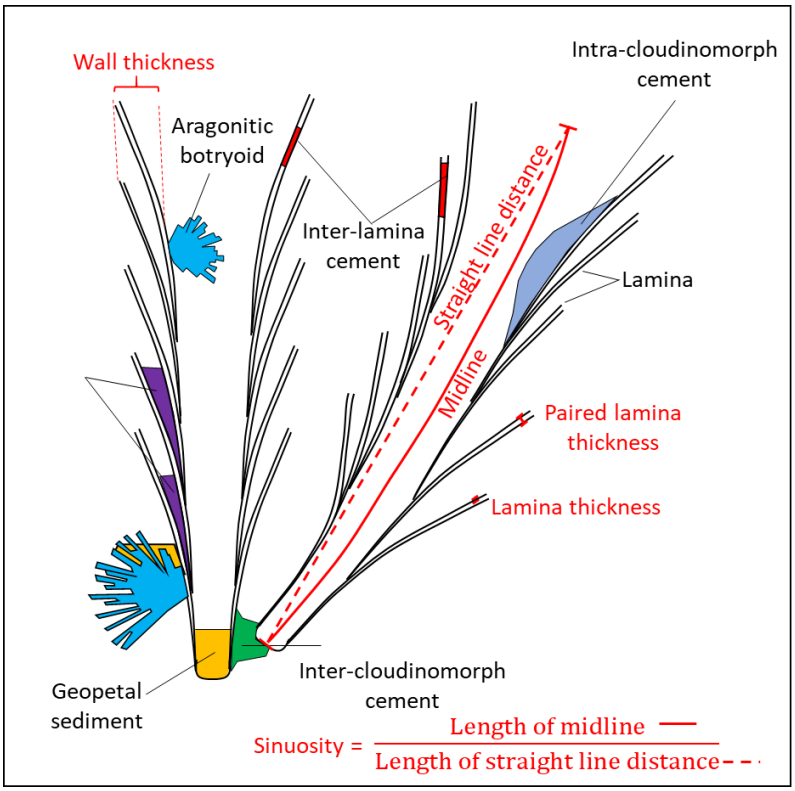

***Figure 4.2**: Schematic of* Cloudina *tubes with terminology (black text) and measurements (red text) used in this chapter derived from 2D surfaces. Sinuosity is defined as the length of the midline over the straight-line distance between the two ends of the tube in longitudinal section. Lamina thickness is the thickness of an individual lamina and paired laminae thickness the thickness of two laminae including the area between. Wall thickness is the sum of all components that form the complete tube wall in transverse section from outer wall to inner wall defining the central cavity. Cements formed between paired laminae are termed* inter-lamina cement*, between sets of paired laminae* inter-funnel cement*, between different tubes* inter-cloudinomorph cement*, and that which forms within the central cavity is termed* intra-cloudinomorph *cement. Inorganic aragonitic botryoidal cements and sediment are also labelled.*

Highly-polished thin sections were used for plane polarised light (PPL) and cathodoluminescent (CL) petrography on a cathodoluminescence Cold Cathode CITL 8200 MK3A attached to a Nikon optiphot microscope at the University of Edinburgh. Samples from Zwartmodder were imaged using a Carl Zeiss SIGMA HD VP Field Emission scanning electron microscope (SEM) at the University of Edinburgh. Sections from Driedoornvlakte and Zebra River were used to quantify major element concentrations (Ca, Mg, Sr) of *Cloudina* and associated diagenetic components via Electron Microprobe analysis (EMPA) following CL images to test for differences in original mineralogy, diagenetic phase, or evidence of vital fractionation. EMPA was undertaken on a Cameca SX100 Electron Microprobe at the University of Edinburgh using a 80s count time, a beam diameter of 3 µm, an accelerating voltage of 15 kV, and a beam current of 35 nA.

All data were statistically analysed using the Kruskal-Wallis Test, after data normalisation. Z-Tests were used on sample sizes where n >50, such as sinuosity, and T-Tests were undertaken where sample sizes were n <50 to provide a statistical comparison of each site, variance was tested to determine which T-Test function to use, i.e. whether datasets had equal or unequal variance.

4.3 Results

4.3.1 Sinuosity of *Cloudina*

The four localities show a varying degree of sinuosity of *Cloudina* tubes which can be seen from the bedding surface (Figures 4.3A-D, 4.4, see Appendix 3.2.1).

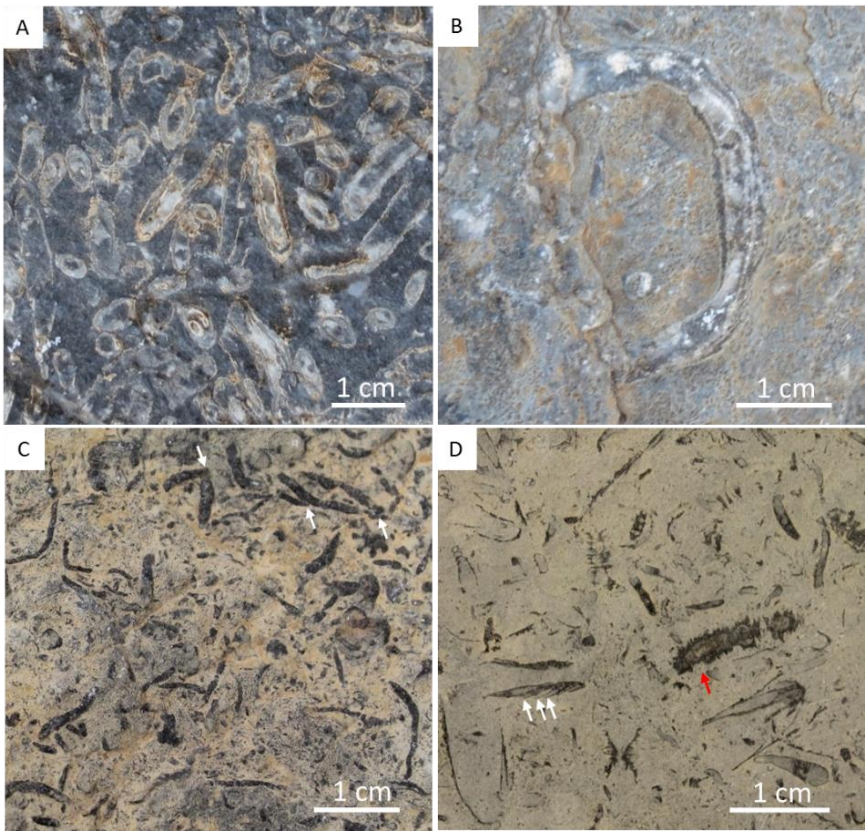

Figure 4.3*: Bedding surface images of* Cloudina *from different coeval communities from the Upper Omkyk Member.* ***A****: Driedoornvlakte, preserved as white or grey calcite cement surrounded by darker calcite cements, predominantly pseudomorphed aragonitic botryoids. The sinuosity of these tubes appears straight.* ***B****: Zebra River, infilled with light sparry calcite cement surrounded by dolomitised micrite with this example being sinuous.* ***C****: Omkyk Farm, cloudinomorphs, probably* Cloudina*, including potential branching individuals (arrowed) as branching can only be proven through the presence of a shared cavity (Shore et al., 2020), preserved as black sparry calcite surrounded by dolomitised wackestone.* ***D****: Zwartmodder, preserved as black sparry calcite surrounded by dolomitised micrite which preserves the fine annulated structure and phlanges (white arrowed). Possible fragments of* Corumbella *may also be present (red arrow).*

At Driedoornvlakte, sinuosity ranges between 1.00 - 1.70 (mean = 1.04, n = 156, standard deviation = 0.07), with the percentage shortening (the amount of shortening as a percentage in relation to the length along the midline) ranging between 0.00 - 41.29% (mean = 3.23%, standard deviation = 4.42). Zebra River and Omkyk both show greater tube sinuosity, from 1.00 - 2.98 (mean = 1.21, n = 98, standard deviation = 0.38) and 1.00 - 2.42 (mean =

1.07, n = 144, standard deviation = 0.15), respectively. Zebra River *Cloudina* show shortening from 0.00 - 66.69% (mean = 13.01%, standard deviation = 15.8), greater than the percentage found at Omkyk, where the shortening ranges between 0.00 - 58.67% (mean = 5.22%, standard deviation = 7.86). Zwartmodder *Cloudina* shows the lowest range of sinuosity, from 1.00 - 1.36 (mean = 1.04, n = 99, standard deviation = 0.06), and shortening between 0.00 - 26.25% (mean = 3.27, standard deviation = 4.57). Comparing the percentage of different ranges of sinuosity values at each locality, *Cloudina* at Zebra River show the greatest sinuosity, accounting for 100% of these values (Figure 4.4B). These also have the lowest percentage of low sinuosity values (12%), whereas *Cloudina* from Driedoornvlakte show the highest percentage of low sinuosity values (37%) (Figure 4.4B).

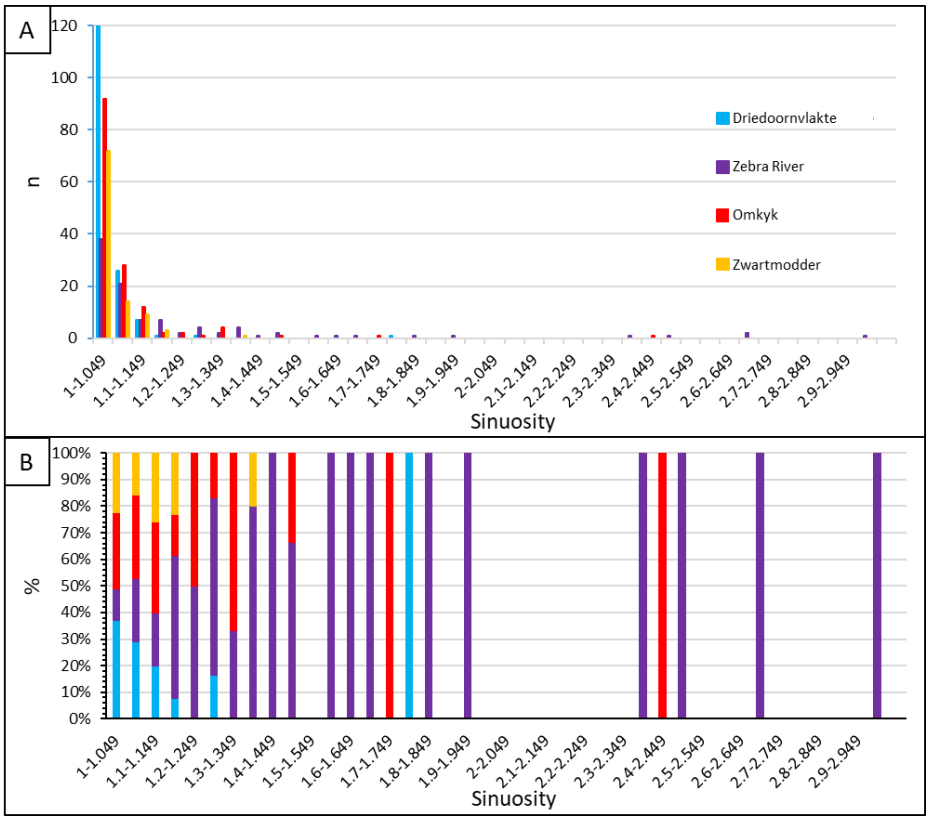

Figure 4.4*: Sinuosity data of* Cloudina *in the Nama Group.* ***A****: Sinuosity.* ***B****: Percentage of* Cloudina *with different sinuosities, based on 2D bedding plane measurements.*

Using the Kruskal-Wallis Test, the H-value for these data is 14.96, with a p-value of 0.002, indicating that the sinuosity of the *Cloudina* tubes varies significantly between sites. Z-tests also confirm that the sinuosity varies between all localities except between Driedoornvlakte and Zwartmodder.

4.3.2 Diagenetic preservation of *Cloudina*

The form of preservation of *Cloudina* varies across the Zaris subbasin transect (Figure 4.3). At Driedoornvlakte, *Cloudina hartmannae* are often surrounded by pseudomorphed aragonitic botryoids (Grant, 1990; Penny et al., 2014; Shore et al., 2020) (Figure 4.3A). Individuals show brittle deformation. *Cloudina* walls are preserved as light grey calcite, or light brown to yellow crusts indicating partial dolomitisation (Figure 4.3A). This inclusion-rich dolomite is brightly luminescent varying between bright yellow to red under CL (Figure 4.5). Laminae are often found as pairs and show brittle deformation, where abundant non-luminescent fine acicular cements with blunt terminations (4.2 – 17.6 µm in length, mean = 11.2 µm; and 2.1 – 7 µm in width, mean = 4.5 µm, n = 17) nucleate from the laminae (Figure 4.5D). This is here termed *inter-lamina cement* (Figure 4.2). Between separate paired laminae is a patchily luminescent cement (Figures 4.5I) – here termed *inter-funnel cement* (Figure 4.2). The paired laminae with inter-lamina cement, and inter-funnel cements constitute the *Cloudina* wall extending from the outer wall to inner wall that forms the central cavity (Figure 4.2).

Figure 4.5 (page 100): *Photomicrographs of* Cloudina hartmannae *and* Cloudina riemkeae *from Driedoornvlakte, Upper Omkyk Member, Nama Group.* ***A****: PPL of attached* Cloudina *with a dolomitised wall (CW) and flled with dolomitised sediment (DS), followed by an inclusion-rich sparry calcite (ISC) and a later clear burial spar (BS).* ***B****: CL image of A, intra-cloudinomorph cement (ICC^1) nucleated from the inner* Cloudina *wall and inter-cloudinomorph cement (ICC^2) formed between the* Cloudina *tubes and nucleated from the outer wall and including the mutual cement (MC) which has the same luminescence as CW. Non-luminescent pseudomorphed aragonitic botryoids (AB) nucleate from ICC^1. These are proceeded by ISC and BS.* ***C****: Inset of B, showing ICC^1 and ICC^2 - cements with same luminescence.* ***D****: Inset of C, showing bright luminescent CW with multiple non-luminescent laminae (white arrows) with small aragonitic needles (orange arrows) nucleating from laminae.* ***E****: PPL of* Cloudina *with a dolomitised wall (CW) composed of laminae (arrowed) with thin sparry calcite infill between the two laminae, surrounded by inclusion-rich sparry calcite (ISC).* ***F****: Transverse PPL of dolomitised individual.* ***G****: CL of C.* ***H****: Inset of F in PPL, of broken, dolomitised* Cloudina *wall (arrowed).* ***I****: Inset of G in CL, of broken bright luminescent* Cloudina *wall (arrowed) exposing the inter-funnel cement (IFC). The rest of the tube is infilled with non-luminescent spar (Sp).* ***J****: CL of E, with dull luminescent cements (arrowed) highlighting cements between the laminae and is surrounded by ISC. AB nucleate from the CW.*

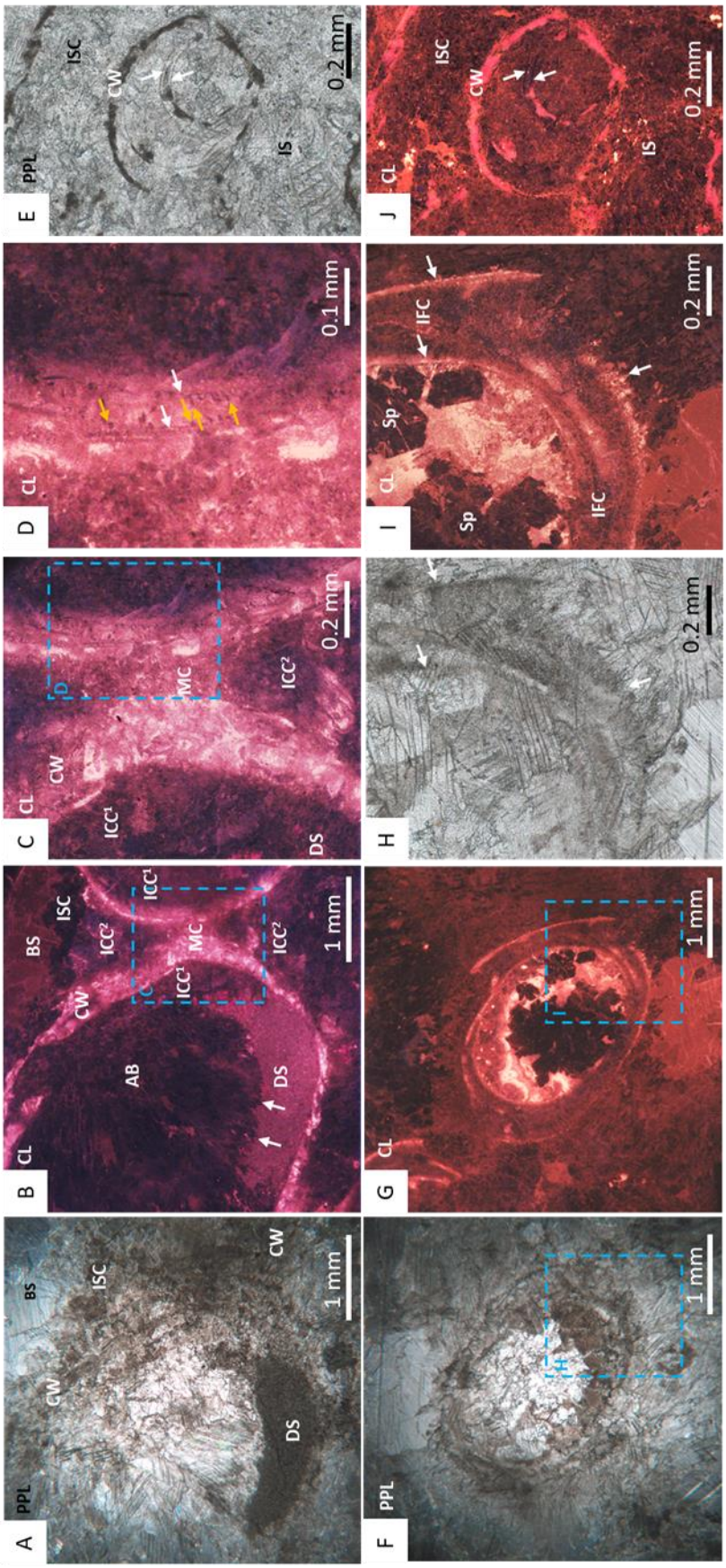
A
PPL
BS
ISC
CW
DS
1 mm
B
CL
BS
ISC
ICC²
CW
ICC¹
MC
AB
DS
1 mm
C
CL
CW
ICC¹
ICC²
MC
ICC²
DS
0.2 mm
D
CL
0.1 mm
E
PPL
ISC
CW
IS
0.2 mm
F
PPL
H
1 mm
G
CL
1 mm
H
0.2 mm
I
CL
Sp
IFC
Sp
IFC
0.2 mm
J
CL
ISC
CW
IS
0.2 mm

Figure 4.5

A further dull, patchily luminescent cement is present, which formed from the innermost laminae and grew upon the inner wall of the tube – here termed *intra-cloudinomorph cement* (Figures 4.2; 4.5B-C;). A cement with similar cathodoluminescence is found between the tubes themselves – here termed *inter-cloudinomorph cement* (Figures 4.2; 4.5B-C), as noted by Penny, et al. (2014). Dolomitised geopetal micrite with red luminescence infills *Cloudina* and postdates the intra-cloudinomorph cement (Figure 4.5A-C). Pseudomorphed aragonitic botryoids, with blunt crystal terminations, nucleate from both the intra- and inter-cloudinomorph cements, and are also covered by geopetal sediment (Figure 4.5B). Breakage of laminae is evident with associated breakage of the inter-funnel cement (Figures 4.5D, F-I).

Cloudina from Zebra River are preserved as calcite surrounded by wackestone (Figure 4.3B). The ornamental features of the tube are not preserved, and the tube cavity is infilled with sparry calcite. Individuals show brittle and ductile deformation. Paired laminae (Figures 4.6K-L) are present, and the inter-lamina space is infilled by acicular crystals (Figures 4.6D, G and N) ranging from 9.4 to 15.5 µm in length (mean = 11.7 µm, n = 6) and 2.1 to 4 µm in width (mean = 3.1 µm), forming the inter-lamina cement. In some areas the laminae are undulating, with a prominent inter-funnel cement infill (Figures 4.6C-G, J-L).

***Figure 4.6 (page 102)**: Photomicrographs of* Cloudina *from Zebra River, Upper Omkyk Member, Nama Group. **A**: PPL of* Cloudina *infilled with sparry calcite surrounded by micritic sediment (S). **B**: CL image of A, with inter-lamina cements (ILC) forming between outer laminae (highlighted in yellow). Pseudomorphed aragonitic botryoids (AB) grow from the laminae, and the inter-funnel cements (IFC) pre-date dull luminescent burial cements with ILC forming between paired laminae. AB infilled the* Cloudina *tube and S surrounds the tube. **C**: Inset of B, PPL showing laminae with a wavy form (yellow arrows). **D**: CL image of E, laminae highlighted by yellow arrows with same form as PPL image. Nucleation of IFC indicates location of laminae. **E**: Inset of B, ILC located between two outer laminae (white arrows). IFC nucleate from inner laminae (yellow arrow). **F**: Inset of B in PPL with lamina visible (arrowed). **G**: CL of F, where the outer lamina shows evidence of 'spalling' (arrowed) and infilled by S. ILC situated between laminae and areas of patchy bright luminescence indicate IFC. AB infills the rest of the tube. **H**: PPL of* Cloudina. *I: Pseudomorphed aragonitic botryoids (AB) outside* Cloudina *tube. Botryoids grow from the outer tube wall into the surrounding sediment (S), and have a different luminescence to those inside the tube. Early IFC grows from the inner* Cloudina *laminae (arrowed). **J**: PPL of a transverse section of a* Cloudina, *which is infilled by dolomitised sediment (S) and two sets of broken paired laminae (arrowed) **K**: CL of J, bright luminescent dolomitised sediment infills the central area of the broken tube. Dull luminescent botryoids (AB) outside the tube. Dull luminescent IFC forms the* Cloudina *skeleton. **L**: Inset of K, with evidence of breakage of the non-luminescent ILC (white arrows) and IFC (black arrows). **M**: PPL of* Cloudina *tube infilled with sparry calcite (SC) with preserved laminae (yellow arrowed). **N**: CL of M, with laminae observed in PPL (yellow arrows), laminae shown in CL (white arrows). Laminae are preserved with the same luminescence as the SC infill with a dull cement ILC between the laminae.*

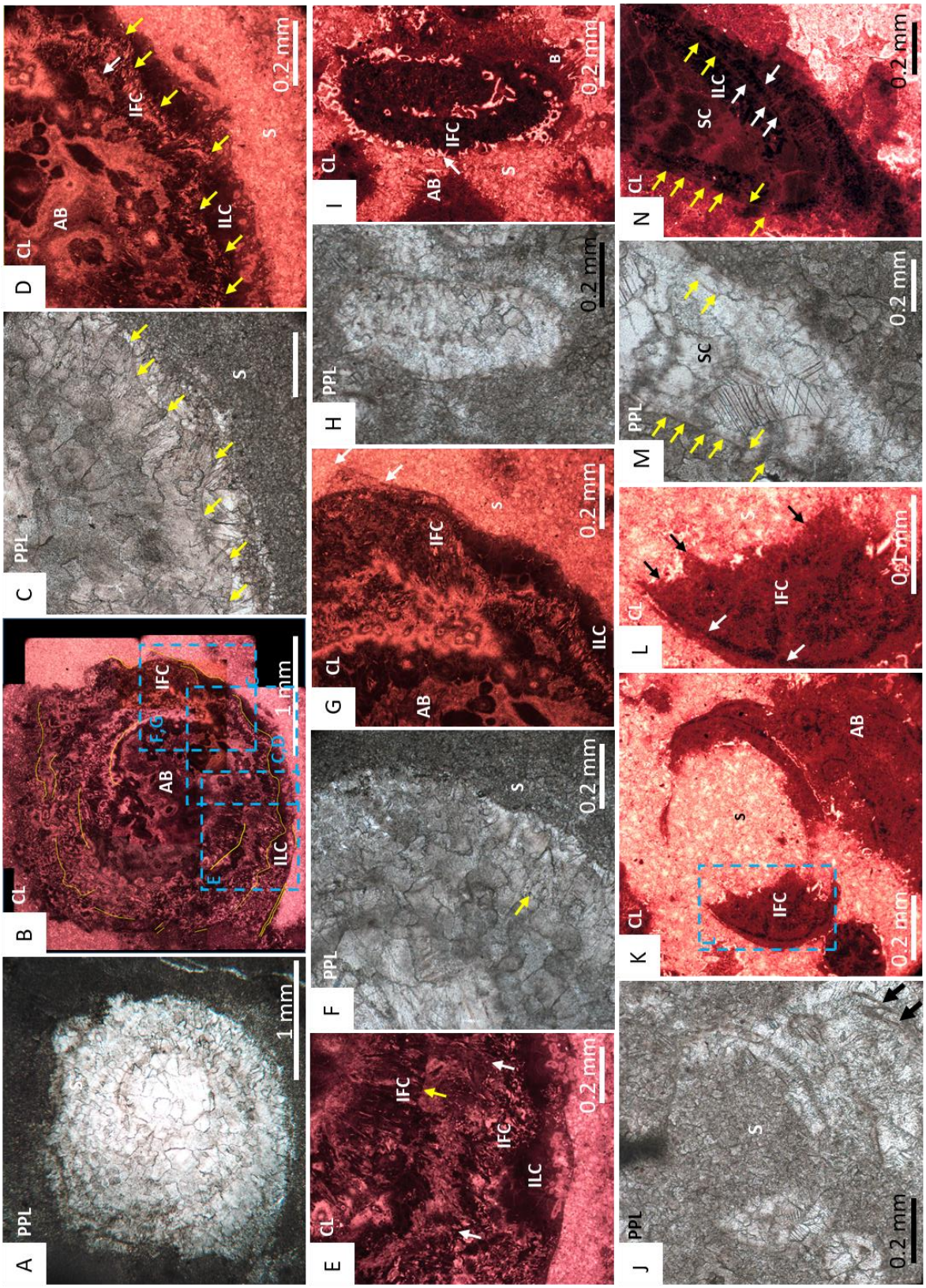
A
PPL
S
1 mm
B
CL
AB
IFC
ILC
E,G
C,D
F
1 mm
C
PPL
S
D
CL
AB
IFC
ILC
S
0.2 mm
E
CL
IFC
IFC
ILC
0.2 mm
F
PPL
S
0.2 mm
G
CL
AB
IFC
S
ILC
0.2 mm
H
PPL
0.2 mm
I
CL
AB
IFC
S
B
0.2 mm
J
PPL
S
0.2 mm
K
CL
IFC
AB
S
0.2 mm
L
CL
IFC
S
0.1 mm
M
PPL
SC
0.2 mm
N
CL
SC
ILC
0.2 mm

Figure 4.6

Patchily luminescent inter-funnel cement is also present, formed by abundant clusters of acicular cements with blunt terminations which nucleate from the laminae (Figures 4.6B, D-E, G). A dull luminescent, pore-lining patchy cement (Figures 4.6C-G) overlies inter-funnel cements. Later tube cavity infill consists of calcite spar with duller luminescence (Figure 4.6B). In *Cloudina riemkeae*, the acicular cements are finer and pore-lining cements are not observed, but inter-funnel cements with dull luminescence are present, followed by more luminescent pseudomorphosed aragonitic botryoids which nucleate from the outer tube walls (Figures 4.6H-I). There is variation in the preservation of the inter-funnel cement, which varies within a single tube: inter-funnel cements close to the exterior of the *Cloudina* tubes are mostly preserved as clear, dull or non-luminescent neomorphic calcite spar, but inter-lamina cements within the central areas of the tubes preserve acicular crystals (Figures 4.4C-D).

The inter-funnel cements in *Cloudina reimkeae* show breakage, with fractured crystal boundaries where sediment has entered the tube (Figures 4.6J-L). Individual or paired laminae also show spalling as a result of breakage of the outer wall (Figure 4.6G).

The cloudinomorphs of Omkyk are dark in colour and composed of large (0.1-1 mm) calcite spar crystals (Figure 4.3C). These also lack ornamentation, but some retain the stacked funnel-in-funnel structure (Shore et al., 2020). Individuals show brittle and ductile deformation. CL highlights three generations of cements within the cloudinomorph tube (Figures 4.7A-B, D). First a thin (200 μm) acicular cement generation, which is not continuous throughout the tube cavity, followed by an isopachous cement with patchy or dull-luminescence with limited zonation (Figure 4.7D). The tube cavity is infilled by zoned sparry cement, which nucleates from the isopachous cement (Figure 4.7D).

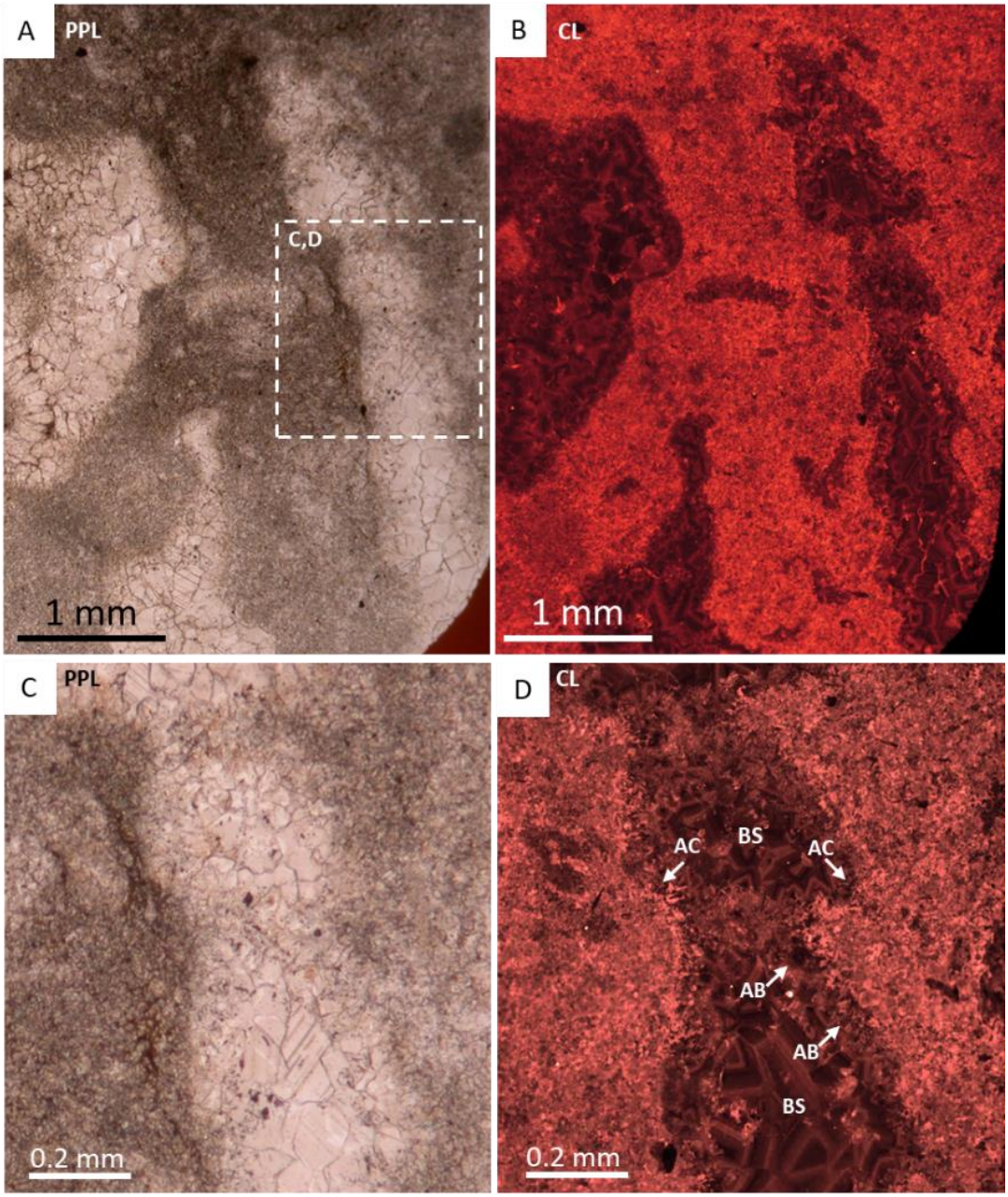

***Figure 4.7**: Photomicrographs of cloudinomorphs, probably* Cloudina*, from Omkyk Farm, Upper Omkyk Member, Nama Group. **A**: PPL image of cloudinomorph tube. **B**: CL image of A. **C**: Inset of A. **D**: CL image of A, with early acicular cements (AC) which vary between bright and non-luminescence. AC is followed by poorly zoned acicular bladed calcite (AB). A well zoned blocky calcite (BS) infills the remaining tube cavity*

Zwartmodder *Cloudina* are also preserved wholly as coarse calcite spar (Figures 4.3D; 4.8A, C). Fine external features, including external phlanges and the annulated outer wall, are well preserved (Figure 4.3D), and *Cloudina* shows evidence of brittle deformation (Figure 4.8C). The *Cloudina* skeleton is preserved a mould, infilled by a centripetal, sparry calcite cement with dull luminescence that becomes brighter towards the centre of the moulds (Figures 4.8A-B). Individual laminae cannot be detected, but inter-lamina and inter-funnel cement are present as sparry calcite (Figure 4.8F). Individual or paired laminae are evident through the spalling of the tube walls in areas where inter-funnel cement is not present and are instead separated by micrite infill (Figure 4.8F). Under CL, the micrite shows three zones of cement growth, dull-luminescent followed by bright luminescent, and a final non-luminescent zone (Figures 4.8B, E-F). These cement zones protrude into the sparry calcite infill, which can also be seen under SEM along with small, cube shaped holes (Figure 4.8G).

Figure 4.8 (page 106)*: Photomicrographs of* Cloudina *from Zwartmodder, Upper Omkyk Member, Nama Group.* ***A****: PPL of compacted* Cloudina *skeleton (CS) surrounded by dolomitised micritic sediment (S).* ***B****: CL of A, featuring dull cement which becomes well-zoned with bright luminescence during later growth. The cement infill is centripetal cement (CC) which nucleates from the wall and grows into the mould formed through dissolution.* ***C****: PPL of broken and spalled laminae.* ***D****: CL of C, the skeletal tube consists of a dull luminescent CC, which in thicker areas is brightly luminescent. Dolomitised micritic sediment surrounds the 'spalling' skeleton.* ***E****: Inset of B, brightly luminescent cement nucleates from sediment grains, which protrude into the* Cloudina *mould (white arrows) and are overgrown by a non-luminescent cement (yellow arrows) that formed before CC.* ***F****: Inset of D, sediment infills areas between spalling potential inter-laminae (I-L?), spalling occurs where CC has not formed between the laminae. Bright luminescent cements on micritic sediment grains which protrude into the* Cloudina *mould which is overgrown by a non-luminescent cement (yellow arrows).* ***G****: Sparry calcite (SC) infill of the* Cloudina *skeleton, where cement crystals protrude from surrounding sediment (white arrows). Cube-shaped holes in the SC may represent plucked micro-dolomite or pyrite crystals.*

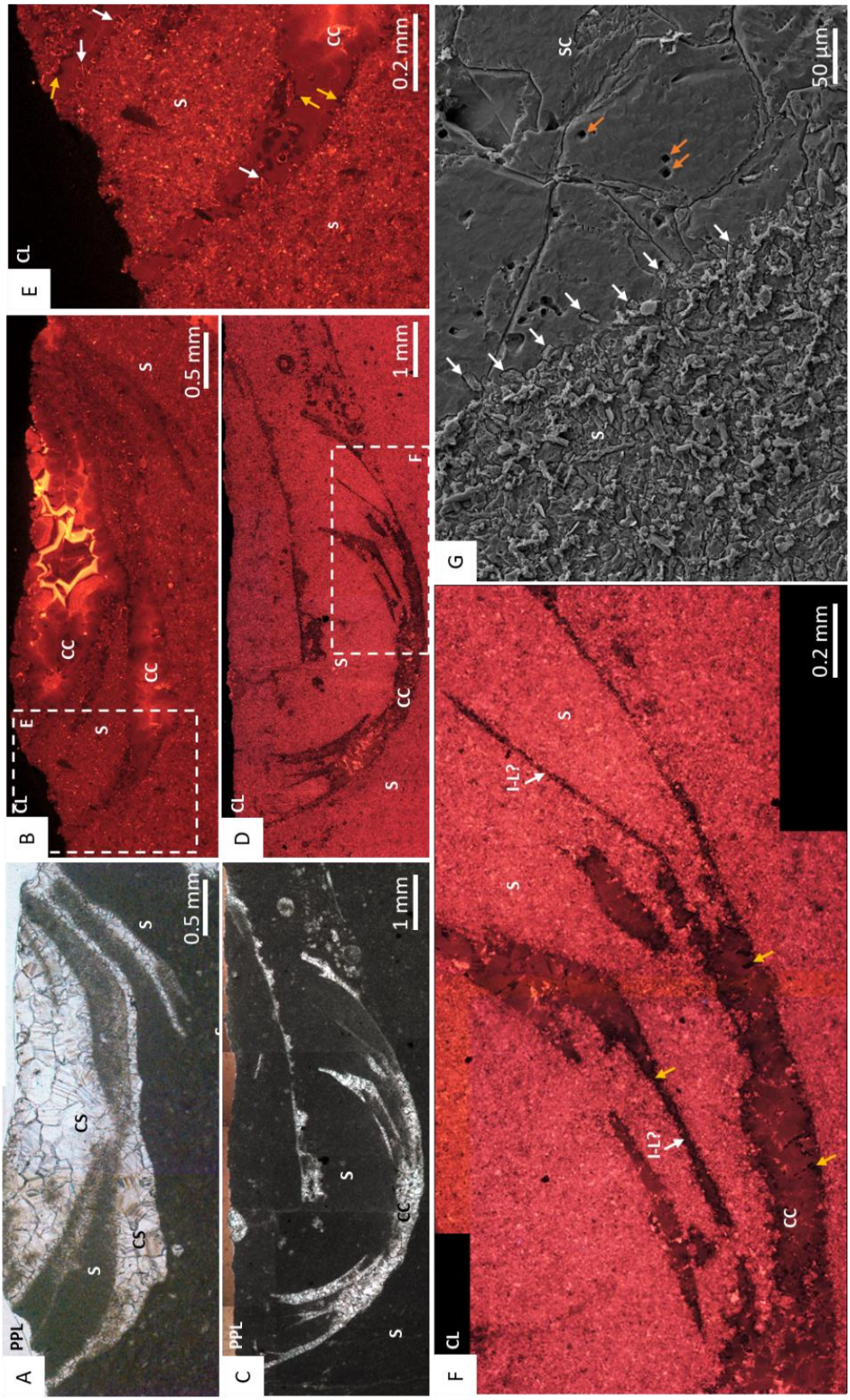
A
PPL
CS
S
0.5 mm
B
CL
E
S
CC
0.5 mm
C
PPL
S
CC
1 mm
D
CL
F
S
CC
1 mm
E
CL
S
CC
0.2 mm
F
CL
I-L?
S
CC
0.2 mm
G
SC
S
50 µm

Figure 4.8

4.3.3 Elemental signatures and distribution

Strontium (Sr) concentrations and the Mg/Ca ratios were sampled from *Cloudina* and associated early cements from Driedoornvlakte and Zebra River using EMPA (Figure 4.9; Tables 4.1 to 4.6; see Appendices 3.2.2 to 3.2.4).

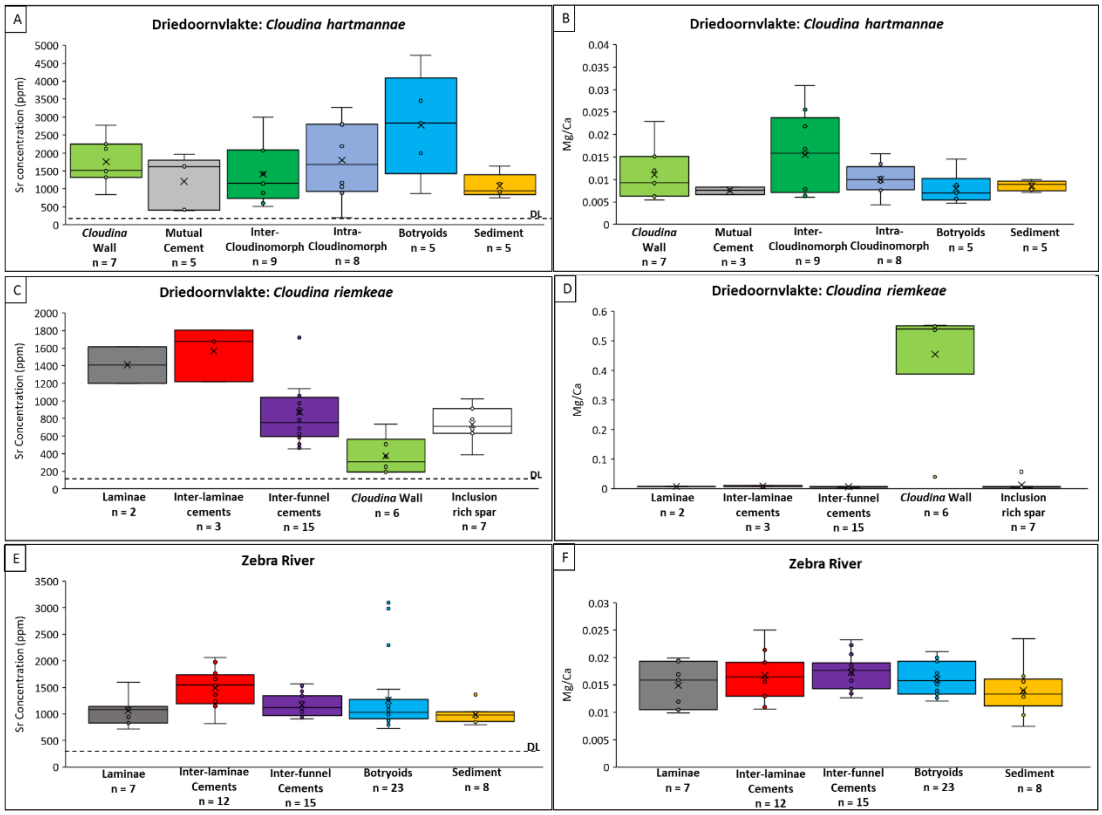

***Figure 4.9**: EMPA data from* Cloudina *and associated cements from Driedoornvlakte and Zebra River, Upper Omkyk Member, Nama Group. **A**: Strontium concentration (ppm). **B**: Mg/Ca ratio of Cloudina riemkeae from Zebra River. **C**: Strontium concentration (ppm) of* Cloudina hartmannae *from Driedoornvlakte. **D**: Mg/Ca ratio of* Cloudina hartmannae *from Driedoornvlakte. **E**: Strontium concentration (ppm) of* Cloudina riemkeae *from Zebra River. **F**: Mg/Ca ratio of* Cloudina riemkeae *from Zebra River. Detection limits for elements are shown as horizontal dashed lines (DL).*

At Driedoornvlakte, the Sr values of *Cloudina* laminae range from 777 to 1617 ppm (mean = 1198.7, n = 3) and Mg/Ca ratios from 0.007 to 0.367 (mean = 0.128, n = 3). Inter-laminae cements have a higher Sr content, from 1221 to 1804 ppm (mean = 1566, n = 3), and Mg/Ca values from 0.008 to 0.012 (mean = 0.009, n = 3). The Sr concentration of the inter-funnel cements vary greatly, even within the one sample, ranging from 457 to 1747 ppm (mean = 860.1 ppm, n = 16), with Mg/Ca ranging from 0.004 to 0.012 (mean = 0.007, n = 16). The degree of dolomitisation in samples makes differentiation between lamina, inter-laminae

cements and inter-funnel cements difficult, so the term '*Cloudina* wall' is used to describe the outer areas of the *Cloudina* tube where these cements are indistinguishable. The Sr values for *Cloudina* walls are highly variable, ranging between 189 and 2773 ppm (mean = 1119.5 ppm, n = 13), with Mg/Ca values ranging between 0.005 and 0.552 (mean = 0.216, n = 13). Values also vary between *Cloudina riemkeae* and *Cloudina hartmannae*, with Sr data ranging from 189 to 736 ppm (mean = 373.83, n = 6) and 840 to 2773 ppm (mean = 1758.7 ppm, n = 7), respectively. Intra-cloudinomorph and inter-cloudinomorph cements range in Sr concentration from 195 to 3267 ppm (mean = 1178.7 ppm, n = 24) and 521 to 3003 (mean = 1409.3, n = 9), respectively. The Mg/Ca of intra-cloudinomorph cements ranges between 0.008 to 0.016 (mean = 0.010, n = 8), with inter-cloudinomorph cements varying from 0.006 and 0.031 (mean = 0.015, n = 9).

At Zebra River, the Sr concentration of laminae varies between 719 and 1596 ppm (mean = 1064.0, n = 7), with Mg/Ca values ranging between 0.010 and 0.025 (mean = 0.017, n = 7). The Sr concentration in the inter-laminae cements have a wide range, from 819 to 1567 ppm (mean = 1490.5 ppm, n = 15), but the Mg/Ca values are more consistent, from 0.011 to 0.025 (mean = 0.017, n = 12). The inter-funnel cements have a more limited range of Sr values, from 904 to 1567 ppm (mean = 1169 ppm, n = 15), with Mg/Ca values ranging from 0.013 to 0.023 (mean = 0.017, n = 15).

The Sr values of pseudomorphed aragonitic botryoids at Driedoornvlakte range between 869 and 4723 (mean = 2578.7, n = 6) which is similar the range seen at Zebra River, from 724 to 3098 ppm (mean = 1257.9 ppm, n = 23). Mg/Ca at Driedoornvlakte is 0.005 to 0.002 (mean = 0.008, n = 6), and Zebra River shows values of 0.012 to 0.021 (mean = 0.016, n = 23). Sediment Mg/Ca content varies between Driedoornvlakte and Zebra River with values ranging between 0.007 and 0.010 (mean = 0.009, n = 5) and 0.007 to 0.023 (mean = 0.014, n = 9), respectively. Sr concentrations have similar ranges with 796 to 1363 ppm (mean = 986.67, n = 9) at Zebra River, and 755 to 1637 ppm (1082.4 ppm, n = 5) at Driedoornvlakte.

The Kruskal-Wallis test shows a statistical difference between the Sr concentration of different cements at Zebra River, between the inter-laminae cements and both laminae ($p = 0.016$) and inter-funnel cements ($p = 0.014$), and between the micritic matrix and both inter-laminae cement ($p = 0.001$) and inter-funnel cement ($p = 0.030$) (Table 4.1). There are no statistical differences in Mg/Ca contents of any measured features (Table 4.2).

Cloudina riemkeae from Driedoornvlakte also shows statistical differences in Sr concentration between the inter-laminae and the inter-funnel cements ($p = 0.041$) (Table 4.3), and between inter-laminae and the inter-funnel cements compared to the *Cloudina* wall ($p = 0.009$ and $p = 0.002$, respectively (Table 4.3). Sr content of the inter-laminae cement and *Cloudina* wall are statistically different to the inclusion-rich spar ($p = 0.023$ and $p = 0.011$, respectively), but this is not the case for the inter-funnel cement ($p = 0.291$) which is recrystallised as an inclusion-rich spar (Figures 4.5E, J; Table 4.3). A significant difference can also be seen between botryoids and *Cloudina hartmannae* inter-cloudinomorph cements ($p = 0.043$, Table 4.4). There is a significant difference between the *Cloudina* wall at Driedoornvlakte and the other *Cloudina*-associated cements, probably as a result of the dolomitisation (Table 4.5). Sr content within internal cements associated with *Cloudina hartmanna*e show no statistical differences, but there is a significant difference between the inter-cloudinomorph cement and botryoidal cements ($p = 0.043$) (Table 4.6).

***Table 4.1**: p-values of* Cloudina*-associated cements, aragonitic botryoids and sediment strontium concentration for Zebra River. Yellow p-values highlight significant values.*

Zebra River *Cloudina*-associated cements T-test p-values (Sr concentration)					
	Lamina	Inter-Laminae Cements	Inter-funnel Cements	Botryoids	Sediment
Laminae	X	0.016	0.406	0.450	0.506
Inter-laminae cement	X	X	0.014	0.180	0.001
Inter-funnel Cement	X	X	X	0.548	0.030
Botryoids	X	X	X	X	0.073
Sediment	X	X	X	X	X

***Table 4.2**: p-values of* Cloudina*-associated cements, aragonitic botryoids and sediment Mg/Ca for Zebra River. Yellow p-values highlight significant values.*

Zebra River *Cloudina*-associated cements T-test p-value (Mg/Ca)					
	Laminae	Inter-laminae cement	Inter-funnel Cement	Botryoids	Sediment
Laminae	X	0.294	0.156	0.419	0.674
Inter-laminae cement	X	X	0.921	0.372	0.123
Intra-funnel Cement	X	X	X	0.213	0.047
Botryoids	X	X	X	X	0.129
Sediment	X	X	X	X	X

***Table 4.3**: p-values of* Cloudina riemkeae*-associated cements and the inclusion-rich spar strontium concentration (ppm) for Driedoornvlakte. Yellow p-values highlight significant values.*

Driedoornvlakte *Cloudina riemkeae*-associated cements T-test p-values (Sr concentration)					
	Lamina	Inter-Laminae	Intra-funnel Cement	*Cloudina* Wall	IR Spar
Lamina	X	0.623	0.256	0.136	0.201
Inter-Laminae	X	X	0.041	0.009	0.023
Intra-funnel Cement	X	X	X	0.002	0.291
Cloudina Wall	X	X	X	X	0.011
IR Spar	X	X	X	X	X

***Table 4.4**: p-values of* Cloudina hartmannae*-associated cements, aragonitic botryoids and sediment strontium concentration (ppm) for Driedoornvlakte. Yellow p-values highlight significant values.*

Driedoornvlakte *Cloudina hartmannae*-associated cements T-test p-values (Sr concentration)						
	Cloudina Wall	Mutual Cement	Inter-cloudinomorph	Intra-cloudinomorph	Botryoids	Sediment
Cloudina Wall	X	0.206	0.376	0.937	0.130	0.062
Mutual Cement	X	X	0.667	0.324	0.065	0.732
Inter-cloudinomorph	X	X	X	0.424	0.043	0.422
Intra-cloudinomorph	X	X	X	X	0.197	0.196
Botryoids	X	X	X	X	X	0.035
Sediment	X	X	X	X	X	X

***Table 4.5**: p-values of* Cloudina riemkeae*-associated cements Mg/Ca ratio for Driedoornvlakte. Yellow p-values highlight significant values.*

Driedoornvlakte *Cloudina riemkeae*-associated cements T-test p-values (Mg/Ca)					
	Lamina	Inter-lamina	Inter-funnel	*Cloudina* Wall	IR Spar
Lamina	X	0.473	0.444	0.026	0.714
Inter-lamina Cements	X	X	0.061	0.008	0.733
Inter-funnel Cements	X	X	X	1.281E-08	0.179
Cloudina Wall	X	X	X	X	1.29E-04
Inclusion-rich Spar	X	X	X	X	X

***Table 4.6**: p-values of* Cloudina hartmannae*-associated cements, aragonitic botryoids and sediment Mg/Ca ratio for Driedoornvlakte. Yellow p-values highlight significant values.*

Driedoornvlakte *Cloudina hartmannae*-associated cements T-test p-values (Mg/Ca)							
	Lamina	Mutual Cement	*Cloudina* Wall	Inter-cloudinomorph Cement	Intra-cloudinomorph Cement	Botryoids	Sediment
Lamina	X	0.703	N/A	N/A	0.062	N/A	N/A
Mutual Cement	X	X	0.084	0.051	0.062	0.107	0.146
Cloudina Wall	X	X	X	0.289	0.691	0.307	0.419
Inter-cloudinomorph Cement	X	X	X	X	0.131	0.078	0.125
Intra-cloudinomorph Cement	X	X	X	X	X	0.305	0.427
Botryoids	X	X	X	X	X	X	0.693
Sediment	X	X	X	X	X	X	X

4.3.4 *Cloudina* lamina thickness

Organic laminae have not been preserved at the studied sites. Laminae are preserved as moulds at Zebra River and Zwartmodder (Figures 4.6; 4.8), at Driedoornvlakte they have been dolomitised (Figure 4.5), whilst at Omkyk laminae are not detectable at all (Figure 4.7). Laminae thickness at Zebra River and Driedoornvlakte were measured using both CL and PPL images and using CL at Zwartmodder. *Cloudina* of Driedoornvlakte and Zebra River have laminae of similar thicknesses, with Driedoornvlakte laminae thicknesses ranging from 2.1 - 9.6 µm (mean = 5 µm, n = 23) and Zebra River *Cloudina* laminae ranging from 3.3 - 10.8 µm in thickness (mean = 6.5 µm, n = 23), with a T = 1.872, and p-value = 0.034 (Figure 4.10A, see Appendix 3.2.5).

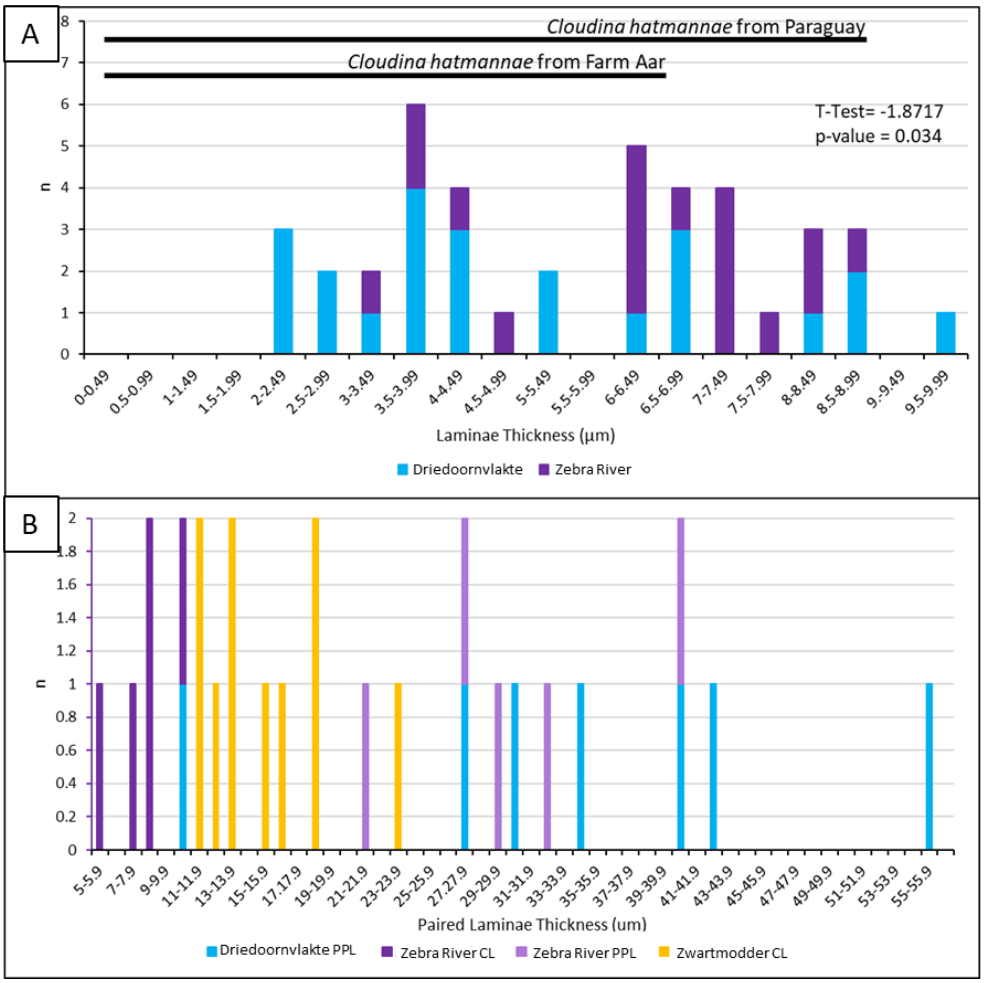

***Figure 4.10**: Features of* Cloudina *walls, including laminae thickness and paired laminae of* Cloudina *of the Upper Omkyk Member, Zaris Subbasin, Namibia. **A**: Lamina thickness, with thicknesses reported from Yang et al. (2020). **B**: Paired laminae thickness*

Paired laminae thickness, however, varies between sites. At Driedoornvlakte from 10.6 - 55.3 µm (mean = 34.3 µm, n = 14), Zebra River from 5.9 - 40.3 µm (mean = 19.3 µm, n=10), and Zwartmodder from 11 - 23.7 µm (mean = 15.4 µm, n = 10) (Figure 4.10B). The spalled features of the *Cloudina* from Zwartmodder are now preserved as centripetal calcite cement (Figure 4.8F) and consist of the inter-lamina cement and two laminae; the thickness of these features is similar to that of the paired laminae at Driedoornvlakte and Zebra River.

These differences are statistically significant (T = 2.32, p-value = 0.040). The Kruskal-Wallis Test shows that paired laminae thickness from Driedoornvlakte, Zebra River and Zwartmodder, are significantly different (H-value = 7.65, p-value = 0.022).

4.3.5 *Cloudina* wall thickness

Cloudina wall thickness is defined as the width between the outer tube wall and the inner tube wall forming the internal cavity (Figure 4.2). Measurements of wall thickness were taken from bedding surfaces at Driedoornvlakte, Zebra River and Zwartmodder. At Driedoornvlakte, maximum wall thickness for any individual *Cloudina* tube ranges from 0.25 - 1.88 mm (mean = 0.93 mm, n = 147) (Figure 4.11A, see Appendix 3.2.5). Ranges were lower at Zebra River and Zwartmodder, from 0.16 - 1.43 mm (mean = 0.51 mm, n = 79) and 0.12 - 1.38 mm (mean = 0.42 mm, n = 87), respectively (Figure 4.11A, see Appendix 3.2.5).

When comparing maximum wall width: maximum tube width, *Cloudina* at Driedoornvlakte show the greatest ratios ranging from 0.077 - 0.505 (mean = 0.235), with Zwartmodder ranging from 0.079 - 0.434 (mean = 0.190), and Zebra River showing the smallest range from 0.065 - 0.375 (mean = 0.235) (Figure 4.11A). All localities show a weak positive correlation between the thickness of the tube and the maximum wall thickness (Figure 4.11B). Ratios are statistically different between Driedoornvlakte and both Zebra River

and Zwartmodder ($p = 0.031$ and $p = 5.77^{-5}$, respectively), but not between Zebra River and Zwartmodder ($p = 0.060$).

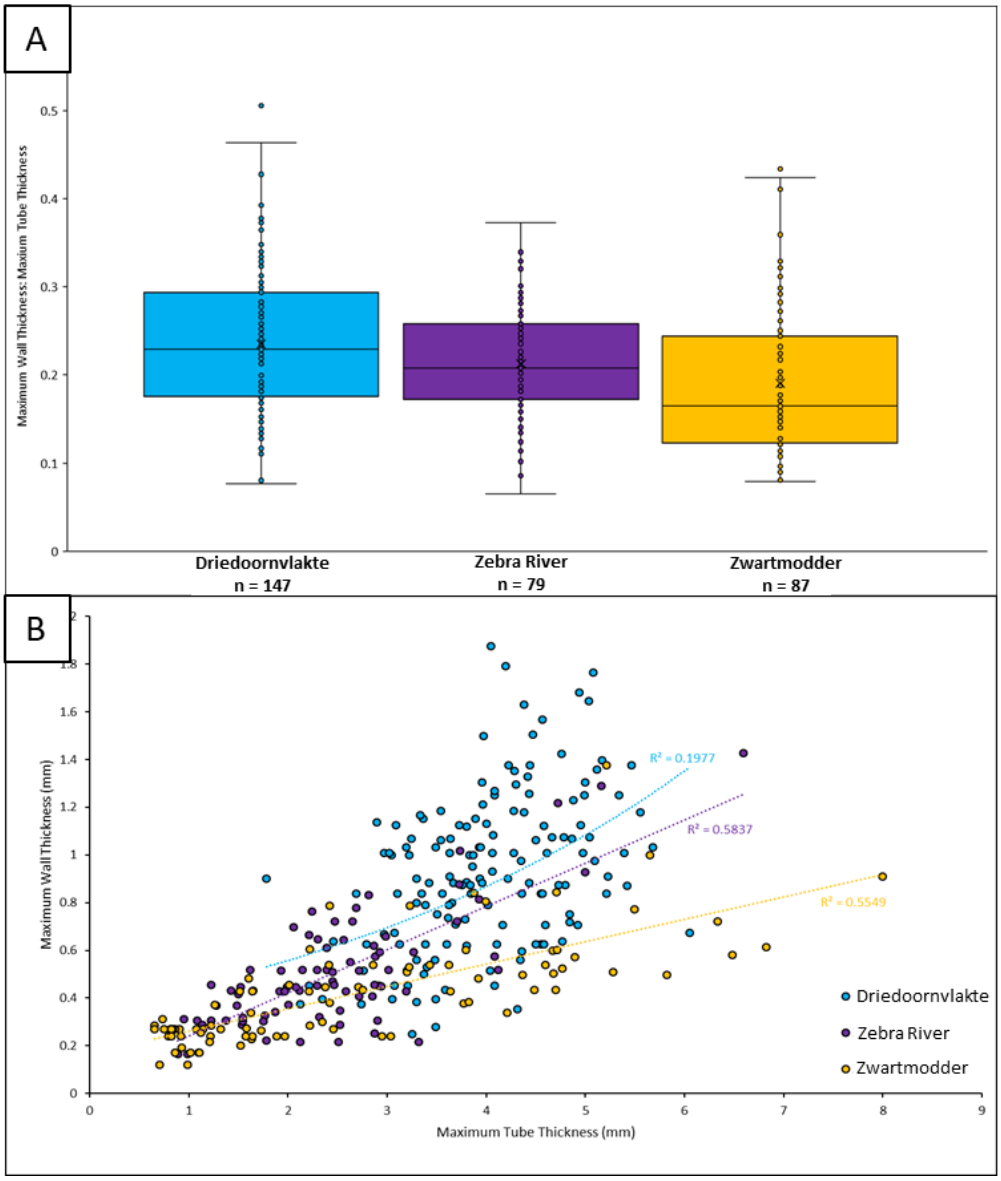

***Figure 4.11**: Wall thicknesses of* Cloudina *of the Upper Omkyk Member, Zaris Subbasin, Namibia. **A**: Distribution of ratios of wall thickness: tube thickness. **B**: Relationship between to wall thickness: tube thickness.*

4.4 Discussion

4.4.1 Sinuosity of *Cloudina*

Cloudina at Driedoornvlakte and Zwartmodder show the lowest sinuosity, and Zebra River the highest (Figure 4.4). This systematic variation (Table 4.7) suggests that sinuosity is in environmentally controlled, and that mineralisation of *Cloudina* occurred via a flexible organic template that allowed adaptation to local environmental conditions. However, it is not known to what degree this characteristic is dictated by environmental conditions. Little is understood on the controls on sinuosity in modern benthos, but orientation to maximise feeding efficiency in ambient currents and local sedimentation regime is thought to be a control in calcareous tubed polychaetes (serpulids) (Bosence, 1973; Sanfilippo, 2009). The lack of understanding on modern benthos sinuosity makes it difficult in creating hypotheses as to what advantage might be gained by increased sinuosity, but sinuosity may be governed by diverse factors such as substrate type and morphology, vertical or horizontal growth, competition for space, nutrient regime, water depth, and response to hydrodynamic energy and water flow.

It should be noted that sinuosity measurements for this study are based on 2D bedding plane measurements, and further insight might be gained by 3D analysis, with methods such as serial sectioning, for both more accurate sinuosity quantification, as well as information about curvature in the third dimension.

***Table 4.7**: Summary of* Cloudina *characteristics from four contemporary localities, Omkyk Member, Zaris Sub-basin, Namibia*

Cloudinomorph Attributes	Localities			
	Driedoornvlakte	Zebra River	Omkyk	Zwartmodder
Laminae	X	X		?
Paired Laminae	X	X		?
Inter-lamina Cement	X	X		?
Aragonite Needle Inter-laminae Cement	X			
Inter-cloudinomorph Cement	X			
Intra-lamina Cement	X	X		
Brittle Deformation	X	X		
Ductile Deformation		X		
Dissolution			X	X
Average Sinuosity	1.04	1.21	1.07	1.04
Mean Lamina Thickness	5 µm	6.5 µm		
Mean Paired Laminae Thickness	30 µm	19.3 µm		15.4 µm
Mean Wall Thickness: Tube Width Ratio	0.235	0.213		0.190

4.4.2 Diagenesis of *Cloudina* and associated cements

Local diagenetic conditions seem to control the expression of laminae, ranging from dolomite replacement of another carbonate phase, to mouldic preservation, individual lamina thickness is always consistent (Figure 4.10, Table 4.7). The micritic microstructure of *Cloudina* walls have not been observed or described for the walls of *Cloudina* in this study, but these modes of preservation presented here are consistent with laminae being organic-rich but calcified.

The lack of a preserved skeletal wall and lamina in *Cloudina* collected from Omkyk and Zwartmodder is evidenced by the mouldic preservation of the tube. Early, fine, acicular isopachous cement generations are present at Omkyk, which grew from the cloudinomorph walls, followed by an infilling well-zoned sparry burial calcite which infilled the rest of the

tube (Shore et al., 2020) (Figure 4.7). Such early isopachous cements are not observed at Zwartmodder, where *Cloudina* are preserved via a sparry infill of moulds, which represent dissolved paired laminae together with inter-lamina cement, as well as inter-funnel cement (Figure 4.8). The dissolution of the original tube pre-dated cement growth around the grains of the surrounding sediment as this cement grew into the void space of the dissolved *Cloudina* skeleton (Figure 4.8E).

The extent of dissolution at the shallow, inner ramp sites of Omkyk and Zwartmodder sites suggest the influence of freshwater via early meteoric diagenesis, suggesting dissolution likely occurred very early on which is in keeping with the inferred high-Mg calcite or aragonite composition of the tubes (Morris et al., 1990; Hua et al., 2003; Wood et al., 2011; Zhuravlev et al., 2012; Becker-Kerber et al., 2017; Pruss et al., 2018). The freshwater influence could provide an explanation for the degradation of the organic material of the *Cloudina*, such as the lamina. The mid-ramp sites, Driedoornvlakte and Zebra River, did not experience freshwater influence during early diagenesis and have preserved very early cements formed in the marine phreatic zone. All these early cements show blunt terminations and are interpreted as having had an originally aragonitic mineralogy.

Cloudina of Zebra River feature undulose laminae, with some evidence of both brittle fracturing and ductile deformation (Figure 4.6G), in contrast to Driedoornvlakte where there is only evidence of brittle deformation in samples observed for this study (Table 4.7). Compaction also caused breakage, i.e. brittle deformation, of *Cloudina* tubes at Zebra River and Zwartmodder, similar to that of a spalling ooid, where the resultant area was infilled by loose, now cemented and dolomitised, sediment (Figures 4.6G; 4.8F). The formation of the inter-lamina and inter-funnel cements occurred prior to the breakage of the *Cloudina* tubes, and that of the laminae, where moulds were later filled by a burial cement (Figures 4.6M-N). The formation of the dull luminescent inter-funnel cement, seen most clearly at Zebra River, occurred before compaction and lithification of the surrounding dolomitised sediment as

evidenced by the sharp fracture of the inter-funnel, and potentially inter-lamina, cements where sediment has infiltrated into the tube (Figure 4.6J-L). All these cements also formed prior to the formation pseudomorphed aragonitic botryoidal cements both inside and outside the tubes, as seen in Driedoornvlakte and Zebra River in this study and in Penny et al. (2014) (Figure 4.5B, 4.6B). Botryoids external to *Cloudina* tube have brighter luminescence than those within the tube, suggesting some degree of diagenetic compartmentalisation. At Zebra River, the pseudomorphed aragonitic acicular crystals are not preserved in the outermost inter-lamina cements, but rather were replaced by the non-luminescent neomorphic cements later in diagenesis which further implies compartmentalisation and protection of the inner areas of the tube from diagenetic fluids.

The *Cloudina*-associated cements, i.e. the inter-lamina, inter-funnel, intra-cloudinomorph, and inter-cloudinomorph cements are all composed of fine, acicular crystal bundles (mean width = ca. 3-5 µm, length = ca. 11 µm) that nucleated on both *Cloudina* laminae and from the outer wall of the tube. The crystals are inferred to be pseudomorphic aragonite due to their blunt terminations. All *Cloudina*-associated cements precipitated prior to transport, breakage and compaction of the tubes, and also pre-dated the cement botryoids, so can be inferred to be very early syn-sedimentary (Penny et al., 2014). The sparry calcite that encases organic lamina noted previously (Yang et al., 2020) is either neomorphic or burial calcite spar that formed after the replacement or dissolution of these original cements during late diagenesis.

Inter-funnel cements, first described by Grant (1990), have also been documented in *Cloudina* from Brazil (Beurlen and Sommer, 1957; Becker-Kerber, 2017), Paraguay (Warren et al., 2011), and Spain (Cortijo et al., 2010), suggesting that such cements are a widespread feature of *Cloudina* present irrespective of early diagenetic setting, mineralogy, or palaeogeographic region. These cements probably formed when *Cloudina* was in-situ and

provided mechanical strength and rigidity to the tube. Due to the widespread nature of these cements it could be suggested that they formed under some degree of biological control.

These cements discussed are similar to those described from the skeleton in the extant sphinctozoan sponge *Vaceletia*, which are suggested to have a basal mode of biomineralisation (Vacelet et al., 2010). In these organisms, biominerals are secreted upon a non-collagenous organic template, which becomes substituted by crystalline aragonite deposited as tangled crystal bundles of aragonite. The organic framework consists of proteins and polysaccharides rich in galactose, glucose and fucose, the latter suggesting that bacterial EPS (exopolymeric substances) may be involved in the production of calcite (Germer et al., 2015). In most cases, the basal parts of the skeleton, which is free from living tissue, is infilled by a micritic granular secondary deposit, potentially similar to the features observed in cloudinomorpsh at Omkyk. The presence of organic matter has led to the suggestion of biofilm or microbial involvement in such cement precipitation for *Cloudina* (Becker-Kerber, 2017). Similar secondary deposition can occur where aragonite crystals continue to grow after soft tissue has vacated a region of the skeleton. This is known in taxa as diverse as scleractinian corals (Enmar et al., 2000) and the algae *Halimeda* (Wizemann et al., 2014). Therefore, it is not clear if these *Cloudina*-associated cements formed during life, or *in-situ* but post-mortem, or in parts of the *Cloudina* skeleton abandoned by soft-tissue.

4.4.3 Elemental signatures and distribution

Elemental signatures of similar cements cannot be compared directly between localities because of differing diagenetic histories, as discussed above with the interaction of phreatic and vadose fluids, but statistically significant differences between phases can be determined for each locality. First, we note statistical differences in Sr concentration between various *Cloudina*-associated cements and botryoidal cements which could indicate that the *Cloudina*-associated cements were of a different origin to the early abiotic cements. However,

the botryoidal cement used for this comparison is located within *Cloudina* tubes, adjacent to intra-cloudinomorph cements and here there is no significant difference in Sr values ($p = 0.197$) (Table 4.4). When comparing the Sr content of inter-cloudinomorph cement to those measured from botryoids outside *Cloudina* tube (data from Wood et al., 2018), no significant difference is found between these cements. This suggests that all cements found within the *Cloudina* tube irrespective of type retain a higher concentration of Sr compared to those cements situated outside tubes, where leaching was more extensive further backing the notion of compartmentalisation. This is supported by the higher mean Sr concentration of the intra-cloudinomorph cement compared to the inter-cloudinomorph cement which we assume formed at coevally due to the similar luminescence of the cements. We find no statistical differences between the *Cloudina*-associated cements, the inorganic botryoids and dolomitised sediment, which suggests that they cannot be distinguished using this criterion.

A similar conclusion was reached from study of Sr content of *Cloudina* from the Tamengo Formation of the Corumbá Group, Brazil (Becker-Kerber et al., 2017). On the basis of the timing of precipitation and the acicular, but non-botryoidal, texture, it can be concluded that all internal cements associated with *Cloudina* precipitated very early but lack any distinctive Sr or Mg/Ca signature that might indicate either a diagenetic origin from a different pore fluid or biological fractionation.

4.4.4 *Cloudina* lamina thickness

The variation of paired lamina thicknesses noted could be due to deformation between the laminae, especially at Zebra River, as laminae are observed to be flexible and visibly undulose at this site. However, these differences in paired lamina thickness are more likely due to the different methods used to measure paired laminae thickness: laminae at Zebra River and Driedoornvlakte were measured using both CL and PPL images, but the CL images show thinner laminae compared to their PPL counterparts (Figure 4.10B). Different methods were

used as, depending on the sample, laminae were not always visible in both PPL and CL. When comparing data of laminae thickness collected from PPL images only, the datasets are not statistically different (T = 0.57) and so the null hypothesis that the paired laminae thickness at Zebra River and Driedoornvlakte is the same is supported, but is not due to the small sample size (p-value = 0.58). This is not the case, however, when comparing the CL data, as T-Test values indicate the paired laminae thickness varies (T = 2.54, p-value = 0.029), especially when spalled laminae are not included with the calculations (T = 4.75, p-value = 0.002). When comparing the thickness of the mouldic-paired laminae seen at Zwartmodder, the values fall in the range of paired laminae at other sites. This suggests that the assumed mouldic laminae are paired laminae with inter-lamina cements, as observed at Driedoornvlakte and Zebra River.

Presumed *Cloudina* laminae at Zwartmodder also occupy a narrower range of paired laminae thicknesses than those from Driedoornvlakte and Zebra River (mean = 15.4 µm). As previously mentioned, these laminae are expressed as sparry-calcite infilled moulds formed by the dissolution of both the paired laminae and the inter-lamina cement, and so this dissolution may account for the increased range of laminae thickness at Zwartmodder as the degree of dissolution was lower at the other sites.

Cloudina laminae from the Mooifontein Member have a thickness of 0.5 - 5 µm, and samples from Paraguay range between 0.5 - 8 µm (Yang et al., 2020), meaning that these lamina thicknesses fit within the range found in this study (Figure 4.10A). However, greater lamina thicknesses are found in this study which may reflect the thickening by dolomitisation see at Driedoornvlakte.

4.4.5 Variability of *Cloudina* wall thickness

The maximum thickness of the *Cloudina* wall and the thickness of the wall as a ratio of tube diameter is variable across the Zaris Subbasin (Figure 4.11B; Table 4.7). The weak

positive correlation between the thickness of the tube and the maximum wall thickness at all localities implies wall thickness is not determined by the width of the tube. These data show that for a given tube width, the thickness of the wall is greatest at Driedoornvlakte, and is significantly and statistically greater than those measured at Zebra River and Zwartmodder.

These data and observations imply *Cloudina* wall thickness is environmentally-controlled, determining the distance between paired laminae sets and also potentially the volumetric extent of inter-lamina and inter-funnel cement formation. Driedoornvlakte was the most hydrodynamically energetic of those localities analysed as suggested by the shelf position and reef status, where rates of carbonate precipitation may have been higher, as shown by the abundant, volumetrically-significant syn-sedimentary botryoidal cements (Penny et al., 2014). This setting could have promoted the rapid precipitation, and increased volumes, of calcium carbonate internal cements. This interpretation is consistent with the observation that only brittle fracture is noted at Driedoornvlakte. However, many other environmental parameters might have been important to produce *Cloudina* with thicker and more heavily calcified and strong skeletal wall within the reef at Driedoornvlakte, such as enhanced food availability or as a response to currents.

4.5 Conclusions

The consistent lamina thickness of *Cloudina* along the Zaris Subbasin shelf suggest that lamina formation was under some degree of biological control, potentially as part of the 'biominerlisation toolkit' (Table 4.7). The mouldic or replacive dolomitised preservation of lamina indicate calcification of an organic-rich structure, potentially during life, from which early, acicular pseudomorphed aragonitic cements could nucleate. The precipitation of these cements pre-dates breakage prior to loose sediment infill, possible transport or compaction, and pseudomorphed aragonitic botryoid precipitation. The presence of such internal cements

is a widespread feature of *Cloudina*, although diagenetic expression varies, with such cements noted within the study have been observed in *Cloudina* from different Ediacaran Basins. Geochemical analysis (Mg/Ca; Sr concentrations), however, shows no statistically significant differences between these *Cloudina*-associated cements and the surrounding sediment or abiotic early forming aragonitic bortyoids, and so no signature of biological fractionation has detected geochemically. Overall, the findings of this study conclude that cements associated with *Cloudina* formed rapidly, but it is unclear as to whether they formed during life, post-mortem, or in parts of the *Cloudina* skeleton that were abandoned by soft-tissue as the animal grew to occupy younger parts of the skeleton, which is suggested in basal forms of biomineralisaion. But the formation of these cements, particularly the inter-lamina and inter-funnel cements, would impart rigidity to the *Cloudina* tube, and the inter-cloudinomorph cements would create attachment between adjacent tubes allowing for the formation of reef structures.

The variation of sinuosity in *Cloudina* in separate communities across the ramp of the Zaris Subbasin (Table 4.7) implies that the curvature of the tube is environmentally-controlled, perhaps to maximise feeding efficiency in any given setting. This complements the findings that *Cloudina* tube diameter is also environmentally variable within the Nama Basin (Wood et al., 2017). Variability in the cloudinomorph wall thickness is not a function of tube width and also differs between localities (Table 4.7) further suggesting the influence of environmental factors in determining the distance between paired laminae sets and the volumetric extent of inter-lamina and inter-funnel cement formation implying *Cloudina* had an ecophenotypic response to their surroundings. This may have been controlled by factors such as carbonate supersaturation or hydrodynamic energy, which varies across the shelf, as thicker walls and only brittle fracture are noted in high-energy reef settings.

Chapter 5: Exceptional Preservation of the Ediacaran Skeletal Metazoan *Namacalathus*, Nama Group, Namibia.

The results reported in Chapter 5 are published as: Shore, A.J., Wood, R.A., Butler, I.B., Zhuravlev, A., McMahon, S., Curtis, A., and Bowyer, F.T., 2021, Ediacaran metazoan reveals lophotrochozoan affinity and deepens root of the Cambrian Explosion: Science Advances, v. 7, no.1. The text in the following chapter is adapted from this paper with the published paper given in Appendix 4.1.

Amy Shore found the material in the field. Amy Shore, Rachel Wood and Andrey Zhuravlev conceived the study. Amy Shore conducted the research, including photographing the sample, measuring dimensions, rendering the 3D model, serial sectioning, and photography under plane polarised light and cathodoluminescence. Ian Butler conducted micro-CT imaging. Amy Shore wrote the first draft of the manuscript.

5.1 Introduction

There is poor understanding of the phylogenetic relationships between Ediacaran and Cambrian taxa. Determining the phylogenetic affinity of Ediacaran taxa is a difficult task due to the lack of exceptional preservation and an absence of defining characteristics of many fossils. Soft-tissue preservation is therefore vital in determining the affinity of Ediacaran biota.

In this chapter the first three-dimensional, pyritised preservation of soft tissue in the Ediacaran metazoan *Namacalathus hermanastes*, from the Nama Group, Namibia, is described. This allows for a strong evolutionary link to be proposed between terminal Ediacaran and early Cambrian taxa.

5.2 Materials and methods

One float sample (237 x 194 x 33 mm) was collected from Zwartmodder Farm (Figure 5.1). An SLR camera and a binocular microscope were used to photograph and document (Figure 5.1) each *Namacalathus*, with ImageJ (Fiji) software (https://imagej.net) used for the quantification of dimensions, such as lumen width and height. Dimensions of the

Figure 5.1*: Museum No. F1547, Museum of the Geological Survey of Namibia. Sample of* in-situ Namacalathus *with individuals numbered; yellow circles indicate those cored for µCT scanning (nos. 4, 32) and serial sectioning (nos. 66, 68). Centimetre scale.*

Namacalathus were only measured if the features in question were fully exposed and preserved.

The float sample was radiographed to determine whether individual *Namacalathus* cups had a density contrast with the surrounding sediment. Due to a high contrast, *Namacalathus* nos. 4 and 32 were cored and underwent micro-computed tomographic (µCT) scanning. Scanning was at 120 kV and 1500 projections (2 x 2 s exposure averaged) were collected and reconstructed by filtered back projection to 824 tomographic slices. The contrast was enhanced by applying the stretch histogram option in ImageJ, while not affecting the original data. 3D model of the scans were rendered using Avizo 9 software. Voxel size of reconstructions equates to 20.7 µm. The pre-defined colour map 'physics.icol' was applied to the model to aid in visualisation of the features of the fossil, but the false colours are not quantitatively correlated to any property of the object. The colour thresholds of the colour map were altered in Avizo (255-65535) in order to remove the background of the surrounding calcium carbonate sediment in order to produce a model of the whole individual. Scanning of *Namacalathus* cup no. 4 was also at 120 kV, using the same data acquisition parameters, and with 633 tomographic slices were reconstructed. The model was rendered using Avizo 9, with a voxel size of 23 µm, using the pre-defined colour map 'greyscale.icol' as the low contrast of the scan did not lend itself to be rendered in false colour.

Namacalathus no. 32 was then cut into 3 sections to observe the internal structure of the *Namacalathus* cup. These sections were finely polished and imaged using binocular microscopy and cathodoluminescence. One of the slices underwent serial sectioning at 26 µm increments which were also imaged through binocular microscopy and cathodoluminescence.

Two highly polished thin sections were made of the slab to describe the lithology using petrographic microscopy. Three highly polished, uncovered thick sections (200-2000 µm) were cut of transverse sections of *Namacalathus* no. 68 for backscatter electron imaging and Energy-dispersive X-ray spectroscopy (EDX) analysis. Two samples (nos. 66 and 68)

were serially sectioned and highly polished at 1 mm and 500 µm increments, respectively, to understand the distribution of iron oxide and its relationship to the calcitic skeleton using light microscopy and cathodoluminescence imaging. Serial sectioning at 1mm of a core plug containing a *Namacalathus* no. 66 allowed to observe the relationship between the iron oxide and the calcite skeleton. A Canoscan Lide 210 flatbed scanner was used to scan each section (4000 dpi for both sections). All work was carried out at the University of Edinburgh

5.3 Results

5.3.1 Lithology

The sample lithology is finely laminated micrite that grades from a mud-rich packstone with some silt-grade quartz and recrystallised bioclasts, often with a stylolitic contact (Figure 5.2A, B). *Namacalathus* individuals are overlain by a thin (< 1 mm) micritic carbonate with silt-grade, angular lithic fragments of quartz, albite, clays, and phosphatic minerals (Figure 5.3C).

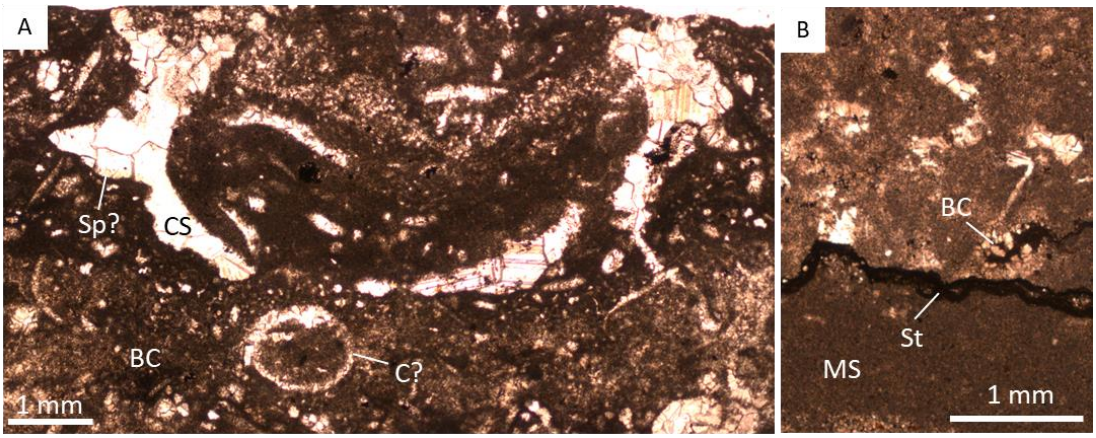

Figure 5.2*: Petrographic images of sample* in-situ Namacalathus *sample.* ***A****: Plane polarised photomicrograph showing upper layer of bioclastic micrite (BM) ~10 mm thick, in plane polarized light. Spiny (Sp) and smooth* Namacalathus *bioclasts are infilled with blocky sparry calcite (CS), along with potential* Cloudina *(C?).* ***B****: Plane polarised photomicrograph of bioclastic upper layer with bioclasts (BC) and cavity with bladed calcite (BC) overlying micritic layer (MS), separated by a stylolite (St).*

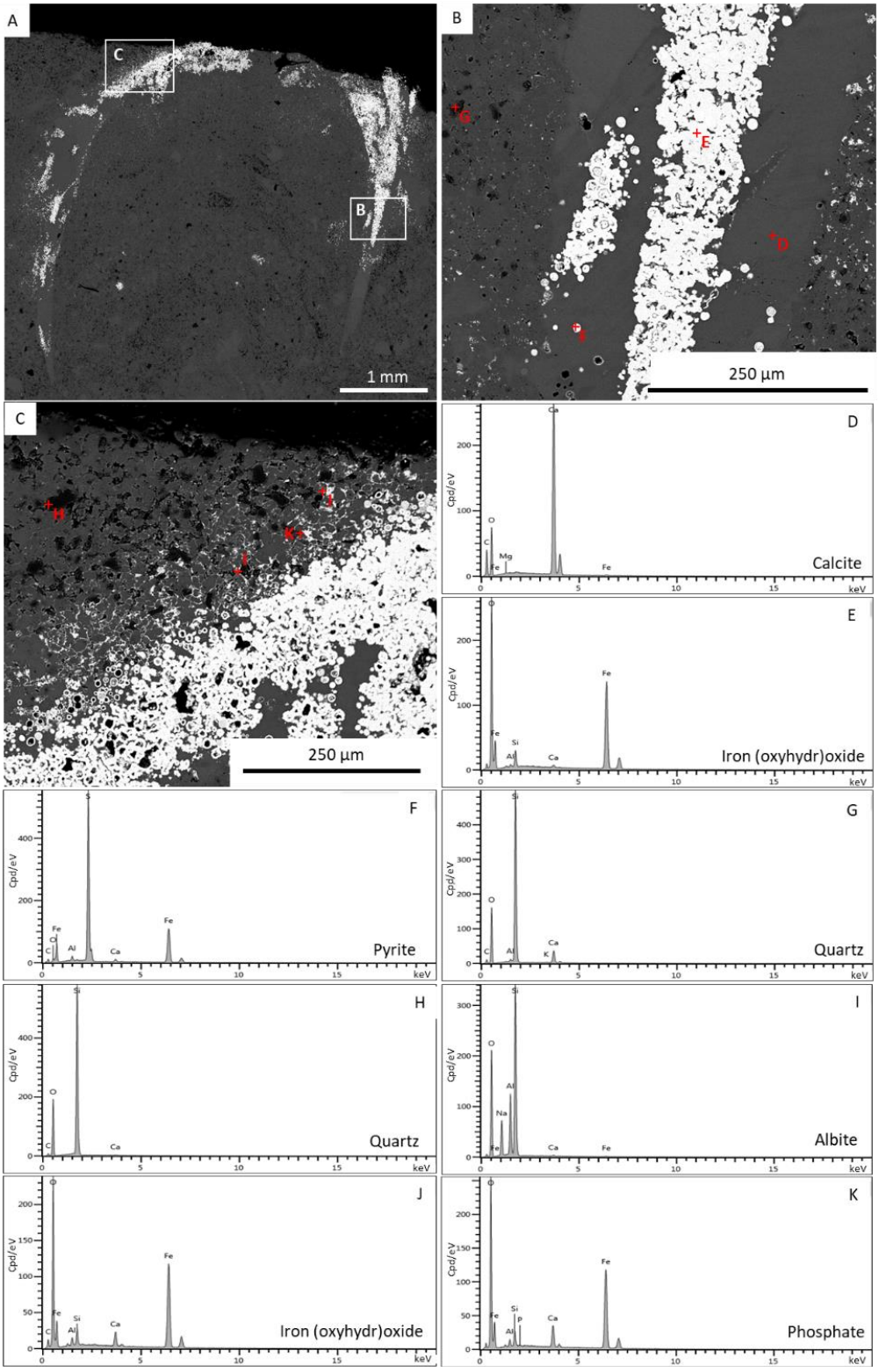

Figure 5.3*: EDX data of* Namacalathus *no. 68 (Figure 5.1).* ***A****: Backscatter SEM image.* ***B****: Inset of A, showing position of EDX data* ***D*** *in outer skeleton and* ***E*** *in central portion of skeleton, and* ***G****, sediment infill.* ***C****: Inset of A, showing position of EDX data* ***H****,* ***I****,* ***J****,* ***K*** *in overlying sediment, S3.* ***D****-****G****: EDX data from points highlighted in B.* ***H****-****K****: EDX data from points highlighted in C.*

5.3.2 *Namacalathus* morphology on the bedding surface

Namacalathus individuals range from 2 to 14 mm in diameter as measured from the bedding surface, although many are partially covered with sediment, and are preserved as reddish-brown to yellow (oxyhydr)oxide minerals, FeOx ['FeOx' here denotes unspecified iron (oxyhydr)oxide] resulting from oxidation of pyrite (FeS_2), or as raised grey limestone casts which sometimes reveal weathered sections through the calcified skeleton (Figure 5.1). Seventy-three individuals (numbered 1 to 73) are found on a bedding plane sample, some with stalks (Figures 5.1; 5.4), with 29% preserved upright in inferred growth position, 48% slightly toppled, and 23% of undetermined orientation (Figure 5.1, see Appendix 4.2.1).

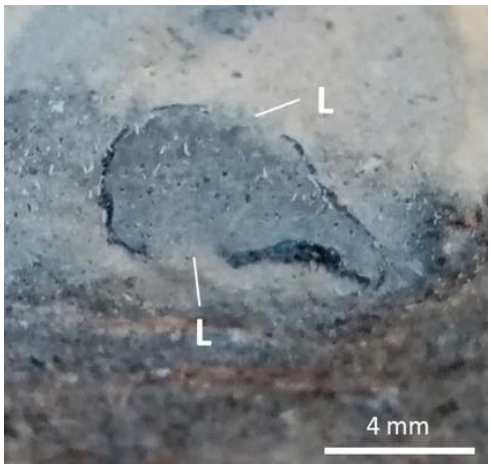

Figure 5.4*: Stalked* Namacalathus *(no. 73, Figure 5.1) surrounded by micrite from the bedding surface with lumens (L).*

The best-preserved individuals show a raised pin cushion-like form, which surrounds the central, apical, opening. The central opening ranges from 1.3 to 12.3 mm (n = 37, mean = 3.6 mm) in diameter and can either show five to seven, but generally six, isoclinal folds which radiate outwards (Figures 5.5A; 5.6A-J, P, Q) or be circular (Figure 5.6K-N). Fold dimensions are variable, ranging from 0.18 to 2.78 mm in height and 0.43 to 4.66 mm in width. Both types of opening are preserved as either a FeOx crust (Figure 5.6A-G, M-Q) or as casts of limestone (Figure 5.6H-L, W-X). In cups where the central opening and lumens are visible. The central opening folds oppose folds across the lumens (Figure 5.6F, G). Full lumens are similarly

observed either as FeOx crusts (Figure 5.6P-U) or casts (Figure 5.6V-Y). Lumen height is smaller where preserved by FeOx (mean = 1.59 mm) compared to limestone casts (mean = 2.34 mm), but preservation style does not notably influence lumen width (mean = 1.8 mm; Figure 5.5B). Small (0.33 to 1.27 mm; Table 5.1), domal or elongate ridge-like swellings are present around the edges of the central opening and lumens (Figures 5.6A, B, C, G, H; 5.7), concentrated either at the apex of folds around the apical opening (Figs. 5.6A, C; 5.7A-B), or parallel to the edges of the lumen in one specimen (Figures 5.6R; 5.7C, D), or as pairs that radiate from the apical opening to the lumens (Figure 5.6C, D, P). The calcitic skeleton is also preserved (Figure 5.6Q, Z, A*ii*-A*v*), revealing robust, radiating spines up to 0.4 mm in length and width where the FeOx crust has not been preserved (Figure 5.6Z-A*v*).

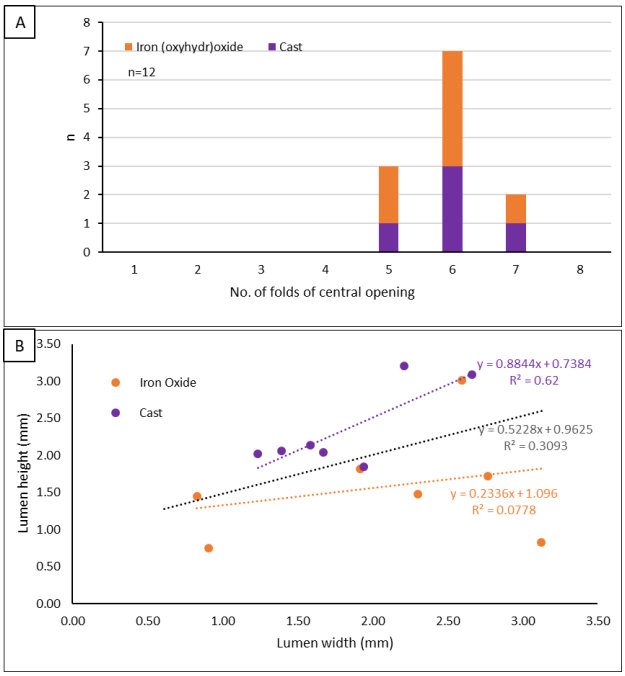

***Figure 5.5**: Preservation style and lumen width in* Namacalathus. ***A**: Histogram of number of folds in* Namacalathus *with a crenulated central opening. **B**: Scatter plot with linear regressions comparing the width and height of lumens preserved in iron (oxyhydr)oxide and as casts in toppled* Namacalathus *individuals.*

***Table 5.1**:* Namacalathus *ridge and dome dimensions*

Individual No. *Namacalathus*	**Ridge/ Dome (mm)**
6	1.23
	0.76
	0.65
4	1.16
9	0.36
	0.52
	0.72
	0.33
	0.43
45	1.18
	0.78
	0.75
70	0.78
	1.27
	0.45
	0.71
	0.77

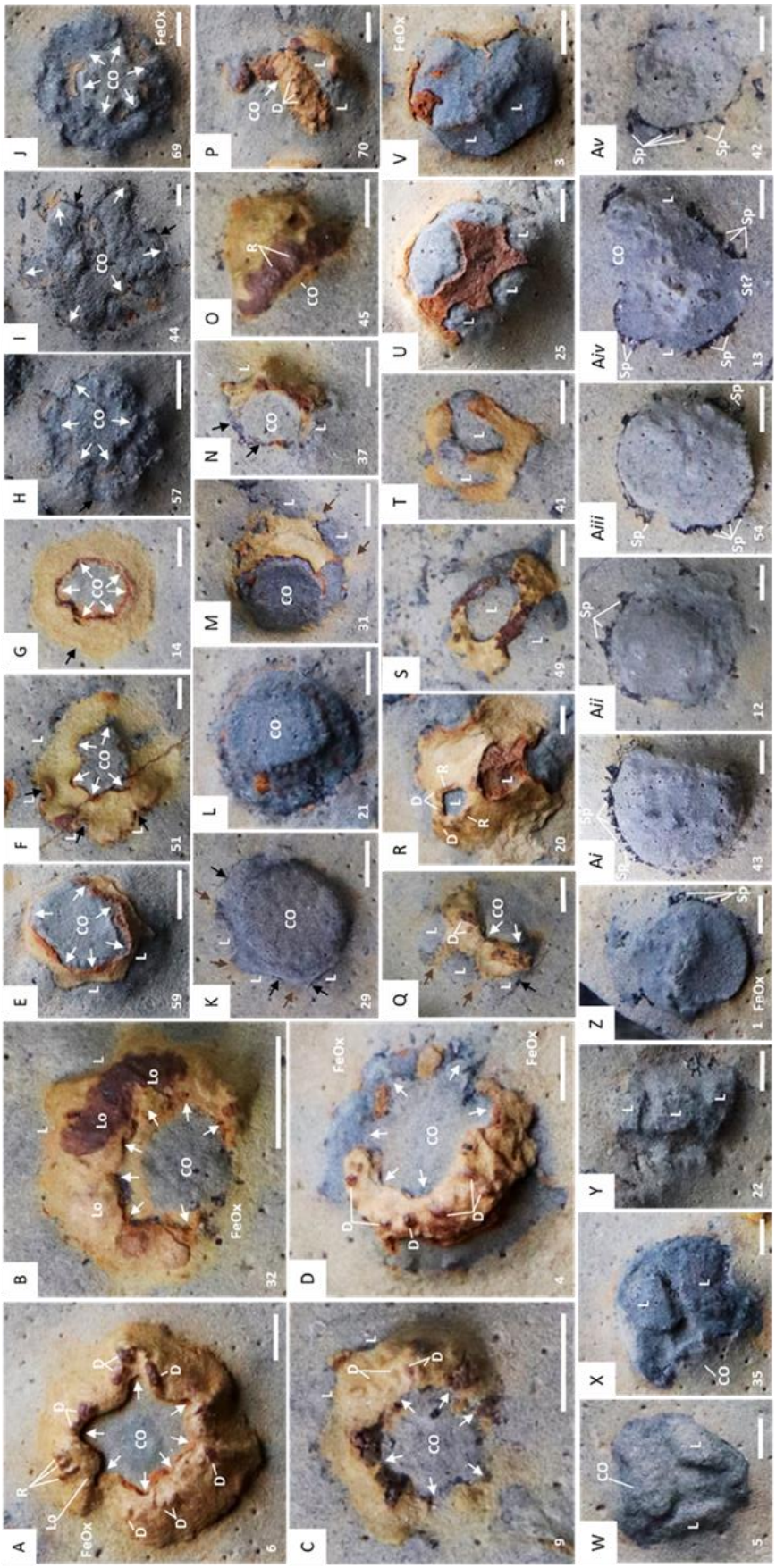
A
B
C
D
E
F
G
H
I
J
K
L
M
N
O
P
Q
R
S
T
U
V
W
X
Y
Z
Ai
Aii
Aiii
Aiv
Av
CO
D
L
Lo
R
Sp
FeOx

Figure 5.6

***Figure 5.6 (page 130)**: Numbered* Namacalathus *cups. Scale bar 2 mm.* ***A- G**: Upright, evidenced by the central opening (CO)* Namacalathus *with crenulated central opening, created by folds (white arrows) preserved in iron (oxyhydr)oxide (FeOx). The tops of lumens (L) have been preserved in some instances* ***A**: Ridges (R) and domes (D) present on the outer wall of the cup around the rim of the central opening with pillow-like lobes (Lo) protruding into the central opening. Iron (oxyhydr)oxide staining of sediment is observed around the fossil (FeOx).* ***F-G**: Transverse cross section of* Namacalathus*. Lumens (L) forms folds on the outer surface (black arrows) folding in the direction to a fold of the central opening.* ***H-J**: Upright* Namacalathus *with crenulated central opening preserved as a cast.* ***K-L**: Upright* Namacalathus *with a circular central opening preserved as a cast.* ***K**: Upright* Namacalathus *with a circular central opening preserved as a cast. The top portion of three lumens are present where the calcite skeleton is observed (black arrows). Sediments adjacent to areas in between lumens indicate iron (oxyhydr)oxide staining (brown arrows).* ***M-N**:* Namacalathus *cups with circular central opening preserved in iron (oxyhydr)oxide.* ***A**, **C**, **D**, **O-Q**: Ridges (R) and domes (D) preserved around the opening rim or lumen in iron (oxyhydr)oxide.* ***Q-U**: Toppled* Namacalathus *cups with lumens (L) preserved as iron (oxyhydr)oxide.* ***Q**: Toppled* Namacalathus *with iron oxide staining the surrounding sediment of the areas between lumens (brown arrows), with calcite skeleton (black arrows) situated below the iron (oxyhydr)oxide.* ***R**: Toppled* Namacalathus *with domes (D) and ridges (R) around the lumen edge.* ***V-Y**: Toppled* Namacalathus *cups with lumens preserved as a cast.* ***Z-Av**: Toppled* Namacalathus *with spines (Sp).* ***Aiv**: a cross section of a* Namacalathus *with a potential stalk base (St?).*

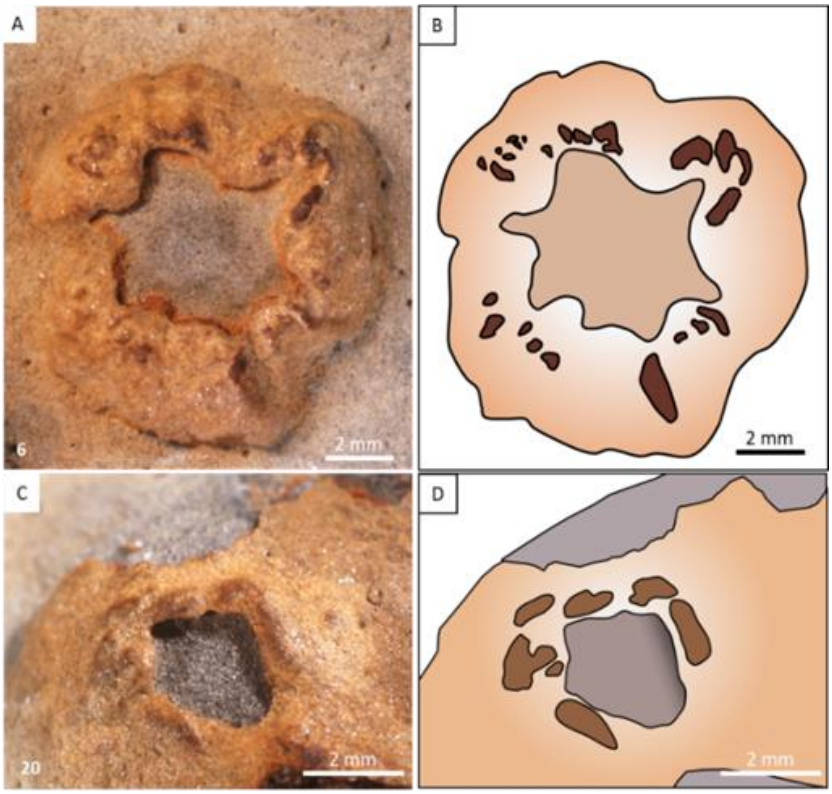

***Figure 5.7**: The distribution of ridges and domes on* Namacalathus *nos. 6 and 20 (Figure 5.1).* ***A**:* Namacalathus *preserved in with FeOx showing domes and ridges around the rim of the folded central opening.* ***B**: Schematic of A, highlighting the morphology and arrangement of the domes and ridges around the folded central opening.* ***C**:* Namacalathus *preserved with iron (oxyhydr)oxide showing domes and ridges around the rim a lumen.* ***D**: Schematic of C, highlighting the morphology and arrangement of the domes and ridges around the lumen.*

5.3.3 Three dimensional reconstruction of *Namacalathus*

X-ray microtomographic (µCT) imaging of two individuals (nos. 4 and 32) show that pyritisation reveals the presence of a cup-shaped calcite skeleton below the bedding plane surface, with the absence of a stalk in individual no. 32 (Figure 5.8). Both visual inspection of the fossils (Figure 5.6) and µCT images reveal the raised pin cushion-like form to be formed of six radially arranged lobes separated by the folds that project into the central opening and into the top of the lumens (Figure 5.7). These are entirely pyritised. A cluster of helically coiled large bacteria, possibly *Obruchevella*, known mostly from Neoproterozoic and Cambrian successions (Knoll, 1992), is also selectively pyritised outside the *Namacalathus* cup (no.32) (Figures 5.8F-H, K-M).

Figure 5.8 (page 133)**: X-ray microtomographic (µCT) reconstruction of* Namacalathus hermanastes. ***A**-**D**, **F**-**I**, **K**-**N**, no. 32, and **E**, **J**, **O**, no. 4 showing the central opening (CO) surrounded by iron (oxyhydr)oxide (FeOx; green-blue), showing lobes (Lo), lumens (L), and folds (yellow arrows). The calcite skeleton (CS; blue) is preserved below the bedding surface, and outlines the L. CT = central tube; Scale bars 2 mm. **A**: Plan view of* Namacalathus *cup. **(B)** False colour µCT slice of core (C-C' of A). **C**, **F**-**H**, **K**-**M**: Reconstruction of* Namacalathus *cup rotated from the central axis. O = large bacterium, possible* Obruchevella. D**, **I**, **N**: Photomicrographs of successive longitudinal surfaces during serial sectioning (A-A', B-B' and D-D' of A), with arrows tracing the membrane across central opening. Arrows show trajectory of cement-filled fractures. **E, J, O**: Rendered 3D model with grey scale CT sections, highlighting Lo, CS and CT. Sp = Spine; P = Pore; CT = Central structure; Fl=flange; white arrows = iron oxide concentration within the cup; blue arrows = way up.*

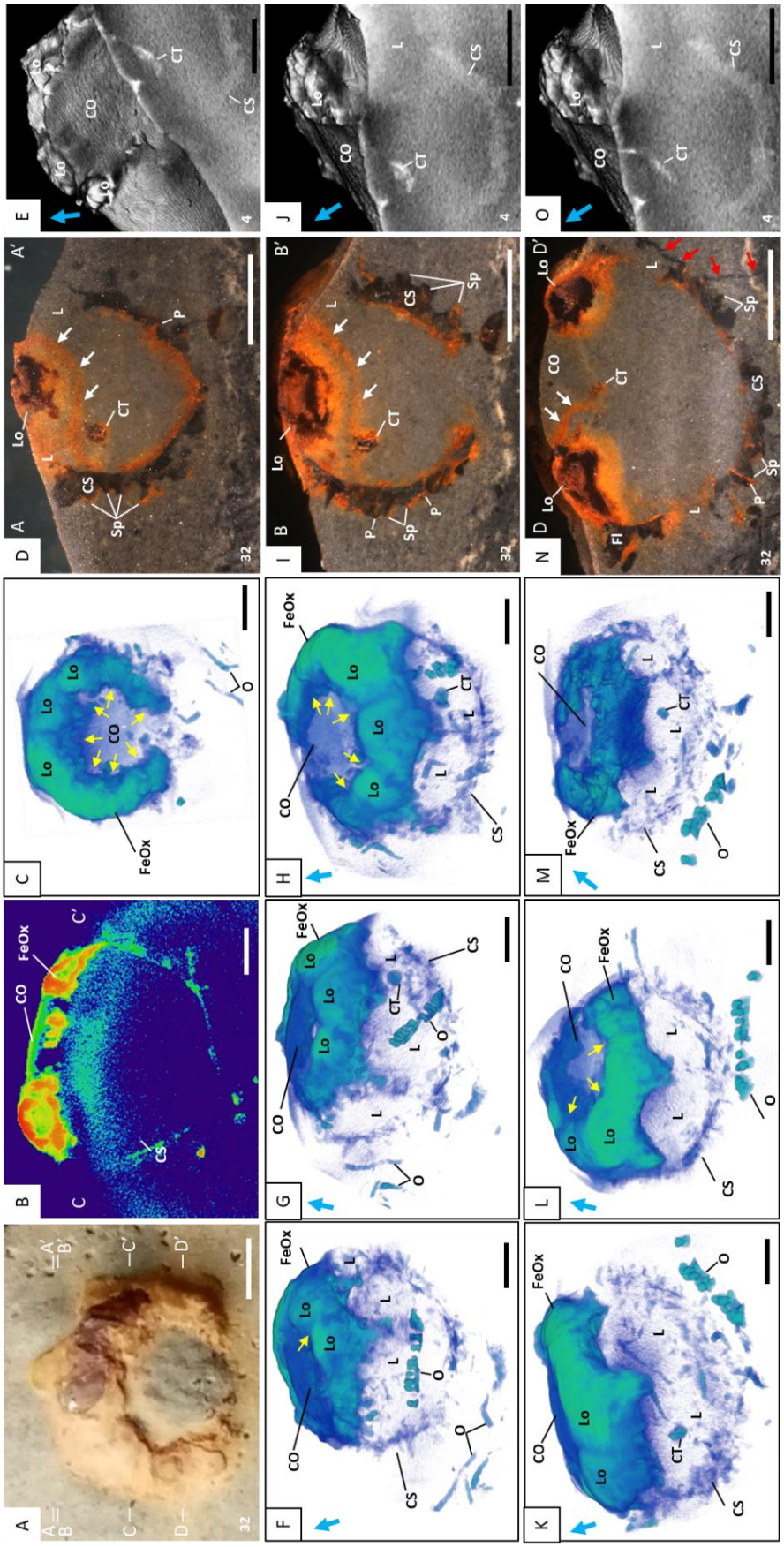

Figure 5.8

5.3.4 Soft tissue distribution in *Namacalathus*

Polished serial sections through *Namacalathus* (no. 32) confirm the presence of an internal calcite skeleton, which is overlain by the lobes (Figure 5.9). Lobes are composed wholly of framboidal pyrite, which are mostly distinct in the central parts of the lobes (Figures 5.9 B-G; 5.10A-C. The majority of the framboids have been oxidised to iron oxides (FeOx) and are here referred to as FeOx framboids that are pseudomorphs after pyrite. Backscattered-electron images also clearly distinguish between the calcitic skeleton with only highly selective or very localised FeOx framboids, and the lobes that are preserved wholly via pyritisation (Figures 5.3, 5.11).

Horizontal calcitic skeletal flanges are present that extend outwards up to 950 µm from the central opening (Figures 5.8D, I, N; 5.9D, E, G; 5.10A; 5.12C, D), which abut with straight edges against the pyritised lobes as revealed by CL imaging (Figure 5.12D). FeOx staining up to 0.5 mm thick is also apparent within the cup adjacent to the inner wall (Figures 5.8D, I, N; 5.9; 5.12), which extends into the lumens in some individuals (Fig. 5.8N; 5.9B-E), and also in patches up to 0.1 mm thick on the outer wall (Figures 5.8I; 5.9F). Thin, FeOx-rich channels 50 to 300 µm wide are present that extend orthogonally through the entire wall thickness, often passing through the central parts of spines (Figure 5.10E, F; 5.12E, F, G). Slits also appear parallel to the skeletal wall (Figure 5.12H) or between spines (Figure 5.12I), and may bifurcate (Figures 5.12I). These slits extend to at least 450 µm in depth (Figures 5.13A-R). FeOx staining is notable on both the outer and inner walls where the channels terminate (Figures 5.8D, I, N; 5.9B-G; 5.12E-I). CL imaging shows the skeleton to be composed of poorly-zoned, dominantly dull-luminescent, blocky neomorphic sparry calcite (Figure 5.12F, R), where separate crystals differing in orientation are present either side of the pyritised pores (Figures 5.12F).

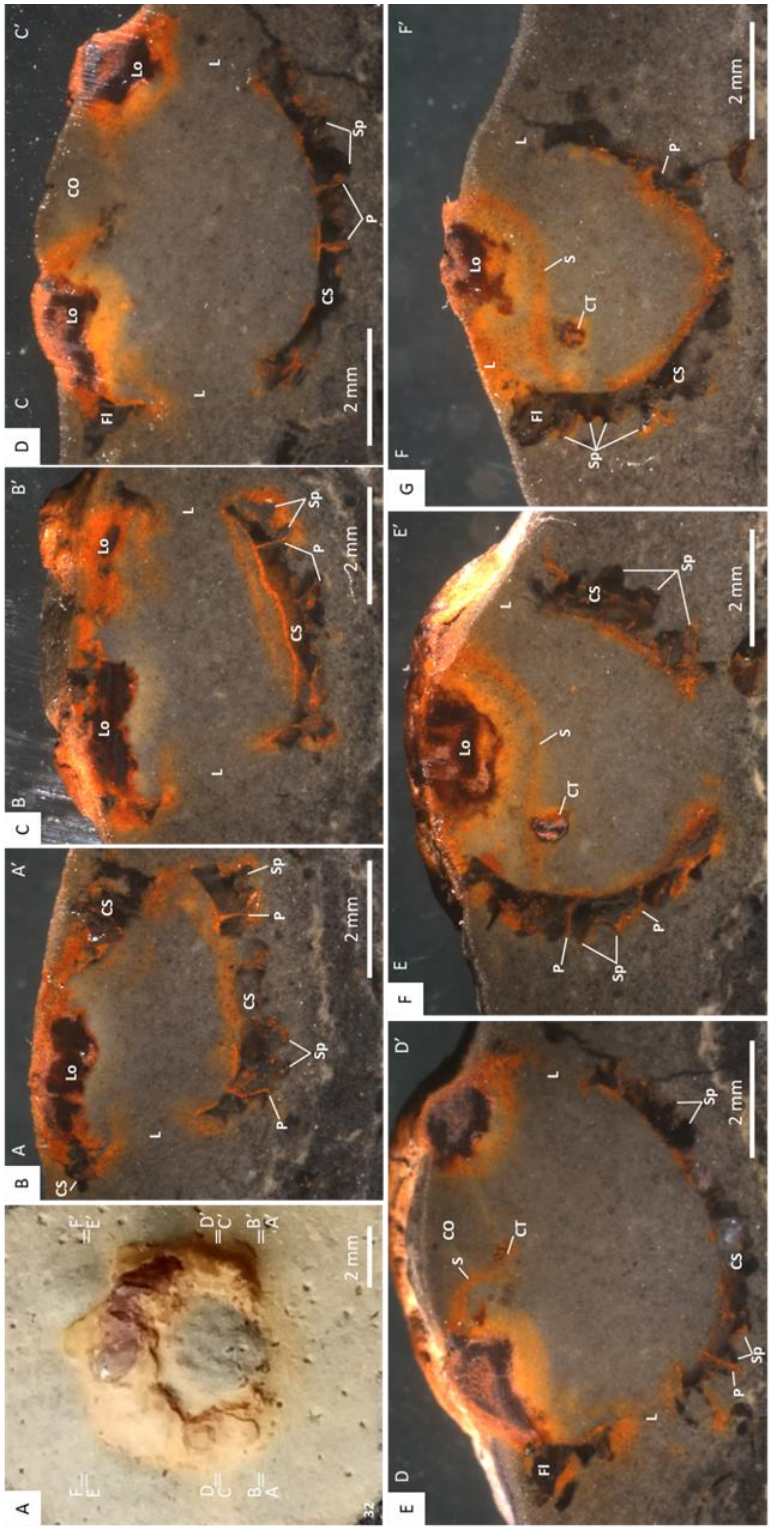

Figure 5.9

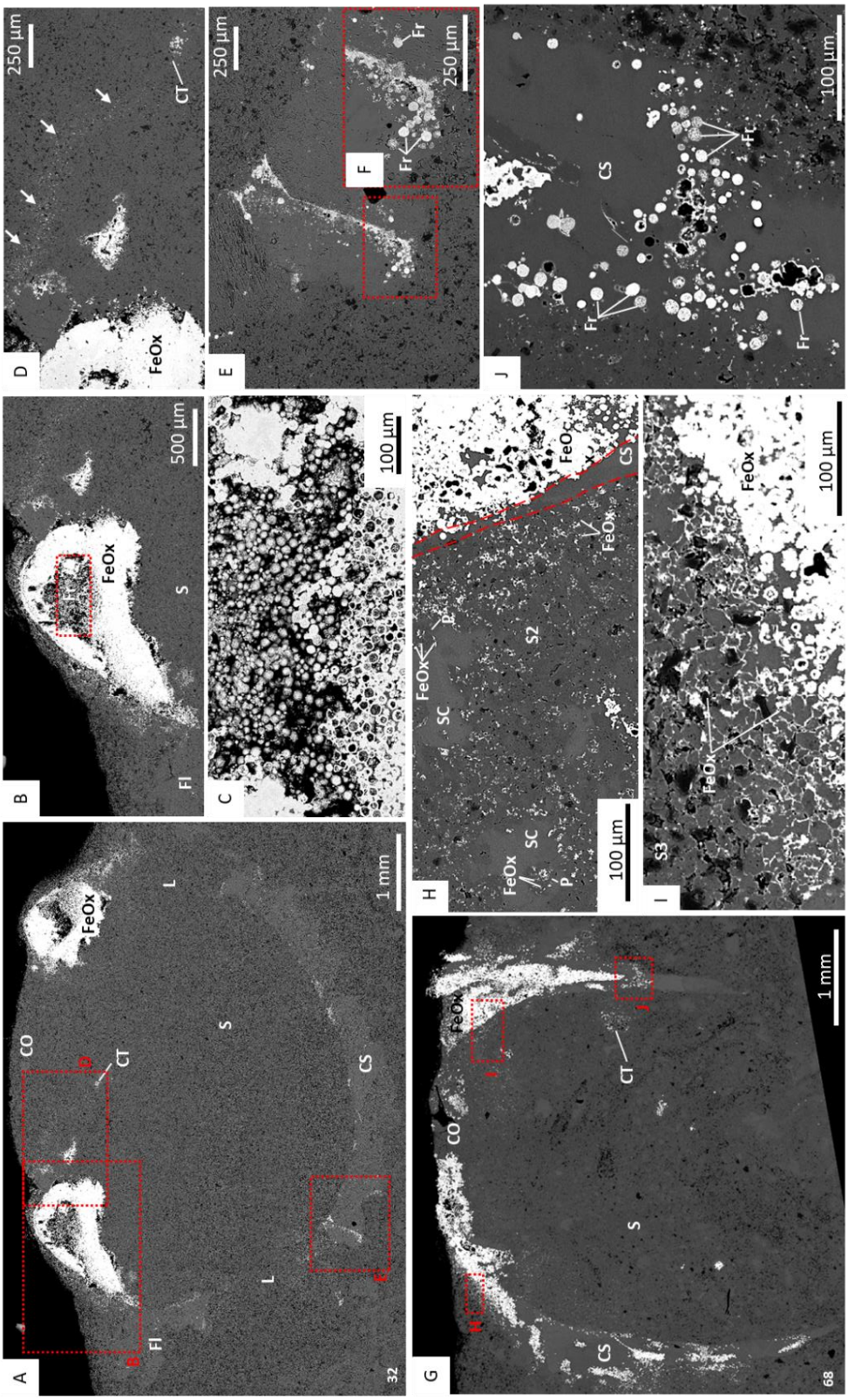
A
B
C
D
E
F
G
H
I
J
FeOx
CO
CT
Fl
S
L
CS
SC
S2
S3
Fr
1 mm
500 µm
250 µm
100 µm

Figure 5.10

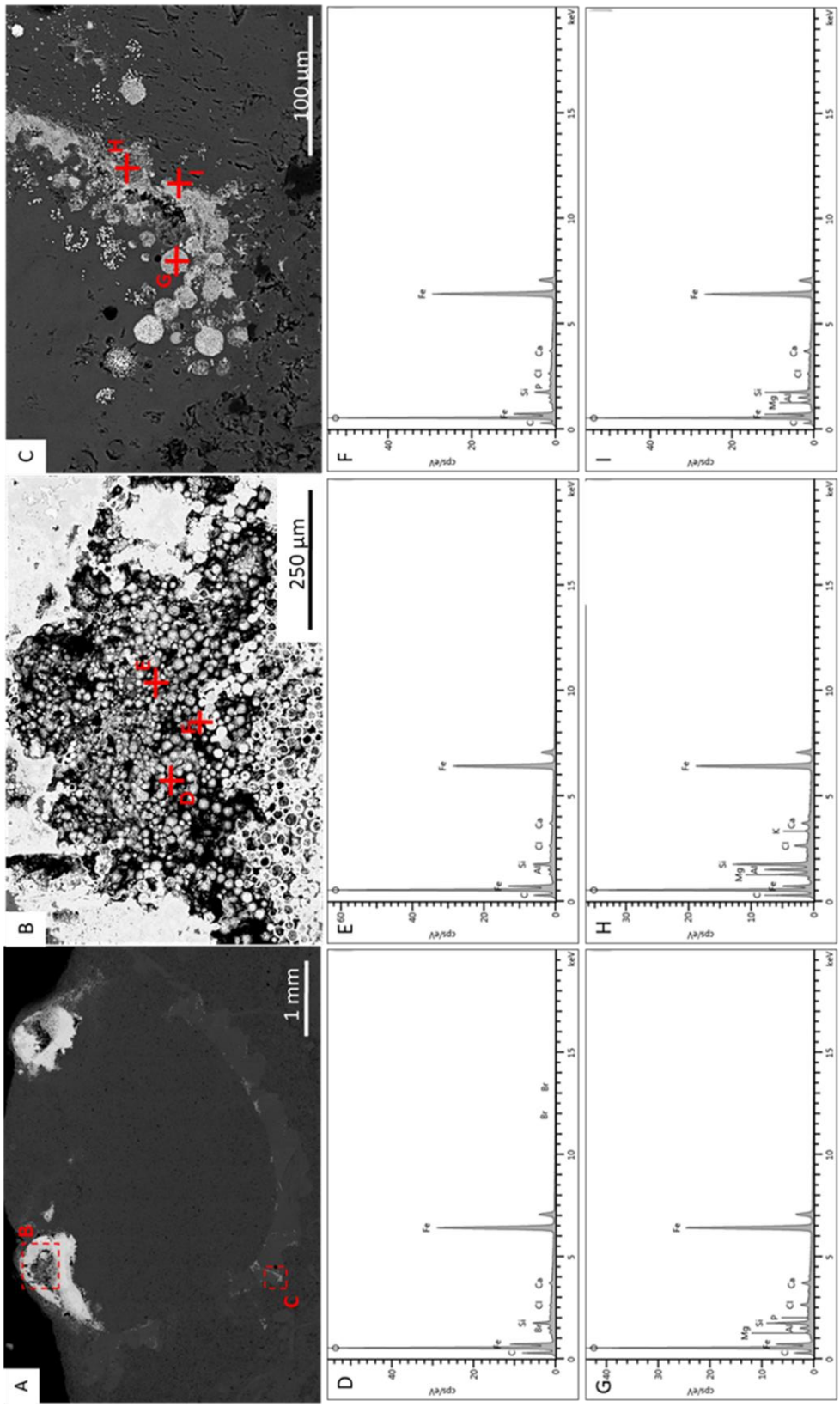

Figure 5.11

***Figure 5.9 (page 135)**: Photomicrographs of successive longitudinal sections of* Namacalathus hermanstes, *no. 32 (see Figure 5.1) highlighting features of the cup. **A**: Plan view of* Namacalathus *cup. **B**: Section A-A' in A, showing the calcitic skeleton (CS) overlain by a lobe (LO) of soft tissue. The skeleton has prominent spines and iron oxide filled pores (P). Lumen (L) are also present. **C**: Section B-B' in A through two lumens. **D**: Section C-C' in A through the central opening (CO) with two lobes with a framboidal pyrite core on either side of the opening. The spiny calcitic skeleton has a flange (Fl) at the top most part of the skeleton. **E**: Section D-D' in A through the central opening. Within the central area of the cup a section of a central tube (CT) with associated this band of iron oxide staining (S). **F**: Section E-E' in A through a lobe of inferred soft tissue and central tubular structure and associated band of iron (oxyhydr)oxide staining. **G**: Section F-F' in A through a lobe of inferred soft tissue and central tubular structure and associated band of iron (oxyhydr)oxide staining.*

***Figure 5.10 (page 136)**: Backscatter SEM images of* Namacalathus hermanastes *(A-F, no. 32, slice D - D' (Figure 5.8N). G-J, no. 68). **A**: SEM image showing calcite skeleton (CS) and flange (Fl) with lumens (L), pyritised/FeOx soft tissue of lobes (FeOx) and central structure (CT), with sediment (S). **B**: Inset of A, soft-tissue lobe of* Namacalathus *at the bedding surface infilled by FeOx framboids (Fr). **C**: Inset of B, showing FeOx framboids. **D**: Inset of A, showing line of FeOx framboids (arrowed) across the central opening (CO) which attach to CT.* **E**: *Inset of A, spine with perpendicular pore infilled with FeOx framboids. **F**: Inset of E, showing FeOx framboids. **G**: FeOx framboids within the central area of the skeleton and CT. **H**: Inset of G, showing middle layer of FeOx framboids (FeOx) in CS widening towards bedding surface, and S2 peloidal sediment with FeOx (arrowed) partially replacing peloids (P). SC = burial sparry calcite. **I**: Inset of G, FeOx cement around angular calcitic and lithic grains of S3. **J**: Inset of G, FeOx framboids (Fr) within the CS.*

Figure 5.11 (page 137)**: EDX data of soft tissue areas of* Namacalathus hermanstes *No. 32. **A**: Backscatter SEM image. **B**: Inset of A, showing position of EDX data (D**-**F**) *within the soft tissue lobe. **C**: Inset of A, showing position of EDX data (**H**, **I**, **J**, **K**) in overlying sediment, S3. **D**-**F:** EDX data from points highlighted in B, highlighting the composition of the framboids within the core of the soft tissue are iron (oxyhydr)oxide. **G**-**H**: EDX data from points highlighted in C, which indicate the composition of the framboids within the channel/pore systems within the skeleton are iron (oxyhydr)oxide.*

***Figure 5.12 (139)**: Photomicrographs (LP) and Cathodoluminescent images (CL) of* Namacalathus hermanastes, *no. 32. Longitudinal section highlighting features of the calcite skeleton (CS) and iron (oxyhydr)oxide (FeOx). **A**: Section D - D' (Fig. 2N), and **B**: Section B - B' (Fig. 2I) showing highlighted areas. **C**, **D**: CS with a flange (Fl) overlain by FeOx (contact arrowed). **E**: Pore (arrowed) along a spine (Sp). **F**: FeOx framboid-lined pore (F) (yellow arrow), forming a crystal boundary (white arrows). **G**: Pores infilled with FeOx framboids (arrowed) and section of a central tubular structure (CT, boxed). **H**: CS with FeOx staining parallel to (white arrows) and on the outer skeletal wall (yellow arrows). FeOx is concentrated where channels penetrate the outer wall of the cup (red arrow). **I**: Channels with bifurcation (blue arrows) and with FeOx in areas between spines (white arrow). Concentrated FeOx located on outer wall and where channels penetrate the inner wall of the cup (red arrows). **J:** Lobe surrounded by FeOx staining (arrowed) connecting to CT (boxed). **K**: FeOx staining coincident with bright luminescent calcite. **L**, **M**: Section of CTS in G and J, with sparry calcite (white arrow) surrounding F (yellow arrows). **N**, **O**: FeOx staining of membrane (arrowed) coincident with brighter luminescence (arrowed), connecting to the CT. **P**: Inset of O, CT with calcite (C) with central F (yellow arrow). **Q**, **R**: CS; lumen (L); with S1 and S2 sediments outside and inside the cup, respectively.*

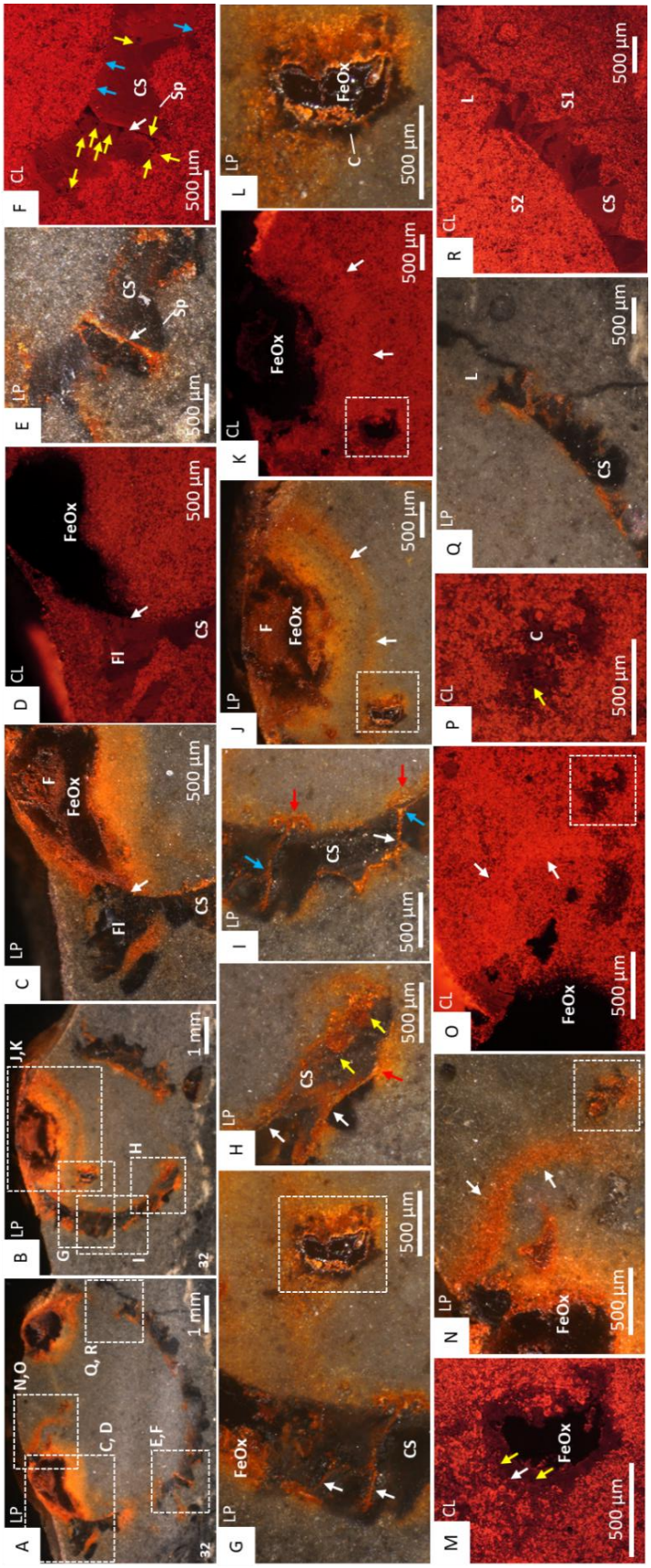
A
LP
N,O
C, D
Q, R
E,F
1 mm
32
B
LP
J,K
G
H
I
1 mm
32
C
LP
F
FeOx
Fl
CS
500 µm
D
CL
FeOx
Fl
CS
500 µm
E
LP
CS
Sp
500 µm
F
CL
CS
Sp
500 µm
G
LP
FeOx
CS
500 µm
H
LP
CS
500 µm
I
LP
CS
500 µm
J
LP
F
FeOx
500 µm
K
CL
FeOx
500 µm
L
LP
C
FeOx
500 µm
M
CL
FeOx
500 µm
N
LP
FeOx
500 µm
O
CL
FeOx
500 µm
P
CL
C
500 µm
Q
LP
L
CS
500 µm
R
CL
L
S2
S1
CS
500 µm

Figure 5.12

A tube-like structure is present within the skeletal cup in three of four *Namacalathus* cups analysed (nos. 4, 32 and 64) and can be distinguished in polished serial sections, as well as imaging via CL and backscatter SEM (Figures 5.8D, I, N; 5.9D-G; 5.12L, M, P; 5.13; 5.14) and μCT (Figure 5.8E, G, H, J, K, M, O). This is often defined by a central area of framboidal FeOx and outer area of non-zoned, dark dull luminescent, sparry calcite (also present as a later stage cement infill within the carbonate sediment). This structure has a clearly-defined elliptical or circular cross-section of up to 400 μm in diameter and may connect with a thin layer of FeOx 100-400 μm thick draped across the central opening of the cup (Figures 5.8D, I, N; 5.9D-G; 5.10A,D; 5.12J,K, N, O). The tube often appears to start within the central opening (Figure 5.13) then descends into the cup moving towards the inner wall, inflating to a more circular section up to 600 μm, then curving to form an asymmetric, J-shaped structure within the cup, sometimes decreasing in width near the inner wall to finally disappear without attachment (Figure 5.13).

FeOx framboids are only abundant and densely-packed in the lobes (Figures 5.10A-C; 5.11A-B), apart from selected areas of the skeleton where they are encased within neomorphic calcite (Figure 5.10J). There are no framboids in the wider sediment. Tangential sections of *Namacalathus* in a further individual (no. 68) which sections the skeletal neomorphic calcite only and not the lobes, shows selective pyritisation of the calcite skeleton where FeOx framboids are concentrated within a well-defined, straight-edged middle layer (Figures 5.10G, 5.14; 5.15). The pyritisation extends to almost the full width of the skeleton in the uppermost parts of the cup, thinning towards the base of the cup where the calcitised outer and inner skeletal layers thicken (Figures 5.10G, 5.14; 5.15). Thin accumulations of FeOx framboids also occur in patches along the inner and outer skeletal surfaces, and additionally pick-out inverted V-shapes within the calcitic parts of the skeleton, the latter in the tangential section (Figure 5.10G, J). In addition, the channel-like structures are also infilled with FeOx framboids (Figures 5.10E, F; 5.12E-I).

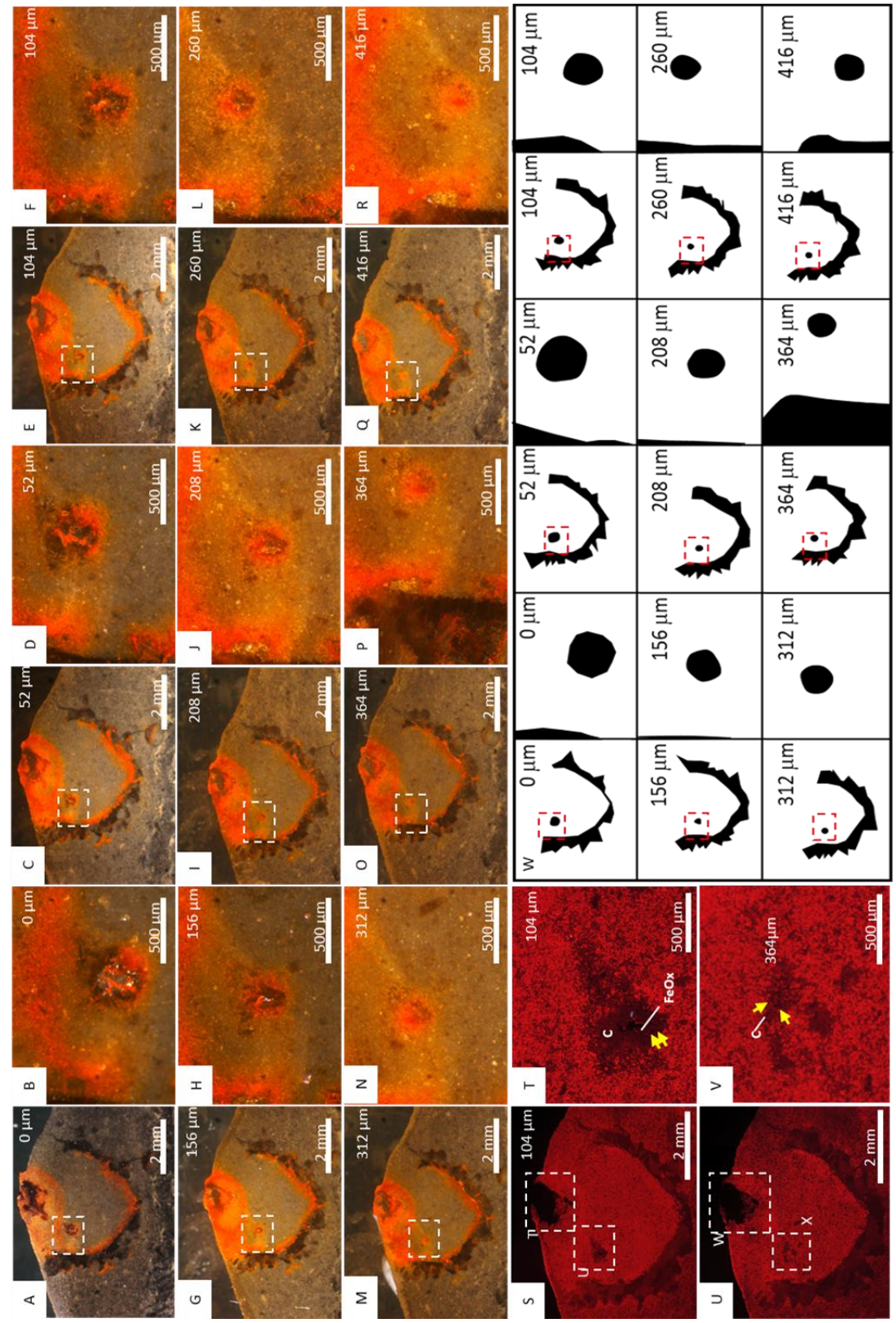
A
0 µm
2 mm
B
0 µm
500 µm
C
52 µm
2 mm
D
52 µm
500 µm
E
104 µm
2 mm
F
104 µm
500 µm
G
156 µm
2 mm
H
156 µm
500 µm
I
208 µm
2 mm
J
208 µm
500 µm
K
260 µm
2 mm
L
260 µm
500 µm
M
312 µm
2 mm
N
312 µm
500 µm
O
364 µm
2 mm
P
364 µm
500 µm
Q
416 µm
2 mm
R
416 µm
500 µm
S
104 µm
T
U
2 mm
T
104 µm
C
FeOx
500 µm
U
W
X
2 mm
V
364µm
C
500 µm
W
0 µm
156 µm
312 µm
0 µm
156 µm
312 µm
52 µm
208 µm
364 µm
52 µm
208 µm
364 µm
104 µm
260 µm
416 µm
104 µm
260 µm
416 µm

Figure 5 .13

***Figure 5.13 (page 141)**: Serial longitudinal sectioning of* Namacalathus hermanstes, *no. 32 (see Figure 5.1), showing internal, tubular structure at 26 µm increments. **A**: Photomicrograph of* Namacalathus *before serial sectioning. **B**: Inset of A highlighting the tubular structure consisting of calcite with an iron (oxyhydr)oxide core. **C**: Photomicrograph of* Namacalathus *cup after second sectioning. **D**: Inset of C highlighting the tubular structure consisting of calcite with an iron (oxyhydr)oxide core. **E**: Photomicrograph of* Namacalathus *cup after fourth sectioning. **F**: Inset of E, highlighting the tubular structure consisting of calcite with an iron (oxyhydr)oxide core. **G**: Photomicrograph of* Namacalathus *cup after sixth sectioning. **H**: Inset of G highlighting the tubular structure consisting of calcite with an iron (oxyhydr)oxide core. **I**: Photomicrograph of* Namacalathus *cup after eighth sectioning. **J**: Inset of I highlighting the tubular structure consisting of calcite with an iron (oxyhydr)oxide core. **K**: Photomicrograph of* Namacalathus *cup after tenth sectioning. **L**: Inset of K highlighting the tubular structure consisting of calcite with an iron (oxyhydr)oxide core. **M**: Photomicrograph of* Namacalathus *cup after twelfth sectioning. **N** Inset of M highlighting calcite surrounded by iron (oxyhydr)oxide staining in the surrounding sediment. **O**: Photomicrograph of* Namacalathus *cup after fourteenth sectioning. **P**: Inset of O highlighting calcite surrounded by iron (oxyhydr)oxide staining in the surrounding sediment. **Q**: Photomicrograph of* Namacalathus *cup after sixteenth sectioning. **R**: Inset of Q highlighting calcite surrounded by iron (oxyhydr)oxide staining in the surrounding sediment. **S**: Cathodoluminescent image of E. **T**: Inset of S, lobe of* Namacalathus *soft tissue preserved as iron (oxyhydr)oxide. **U**: inset of S, central tubular structure consisting of iron (oxyhydr)oxide surrounded by calcite (C) with framboids (arrowed). **V**: Cathodoluminescent image of O. **W**: inset of V, lobe of* Namacalathus *soft tissue preserved at iron (oxyhydr)oxide (FeOx). **X**: Inset of V, central tubular structure consisting of calcite (C) with pyrite framboids (arrowed). **W**: Schematic of the slices presented in A-R, with corresponding figure labels, highlighting skeleton and J-shaped central tubular structure.*

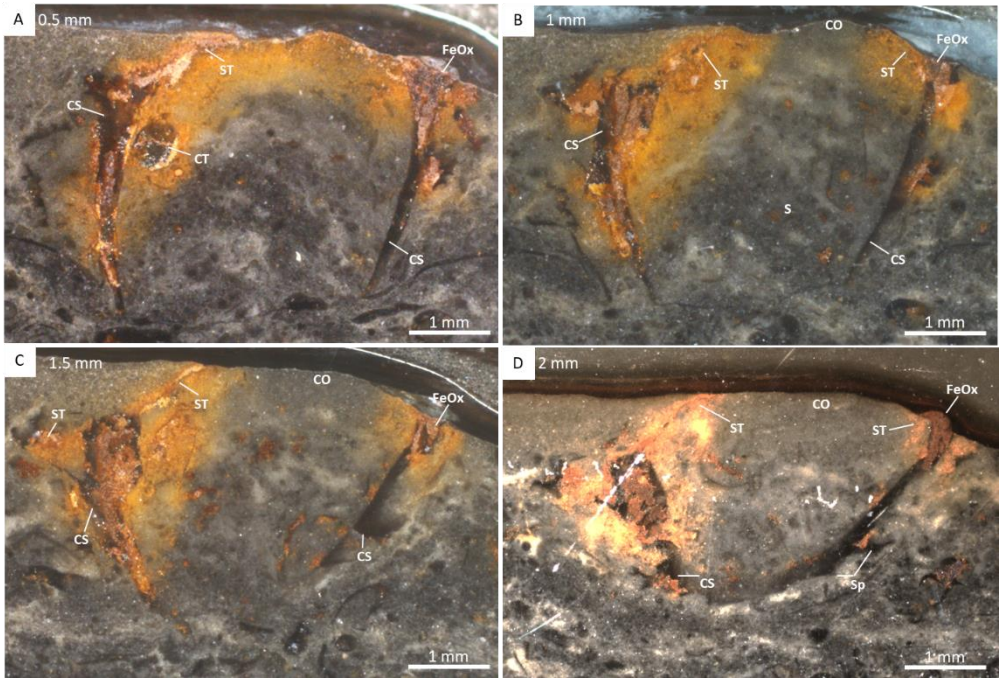

***Figure 5.14**: Photomicrographs of successive parallel polished surfaces of* Namacalathus cup *no. 68, at 0.5 mm intervals though central zone, showing distribution of iron (oxyhydr)oxide (FeOx), calcite skeleton (CS), skeletal spines (Sp), central opening (CO) and soft tissue at and beneath bedding plane (ST). The lower part of the calcitic skeleton has been compacted in A and B. **A**: Section of cup at 0.5 mm, showing distribution of ST and FeO throughout the upper part of the cup. **B**: Section of cup at 1 mm, showing distribution of ST on both sides and FeOx localized under ST in the upper part of the cup, with central opening lacking FeOx staining. **C**: Section of cup at 1.5 mm, showing distribution of ST on left sides and with central opening lacking FeOx staining. **D**: Section of cup at 2 mm, showing distribution of ST on left side with central opening lacking FeOx staining.*

CL imaging shows zoned calcite cements growing around uncompacted sediment, which project into the neomorphic calcite skeleton of *Namacalathus* and other neomorphosed bioclastic grains (Figure 5.12F). The dominant bright CL zone of the zoned calcite cements growing around uncompacted sediment, coincides with visible FeOx staining near the upper parts of the cup (Figures 5.8D, I N; 5.9 5.15), and also with the thin layer of FeOx across the central opening (Figures 5.8D, I, N; 5.9; 5.12N, O). SEM images of this area confirms the presence of a line of framboidal FeOx (Figure 5.10D).

Peloids are abundant in the area with visible iron staining, where the peloids are partially replaced by pyrite/FeOx (Figure 5.10H). Likewise, sediment grains in the bed surface overlying the *Namacalathus* individuals are coated by pyrite/FeOx cements (Figure 5.10I). Thus, CL imaging reveals three carbonate sediment types associated with the *Namacalathus* cups (Figure 5.15) – a bioclast-rich sediment infilling the bottom of cups (S1), peloid-rich sediment with partial pyrite/FeOx replacement in the upper part of cups (S2) and an overlying lithic-rich sediment with pyrite/FeOx cements (S3) (Figures 5.10H, I; 5.12R; 5.15).

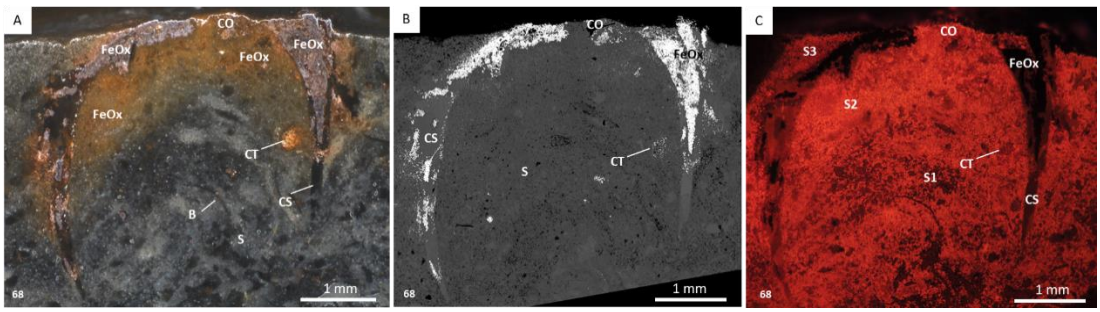

Figure 5.15*: Micrographs of* Namacalathus hermanstes*, no. 68.* ***A****: Light micrograph image showing calcite skeleton (CS), pyritised/FeOx soft tissue of lobes (Lo) and central structure (CT), with sediment (S) and bioclasts (B).* ***B****: SEM image highlighting FeOx/pyrite within the central area of the skeleton.* ***C****: Cathodoluminescent image showing CS, areas of pyrite/FeOx, and distribution of sediments S1, S2 and S3.*

5.4 Discussion

The lobes around the central opening are inferred to represent ancient soft-tissue, preserved via extensive pyritisation. This is supported by the diverse morphological expression of the central opening in different individuals, which show lobes with both a variable number, and dimension, of folds (Figures 5.5A; 5.6; Table 5.2). Both the central opening and lumens are covered by a FeOx crust which extends over these skeletal structures to create consistently smaller, partially occluded, openings. The variable constriction and scalloping of the central opening in particular suggests the soft-tissue here could potentially extend or contract. The lobate central opening form seen in many individuals might indicate soft tissue preservation in a state of either relaxation or contraction.

The early precipitation of both pyrite and calcite cements is responsible for this exceptional, three-dimensional preservation of inferred soft tissue (Butterfield, 2003). This type of preservation occurs in sulfate-reducing environments with high concentrations of highly reactive iron but low or very localised availability of organic carbon available during early diagenesis, where pyrite precipitation is only associated with labile tissues and cellular structure is destroyed (Butterfield, 2003) and where the form of pyrite may reflect the relative susceptibility to decay of the original material (Botting et al., 2001; Osés et al., 2017*)*. Furthermore, pyrite framboid formation can occur within hours to days on organic matter under these conditions (Rickard, 2019). It is infered that framboidal pyrite formed very early and replaced both soft tissue and the inferred organic-rich parts of the skeleton. The occurrence of pyritised bacteria, here found alongside *Namacalathus*, is highly unusual in the fossil record and confirms that pyritisation was rapid enough to replicate soft tissue.

The bright CL zone of early calcite cements associated with sediment within the upper part of cups (S2) is indicative of high Mn and low Fe pore water conditions (Figures 5.8D, I N; 5.9 5.15). The sediment of S2 is also characterised by FeOx staining which is inferred to derive from the oxidation of pyrite. This confirms the coincidence of both early pyrite and

early calcite cementation. Early carbonate cement formation is known to be facilitated by cell walls, extracellular polymeric substances (EPS), organic matter degradation, and other metabolic or microbial processes where peloids may form (e.g. Obst et al., 2009). Local dissolution around pyritised soft tissue, perhaps induced by limited oxidation of pyrite, led to the formation of molds which later became infilled with a burial calcite spar cement.

Similar three-dimensional preservation of soft tissues in pyrite is found in the uppermost Ediacaran Gaojiashan Member of the Dengying Formation (Schiffbauer et al., 2014) and the Lower Ordovician Fenxiang Formation of China (Baliński and Sun, 2013), the Upper Ordovician Llanfawr Lagerstätte of Wales *(*Botting et al., 2011*)*, and the Lower Cretaceous Santana Formation of Brazil (Osés et al., 2017), often created by rapid entombment via storms or slumping sediments. In the Nama Group, the proximal, very shallow, low energy environment provided both a fine-grained medium and sufficient calcium carbonate saturation to facilitate early cementation. The *Namacalathus* individuals may also have been rapidly buried, in life, by a thin incursion of terrestrially derived lithic-rich sediment, with the folds of the central apical opening may represent a contracted state. The folding is unlikely to be taphonomic as the number of folds appears to correlate with lumen number. Cloudinids in siliciclastic-dominated beds of the Wood Canyon Formation, Nevada show more spatially restricted framboidal pyritisation that preserves cylindrical internal structures recently interpreted as possible digestive tracts (Schiffbauer et al., 2020). Internal digestive tissue is otherwise completely unknown from the Ediacaran record although common in Cambrian Lagerstätten (Schiffbauer et al., 2020). In sum, the processes operating in this preservational setting have created a taphonomically unique Lagerstätte.

The pyrite-rich middle layer within the *Namacalathus* skeleton, not present in all cups but prominent in no. 68, confirms the presence of a tripartite skeleton with an organic-rich central portion (Zhuravlev et al., 2015). FeOx framboids in thin layers within other parts of the skeleton also suggests the presence of thinner organic-rich layers, parallel to potential

accretionary growth lines. The thickness of the pyritised middle layer increases towards the upper part of the skeletal cup. This middle layer may have formed an organic template upon which the outer and inner calcareous layers formed, and as such was the area of active skeletal growth, as observed in modern corals and lophophorates (e.g. Williams et al., 2004). The presence of thick lobes at the top of some cups, as featured in no. 32, could also imply a thickening of this layer where the skeleton is in contact with lobes suggesting that this may have been the area of initial skeletonogenesis.

Namacalathus did not grow to a finite size as the cup size is highly variable, and likewise not all individuals are spiny. *Namacalathus* does not appear to have grown via marginal accretion. But individual bryozoan zooid skeletons do not grow accretionally even in runner-type colonies, which consist of essentially isolated individuals, and skeletal resorption occurs in both brachiopods (Streng and Holmer, 2005) and bryozoans (Taylor and Weedon, 2000), which represent crown group lophophorates. Inferred populations of *Namacalathus* often share a similar size range (Zhuravlev et al., 2015). This raises the possibly of a single episode of calcification within an individual life cycle, where further skeletal modification occurred via partial resorption. Such resorption could take place within the microenvironment created by the soft tissue covering the skeleton externally (a periostracum), internally via the body wall, or via the multiple penetrating pores.

The FeOx staining noted extensively within the cup and the lumens, surrounding the inner wall of the cup, in thin patches on the outside the cup, and also thin layer draped across the central opening, suggests the presence of further soft-tissue. The FeOx staining around the lumens in some cases extends from the outer wall to the inner wall of the skeleton. The small ridges and domes found primarily associated with the central opening and lumens are also found away from these areas. These could represent some soft-tissue features but may equally have formed by the pyrite weathering process.

The internal curved, tube-like structure with a clear elliptical or circular cross-section is present in three specimens (Figure 5.16) and is preserved via dense FeOx framboids, so is consistent with a structure consisting of highly localised organic matter. The thin, membrane-like structure across the aboral opening might represent a post-mortem feature, such as a relic of bacterial decay. But the preservation of this structure also via FeOx framboids suggests the same process of very early diagenetic replacement of localised organic matter. The tube-like structure also has an apparent connection to this membrane, as evidenced by the form of FeOx staining around the structure and its overall position. The tube-like structure may represent a retractor muscle band, but more likely had a feeding function: a pharynx, coelomic cavity, body cavity extension, or potentially a partially-preserved U-shaped gut. It is noted that the framboidal pyritic preservation of this feature is like that of the soft-tissue structure recently interpreted as a gut in cloudinids of the Wood Canyon Formation, Nevada (Schiffbauer et al., 2020).

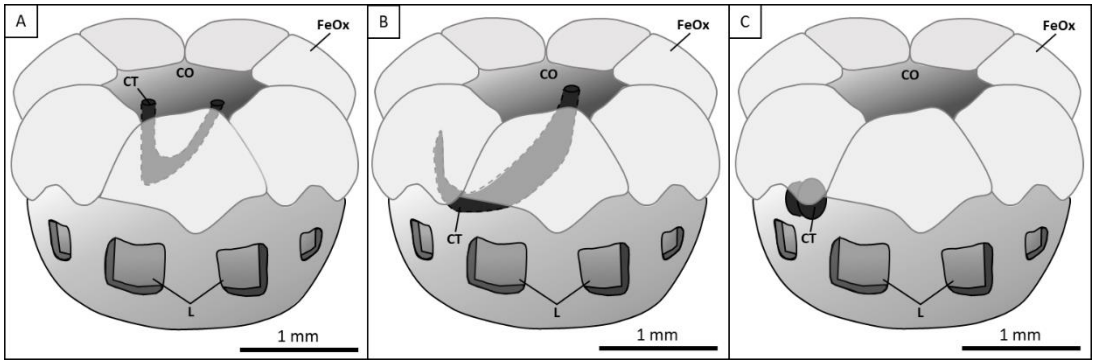

Figure 5.16: *Schematic reconstruction of the central tubular structure, and potential gut, in* Namacalathus hermanastes*, relative to the calcitic skeleton (CS), the iron (oxyhydr)oxide (FeOx) lobes and the central opening (CO). Museum No. F1547, Museum of the Geological Survey of Namibia.* ***A****: no. 4;* ***B****: no. 32;* ***C****: no. 68.*

Two new types of fine tubular openings within the skeleton are noted here in *Namacalathus*: pores that penetrate the wall itself, and channels that penetrate the spines. Inferred pseudopunctae present as columnar inflections of skeletal wall microlaminae have been noted previously (Zhuravlev et al., 2015). The presence of FeOx framboids within the pores and channels is suggestive of the presence of further soft-tissue within these features,

and these framboids sometimes connect with the thin external and thick internal FeOx-rich layers on the skeletal walls of *Namacalathus*. This, together with the observations that different calcite crystals are present either side of the pores, and that these pores are not planar or continuous throughout the fossils, suggests these are primary biological features: diagenetic fractures would cross-cut individual crystals of calcite and potentially extend beyond the cup into sediment. The diagenetic cement-filled fractures present in the samples, outside of the *Namacalathus* fossil, are more extensive than and have a different orientation to the pores and channels. These later diagenetic fractures are also filled with the same dull luminescent calcite cement zone as found throughout the calcitic skeleton (Figure 5.12E, F, Q, R). No unique calcite cement zone is localised within the pores. The pores are restricted to the skeleton only, and unlike the pores, FeOx framboids are absent in both the fractures and sediment surrounding *Namacalathus* individuals.

In sum, *Namacalathus* possesses a goblet-shaped calcareous skeleton with a hollow stalk and central opening, generally hexaradial symmetry with lateral facets bearing large lumens. Soft tissue follows the internal skeleton, and the lumens do not have a localised, diagenetic, dissolution origin as previously suggested (Grotzinger et al., 2000). In addition, we note the presence of 5 to 7 folds of variable height formed between radially arranged lobes that extend from and beyond the central apical opening to lateral lumens, organic-rich pores and channels within the skeletal wall, an internal, asymmetric, J-shaped tube-like structure, and inferred soft-tissue adhering to the inner skeletal wall, an internal membrane abutting the central opening, and a thin organic-rich external covering. A foliate microstructure with concordant columnar inflections and a middle organic-rich layer, and asexual reproduction expressed by bilateral budding have been noted previously in *Namacalathus* (Grotzinger et al., 2000; Zhuravlev et al., 2015).

The external FeOx layer has a lobate pattern around the central opening, with variable constriction and scalloping. The folds, and their correlation with the number of lumens,

suggests that this arrangement might be integral to the feeding process of *Namacalathus*. These may represent a cnidarian-like polyp, or radially-arranged, parietal diaphragm dilatator muscles. In some bryozoan groups, contraction of these muscles pulls the frontal membrane of the polyp inwards with protrusion of the tentacle collar (Mukai et al., 1997).

The thin organic structure that traverses the apical opening of *Namacalathus* may represent a frontal membrane or very large supportive mesentery, and so the position of the tubular structure below might correspond to the coelomic cavity. In such a case, a retraction mechanism can also be inferred in *Namacalathus*, where muscle bundles may connect the frontal membrane and body wall (Figures 5.8D, E, I, J, N, O; 5.9D-G; 5.12G, J-P; 5.13; 5.14; 5.17). The patchy, external coating of FeOx over the skeletal cup may represent an organic-rich covering, perhaps of resembling a periostracum.

The generally six, large lateral lumens could suggest a solitary organism with soft tissue within the lumens that extends into the central cup, formed by external body wall invaginations (Figure 5.17). This arrangement is noted in the brood chambers found in bryozoans (Mukai et al., 1997). However, the extension of soft tissue into the lumens might also suggest that these structures allowed for the movement of water in or out of to the lumens and then into the cup as part of the feeding mechanism.

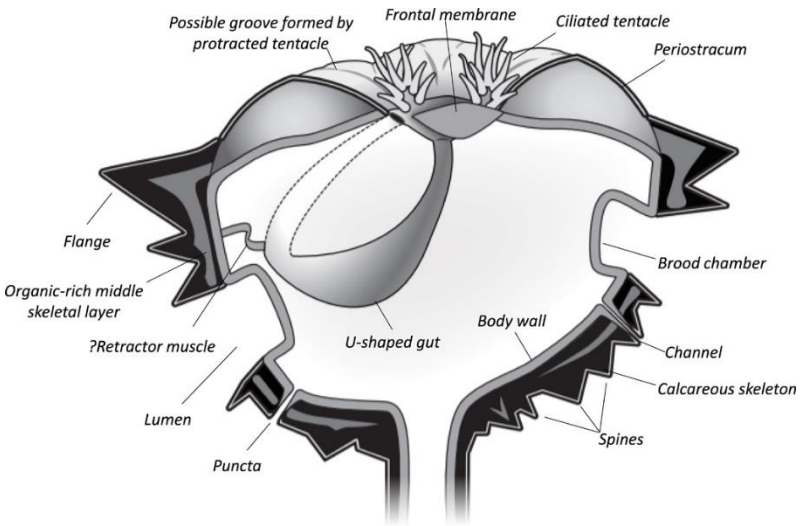

***Figure 5.17**: Reconstruction of* Namacalathus hermanastes *as a stem-group lophotrochozoan.*

The organic-rich pores and channels within the skeletal wall that connect to the thin external and thick internal FeOx-rich layers in *Namacalathus* may be homologous to punctae and channels of similar size in brachiopods, extinct tommotiids and microconchids, and to pseudopunctae in bryozoans, which house through-wall mantle outgrowths, including branching structures, and other sensory structures (Mukai et al., 1997; Williams, 1997; Garbelli, 2017). Punctae and channels in these groups connect the external periostracum with the internal body wall. Punctae, pseudopunctae and channels are highly variable in their number ranging from sparse to abundant, and also size and general expression in lophophorates (i.e. brachiopods, bryozoans), including stem lophophorates (i.e. tentaculitoids, tommotiids) (Mukai et al., 1997; Williams, 1997; Garbelli, 2017). Such structures are absent in mollusk shells due to the presence of a thick periostracum.

In sum, the radial and facetted hexaradial calyx favors an affinity within the Cnidaria, and some extinct Palaeozoic corals also have a similar foliated skeletal microstructure (Jakubowicz et al., 2015) to *Namacalathus*. But hexaradial symmetry is also found in lophophorates (including extinct tommotiids and tentaculitoids), and the presence of possible organic-rich punctae and channels within the skeletal walls emphasises a similarity to the sensory porosity observed in lophophorates (brachiopods, tommotiids, microconchids) (Garbelli, 2017; Taylor et al., 2010), as does the presence of a possible J- or U-shaped gut and frontal membrane (Table 5.2).

A consensus tree for 54 lophotrochozoan taxa where *Namacalathus* occupies a basal position reveals that such ‘canaliculate’ microstructure and ‘punctae’ have multiple origins across the brachiozoan total group but, nonetheless, are entirely restricted to this group (Sun et al., 2018). The fossil record of biomineralised stem group lophotrochozoans is abundant from the early Cambrian onwards, where the possession of a calcareous skeleton or external sclerites likely represents the independent acquisition of skeletons of variable mineralogy in sessile, attached benthic fossil taxa which have features shared with *Namacalathus*. These

include tommotiids (Skovsted et al., 2008) and hyoliths which were pedunculate and tentaculate organisms lacking a lophophore (Sun et al., 2018). Some goblet-shaped Cambrian forms that resemble *Namacalathus* such as *Cotyledion tylodes* from the Chengjiang Lagerstätte, may represent stem lophophorates and also show an upper calyx and elongate stalk, with a central canal interpreted as an extension of the calycal cavity, a U-shaped gut with a mouth and aboral anus ringed by retractable marginal tentacles, and an outer surface covered by external sclerites which may have been mineralised (Zhang et al., 2013).

Cotyledion and some other Cambrian stalked fossils, namely, *Dinomischus* and *Siphusauctum* have been compared with entoprocts (Conway Morris, 1997; Zhang et al., 2013; Kimmig et al., 2017). These fossils are relatively large (over 15 mm in height) while extant entoprocts are extremely small (less than 1 mm) and non-biomineralised. The Entoprocta are an enigmatic monophyletic, acoelomate, group which occupy a phylogenetically basal position among lophotrochozoans, close to molluscs (Marlétaz et al, 2019). *Namacalathus* displays many similarities with the entoprocts, including the goblet-shaped overall morphology, hexaradial symmetry, and a possible U-shaped gut (where both mouth and anus are within a tentacle collar).

From the observations presented here, the *Namacalathus* lacks preserved features of an aquiferous filtration system to support a poriferan affinity or any skeletal structures such as septa that might confirm a total group cnidarian affinity (Table 5.2). A cnidarian affinity is, however, possible. Yet more probably, *Namacalathus* may represent a total group lophotrochozoan. At present bilateral symmetry in *Namacalathus* is only supported by the observation of paired bilateral budding (Zhuravlev et al., 2015). But we note that tommotiids, tentaculitoids, and some bryozoans have radially-constructed skeletons and their bilateral symmetry can only be recognised in preserved soft-tissues.

Table 5.2: *Distribution of features observed in* Namacalathus *(Grotzinger et al., 2000; Zhuravlev et al., 2015; this study), among high-rank taxa of extant and extinct organisms (Williams et al., 1997 Hooper and Van Soest, 2002; Seilacher et al., 2003; Knoll, 2003; Armstrong and Brasier et al., 2005; Taylor et al., 2009; Taylor et al., 2010; Park et al., 2011; Coronado et al., 2013; Antcliffe et al., 2014; Kouchinsky et al., 2014; Jakubowicz et al., 2015; Merkel et al., 2015; Taylor et al., 2015; Borisanova et al., 2016; Whelan et al., 2017; Bagaeva et al., 2019; Zhao et al., 2019).*

Namacalathus	**Protists**	**Coralline algae**	**Porifera**	**Cnidaria**	**Ctenophora**	**Scleroctenophora +'dinomischids'**	**Lophophorata**
Goblet shape	X	X	X	X		X	X
Hexaradial symmetry				X		X	X
Lateral lumens		X		X			X
Calcareous biomineralisation	X	X	X	X			X
Foliated microstructure				fossils only			X
Radially-arranged lobes [this study]			X	X	X	X	X
Bilateral budding				X			X
Skeletal pores/punctae[this study]	X		X				X
U-shaped gut[this study]							X

Molecular phylogeny data support that lophotrochozoans were present in the Ediacaran (Cunningham et al., 2017). Sessile extant lophotrochozoan phyla such as annelids, molluscs, brachiopods and phoronids have been suggested to have their origins in the earliest Cambrian small skeletal fauna (e.g. Zhang et al., 2013), and are indicative of the Cambrian Explosion. But if it was possible to now extend the origin of the Lophotrochozoa to the terminal Ediacaran a phylogenetic connection would be established between Ediacaran and early Cambrian taxa, faunas that were previously thought distinct. In so doing the roots of the Cambrian Explosion itself would extend back into the Ediacaran, where possible total group lophotrochozoans such as *Namacalathus* show a combination of features that became typical of both later lophophorates, and representatives of the entoproctan-molluscan-annelidan branch.

5.5 Conclusions

Exceptional preservation is key to understanding the morphology of the Ediacaran faunas and their potential affinities, which have proven to be problematic to determine. Within this chapter the first three-dimensional, pyritised soft tissue found in *Namacalathus* from the Upper Omkyk Member of the Nama Group has been described through the discovery of a new taphonomically unique Lagerstätte. The soft-tissue, preserved as iron-oxide, follows the underlying form of the cup-shaped calcitic skeleton with a stalk and around six radially arranged lumens and lobes with variable folding projecting into the apical opening. And asymmetric tubular structure within the cup, a middle layer of the tripartite skeleton and skeletal pores are selectively pyritised. These new observations suggest the presence of an apical opening capable of contraction which may have been involved in feeding, and a possible J-shaped gut. These features could suggest a total group lophotrochozoan affinity which supports molecular phylogenies and could suggest that the origin of modern lophotrochozoans, and even their ability to biomineralise, may be found within the Ediacaran and so deepening the roots of the Cambrian Explosion.

Chapter 6: Conclusions and Discussion

6.1 Conclusions

The findings presented in this thesis provide further understanding of the nature of the biomineralising Ediacaran fauna of the Nama Group, Namibia (ca. 550-538 Ma), and the environment in which they lived through the use of a range of novel techniques.

New phosphorus speciation data combined with the local redox proxies, Fe speciation and cerium anomalies from the Nama Group, Namibia, suggest that anoxic conditions prevailed between ~550 to 547 Ma, promoting drawdown of bioavailable phosphorus but also the partial release of phosphorus back into the water column. It is at this time the first metazoans are recorded within the Nama Basin. However, from ~547 Ma the Nama Group sedimentary rocks record a deepening of the oxycline, with a full ventilation of the outer ramp being achieved by ~542 Ma. Chemical index of alteration data, a chemical weathering proxy, show a reduction of continental weathering and the lowering of nutrient input, allowed for the ventilation of the basin which was further promoted by the lowering the rates of anoxic phosphorus recycling into the water column. The fluctuating, but mostly anoxic, conditions of the Nama Group prior to 547 Ma limited where Ediacaran organisms could live. Yet, the ventilation and stable oxic conditions of the Nama Group at ~542 Ma allowed for the radiation of mobile taxa which were able to inhabit deeper areas of the basin. This study highlights the controls of redox conditions on terminal Ediacaran biota which may have been driven by changes in regional nutrient cycling.

Microbial mat communities within the inner-ramp environments of the Omkyk Member were common, where cloudinomorphs and *Namacalathus* are observed attached to generations of microbial mats. It is possible that the microbial mats may have acted as oxygen oases for these calcifying organisms allowing for these communities to grow in settings with fleeting oxygenation (Xiao et al., 2019). Within these communities, and in other deeper environments of the same age, *Cloudina* were able to attach to one another, as well as to *Namacalathus*, to produce a *Cloudina*-supported reef

framework. These attachment structures, or inter-cloudinomorph cements, and other *Cloudina*-associated cements are found at multiple sites within the Nama Group, across different environmental and diagenetic settings. These cements, particularly the inter-laminae cements, nucleate from a calcified, organic-rich laminae, and are found consistently across cloudinomorphs of a similar age within the Nama Group, and moreover have been noted to be associated with *Cloudina* in other Ediacaran Basins. These *Cloudina*-associated cements formed prior to transportation, syn-sedimentary processes and inorganic cement formation. This suggests a biological origin, which was potentially part of the 'biomineralisation toolkit' (Murdock and Donoghue, 2011). However, the thickness of the *Cloudina* walls, paired lamina thickness, and sinuosity varies across the shelf. This suggests that these characteristics were environmentally controlled, potentially influenced by the hydrodynamic energy regime and variable supersaturation of the seawater with respect to calcium carbonate.

The affinity of biomineralising Ediacaran fauna is still heavily debated, partly due to the lack diagnostic features and soft-tissue preservation. The finding of polytomous branching of a cloudinomorph of the Omkyk Member suggests a non-bilaterian affinity, which contradicts an annelid affinity as suggested by the inferred gut found in the Nevadan Wood Canyon Formation (Schiffbauer et al., 2020). This could imply that the stacked funnel, tubular morphology of cloudinomorphs is convergent.

The finding of a Lagerstätte type deposit within the Omkyk Member of the Nama Group has allowed for the preservation of soft tissue through pyritisation, now found as iron oxide. This preservation of *Namacalathus* reveals new soft tissue features, such as skeletal pores, a crenulated apical opening, apical lobes, and a potential U-shaped gut. These previously unseen features provide further insight to the affinity of *Namacalathus*. Cambrian goblet-shaped organisms, such as *Cotyledion tylodes*, have been inferred to be lophotrochazoans and appear to have the same morphology as *Namacalathus*, including a U-shaped gut (Zhang et al., 2013). A cnidarian affinity may be possible for *Namacalathus* due to the hexaradial symmetry, foliated skeletal structure and lumens, which could have been used as part of a feeding mechanism. However, a lophotrochocoan affinity is more likely based on the features

preserved through soft-tissue preservation. A lophotrochazoan affinity supports an origin for this group, and an ability to biomineralise, before the Cambrian.

Ediacaran skeletal metazoans from the Nama Group include forms which may represent both cnidarian-grade and lophotrochozoan bilaterians. These organisms were limited to oxic environments which was largely determined by nutrient availability within the Nama Basin, but habitable areas expanded through time. The increase in oxygenation through time allowed for metabolically more demanding innovations, such as mobility and biomineralisation. Such characteristics of complexity are more often attributed to Cambrian faunas. In sum, these new insights deepen the roots of the Cambrian Explosion into the Ediacaran.

6.2 Discussion and future work

6.2.1 Nutrient cycling and the rise of oxygen and metazoan evolution

Ediacaran organisms and communities are linked with redox conditions and only inhabited areas which were fully oxygenated (Wood et al., 2015; Tostevin et al., 2016). Ediacaran biomineralisers however, such as *Namacalathus*, have been noted in sediments deposited in a dominantly ferruginous water column and so can opportunistically inhabit shallow shelf areas of short-lived oxygenation where anoxia was potentially introduced by the periodic upwelling of anoxic waters (Wood et al., 2015).

Cloudina and *Namacalathus* were, however, were generalist taxa living in multiple environments across the Nama Basin. The ability of *Cloudina* and *Namacalathus* to inhabit areas of fleeting oxia could explain why these organisms were able to occupy multiple areas along the shelf, unlike *Namapoikia* which is only found at one site in a cryptic niche. *Namapoikia* is suggested to be long-lived, and so this taxon may have needed stable oxygen conditions over longer timescales (Wood et al., 2015).

This work highlights the importance of nutrient cycling as a control on the eventual ventilation of the Nama Basin at ~542 Ma, which was ultimately controlled by continental erosion. The stabilisation

of oxygenated conditions within the Nama Group allowed for the expansion of the Ediacaran communities and allowed them to inhabit deeper parts of the basin and led to the radiation of motile taxa in these areas due to the decreasing metabolic cost on the taxa. This is evident by the lack of soft-bodied, skeletal and ichnotaxa observed in sediments deposited during anoxic conditions within the Nama Group (Bowyer et al., 2020). But the redox and nutrient cycling scenario of the Nama Basin will not be universal for all Ediacaran basins. Phosphorus speciation is a local proxy used in understanding nutrient cycling. It is known from previous studies that local redox conditions vary between basins and so it is expected that nutrient cycling will also vary across these basins. The Ediacaran Yangtze Platform, S. China, in particular, which occupied a very different palaeogeographic position, records euxinic conditions which were not present during the deposition of the Nama Group (Wood et al., 2015; Cui et al., 2016; Och et al., 2016; Bowyer et al., 2020). With this in mind, multi-proxy studies involving Fe speciation, and potentially other nutrient cycling proxies, need to be undertaken on sedimentary successions from other Ediacaran basins in order to understand the regional controls of redox at this time. These data will also aid in the understanding of the controls on the distribution and ecology of Ediacaran communities.

A comparison of the data collected from these future multi-proxy studies could aid in the understanding of the variations in population densities between Ediacaran Basins. *Cloudina* and *Namacalathus* are notably abundant in the Nama Basin compared to many other basins. This could potentially be due to local redox conditions, nutrient cycling or other factors arising from the palaeocontinental position of the Kalahari craton. As mentioned in Chapter 2, there could have been a "sweet-spot" for metabolically costly modes of life, such as motile behaviours and biomineralisation, with the formation of a reef complex at Driedoornvlakte potentially caused by a combination of high nutrient content of the water column with a well-ventilated setting of the mid-ramp area. This is why integrated, multi-proxy investigations are vital in understanding the complexity of Ediacaran communities.

6.2.2 Ecology and environmental control on biomineralisation of Ediacaran calcifiers

Dichotomous branching has been noted in *Cloudina hartmannae* and *Cloudina carinata* which gives evidence of asexual reproduction (Hua et al., 2005; Cortijo et al. 2010). It has been proposed that *Cloudina* can branch both sexually and asexually, forming spherical embryos or conical tubes, respectively (Cortijo et al., 2015). The form of *Cloudina* dispersal could explain the wide geographical distribution of the taxon. However, the finding of polytomous branching within the Omkyk Member of the Nama Group (Chapter 3) shows a different form of branching, with external budding, unlike the deep-seated branching found in the dichotomous branching examples (Hua et al., 2005; Cortijo et al., 2010). This form of branching may have aided in the formation of complex and dense cloudinomorph-supported reef structures.

The ability of *Cloudina* to form reef frameworks, evidenced by cloudinomorph attachment sites, is seen across the Zaris Subbasin, so suggesting that biomineralisation is an important ecological habit (Penny et al., 2014; Shore et al., 2020). These reef frameworks also have a *Namacalathus* component (Shore et al., 2020). It is unknown as to why the formation of reef structures were beneficial to *Cloudina*. Predation, greater feeding efficiency, stabilisation or the utilisation of substrates are all potential factors that may have influenced reef formation and these may also control the large range sinuosity found in *Cloudina* and other ecophenotypic responses. With the discovery of potential *Cloudina* reefs within the Ibor Group, Spain, (Álvaro et al., 2019) it would be beneficial to compare the characteristics of the two reefs, in terms of geometry and distribution of the biomineralising fauna. It would also be interesting to determine if attachment structures are present between *Cloudina* of the Ibor Group, as this could give further insight into the environmental conditions needed for such structures, and whether these structures were in fact under biological control. If *Cloudina*-reef frameworks are present in multiple basins could imply that these organisms may have had some effect on the global carbon cycle and played a major part as ecosystem engineers on a larger scale (Wood and Curtis, 2015).

It had long been thought that *Cloudina* was one of the first metazoan biomineralisers, but this was debated recently as it was suggested that the *Cloudina* skeleton was actually formed during diagenesis (Yang et al., 2020). However, findings from this thesis suggest that these organisms had

mineralised laminae from which other *Cloudina*-associated cements could nucleate. Even though this mineralisation occurred early on, and may have been of biological origin, it was environmentally controlled. This control might offer further insight into the causes or triggers behind the appearance of biomineralisation during this time but the biomineralisation toolkit needed to have been present for this to occur in multiple, unrelated, taxa (Murdock and Donoghue, 2011; Murdock, 2020).

Insights from biomineralisation can be useful in determining affinity for calcifying Ediacaran taxa. *Namapoikia*, for example, had an organic matrix which underwent rapid thickening that calcified through time, and so older areas of the skeleton show greater calcification (Wood and Penny, 2016). This form of biomineralisation is comparable to that of the sphinctozoan-grade sponge *Valeletia* (Germer et al., 2015).

Methods such as electron backscatter diffraction and secondary electron imaging of well-preserved *Cloudina* skeletons, and potentially other Ediacaran calcifiers, should be used in order to fully understand the microstructures of taxa and infer which parts of the skeleton formation were under biological versus environmental control by analysing the orientation of the original crystals.

6.2.3 New Lagerstätte within the Omkyk Member

The findings of soft tissue preservation within the carbonate Omkyk Member of the Nama Group indicates a new type of Lagerstätte that allows for the preservation of features not previously seen in Ediacaran biomineralising taxa. In this inner-ramp setting, the early precipitation of calcite cements and pyrite has allowed for exceptional preservation. This setting was sulphate-reducing with high concentrations of highly reactive iron and a low availability of organic carbon, which is a feature across the whole of the Nama Basin. These conditions must have been present during early diagenesis allowing for pyrite precipitation, as precipitation of pyrite can occur within hours on organic matter under such prime conditions (Butterfield, 2003; Rickard, 2019).

Further work needs to be carried out on specimens collected from Ediacaran Lagerstätte to identify new soft tissue features that may offer further insight into the preservation and the affinity of

taxa from this time. *Cloudina* preserved in a similar manner to *Namacalathus* are present on the float sample described in Chapter 5. It would be particularly helpful to excavate the horizon from which the float sample derived as the *Namacalathus* appear to be in life position with evidence of microbial mat attachment, and so potentially offering surfaces with extensive, preservation of *in-situ* individuals. Such surfaces would offer an unprecedented insight into the ecological dynamics of these carbonate-hosted, Ediacaran skeletal metazoan communities.

6.2.4 Affinity and deepening the roots of the Cambrian Explosion

The findings of this thesis highlight the possible presence of both cnidarians and lophotrochozoans in the Ediacaran in the Nama Group, and supports previous molecular clock data for an Ediacaran origin of these groups (Cunningham et al., 2017).

There has been much debate as to what caused the change in biota at the Ediacaran-Cambrian boundary. This change could signify a transition or replacement by Cambrian taxa from soft-bodied and skeletal Ediacaran biota, a taphonomic bias, or mass extinction (Laflamme et al., 2013; Darroch et al., 2015; Geyer and Landing, 2017; Muscente et al., 2017). Yet, there appears to be growing evidence of Ediacaran taxa transitioning into the Cambrian as well as characteristics which are usually attributed to organisms of the Cambrian, such as motile behaviours and grazing patterns, now found in Ediacaran specimens (Buatois, 2018; Chen et al., 2019; Wood et al., 2019). The transition of biota, rather than replacement, across the boundary is becoming a more prominent hypothesis as better preserved Ediacaran metazoan specimens are being discovered.

However, further work needs to be undertaken in order to understand this change. A full grasp of the affinities of the Ediacaran biota will aid in the understanding of this transition through observations of preserved soft-tissue, 3D modelling, and other techniques presented in this thesis.

References

ADAMS, E. W., GROTZINGER, J. P., WATTERS, W. A., SCHRODER, S., MCCORMICK, D. S. & AL-SIYABI, H. A. 2005. Digital characterization of thrombolite-stromatolite reef distribution in a carbonate ramp system (terminal Proterozoic, Nama Group, Namibia). *AAPG bulletin,* 89**,** 1293-1318.

ADAMS, E. W., SCHRÖDER, S., GROTZINGER, J. P. & MCCORMICK, D. S. 2004. Digital reconstruction and stratigraphic evolution of a microbial-dominated, isolated carbonate platform (terminal Proterozoic, Nama Group, Namibia). *Journal of Sedimentary Research,* 74**,** 479-497.

ALCOTT, L. J., MILLS, B. J. & POULTON, S. W. 2019. Stepwise Earth oxygenation is an inherent property of global biogeochemical cycling. *Science,* 366**,** 1333-1337.

ALGEO, T. J. & INGALL, E. 2007. Sedimentary Corg: P ratios, paleocean ventilation, and Phanerozoic atmospheric pO2. *Palaeogeography, Palaeoclimatology, Palaeoecology,* 256**,** 130-155.

ÁLVARO, J. J., CORTIJO, I., JENSEN, S., MUS, M. M. & PALACIOS, T. 2020. *Cloudina*-microbial reef resilience to substrate instability in a Cadomian retro-arc basin of the Iberian Peninsula. *Precambrian Research,* 336**,** 105479.

AMTHOR, J. E., GROTZINGER, J. P., SCHRODER, S., BOWRING, S. A., RAMEZANI, J., MARTIN, M. W. & MATTER, A. 2003. Extinction of *Cloudina* and *Namacalathus* at the Precambrian-Cambrian boundary in Oman. *Geology,* 31**,** 431-434.

ANDERSON, L., DELANEY, M. & FAUL, K. 2001. Carbon to phosphorus ratios in sediments: Implications for nutrient cycling. *Global Biogeochemical Cycles,* 15**,** 65-79.

ANTCLIFFE, J. B., CALLOW, R. H. & BRASIER, M. D. 2014. Giving the early fossil record of sponges a squeeze. *Biological Reviews,* 89**,** 972-1004.

ARMSTRONG, H. A. & BRASIER, M. D. 2005. *Microfossils, 2d ed. Blackwell, Malden, MA (2005).* Blackwell, Malden, MA

BAGAEVA, T. S., KUPAEVA, D. M., VETROVA, A. A., KOSEVICH, I. A., KRAUS, Y. A. & KREMNYOV, S. V. 2019. cWnt signaling modulation results in a change of the colony architecture in a hydrozoan. *Developmental Biology,* 456**,** 145-153.

BAILEY, J.V., JOYE, S.B., KALANETRA, K.M., FLOOD, B.E. & CORSETTI, F.A., 2007. Evidence of giant sulphur bacteria in Neoproterozoic phosphorites. *Nature*, 445, 198-201.

BALINSKI, A. & SUN, Y., 2015. Fenxiang biota: a new Early Ordovician shallow-water fauna with soft-part preservation from China. *Science bulletin*, 60, 812-818.

BARRÓN-DÍAZ, A.J., PAZ-MORENO, F.A., LOZANO-SANTA CRUZ, R., HERRERA-URBINA, S., CENTENO-GARCÍA, E. & LÓPEZ-MARTÍNEZ, M., 2019. Early Cambrian alkaline volcanism on the southern margin of Laurentia: Evidence in the volcaniclastic units from the Puerto Blanco Formation in the Caborca block, NW Mexico. *International Geology Review*, *61*(10), pp.1189-1206.

BECKER-KERBER, B., PACHECO, M. L. A. F., RUDNITZKI, I. D., GALANTE, D., RODRIGUES, F. & DE MORAES LEME, J. 2017. Ecological interactions in *Cloudina* from the Ediacaran of Brazil: implications for the rise of animal biomineralization. *Scientific Reports,* 7**,** 1-11.

BENGTSON, S. 2004. Early skeletal fossils. *Paleontological Society Papers,* 10**,** 67.

BENGTSON, S. & ZHAO, Y. 1992. Predatorial borings in late Precambrian mineralized exoskeletons. *Science,* 257**,** 367-369.

BERKNER, L. V. & MARSHALL, L. C. 1965. On the Origin and Rise of Oxygen Concentration in the Earth's Atmosphere. *Journal of the Atmospheric Science*.

BERNER, R. 1990. Diagenesis of phosphorus in sediments from non-upwelling areas. *Phosphate Deposits of the World Volume 3: Neogene to Modern Phosphorites.* Cambridge University Press.

BERNER, R. A. 1973. Phosphate removal from sea water by adsorption on volcanogenic ferric oxides. *Earth and Planetary Science Letters,* 18**,** 77-86.

BEURLEN, K. & SOMMER, F. W. 1957. *Observações estratigráficas e paleontológicas sôbre o calcário Corumbá*, DNPM.

BICKNELL, R. D. & PATERSON, J. R. 2018. Reappraising the early evidence of durophagy and drilling predation in the fossil record: implications for escalation and the Cambrian Explosion. *Biological Reviews,* 93**,** 754-784.

BOAG, T. H., DARROCH, S. A. & LAFLAMME, M. 2016. Ediacaran distributions in space and time: testing assemblage concepts of earliest macroscopic body fossils. *Palaeobiology,* 42**,** 574-594.

BORISANOVA, A. 2016. A new species of solitary Entoprocta, *Loxosomella angusta* sp. n., from the White Sea. *Invertebrate Zoology,* 13**,** 43-50.

BOSENCE, D. 1973. Recent serpulid reefs, Connemara, Eire. *Nature,* 242**,** 40-41.

BOTTING, J. P., MUIR, L. A., SUTTON, M. D. & BARNIE, T. 2011. Welsh gold: A new exceptionally preserved pyritized Ordovician biota. *Geology,* 39**,** 879-882.

BOTTJER, D. J. 2010. The Cambrian substrate revolution and early evolution of the phyla. *Journal of Earth Science,* 21**,** 21-24.

BOUOUGRI, E. H., PORADA, H., WEBER, K. & REITNER, J. 2011. Sedimentology and palaeoecology of Ernietta-bearing Ediacaran deposits in southern Namibia: implications for infaunal vendobiont communities. *Advances in stromatolite geobiology.* Springer.

BOWRING, S. A., GROTZINGER, J. P., CONDON, D. J., RAMEZANI, J., NEWALL, M. J. & ALLEN, P. A. 2007. Geochronologic constraints on the chronostratigraphic framework of the Neoproterozoic Huqf Supergroup, Sultanate of Oman. *American Journal of Science,* 307**,** 1097-1145.

BOWYER, F., SHORE, A., WOOD, R., ALCOTT, L., THOMAS, A., BUTLER, I., CURTIS, A., HAINANAN, S., CURTIS-WALCOTT, S. & PENNY, A. 2020. Regional nutrient decrease drove redox stabilisation and metazoan diversification in the late Ediacaran Nama Group, Namibia. *Scientific Reports,* 10**,** 1-11.

BOWYER, F., WOOD, R. & POULTON, S. 2017. Controls on the evolution of Ediacaran metazoan ecosystems: a redox perspective. *Geobiology,* 15**,** 516-551.

BRAIN, C. K. 2001. Some observations on Cloudina, a terminal Proterozoic index fossil from Namibia. *Journal of African Earth Sciences,* 33**,** 475-480.

BRASIER, M., COWIE, J. & TAYLOR, M. 1994. Decision on the Precambrian-Cambrian boundary stratotype. *Episodes Journal of International Geoscience,* 17**,** 3-8.

BRENNAN, S. T., LOWENSTEIN, T. K. & HORITA, J. 2004. Seawater chemistry and the advent of biocalcification. *Geology,* 32**,** 473-476.

BRISTOW, T. F. & KENNEDY, M. J. 2008. Carbon isotope excursions and the oxidant budget of the Ediacaran atmosphere and ocean. *Geology,* 36**,** 863-866.

BUATOIS, L.A., ALMOND, J., MÁNGANO, M.G., JENSEN, S. AND GERMS, G.J., 2018. Sediment disturbance by Ediacaran bulldozers and the roots of the Cambrian explosion. *Scientific reports*, *8*(1), 1-9.

BURNS, S. & MATTER, A. 1993. Carbon isotopic record of the latest Proterozoic from Oman. *Eclogae Geologicae Halvertiae,* 86**,** 595-607.

BUTTERFIELD, N. J. 2003. Exceptional fossil preservation and the Cambrian explosion. *Integrative and comparative biology,* 43**,** 166-177.

CAI, Y., HUA, H., SCHIFFBAUER, J. D., SUN, B. & YUAN, X. 2014. Tube growth patterns and microbial mat-related lifestyles in the Ediacaran fossil Cloudina, Gaojiashan Lagerstätte, South China. *Gondwana Research,* 25**,** 1008-1018.

CANFIELD, D. E., KNOLL, A. H., POULTON, S. W., NARBONNE, G. M., & DUNNING, G. R. (2020). Carbon isotopes in clastic rocks and the Neoproterozoic carbon cycle. *American Journal of Science*, *320*(2), 97-124.

CANFIELD, D. E., POULTON, S. W., KNOLL, A. H., NARBONNE, G. M., ROSS, G., GOLDBERG, T. & STRAUSS, H. 2008. Ferruginous conditions dominated later Neoproterozoic deep-water chemistry. *Science,* 321**,** 949-952.

CANFIELD, D. E., POULTON, S. W. & NARBONNE, G. M. 2007. Late-Neoproterozoic deep-ocean oxygenation and the rise of animal life. *Science,* 315**,** 92-95.

CAO, M., DAINES, S. J., LENTON, T. M., CUI, H., ALGEO, T. J., DAHL, T. W., SHI, W., CHEN, Z.-Q., ANBAR, A. & ZHOU, Y.-Q. 2020. Comparison of Ediacaran platform and slope δ238U records in South China: Implications for global-ocean oxygenation and the origin of the Shuram Excursion. *Geochimica et Cosmochimica Acta,* 287**,** 111-124.

CHEN, Z., BENGTSON, S., ZHOU, C. M., HUA, H. & YUE, Z. 2008. Tube structure and original composition of Sinotubulites: shelly fossils from the late Neoproterozoic in southern Shaanxi, China. *Lethaia,* 41**,** 37-45.

CHEN, Z., ZHOU, C., MEYER, M., XIANG, K., SCHIFFBAUER, J. D., YUAN, X. & XIAO, S. 2013. Trace fossil evidence for Ediacaran bilaterian animals with complex behaviors. *Precambrian Research,* 224**,** 690-701.

CHEN, Z., ZHOU, C., XIAO, S., WANG, W., GUAN, C., HUA, H. & YUAN, X. 2014. New Ediacara fossils preserved in marine limestone and their ecological implications. *Scientific Reports,* 4**,** 4180.

CHEN, Z., ZHOU, C., YUAN, X. & XIAO, S. 2019. Death march of a segmented and trilobate bilaterian elucidates early animal evolution. *Nature,* 573**,** 412-415.

COHEN, P. A., SCHOPF, J. W., BUTTERFIELD, N. J., KUDRYAVTSEV, A. B. & MACDONALD, F. A. 2011. Phosphate biomineralization in mid-Neoproterozoic protists. *Geology,* 39**,** 539-542.

COLMAN, A. S. & HOLLAND, H. D. 2000. The global diagenetic flux of phosphorus from marine sediments to the oceans: redox sensitivity and the control of atmospheric oxygen levels. *Marine Authigenesis: From global to microbial***,** 53–77.

CONDON, D., ZHU, M. Y., BOWRING, S., WANG, W., YANG, A. H. & JIN, Y. G. 2005. U-Pb ages from the neoproterozoic Doushantuo Formation, China. *Science,* 308**,** 95-98.

CORONADO, I., PÉREZ-HUERTA, A. & RODRÍGUEZ, S. 2013. Primary biogenic skeletal structures in *Multithecopora* (Tabulata, Pennsylvanian). *Palaeogeography, Palaeoclimatology, Palaeoecology,* 386**,** 286-299.

CORSETTI, F. A. & HAGADORN, J. W. 2000. Precambrian-Cambrian transition: Death Valley, United States. *Geology,* 28**,** 299-302.

CORTIJO, I., CAI, Y., HUA, H., SCHIFFBAUER, J. D. & XIAO, S. 2015. Life history and autecology of an Ediacaran index fossil: Development and dispersal of *Cloudina*. *Gondwana Research,* 28**,** 419-424.

CORTIJO, I., MUS, M. M., JENSEN, S. & PALACIOS, T. 2010. A new species of *Cloudina* from the terminal Ediacaran of Spain. *Precambrian Research,* 176**,** 1-10.

COUSO, J. P. 2009. Segmentation, metamerism and the Cambrian explosion. *International Journal of Developmental Biology,* 53**,** 1305-1316.

CRIMES, T. & FEDONKIN, M. 1996. Biotic changes in platform communities across the Precambrian Phanerozoic boundary. *Rivista Italiana di Paleontologia e Stratigrafia* 102.

CRIMES, T. P. & GERMS, G. J. 1982. Trace fossils from the Nama Group (Precambrian-Cambrian) of Southwest Africa (Namibia). *Journal of Paleontology***,** 890-907.

CUI, H., KAUFMAN, A. J., XIAO, S., PEEK, S., CAO, H., MIN, X., CAI, Y., SIEGEL, Z., LIU, X. M. & PENG, Y. 2016. Environmental context for the terminal Ediacaran biomineralization of animals. *Geobiology,* 14**,** 344-363.

CUI, H., KAUFMAN, A. J., XIAO, S., ZHOU, C. & LIU, X.-M. 2017. Was the Ediacaran Shuram Excursion a globally synchronized early diagenetic event? Insights from methane-derived authigenic carbonates in the uppermost Doushantuo Formation, South China. *Chemical Geology,* 450**,** 59-80.

CUNNINGHAM, J. A., LIU, A. G., BENGTSON, S. & DONOGHUE, P. C. 2017. The origin of animals: can molecular clocks and the fossil record be reconciled? *BioEssays,* 39**,** 1-12.

DARROCH, S. A., CRIBB, A. T., BUATOIS, L. A., GERMS, G. J., KENCHINGTON, C. G., SMITH, E. F., MOCKE, H., O'NEIL, G. R., SCHIFFBAUER, J. D. & MALONEY, K. M.

2020. The trace fossil record of the Nama Group, Namibia: Exploring the terminal Ediacaran roots of the Cambrian explosion. *Earth-Science Reviews***,** 103435.

DARROCH, S. A., SMITH, E. F., LAFLAMME, M. & ERWIN, D. H. 2018. Ediacaran extinction and Cambrian explosion. *Trends in ecology evolution,* 33**,** 653-663.

DARROCH, S. A., SPERLING, E. A., BOAG, T. H., RACICOT, R. A., MASON, S. J., MORGAN, A. S., TWEEDT, S., MYROW, P., JOHNSTON, D. T. & ERWIN, D. H. 2015. Biotic replacement and mass extinction of the Ediacara biota. *Proceedings of the Royal Society B: Biological Sciences* 282**,** 20151003.

DEBRENNE, F. & ZHURAVLEV, A. Y. 1997. Cambrian food web: a brief review. *Geobios,* 30**,** 81-188.

DERRY, L. A. 2010. A burial diagenesis origin for the Ediacaran Shuram–Wonoka carbon isotope anomaly. *Earth and Planetary Science Letters* 294**,** 152-162.

DICKENS, G. R., O'NEIL, J. R., REA, D. K. & OWEN, R. M. 1995. Dissociation of oceanic methane hydrate as a cause of the carbon isotope excursion at the end of the Paleocene. *Paleoceanography,* 10**,** 965-971.

DROSER, M. L. & GEHLING, J. G. 2015. The advent of animals: the view from the Ediacaran. *Proceedings of the National Academy of Sciences,* 112**,** 4865-4870.

DROSER, M. L., GEHLING, J. G. & JENSEN, S. R. 1999. When the worm turned: Concordance of Early Cambrian ichnofabric and trace-fossil record in siliciclastic rocks of South Australia. *Geology,* 27**,** 625-628.

EGGER, M., JILBERT, T., BEHRENDS, T., RIVARD, C. & SLOMP, C. P. 2015. Vivianite is a major sink for phosphorus in methanogenic coastal surface sediments. *Geochimica et Cosmochimica Acta,* 169**,** 217-235.

ENMAR, R., STEIN, M., BAR-MATTHEWS, M., SASS, E., KATZ, A. & LAZAR, B. 2000. Diagenesis in live corals from the Gulf of Aqaba. I. The effect on paleo-oceanography tracers. *Geochimica et Cosmochimica Acta* 64**,** 3123-3132.

EVANS, S. D., HUGHES, I. V., GEHLING, J. G. & DROSER, M. L. 2020. Discovery of the oldest bilaterian from the Ediacaran of South Australia. *Proceedings of the National Academy of Sciences of the United States of America,* 117**,** 7845-7850.

FAIRCHILD, I. J., SPENCER, A. M., ALI, D. O., ANDERSON, R. P., ANDERTON, R., BOOMER, I., DOVE, D., EVANS, J. D., HAMBREY, M. J. & HOWE, J. 2018. Tonian-Cryogenian boundary sections of Argyll, Scotland. *Precambrian Research,* 319**,** 37-64.

FAUL, K. L., PAYTAN, A. & DELANEY, M. L. 2005. Phosphorus distribution in sinking oceanic particulate matter. *Marine Chemistry,* 97**,** 307-333.

FEDONKIN, M. A., SIMONETTA, A. & IVANTSOV, A. Y. 2007. New data on *Kimberella*, the Vendian mollusc-like organism (White Sea region, Russia): palaeoecological and evolutionary implications. *Geological Society, London, Special Publications,* 286**,** 157-179.

FENG, W. M., CHEN, Z. & SUN, W. G. 2003. Diversification of skeletal microstructures of organisms through the interval from the latest Precambrian to the Early Cambrian. *Science in China Series D-Earth Sciences,* 46**,** 977-985.

FIKE, D., GROTZINGER, J., PRATT, L. & SUMMONS, R. 2006. Oxidation of the Ediacaran ocean. *Nature,* 444**,** 744-747.

FILIPPELLI, G. M. 2008. The global phosphorus cycle: past, present, and future. *Elements,* 4(2), 89-95.

FILIPPELLI, G. M. & DELANEY, M. L. 1996. Phosphorus geochemistry of equatorial Pacific sediments. *Geochimica et Cosmochimica Acta,* 60**,** 1479-1495.

FRANKEL, R. B. & BAZYLINSKI, D. A. 2003. Biologically induced mineralization by bacteria. *In:* DOVE, P. M., DEYOREO, J. J. & WEINER, S. (eds.) *Biomineralization.* Chantilly: Mineralogical Soc Amer & Geochemical Soc.

FROELICH, P., BENDER, M., LUEDTKE, N., HEATH, G. & DEVRIES, T. 1982. The marine phosphorus cycle. *American Journal of Science,* 282**,** 474-511.

GARBELLI, C. 2017. Shell microstructures in Lopingian brachiopods: Implications for fabric evolution and calcification. *Rivista Italiana di Paleontologia e Stratigrafia,* 123.

GAUCHER, C., FRIMMEL, H. E. & GERMS, G. J. 2009. Tectonic events and palaeogeographic evolution of southwestern Gondwana in the Neoproterozoic and Cambrian. *Developments in Precambrian Geology,* 16**,** 295-316.

GEHLING, J. G. & DROSER, M. L. 2009. Textured organic surfaces associated with the Ediacara biota in South Australia. *Earth-Science Reviews,* 96**,** 196-206.

GERMER, J., MANN, K., WÖRHEIDE, G. & JACKSON, D. J. 2015. The Skeleton Forming Proteome of an Early Branching Metazoan: A Molecular Survey of the Biomineralization Components Employed by the Coralline Sponge Vaceletia Sp. *PloS one,* 10**,** e0140100.

GERMS, G. 1983. Implications of a sedimentary facies and depositional environmental analysis of the Nama Group in South West Africa/Namibia. *Special Publications of the Geological Society of South Africa,* 11**,** 89–114.

GERMS, G. & GAUCHER, C. 2012. Nature and extent of a late Ediacaran (ca. 547 Ma) glacigenic erosion surface in southern Africa. *South African Journal of Geology,* 115**,** 91-102.

GERMS, G. & GRESSE, P. 1991. The foreland basin of the Damara and Gariep orogens in Namaqualand and southern Namibia: stratigraphic correlations and basin dynamics. *South African Journal of Geology,* 94**,** 159-169.

GERMS, G. J. 1972. New shelly fossils from Nama Group, south west Africa. *American Journal of Science,* 272**,** 752-761.

GERMS, G. J. 1973. A reinterpretation of *Rangea schneiderhoehni* and the discovery of a related new fossil from the Nama Group, South West Africa. *Lethaia,* 6**,** 1-9.

GEYER, G. AND LANDING, E., 2017. The Precambrian–Phanerozoic and Ediacaran–Cambrian boundaries: a historical approach to a dilemma. *Geological Society, London, Special Publications*, *448*(1), 311-349.

GILBERT, P., PORTER, S. M., SUN, C.-Y., XIAO, S., GIBSON, B. M., SHENKAR, N. & KNOLL, A. H. 2019. Biomineralization by particle attachment in early animals. *Proceedings of the National Academy of Sciences* 116**,** 17659-17665.

GRANT, S. 1990. Shell structure and distribution of *Cloudina*, a potential index fossil for the terminal Proterozoic. *American Journal of Science,* 290**,** 261-294.

GRAZHDANKIN, D. 2014. Patterns of evolution of the Ediacaran soft-bodied biota. *Journal of Paleontology,* 88**,** 269-283.

GRAZHDANKIN, D., KONTOROVICH, A., KONTOROVICH, V., SARAEV, S., FILIPPOV, Y. F., EFIMOV, A., KARLOVA, G., KOCHNEV, B., NAGOVITSIN, K. & TERLEEV, A. 2015. Vendian of the Fore-Yenisei sedimentary basin (southeastern West Siberia). *Russian Geology Geophysics,* 56**,** 560-572.

GROTZINGER, J., ADAMS, E. & SCHRODER, S. 2005. Microbial–metazoan reefs of the terminal Proterozoic Nama Group (c. 550–543 Ma), Namibia. *Geological Magazine,* 142**,** 499-517.

GROTZINGER, J. & MILLER, R. 2008. The Nama Group. *The geology of Namibia, Geological Society of Namibia,* 2**,** 13229-13272.

GROTZINGER, J. P., BOWRING, S. A., SAYLOR, B. Z. & KAUFMAN, A. J. 1995. Biostratigraphic and geochronologic constraints on early animal evolution. *Science,* 270**,** 598-604.

GROTZINGER, J. P., FIKE, D. A. & FISCHER, W. W. 2011. Enigmatic origin of the largest-known carbon isotope excursion in Earth's history. *Nature Geoscience,* 4**,** 285-292.

GROTZINGER, J. P., WATTERS, W. A. & KNOLL, A. H. 2000. Calcified metazoans in thrombolite-stromatolite reefs of the terminal Proterozoic Nama Group, Namibia. *Palaeobiology,* 26**,** 334-359.

HALL, M., KAUFMAN, A. J., VICKERS-RICH, P., IVANTSOV, A., TRUSLER, P., LINNEMANN, U., HOFMANN, M., ELLIOTT, D., CUI, H. & FEDONKIN, M. 2013. Stratigraphy, palaeontology and geochemistry of the late Neoproterozoic Aar Member, southwest Namibia: Reflecting environmental controls on Ediacara fossil preservation during the terminal Proterozoic in African Gondwana. *Precambrian Research,* 238**,** 214-232.

HAMMARLUND, E. U. 2020. Harnessing hypoxia as an evolutionary driver of complex multicellularity. *Interface Focus,* 10.

HAN, J., CAI, Y., SCHIFFBAUER, J. D., HUA, H., WANG, X., YANG, X., UESUGI, K., KOMIYA, T. & SUN, J. 2017. A *Cloudina*-like fossil with evidence of asexual reproduction from the lowest Cambrian, South China. *Geological Magazine,* 154**,** 1294-1305.

HODGIN, E.B., NELSON, L.L., WALL, C.J., BARRÓN-DÍAZ, A.J., WEBB, L.C., SCHMITZ, M.D., FIKE, D.A., HAGADORN, J.W. & SMITH, E.F., 2021. A link between rift-related volcanism and end-Ediacaran extinction? Integrated chemostratigraphy, biostratigraphy, and U-Pb geochronology from Sonora, Mexico. *Geology*, *49*(2), 115-119.

HOFFMAN, P. F., KAUFMAN, A. J., HALVERSON, G. P. & SCHRAG, D. P. 1998. A Neoproterozoic snowball earth. *Science,* 281**,** 1342-1346.

HOFMANN, H. J. & MOUNTJOY, E. W. 2001. *Namacalathus-Cloudina* assemblage in Neoproterozoic Miette Group (Byng Formation), British Columbia: Canada's oldest shelly fossils. *Geology,* 29**,** 1091-1094.

HOOPER, J. N. & VAN SOEST, R. W. 2002. Systema Porifera. A guide to the classification of sponges. *Systema Porifera.* Springer.

HUA, H., CHEN, Z., YUAN, X., ZHANG, L. & XIAO, S. 2005. Skeletogenesis and asexual reproduction in the earliest biomineralizing animal *Cloudina*. *Geology,* 33**,** 277-280.

HUA, H., PRATT, B. R. & ZHANG, L. Y. 2003. Borings in *Cloudina* shells: Complex predator-prey dynamics in the terminal neoproterozoic. *Palaios,* 18**,** 454-459.

HULDTGREN, T., CUNNINGHAM, J.A., YIN, C., STAMPANONI, M., MARONE, F., DONOGHUE, P.C. & BENGTSON, S., 2011. Fossilized nuclei and germination structures identify Ediacaran "animal embryos" as encysting protists. *Science*, 334, 1696-1699.

HUSSON, J. M., LINZMEIER, B. J., KITAJIMA, K., ISHIDA, A., MALOOF, A. C., SCHOENE, B., PETERS, S. E. & VALLEY, J. W. 2020. Large isotopic variability at the micron-scale in 'Shuram'excursion carbonates from South Australia. *Earth Planetary Science Letters* 538**,** 116211.

INGALL, E. & JAHNKE, R. 1994. Evidence for enhanced phosphorus regeneration from marine sediments overlain by oxygen depleted waters. *Geochemica et Cosmochimica Acta,* 58**,** 2571-2575.

INGALL, E. D., BUSTIN, R. & VAN CAPPELLEN, P. 1993. Influence of water column anoxia on the burial and preservation of carbon and phosphorus in marine shales. *Geochimica et Cosmochimica Acta,* 57**,** 303-316.

INGALL, E. D. & VAN CAPPELLEN, P. 1990. Relation between sedimentation rate and burial of organic phosphorus and organic carbon in marine sediments. *Geochimica et Cosmochimica Acta,* 54**,** 373-386.

JACKSON, D. J., MACIS, L., REITNER, J., DEGNAN, B. M. & WÖRHEIDE, G. 2007. Sponge paleogenomics reveals an ancient role for carbonic anhydrase in skeletogenesis. *Science,* 316**,** 1893-1895.

JAKUBOWICZ, M., BERKOWSKI, B., CORREA, M. L., JAROCHOWSKA, E., JOACHIMSKI, M. & BELKA, Z. 2015. Stable isotope signatures of middle Palaeozoic ahermatypic rugose corals–deciphering secondary alteration, vital fractionation effects, and palaeoecological implications. *PloS ONE* 10.

JENSEN, S. 2003. The Proterozoic and earliest Cambrian trace fossil record; patterns, problems and perspectives. *Integrative Comparative Biology* 43**,** 219-228.

JENSEN, S. & RUNNEGAR, B. 2005. A complex trace fossil from the Spitskop Member (terminal Ediacaran–? Lower Cambrian) of southern Namibia. *Geological Magazine,* 142**,** 561-569.

JENSEN, S. R., SAYLOR, B. Z., GEHLING, J. G. & GERMS, G. J. 2000. Complex trace fossils from the terminal Proterozoic of Namibia. *Geology,* 28**,** 143-146.

JILBERT, T., SLOMP, C., GUSTAFSSON, B. G. & BOER, W. 2011. Beyond the Fe-P-redox connection: preferential regeneration of phosphorus from organic matter as a key control on Baltic Sea nutrient cycles. *Biogeosciences,* 8**,** 1699-1722.

JOHNSON, J. & GROTZINGER, J. 2006. Affect of sedimentation on stromatolite reef growth and morphology, Ediacaran Omkyk Member (Nama Group), Namibia. *South African Journal of Geology* 109**,** 87-96.

JONES, C., NOMOSATRYO, S., CROWE, S. A., BJERRUM, C. J. & CANFIELD, D. E. 2015. Iron oxides, divalent cations, silica, and the early earth phosphorus crisis. *Geology* 43**,** 135-138.

KAUFMAN, A. J., HAYES, J., KNOLL, A. H. & GERMS, G. J. 1991. Isotopic compositions of carbonates and organic carbon from upper Proterozoic successions in Namibia: stratigraphic variation and the effects of diagenesis and metamorphism. *Precambrian Research,* 49**,** 301-327.

KIMMIG, J., STROTZ, L. C. & LIEBERMAN, B. S. 2017. The stalked filter feeder *Siphusauctum lloydguntheri* n. sp. from the middle Cambrian (Series 3, Stage 5) Spence Shale of Utah: its biological affinities and taphonomy. *Journal of Paleontology,* 91**,** 902-910.

KIMURA, H. & WATANABE, Y., 2001. Oceanic anoxia at the Precambrian-Cambrian boundary. *Geology,* 29, .995-998.

KNOLL, A. H. 1992. The early evolution of eukaryotes: a geological perspective. *Science,* 256**,** 622-627.

KNOLL, A. H. 2003. Biomineralization and evolutionary history. *Reviews in Mineralogy and Geochemistry,* 54**,** 329-356.

KNOLL, A. H. & CARROLL, S. B. 1999. Early animal evolution: emerging views from comparative biology and geology. *Science,* 284**,** 2129-2137.

KNOLL, A. H. & SPERLING, E. A. 2014. Oxygen and animals in Earth history. *Proceedings of the National Academy of Sciences,* 111**,** 3907-3908.

KOUCHINSKY, A., HOLMER, L. E., STEINER, M. & USHATINSKAYA, G. T. 2014. The new stem-group brachiopod *Oymurania* from the lower Cambrian of Siberia. *Acta Palaeontologica Polonica,* 60**,** 963-980.

KOWALEWSKI, M. & KELLEY, P. 2002. The fossil record of predation: an overview of analytical methods. *Paleontological Society Papers,* 8**,** 3-42.

KRAAL, P. & SLOMP, C. P. 2014. Rapid and extensive alteration of phosphorus speciation during oxic storage of wet sediment samples. *PLoS One,* 9**,** e96859.

LAFLAMME, M., DARROCH, S. A., TWEEDT, S. M., PETERSON, K. J. & ERWIN, D. H. 2013. The end of the Ediacara biota: Extinction, biotic replacement, or Cheshire Cat? *Gondwana Research,* 23**,** 558-573.

LANDING, E. 1994. Precambrian-Cambrian boundary global stratotype ratified and a new perspective of Cambrian time. *Geology,* 22**,** 179-182.

LENTON, T. M. & WATSON, A. J. 2000. Redfield revisited: 1. Regulation of nitrate, phosphate, and oxygen in the ocean. *Global biogeochemical cycles,* 14**,** 225-248.

LI, Z., CAO, M., LOYD, S. J., ALGEO, T. J., ZHAO, H., WANG, X., ZHAO, L. & CHEN, Z.-Q. 2020. Transient and stepwise ocean oxygenation during the late Ediacaran Shuram Excursion: Insights from carbonate δ238U of northwestern Mexico. *Precambrian Research,* 344**,** 105741.

LINNEMANN, U., OVTCHAROVA, M., SCHALTEGGER, U., GÄRTNER, A., HAUTMANN, M., GEYER, G., VICKERS-RICH, P., RICH, T., PLESSEN, B. & HOFMANN, M. 2019. New high-resolution age data from the Ediacaran–Cambrian boundary indicate rapid, ecologically driven onset of the Cambrian explosion. *Terra Nova,* 31**,** 49-58.

LIU, A. G. & TINDAL, B. H. 2020. Ediacaran macrofossils prior to the~ 580 Ma Gaskiers glaciation in Newfoundland, Canada. *Lethaia*.

LIVINGSTON, B., KILLIAN, C., WILT, F., CAMERON, A., LANDRUM, M., ERMOLAEVA, O., SAPOJNIKOV, V., MAGLOTT, D., BUCHANAN, A. & ETTENSOHN, C. 2006. A genome-wide analysis of biomineralization-related proteins in the sea urchin *Strongylocentrotus purpuratus*. *Developmental biology,* 300**,** 335-348.

LOWENSTAM, H. A. 1981. Minerals formed by organisms. *Science***,** 1126-1131.

LOWENSTAM, H. A. & WEINER, S. 1989. On Biomineralization. *Oxford University Press***,** 1126-1131.

LU, M., ZHU, M., ZHANG, J., SHIELDS-ZHOU, G., LI, G., ZHAO, F., ZHAO, X. & ZHAO, M. 2013. The DOUNCE event at the top of the Ediacaran Doushantuo Formation, South China: Broad stratigraphic occurrence and non-diagenetic origin. *Precambrian Research,* 225**,** 86-109.

MACDONALD, F. A., PRUSS, S. B. & STRAUSS, J. V. 2014. Trace Fossils with Spreiten from the Late Ediacaran Nama Group, Namibia: Complex Feeding Patterns Five Million Years Before The Precambrian–Cambrian BoundaryCOMPLEX EDIACARAN TRACE FOSSILS. *Journal of Paleontology,* 88**,** 299-308.

MARLÉTAZ, F., PEIJNENBURG, K. T., GOTO, T., SATOH, N. & ROKHSAR, D. S. 2019. A new spiralian phylogeny places the enigmatic arrow worms among gnathiferans. *Current Biology,* 29**,** 312-318. e3.

MARTIN, M. W., GRAZHDANKIN, D. V., BOWRING, S. A., EVANS, D. A. D., FEDONKIN, M. A. & KIRSCHVINK, J. L. 2000. Age of Neoproterozoic bilatarian body and trace fossils, White Sea, Russia: Implications for metazoan evolution. *Science,* 288**,** 841-845.

MÄRZ, C., POULTON, S. W., BECKMANN, B., KÜSTER, K., WAGNER, T. & KASTEN, S. 2008. Redox sensitivity of P cycling during marine black shale formation: dynamics of sulfidic and anoxic, non-sulfidic bottom waters. *Geochimica et Cosmochimica Acta,* 72**,** 3703-3717.

MÄRZ, C., POULTON, S. W., WAGNER, T., SCHNETGER, B. & BRUMSACK, H.-J. 2014. Phosphorus burial and diagenesis in the central Bering Sea (Bowers Ridge, IODP Site U1341): Perspectives on the marine P cycle. *Chemical Geology,* 363**,** 270-282.

MÄRZ, C., RIEDINGER, N., SENA, C. & KASTEN, S. 2018. Phosphorus dynamics around the sulphate-methane transition in continental margin sediments: Authigenic apatite and Fe (II) phosphates. *Marine Geology,* 404**,** 84-96.

MCFADDEN, K. A., HUANG, J., CHU, X., JIANG, G., KAUFMAN, A. J., ZHOU, C., YUAN, X. & XIAO, S. 2008. Pulsed oxidation and biological evolution in the Ediacaran Doushantuo Formation. *Proceedings of the National Academy of Sciences,* 105**,** 3197-3202.

MCKIRDY, D. M., BURGESS, J. M., LEMON, N. M., YU, X., COOPER, A. M., GOSTIN, V. A., JENKINS, R. J. & BOTH, R. A. 2001. A chemostratigraphic overview of the late Cryogenian interglacial sequence in the Adelaide Fold-Thrust Belt, South Australia. *Precambrian Research,* 106**,** 149-186.

MEHRA, A. & MALOOF, A. 2018. Multiscale approach reveals that Cloudina aggregates are detritus and not in situ reef constructions. *Proceedings of the National Academy of Sciences,* 115**,** E2519-E2527.

MEHRA, A., WATTERS, W. A., GROTZINGER, J. P. & MALOOF, A. C. 2020. Three-dimensional reconstructions of the putative metazoan *Namapoikia* show that it was a microbial construction. *Proceedings of the National Academy of Sciences,* 117**,** 19760-19766.

MERKEL, J., LIEB, B. & WANNINGER, A. 2015. Muscular anatomy of an entoproct creeping-type larva reveals extraordinary high complexity and potential shared characters with mollusks. *BMC evolutionary biology,* 15**,** 130.

MEYER, M., XIAO, S., GILL, B. C., SCHIFFBAUER, J. D., CHEN, Z., ZHOU, C. & YUAN, X. 2014. Interactions between Ediacaran animals and microbial mats: Insights from *Lamonte trevallis*, a new trace fossil from the Dengying Formation of South China. *Palaeogeography, Palaeoclimatology, Palaeoecology,* 396**,** 62-74.

MORRIS, S. C. 1977. A new entoproct-like organism from the Burgess Shale of British Columbia. *Palaeontology,* 20**,** 823-845.

MORRIS, S. C., MATTES, B. W. & MENGE, C. 1990. The early skeletal organism *cloudina* - new occurrences from Oman and possibly China. *American Journal of Science,* 290A**,** 245-260.

MUKAI, H., TERAKADO, K. & REED, C. 1997. Microscopic anatomy of invertebrates. *V,* 13**,** 45-206.

MURDOCK, D. J. & DONOGHUE, P. C. 2011. Evolutionary origins of animal skeletal biomineralization. *Cells Tissues Organs,* 194**,** 98-102.

MURDOCK, D. J. E. 2020. The 'biomineralization toolkit' and the origin of animal skeletons. *Biological Reviews***,** 21.

MUSCENTE, A.D., SCHIFFBAUER, J.D., BROCE, J., LAFLAMME, M., O'DONNELL, K., BOAG, T.H., MEYER, M., HAWKINS, A.D., HUNTLEY, J.W., MCNAMARA, M. AND MACKENZIE, L.A., 2017. Exceptionally preserved fossil assemblages through geologic time and space. *Gondwana Research, 48,* pp.164-188.

NARBONNE, G. M., SAYLOR, B. Z. & GROTZINGER, J. P. 1997. The youngest Ediacaran fossils from southern Africa. *The youngest Ediacaran fossils from southern Africa,* 71**,** 953-967.

NESBITT, H. & YOUNG, G. 1982. Early Proterozoic climates and plate motions inferred from major element chemistry of lutites. *Nature,* 299**,** 715-717.

NURSALL, J. R. 1959. Oxygen as a prerequisite to the origin of the metazoa. *Nature,* 183**,** 1170-1172.

O'NEIL, G. R., TACKETT, L. S. & MEYER, M. 2020. Petrographic evidence for ediacaran microbial mat-targeted behaviors from the great basin, United States. *Precambrian Research,* 345**,** 105768.

OBST, M., DYNES, J., LAWRENCE, J., SWERHONE, G., BENZERARA, K., KARUNAKARAN, C., KAZNATCHEEV, K., TYLISZCZAK, T. & HITCHCOCK, A. 2009. Precipitation of amorphous CaCO3 (aragonite-like) by cyanobacteria: a STXM study of the influence of EPS on the nucleation process. *Geochimica et Cosmochimica Acta,* 73**,** 4180-4198.

OCH, L. M., CREMONESE, L., SHIELDS-ZHOU, G. A., POULTON, S. W., STRUCK, U., LING, H., LI, D., CHEN, X., MANNING, C. & THIRLWALL, M. 2016. Palaeoceanographic controls on spatial redox distribution over the Yangtze Platform during the Ediacaran–Cambrian transition. *Sedimentology,* 63**,** 378-410.

OKADA, Y., SAWAKI, Y., KOMIYA, T., HIRATA, T., TAKAHATA, N., SANO, Y., HAN, J. & MARUYAMA, S. 2014. New chronological constraints for Cryogenian to Cambrian rocks in the Three Gorges, Weng'an and Chengjiang areas, South China. *Gondwana Research,* 25**,** 1027-1044.

OSÉS, G. L., PETRI, S., VOLTANI, C. G., PRADO, G. M., GALANTE, D., RIZZUTTO, M. A., RUDNITZKI, I. D., DA SILVA, E. P., RODRIGUES, F. & RANGEL, E. C. 2017. Deciphering pyritization-kerogenization gradient for fish soft-tissue preservation. *Scientific Reports,* 7**,** 1-15.

PARK, T.-Y., WOO, J., LEE, D.-J., LEE, D.-C., LEE, S.-B., HAN, Z., CHOUGH, S. K. & CHOI, D. K. 2011. A stem-group cnidarian described from the mid-Cambrian of China and its significance for cnidarian evolution. *Nature Communications,* 2**,** 1-6.

PENNY, A. M., WOOD, R., CURTIS, A., BOWYER, F., TOSTEVIN, R. & HOFFMAN, K.-H. 2014. Ediacaran metazoan reefs from the Nama Group, Namibia. *Science,* 344**,** 1504-1506.

PENNY, A. M., WOOD, R., ZHURAVLEV, A. Y., CURTIS, A., BOWYER, F. & TOSTEVIN, R. 2017. Intraspecific variation in an Ediacaran skeletal metazoan: *Namacalathus* from the Nama Group, Namibia. *Geobiology,* 15**,** 81-93.

PLANAVSKY, N. J., ROBBINS, L. J., KAMBER, B. S. & SCHOENBERG, R. 2020. Weathering, alteration and reconstructing Earth's oxygenation. *Interface Focus,* 10**,** 20190140.

PORTER, S. M. 2007. Seawater chemistry and early carbonate biomineralization. *Science,* 316**,** 1302-1302.

POULTON, S. W. & CANFIELD, D. E. 2005. Development of a sequential extraction procedure for iron: implications for iron partitioning in continentally derived particulates. *Chemical Geology,* 214**,** 209-221.

POULTON, S. W. & CANFIELD, D. E. 2006. Co-diagenesis of iron and phosphorus in hydrothermal sediments from the southern East Pacific Rise: Implications for the evaluation of paleoseawater phosphate concentrations. *Geochimica et Cosmochimica Acta,* 70**,** 5883-5898.

POULTON, S. W., HENKEL, S., MÄRZ, C., URQUHART, H., FLÖGEL, S., KASTEN, S., SINNINGHE DAMSTÉ, J. S. & WAGNER, T. 2015. A continental-weathering control on orbitally driven redox-nutrient cycling during Cretaceous Oceanic Anoxic Event 2. *Geology,* 43**,** 963-966.

POULTON, S. W., KROM, M. D. & RAISWELL, R. 2004. A revised scheme for the reactivity of iron (oxyhydr) oxide minerals towards dissolved sulfide. *Geochimica et cosmochimica acta,* 68**,** 3703-3715.

PRUSS, S. B., BLATTLER, C. L., MACDONALD, F. A. & HIGGINS, J. A. 2018. Calcium isotope evidence that the earliest metazoan biomineralizers formed aragonite shells. *Geology,* 46**,** 763-766.

REDFIELD, A. C. 1958. The biological control of chemical factors in the environment. *American Scientist,* 46**,** 230A-221.

REINHARD, C. T., PLANAVSKY, N. J., GILL, B. C., OZAKI, K., ROBBINS, L. J., LYONS, T. W., FISCHER, W. W., WANG, C., COLE, D. B. & KONHAUSER, K. O. 2017. Evolution of the global phosphorus cycle. *Nature,* 541**,** 386-389.

REINHARD, C. T., PLANAVSKY, N. J., OLSON, S. L., LYONS, T. W. & ERWIN, D. H. 2016. Earth's oxygen cycle and the evolution of animal life. *Proceedings of the National Academy of Sciences,* 113**,** 8933-8938.

REITNER, J. & WÖRHEIDE, G. 2002. Non-lithistid fossil Demospongiae—origins of their palaeobiodiversity and highlights in history of preservation. *Systema Porifera.* Springer.

RETALLACK, G. J., MATTHEWS, N. A., MASTER, S., KHANGAR, R. G. & KHAN, M. 2021. *Dickinsonia* discovered in India and late Ediacaran biogeography. *Gondwana Research,* 90**,** 165-170.

RICKARD, D. 2019. How long does it take a pyrite framboid to form? *Earth Planetary Science Letters* 513**,** 64-68.

ROONEY, A.D., CANTINE, M.D., BERGMANN, K.D., GÓMEZ-PÉREZ, I., AL BALOUSHI, B., BOAG, T.H., BUSCH, J.F., SPERLING, E.A. and STRAUSS, J.V., 2020. Calibrating the coevolution of Ediacaran life and environment. *Proceedings of the National Academy of Sciences*, *117*(29), 16824-16830.

ROSE, C. V., SWANSON-HYSELL, N. L., HUSSON, J. M., POPPICK, L. N., COTTLE, J. M., SCHOENE, B. & MALOOF, A. C. 2012. Constraints on the origin and relative timing of the Trezona δ13C anomaly below the end-Cryogenian glaciation. *Earth Planetary Science Letters* 319**,** 241-250.

ROTHMAN, D. H., HAYES, J. M. & SUMMONS, R. E. 2003. Dynamics of the Neoproterozoic carbon cycle. *Proceedings of the National Academy of Sciences,* 100**,** 8124-8129.

RUTTENBERG, K. 2003. The global phosphorus cycle. *Treatise on Geochemistry,* 8**,** 682.

RUTTENBERG, K. C. 1992. Development of a sequential extraction method for different forms of phosphorus in marine sediments. *Limnology, oceanography* 37**,** 1460-1482.

RUTTENBERG, K. C. & BERNER, R. A. 1993. Authigenic apatite formation and burial in sediments from non-upwelling, continental margin environments. *Geochimica et cosmochimica acta,* 57**,** 991-1007.

SAHOO, S. K., PLANAVSKY, N., JIANG, G., KENDALL, B., OWENS, J., WANG, X., SHI, X., ANBAR, A. & LYONS, T. 2016. Oceanic oxygenation events in the anoxic Ediacaran ocean. *Geobiology,* 14**,** 457-468.

SANFILIPPO, R. 2009. Systematics and life habit in Serpula israelitica Amoureux, 1977 (Polychaeta Serpulidae) from the Mediterranean with remarks on other soft-bottom serpulids. *Journal of Natural History,* 43**,** 2009-2025.

SAYLOR, B. Z. & GROTZINGER, J. P. 1996. Reconstruction of important Proterozoic-Cambrian boundary exposures through the recognition of thrust deformation in the Nama Group of southern Namibia. *Communications of the Geological Survey of Namibia,* 11**,** 1-12.

SAYLOR, B. Z., GROTZINGER, J. P. & GERMS, G. J. 1995. Sequence stratigraphy and sedimentology of the Neoproterozoic Kuibis and Schwarzrand subgroups (Nama Group), southwestern Namibia. *Precambrian Research,* 73**,** 153-171.

SAYLOR, B. Z., KAUFMAN, A. J., GROTZINGER, J. P. & URBAN, F. 1998. A composite reference section for terminal Proterozoic strata of southern Namibia. *Journal of Sedimentary Research,* 68**,** 1223-1235.

SCHIFFBAUER, J. D., SELLY, T., JACQUET, S. M., MERZ, R. A., NELSON, L. L., STRANGE, M. A., CAI, Y. & SMITH, E. F. 2020. Discovery of bilaterian-type through-guts in cloudinomorphs from the terminal Ediacaran Period. *Nature Communications,* 11**,** 1-12.

SCHIFFBAUER, J. D., XIAO, S., CAI, Y., WALLACE, A. F., HUA, H., HUNTER, J., XU, H., PENG, Y. & KAUFMAN, A. J. 2014. A unifying model for Neoproterozoic–Palaeozoic exceptional fossil preservation through pyritization and carbonaceous compression. *Nature Communications,* 5**,** 1-12.

SCHMITZ, M. 2012. Radiogenic isotope geochronology. *The geologic time scale.* Elsevier.

SCHRAG, D. P., BERNER, R. A., HOFFMAN, P. F. & HALVERSON, G. P. 2002. On the initiation of a snowball Earth. *Geochemistry, Geophysics, Geosystems,* 3**,** 1-21.

SCOTESE, C. R. 2009. Late Proterozoic plate tectonics and palaeogeography: a tale of two supercontinents, Rodinia and Pannotia. *Geological Society, London, Special Publications,* 326**,** 67-83.

SCRUTTON, C. T. 1987. A REVIEW OF FAVOSITID AFFINITIES. *Palaeontology,* 30**,** 485-492.

SEILACHER, A. 1992. Vendobionta and Psammocorallia: lost constructions of Precambrian evolution. *Journal of the Geological Society,* 149**,** 607-613.

SEILACHER, A., GRAZHDANKIN, D. & LEGOUTA, A. 2003. Ediacaran biota: The dawn of animal life in the shadow of giant protists. *Paleontological Research,* 7**,** 43-54.

SELLY, T., SCHIFFBAUER, J. D., JACQUET, S. M., SMITH, E. F., NELSON, L. L., ANDREASEN, B. D., HUNTLEY, J. W., STRANGE, M. A., O'NEIL, G. R. & THATER, C. A. 2020. A new cloudinid fossil assemblage from the terminal Ediacaran of Nevada, USA. *Journal of Systematic Palaeontology,* 18**,** 357-379.

SHIELDS, G. A., MILLS, B. J., ZHU, M., RAUB, T. D., DAINES, S. J. & LENTON, T. M. 2019. Unique Neoproterozoic carbon isotope excursions sustained by coupled evaporite dissolution and pyrite burial. *Nature Geoscience,* 12**,** 823-827.

SHORE, A., WOOD, R., CURTIS, A. & BOWYER, F. 2020. Multiple branching and attachment structures in cloudinomorphs, Nama Group, Namibia. *Geology*.

SKOVSTED, C. B., BROCK, G. A., PATERSON, J. R., HOLMER, L. E. & BUDD, G. E. 2008. The scleritome of *Eccentrotheca* from the Lower Cambrian of South Australia: Lophophorate affinities and implications for tommotiid phylogeny. *Geology,* 36**,** 171-174.

SLOMP, C., VAN DER GAAST, S. & VAN RAAPHORST, W. 1996. Phosphorus binding by poorly crystalline iron oxides in North Sea sediments. *Marine Chemistry,* 52**,** 55-73.

SLOMP, C. P., THOMSON, J. & DE LANGE, G. J. 2004. Controls on phosphorus regeneration and burial during formation of eastern Mediterranean sapropels. *Marine Geology,* 203**,** 141-159.

SMITH, E.F., NELSON, L.L., STRANGE, M.A., EYSTER, A.E., ROWLAND, S.M., SCHRAG, D.P. & MACDONALD, F.A., 2016. The end of the Ediacaran: Two new exceptionally preserved body fossil assemblages from Mount Dunfee, Nevada, USA. *Geology*, *44*(11), 911-914.

SMITH, E., NELSON, L., TWEEDT, S., ZENG, H. & WORKMAN, J. B. 2017. A cosmopolitan late Ediacaran biotic assemblage: new fossils from Nevada and Namibia support a global biostratigraphic link. *Proceedings of the Royal Society B: Biological Sciences* 284**,** 20170934.

SMITH, M. P. & HARPER, D. A. 2013. Causes of the Cambrian explosion. *Science,* 341**,** 1355-1356.

SMITH, O.A., 1998. Terminal Proterozoic carbonate platform development: stratigraphy and sedimentology of the Kuibis Subgroup (ca. 550–548 Ma). *Northern Nama Basin, Namibia [unpublished M. Sc. thesis]: Cambridge, Massachusetts, Massachusetts Institute of Technology*.

STANLEY, S. M. & HARDIE, L. A. 1998. Secular oscillations in the carbonate mineralogy of reef-building and sediment-producing organisms driven by tectonically forced shifts in seawater chemistry. *Palaeogeography, Palaeoclimatology, Palaeoecology,* 144**,** 3-19.

STEWART, J.H., MCMENAMIN, M.A. & MORALES-RAMIREZ, J.M., 1984. Upper Proterozoic and Cambrian rocks in the Caborca region. *Sonora, Mexico—Physical stratigraphy, biostratigraphy, paleocurrent studies, and regional relations: US Geological Survey Professional Paper*, 1309, 36.

STRENG, M. & HOLMER, L. E. 2005. Discovery of a new type of shell structure within the organophosphatic brachiopods and the status of the family Curticiidae. *GFF,* 127**,** 7-16.

SUN, H., SMITH, M. R., ZENG, H., ZHAO, F., LI, G. & ZHU, M. 2018. Hyoliths with pedicles illuminate the origin of the brachiopod body plan. *Proceedings of the Royal Society B: Biological Sciences,* 285**,** 20181780.

SUN, W., YIN, Z., CUNNINGHAM, J. A., LIU, P., ZHU, M. & DONOGHUE, P. C. 2020. Nucleus preservation in early Ediacaran Weng'an embryo-like fossils, experimental taphonomy of nuclei and implications for reading the eukaryote fossil record. *Interface Focus,* 10**,** 20200015.

TARHAN, L. G. 2018. The early Paleozoic development of bioturbation—evolutionary and geobiological consequences. *Earth-Science Reviews,* 178**,** 177-207.

TARHAN, L. G., DROSER, M. L., COLE, D. B. & GEHLING, J. G. 2018. Ecological expansion and extinction in the late Ediacaran: Weighing the evidence for environmental and biotic drivers. *Integrative Comparative Biology* 58**,** 688-702.

TARHAN, L. G., MYROW, P. M., SMITH, E. F., NELSON, L. L. & SADLER, P. M. J. G. 2020. Infaunal augurs of the Cambrian explosion: An Ediacaran trace fossil assemblage from Nevada, USA. 18**,** 486-496.

TAYLOR, E. L., TAYLOR, T. N. & KRINGS, M. 2009. *Paleobotany: the biology and evolution of fossil plants*, Academic Press.

TAYLOR, P. D., LOMBARDI, C. & COCITO, S. 2015. Biomineralization in bryozoans: present, past and future. *Biological Reviews,* 90**,** 1118-1150.

TAYLOR, P. D., VINN, O. & WILSON, M. A. 2010. Evolution of biomineralisation in 'lophophorates'. *Special Papers in Palaeontology,* 84**,** 317-333.

TAYLOR, P. D. & WEEDON, M. J. 2000. Skeletal ultrastructure and phylogeny of cyclostome bryozoans. *Zoological Journal of the Linnean Society,* 128**,** 337-399.

TERLEEV, A., LUCHININA, V., SOSNOVSKAYA, O. & BAGMET, G. 2004. Calcareous algae and lower boundary of the Cambrian in the western Altai-Sayan Folded Area. *Geologiya i Geofizika,* 45**,** 485-491.

TERLEEV, A.A., POSTNIKOV, A.A., TOKAREV, D.A., SOSNOVSKAYA, O.V. & BAGMET, G.N., 2011, July. Cloudina–Namacalathus–Korilophyton association in the Vendian of the Altay-Sayan Foldbelt (Siberia). In *Proc. of Int. Conf. Neoproterozoic Sedimentary Basins: Stratigraphy, Geodynamics and Petroleum Potential*, 96-98.

THOMPSON, J., POULTON, S. W., GUILBAUD, R., DOYLE, K. A., REID, S. & KROM, M. D. 2019. Development of a modified SEDEX phosphorus speciation method for ancient rocks and modern iron-rich sediments. *Chemical Geology,* 524**,** 383-393.

TOSTEVIN, R. (2021). Cerium Anomalies and Paleoredox. *Cambridge University Press*.

TOSTEVIN, R., CLARKSON, M. O., GANGL, S., SHIELDS, G. A., WOOD, R. A., BOWYER, F., PENNY, A. M. & STIRLING, C. H. 2019. Uranium isotope evidence for an expansion of anoxia in terminal Ediacaran oceans. *Earth and Planetary Science Letters,* 506**,** 104-112.

TOSTEVIN, R. & MILLS, B. J. 2020. Reconciling proxy records and models of Earth's oxygenation during the Neoproterozoic and Palaeozoic. *Interface Focus,* 10**,** 20190137.

TOSTEVIN, R., SHIELDS, G. A., TARBUCK, G. M., HE, T., CLARKSON, M. O. & WOOD, R. A. 2016a. Effective use of cerium anomalies as a redox proxy in carbonate-dominated marine settings. *Chemical Geology,* 438**,** 146-162.

TOSTEVIN, R., WOOD, R., SHIELDS, G., POULTON, S., GUILBAUD, R., BOWYER, F., PENNY, A., HE, T., CURTIS, A. & HOFFMANN, K. 2016b. Low-oxygen waters limited habitable space for early animals. *Nature Communications,* 7**,** 1-9.

TOWE, K. M. 1970. Oxygen-collagen priority and the early metazoan fossil record. *Proceedings of the National Academy of Sciences,* 65**,** 781-788.

TUCKER, M. E. & WRIGHT, V. P. 2009. *Carbonate sedimentology,* John Wiley & Sons.

TUREKIAN, K. K. & WEDEPOHL, K. H. 1961. Distribution of the elements in some major units of the earth's crust. *Geological society of America bulletin,* 72**,** 175-192.

TYRRELL, T. 1999. The relative influences of nitrogen and phosphorus on oceanic primary production. *Nature,* 400**,** 525-531.

VACELET, J., WILLENZ, P. & HARTMAN, W. 2010. Treatise Online, no. 1, Part E, Revised, Volume 4, Chapter 1: Living hypercalcified sponges. *Treatise Online,* 4.

VAN CAPPELLEN, P. & INGALL, E. D. 1996. Redox stabilization of the atmosphere and oceans by phosphorus-limited marine productivity. *Science,* 271**,** 493-496.

VENDRASCO, M. J., KOUCHINSKY, A. V., PORTER, S. M. & FERNANDEZ, C. Z. 2011. Phylogeny and escalation in *Mellopegma* and other Cambrian molluscs. *Palaeontologia Electronica,* 14**,** 1-44.

VENDRASCO, M. J., PORTER, S. M., KOUCHINSKY, A. V., LI, G. & FERNANDEZ, C. Z. 2010. Shell microstructures in early mollusks. *The Festivus,* 42**,** 43-54.

VICKERS-RICH, P., IVANTSOV, A. Y., TRUSLER, P. W., NARBONNE, G. M., HALL, M., WILSON, S. A., GREENTREE, C., FEDONKIN, M. A., ELLIOTT, D. A. & HOFFMANN, K. H. 2013. Reconstructing *Rangea*: new discoveries from the Ediacaran of southern Namibia. *Journal of African Earth Sciences,* 87**,** 1-15.

VINN, O. & ZATON, M. 2012. Inconsistencies in proposed annelid affinities of early biomineralized organism *Cloudina* (Ediacaran): structural and ontogenetic evidences. *Carnets de Géologie***,** 39-47.

WAGGONER, B. 2003. The Ediacaran biotas in space and time. *Integrative and Comparative Biology,* 43**,** 104-113.

WARREN, L. V., FAIRCHILD, T. R., GAUCHER, C., BOGGIANI, P. C., POIRE, D. G., ANELLI, L. E. & INCHAUSTI, J. C. 2011. *Corumbella* and in situ *Cloudina* in association with thrombolites in the Ediacaran Itapucumi Group, Paraguay. *Terra Nova,* 23**,** 382-389.

WARREN, L. V., QUAGLIO, F., SIMOES, M. G., GAUCHER, C., RICCOMINI, C., POIRE, D. G., FREITAS, B. T., BOGGIANI, P. C. & SIAL, A. N. 2017. *Cloudina-Corumbella-Namacalathus* association from the Itapucumi Group, Paraguay: Increasing ecosystem complexity and tiering at the end of the Ediacaran. *Precambrian Research,* 298**,** 79-87.

WEINER, S. & DOVE, P. M. 2003. An overview of biomineralization processes and the problem of the vital effect. *In:* DOVE, P. M., DEYOREO, J. J. & WEINER, S. (eds.) *Biomineralization.*

WHEAT, C. G., MCMANUS, J., MOTTL, M. J. & GIAMBALVO, E. 2003. Oceanic phosphorus imbalance: Magnitude of the mid-ocean ridge flank hydrothermal sink. *Geophysical research letters,* 30.

WHELAN, N. V., KOCOT, K. M., MOROZ, T. P., MUKHERJEE, K., WILLIAMS, P., PAULAY, G., MOROZ, L. L. & HALANYCH, K. M. 2017. Ctenophore relationships and their placement as the sister group to all other animals. *Nature ecology evolution,* 1**,** 1737-1746.

WILLIAMS, A. 1997. Part H (revised), Brachiopoda (Introduction). . *Treatise on Invertebrate Paleontology.*

WILLIAMS, A., HOLMER, L. E. & CUSACK, M. 2004. Chemico-structure of the organophosphatic shells of siphonotretide brachiopods. *Palaeontology,* 47**,** 1313-1337.

WILLE, M., NÄGLER, T.F., LEHMANN, B., SCHRÖDER, S. & KRAMERS, J.D., 2008. Hydrogen sulphide release to surface waters at the Precambrian/Cambrian boundary. *Nature*, 453, 767-769.

WILSON, J. P., GROTZINGER, J. P., FISCHER, W. W., HAND, K. P., JENSEN, S., KNOLL, A. H., ABELSON, J., METZ, J. M., MCLOUGHLIN, N. & COHEN, P. A. 2012. Deep-water incised valley deposits at the ediacaran-cambrian boundary in southern namibia contain abundant *treptichnus pedum*, Namibian Incised Valleys And T. Pedum. *Palaios,* 27**,** 252-273.

WIZEMANN, A., MEYER, F. W. & WESTPHAL, H. 2014. A new model for the calcification of the green macro-alga Halimeda opuntia (Lamouroux). *Coral Reefs,* 33**,** 951-964.

WOOD, R., BOWYER, F., PENNY, A. & POULTON, S. W. 2018. Did anoxia terminate Ediacaran benthic communities? Evidence from early diagenesis. *Precambrian Research,* 313**,** 134-147.

WOOD, R. & CURTIS, A. 2015. Extensive metazoan reefs from the Ediacaran Nama Group, Namibia: the rise of benthic suspension feeding. *Geobiology,* 13**,** 112-122.

WOOD, R., CURTIS, A., PENNY, A., ZHURAVLEV, A. Y., CURTIS-WALCOTT, S., IIPINGE, S. & BOWYER, F. 2017a. Flexible and responsive growth strategy of the Ediacaran skeletal Cloudina from the Nama Group, Namibia. *Geology,* 45**,** 259-262.

WOOD, R., IVANTSOV, A. Y. & ZHURAVLEV, A. Y. 2017b. First macrobiota biomineralization was environmentally triggered. *Proceedings of the Royal Society B: Biological Sciences,* 284**,** 20170059.

WOOD, R., LIU, A. G., BOWYER, F., WILBY, P. R., DUNN, F. S., KENCHINGTON, C. G., CUTHILL, J. F. H., MITCHELL, E. G. & PENNY, A. 2019. Integrated records of environmental change and evolution challenge the Cambrian Explosion. *Nature ecology evolution,* 3**,** 528-538.

WOOD, R. & PENNY, A. 2018. Substrate growth dynamics and biomineralization of an Ediacaran encrusting poriferan. *Proceedings of the Royal Society B-Biological Sciences,* 285.

WOOD, R., POULTON, S. W., PRAVE, A. R., HOFFMANN, K.-H., CLARKSON, M., GUILBAUD, R., LYNE, J., TOSTEVIN, R., BOWYER, F. & PENNY, A. 2015. Dynamic redox conditions control late Ediacaran metazoan ecosystems in the Nama Group, Namibia. *Precambrian Research,* 261**,** 252-271.

WOOD, R. A. 2011. Paleoecology of the earliest skeletal metazoan communities: implications for early biomineralization. *Earth-Science Reviews,* 106**,** 184-190.

WOOD, R. A., GROTZINGER, J. P. & DICKSON, J. A. D. 2002. Proterozoic modular biomineralized metazoan from the Nama Group, Namibia. *Science,* 296**,** 2383-2386.

XIAO, S., CHEN, Z., PANG, K., ZHOU, C. & YUAN, X. 2021. The Shibantan Lagerstätte: insights into the Proterozoic–Phanerozoic transition. *Journal of the Geological Society,* 178.

XIAO, S.H., NARBONNE, G.M., 2020. The Ediacaran Period, in: Gradstein, F.M., Ogg, J.G., Schmitz, M.D., Ogg, G.M. (Eds.), Geological Time Scale 2020. *Elsevier B.V.*, pp. 521–561

XIAO, S., ZHANG, Y. & KNOLL, A. H. 1998. Three-dimensional preservation of algae and animal embryos in a Neoproterozoic phosphorite. *Nature,* 391**,** 553-558.

YANG, B., STEINER, M., SCHIFFBAUER, J. D., SELLY, T., WU, X., ZHANG, C. & LIU, P. 2020. Ultrastructure of Ediacaran cloudinids suggests diverse taphonomic histories and affinities with non-biomineralized annelids. *Scientific Reports,* 10**,** 1-12.

YOUNG, G. M. 2013. Precambrian supercontinents, glaciations, atmospheric oxygenation, metazoan evolution and an impact that may have changed the second half of Earth history. *Geoscience Frontiers,* 4**,** 247-261.

YUAN, X., CHEN, Z., XIAO, S., ZHOU, C. & HUA, H. 2011. An early Ediacaran assemblage of macroscopic and morphologically differentiated eukaryotes. *Nature,* 470**,** 390-393.

YUAN, X., CHEN, Z., XIAO, S., WAN, B., GUAN, C., WANG, W., ZHOU, C. & HUA, H., 2013. The Lantian biota: a new window onto the origin and early evolution of multicellular organisms. *Chinese Science Bulletin*, 58, 701-707.

ZHANG, F., XIAO, S., KENDALL, B., ROMANIELLO, S. J., CUI, H., MEYER, M., GILLEAUDEAU, G. J., KAUFMAN, A. J. & ANBAR, A. D. 2018. Extensive marine anoxia during the terminal Ediacaran Period. *Science Advances,* 4**,** eaan8983.

ZHANG, F., XIAO, S., ROMANIELLO, S. J., HARDISTY, D., LI, C., MELEZHIK, V., POKROVSKY, B., CHENG, M., SHI, W. & LENTON, T. M. 2019. Global marine redox changes drove the rise and fall of the Ediacara biota. *Geobiology,* 17**,** 594-610.

ZHANG, Z., HOLMER, L. E., SKOVSTED, C. B., BROCK, G. A., BUDD, G. E., FU, D., ZHANG, X., SHU, D., HAN, J. & LIU, J. 2013. A sclerite-bearing stem group entoproct from the early Cambrian and its implications. *Scientific Reports,* 3**,** 1066.

ZHAO, Y., VINTHER, J., PARRY, L. A., WEI, F., GREEN, E., PISANI, D., HOU, X., EDGECOMBE, G. D. & CONG, P. 2019. Cambrian sessile, suspension feeding stem-group ctenophores and evolution of the comb jelly body plan. *Current Biology,* 29**,** 1112-1125.

ZHU, M.-Y., LI, G.-X., ZHANG, J.-M., STEINER, M., QIAN, Y., & JIANG, Z.-W., 2001, Early Cambrian stratigraphy of east Yunnan, southwestern China: A synthesis: Acta Palaeontologica Sinica , 40, 4–39.

ZHU, M., GEHLING, J. G., XIAO, S., ZHAO, Y. & DROSER, M. L. 2008. Eight-armed Ediacara fossil preserved in contrasting taphonomic windows from China and Australia. *Geology,* 36**,** 867-870.

ZHURAVLEV, A. Y., LINAN, E., VINTANED, J. A. G., DEBRENNE, F. & FEDOROV, A. B. 2012. New finds of skeletal fossils in the terminal Neoproterozoic of the Siberian Platform and Spain. *Acta Palaeontologica Polonica,* 57**,** 205-224.

ZHURAVLEV, A. Y., WOOD, R. & PENNY, A. 2015. Ediacaran skeletal metazoan interpreted as a lophophorate. *Proceedings of the Royal Society B: Biological Sciences* 282**,** 1860.

ZHURAVLEV, A. Y. & WOOD, R. A. 2008. Eve of biomineralization: Controls on skeletal mineralogy. *Geology,* 36**,** 923-926.

Appendix 1: Phosphorus Cycling and Oxygenation in the Nama Group, Namibia

Appendix 1.1 Bowyer et al. (2020)

Regional nutrient decrease drove redox stabilisation and metazoan diversification in the late Ediacaran Nama Group, Namibia

SCIENTIFIC REPORTS
nature research

OPEN

Regional nutrient decrease drove redox stabilisation and metazoan diversification in the late Ediacaran Nama Group, Namibia

F. T. Bowyer[1,6*], A. J. Shore[1], R. A. Wood[1], L. J. Alcott[2], A. L. Thomas[1], I. B. Butler[1], A. Curtis[1], S. Hainanan[3], S. Curtis-Walcott[4], A. M. Penny[5] & S. W. Poulton[2]

The late Ediacaran witnessed an increase in metazoan diversity and ecological complexity, marking the inception of the Cambrian Explosion. To constrain the drivers of this diversification, we combine redox and nutrient data for two shelf transects, with an inventory of biotic diversity and distribution from the Nama Group, Namibia (~550 to ~538 Million years ago; Ma). Unstable marine redox conditions characterised all water depths in inner to outer ramp settings from ~550 to 547 Ma, when the first skeletal metazoans appeared. However, a marked deepening of the redoxcline and a reduced frequency of anoxic incursions onto the inner to mid-ramp is recorded from ~547 Ma onwards, with full ventilation of the outer ramp by ~542 Ma. Phosphorus speciation data show that, whilst anoxic ferruginous conditions were initially conducive to the drawdown of bioavailable phosphorus, they also permitted a limited degree of phosphorus recycling back to the water column. A long-term decrease in nutrient delivery from continental weathering, coupled with a possible decrease in upwelling, led to the gradual ventilation of the Nama Group basins. This, in turn, further decreased anoxic recycling of bioavailable phosphorus to the water column, promoting the development of stable oxic conditions and the radiation of new mobile taxa.

The earliest candidate metazoan body fossils appear in the fossil record in the Ediacaran at ~571 Ma[1], with the first uncontroversial surface traces created by motile organisms known from ~560 Ma[2], followed by skeletal hardparts at ~550 Ma[3]. The Ediacaran-Cambrian boundary, as currently defined, is placed at ~541 Ma, and by ~520 Ma most major phyla had appeared, marking the end of the Cambrian Explosion. While the oxygen requirements of Ediacaran metazoans are unknown, it has been widely suggested that an increase in the dissolved oxygen concentration of marine environments enabled the rise of metabolically active ecologies, including large body size, bilaterian burrowing and biomineralisation[4]. The key to clarifying the relationships between redox and early metazoan diversification and complexity lies in high resolution studies that integrate local redox with biotic distribution[5,6].

The late Ediacaran (c. 580–541 Ma) oceans were likely characterised by low oxygen levels[7], and individual basins of the Ediacaran and Cambrian that were openly connected to the global ocean exhibit continued regional redox heterogeneity on million year timescales[5,8,9]. Whilst some mid-shelf and lower slope environments record a transition to permanent, stable oxia as early as ~577 Ma, other lower slope settings were characterised by continued anoxic and ferruginous (free Fe(II)) or even euxinic (free aqueous hydrogen sulfide) water column conditions (see review ref. [9]). Indeed, ferruginous water column conditions have been recorded from shallow marine sediments deposited above fair weather wave base in the final 10 million years of the Ediacaran[5,6]. The observed variability in the local redox of late Ediacaran and early Cambrian marine environments may correspond to the relative distance from, and spatial extent of, oxygen minimum zones (OMZs) that developed in response to local productivity and resultant organic matter remineralization[10]. Spatially variable rates of primary production, in

[1]University of Edinburgh, School of GeoSciences, James Hutton Road, Edinburgh, EH9 3FE, UK. [2]University of Leeds, School of Earth and Environment, Leeds, LS2 9JT, UK. [3]Ministry of Mines and Energy, 6 Aviation Road, Private Bag, 13297, Windhoek, Namibia. [4]Department of Physics, Imperial College, London, SW7 2AZ, UK. [5]Finnish Museum of Natural History, University of Helsinki, Jyrängöntie 2, 00560, Helsinki, Finland. [6]Present address: University of Leeds, School of Earth and Environment, Leeds, LS2 9JT, UK. *email: F.T.Bowyer@leeds.ac.uk

turn, are likely to reflect the provision of limiting nutrients, in particular phosphorus (P), which is commonly considered the ultimate limiting nutrient on geological timescales[11].

Here, we utilise iron (Fe) and P speciation data across two shelf transects to create a 4D reconstruction of local-scale redox and nutrient cycling dynamics in the Ediacaran to early Cambrian Nama Group, Namibia (~550–538 Ma). Previous palaeoredox studies of the Nama Group have demonstrated the limitation imposed on skeletal metazoans by low oxygen waters[5,6]. By contrast, potentially detrimental incursions of ferruginous waters into the shallowest marine settings that were host to abundant soft-bodied organisms and trace makers, have been largely overlooked in geochemical studies as a consequence of fossil preservation within coarse siliciclastics that are not well-suited to geochemical redox analyses. However, the well-defined sequence stratigraphic framework of the Nama Group enables analysis of down-dip shales deposited time-equivalent to shallow, fossiliferous sandstone layers, and construction of variable-depth geochemical transects. This enables the relative position of the redoxcline to be tracked through time, as well as quantification of the incursion frequency of anoxic waters onto the shallow, inner ramp. We combine this approach with a recent compilation of biotic diversity and distribution throughout the Nama Group in order to clarify the relationship between local redox stability and benthic colonisation.

Geological Setting: The Nama Group, Namibia

The Nama Group comprises a mixed carbonate and siliciclastic ramp succession deposited within a foreland basin on the Kalahari Craton during convergence along two orogenic belts; the Damara to the north and the Gariep to the southwest[12] (Fig. 1a–d). Zircons within silicified air-fall tuff deposits yield ID-TIMS U-Pb ages that constrain deposition between approximately 547 and 538 Ma[13–15]. The lowermost dated ash layer occurs at a maximum of >500 m above the basal Nama unconformity, and an approximate age of 550–553 Ma for the base of the Nama Group has been extrapolated from inferred rates of sedimentation[16], suggesting that deposition of the Kuibis and Schwarzrand subgroups persisted for ~12 Myr.

Sequence stratigraphy and $\delta^{13}C_{carb}$ chemostratigraphy are well established[16–19], and detailed mapping of individual members enables parasequence level correlation across distances of up to 100 km[19]. Sediments were deposited in two sub-basins, the Zaris and the Witputs, that deepened to the northwest and southwest, respectively, with distance from a basement forebulge, the Osis Arch (Fig. 1b)[12]. The Nama Group is divided into the lower Kuibis and upper Schwarzrand Subgroups (Fig. 1c), which are further subdivided based on regional facies and sequence stratigraphic mapping[12,18,19]. During deposition of the Kuibis Subgroup, the two sub-basins show an independent stratigraphy imposed by the Osis Arch[16,18] (Fig. 1b). Sub-basin connectivity increased due to transgression during deposition of the Schwarzrand Subgroup and gradual infill of the Zaris sub-basin[12,18]. Connection to the open ocean throughout Nama Group deposition is corroborated by strontium isotopic data[20], normal marine rare earth element profiles[6], and carbon isotopic data that are globally correlative. A gradual, basin-wide transition from negative to positive carbonate carbon isotope values may record the local expression of recovery from the presumed-global Shuram excursion (however this remains uncertain), but overlying strata are not known to record (or may predate) the basal Cambrian negative carbon isotope excursion (BACE)[5,16].

Almost 90 years of palaeontological study in the Nama Group has uncovered a diverse fossil record including the soft-bodied macro-organisms *Pteridinium*, *Rangea*, *Ernietta*, *Nasepia*, *Namalia*, and *Swartpuntia*[21–23]. Microbially-induced sedimentary structures (MISS), stromatolites, thrombolites and organic walled microfossils, including leiosphaerid acritarchs are also described[24]. Carbonate rocks host the skeletal taxa *Namacalathus*, *Cloudina*, and *Namapoikia*[3,25]. The Nama Group also hosts a rich suite of ichnofossils, including the first representatives of treptichnids[26], and first traces of extensive, but localised, sediment bulldozing[27].

Previous geochemical studies utilising Fe-S-C systematics and rare earth element profiles have revealed a highly heterogeneous palaeoredox environment for the Kuibis Subgroup, and constrain deposition under variably oxic, dysoxic manganous, and anoxic ferruginous waters in inner to outer-ramp facies[5–7]. Repeated incursions of ferruginous anoxia into inner shelf environments are considered to reflect changes in the position of the redoxcline, which was, in large part, controlled by changing relative sea level[5,9].

Methods

Full details of all analytical procedures, including the full dataset, are provided in the Supplementary Information, which includes additional palaeontological information, GPS coordinates and stratigraphic logs. A composite $\delta^{13}C_{carb}$ curve tied to major sequence boundaries was constructed using sequence stratigraphy, in order to correlate sample position in the Kuibis subgroup across the Osis Arch (see Supplementary Information). Compiled iron and phosphorus speciation data are placed within this framework and partitioned into four broad settings (incorporating inner, mid and outer ramp) based on sedimentary depth indicators and proximity to the Osis Arch[5,7,12,18] (see Supplementary Information for discussion).

Iron speciation[28] is the primary palaeoredox proxy employed in this study, and the compilation incorporates new and previously published data from shales (n = 218) and carbonates (n = 104). A sequential leach separates iron carbonates (Fe_{carb}), oxides (Fe_{ox}) and magnetite (Fe_{mag}), which, in addition to pyrite (Fe_{py}), operationally defines an iron pool that is considered highly reactive (Fe_{HR}) to reduction under anoxic conditions[29,30]. Anoxic water column conditions commonly promote enrichments in Fe_{HR} relative to total iron (Fe_T) via the water column precipitation of unsulfidized Fe_{HR} minerals in ferruginous basins and Fe sulfides in euxinic settings[31]. Extensive calibration in modern and ancient settings suggests that $Fe_{HR}/Fe_T < 0.22$ provides a robust indication of oxic water column depositional conditions, while ratios >0.38 suggest anoxic deposition[31]. Values between 0.22 to 0.38 are considered equivocal due to the potential for muted Fe_{HR}/Fe_T under anoxic conditions due to rapid deposition, or diagenetic transformation of unsulfidized Fe_{HR} to poorly reactive sheet silicates[32]. In the latter case, further insight can be gained by considering total Fe/Al ratios, which are not affected by diagenetic modification of individual Fe pools. Calibration studies suggest that Fe/Al > ~0.66 indicates deposition from an anoxic water

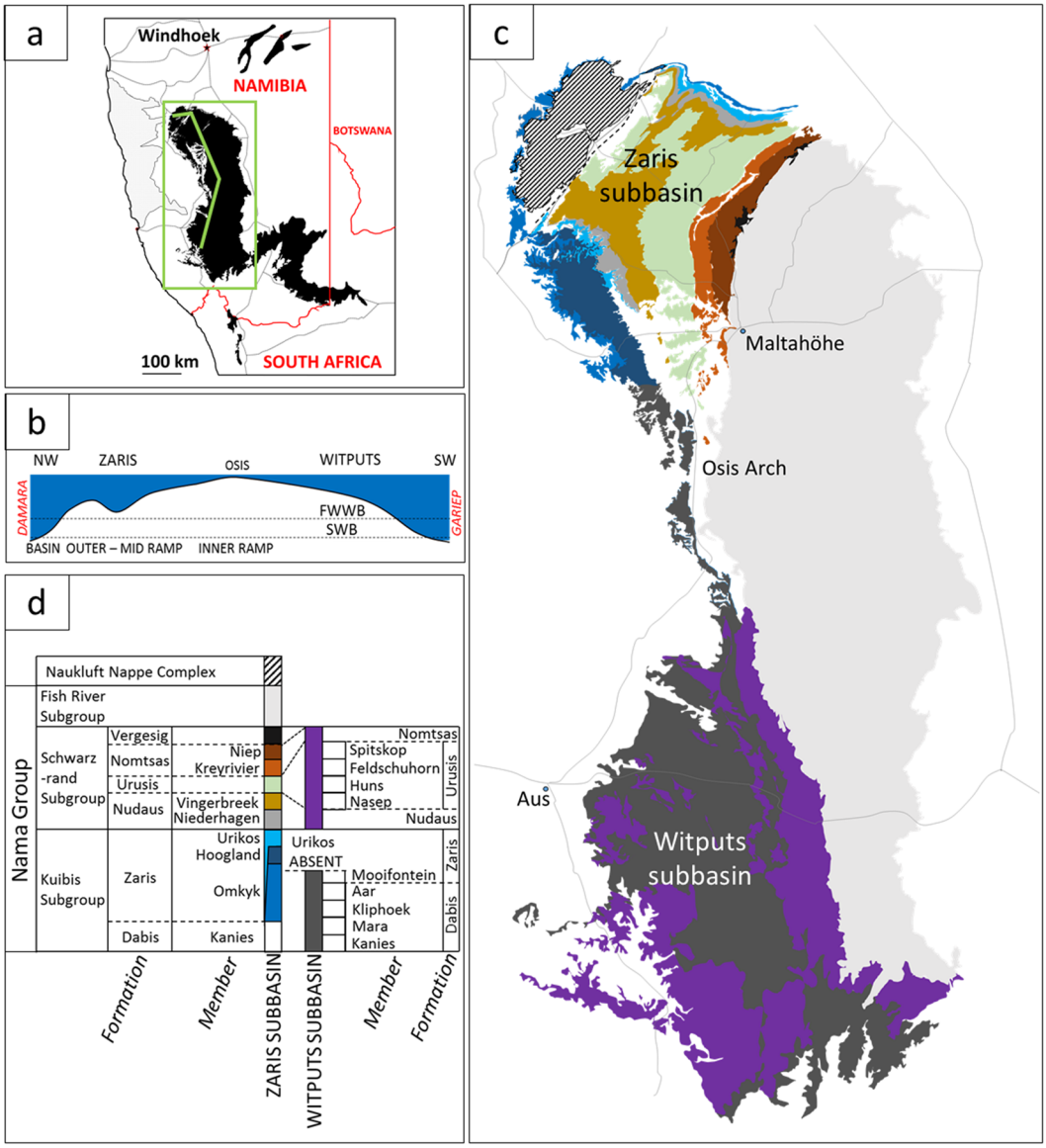

Figure 1. Geological setting of the Nama Group, Namibia. (**a**) Regional map showing outcrop of Nama Group with green box delineating study area and line of cross section in (**b**) through basins in Namibia. (**b**) Schematic cross section of palaeobathymetry in the Kuibis Subgroup. (**c**) Geological map of Nama Group, Namibia. Redrawn using 1:1000000 map and 1:250000 map of Mariental (2416), Geological Survey of Namibia, Ministry of Mines and Energy. (**d**) Stratigraphic key for geological map shown in (c).

column[33,34]. The proportion of Fe_{HR} contributed by Fe_{py} distinguishes between ferruginous and euxinic conditions, with $Fe_{py}/Fe_{HR} > 0.7–0.8$ indicative of a euxinic water column[32].

The majority of the compiled iron speciation data (~70%) relate to shales interbedded between carbonates. For carbonates, discerning palaeoredox conditions can be complicated by their potential sensitivity to external inputs of Fe_{HR} during diagenesis, which is particularly the case for carbonates with a low overall Fe content[5,34]. However, a detailed calibration suggests that Fe-speciation and Fe/Al results tend to be robust when Fe_T is >0.5 wt%, providing the sediments have not been subject to deep burial dolomitization[34]. All carbonate iron speciation data in this compilation have been published previously[5] and comply with the requisite minimum total Fe concentration (Fe_T) of 0.5 wt%[34]. Furthermore, there is no evidence for deep burial dolomitization in this succession, and an early origin for Nama Group dolomite is attributed either to evaporitic conditions[35], akin to modern dolomitizing environments, or to early diagenetic dolomitization of Fe-rich, high magnesium calcite precursor cements, precipitated in pore fluids that were openly connected to the overlying ferruginous water column[36]. Importantly, Fe-speciation data from interbedded shale and carbonate samples of the Nama Group generally give consistent interpretations, suggesting that their redox interpretation is robust[5], but where differences exist we place emphasis on the shale record.

We employ the chemical index of alteration (CIA)[37] to assess changes in the degree of chemical weathering (see Supplementary Information for further discussion). Chemical weathering plays a major role in controlling

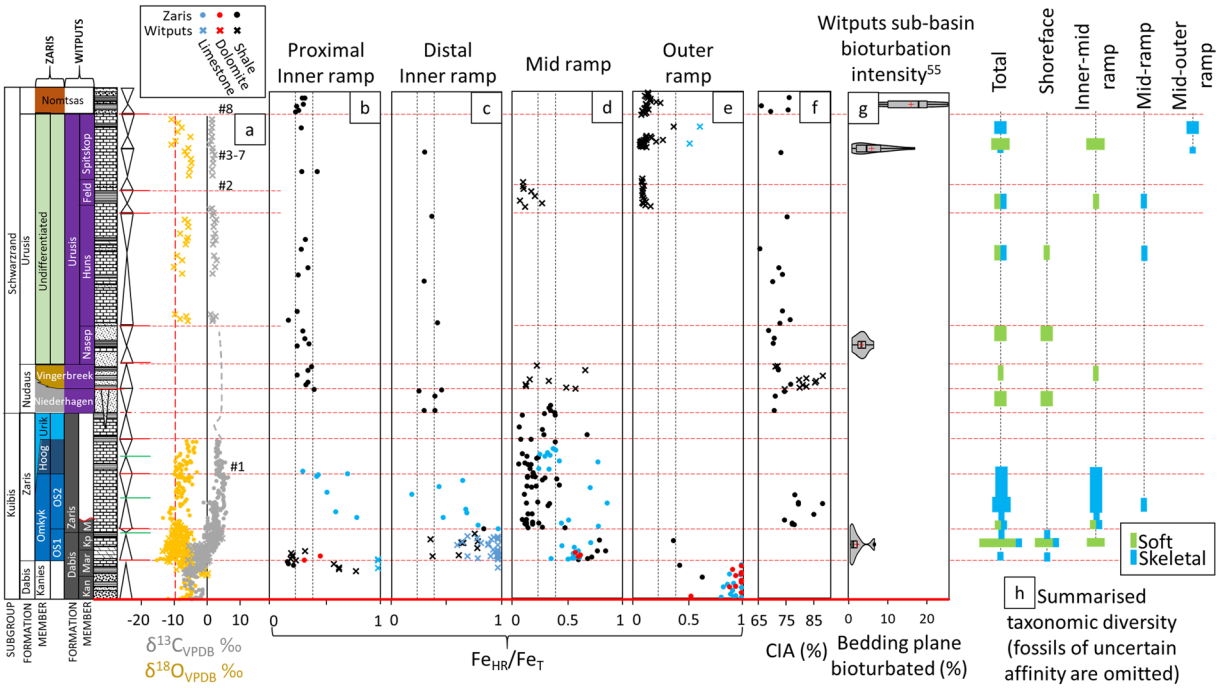

Figure 2. Carbonate C isotopes, redox and fossil occurrences in the Nama Group, Namibia, following reference section of (16). (**a**) Composite $\delta^{13}C_{carb}$ profile (see Supplementary Information). Hashed numbers correspond to the position of dated ash beds: #1, 547.36 ± 0.65 Ma[14]; #2, 542.68 ± 2.80 Ma[13,52]; #3–7, 540.095 ± 0.099 Ma to 538.99 ± 0.21 Ma[15]; #8, 538.58 ± 0.19 Ma[15]. (**b-e**) Compiled Fe_{HR}/Fe_T data, separated according to relative depth from inner to outer ramp. Anoxic water column conditions are indicated by $Fe_{HR}/Fe_T > 0.38$, ratios of Fe_{py}/Fe_{HR} are ubiquitously <0.3, characteristic of a ferruginous water column and consequently, ratios of Fe_{py}/Fe_{HR} are omitted. (**f**) Chemical index of alteration (CIA). (**g**) Violin plots of bioturbation intensity for the Witputs sub-basin after (55). (**h**) Summarised taxonomic diversity of published Nama Group body fossil occurrences (see Figure S12 and Table S1 for details).

the mineralogical composition of fine-grained siliciclastic rocks and is therefore a key metric to consider when evaluating compositional changes in their major element distribution. All shale samples for which new data are presented in this study (n = 113) were subjected to a total digestion for the analysis of major element (Al, Ca, Fe, K, Mn, Na, P, Ti) concentrations.

Finally, a selection of representative shale samples (n = 48) across all depositional settings and time intervals were analysed for total organic carbon (TOC) and phosphorus speciation using a modified version of the SEDEX extraction scheme[38] (see Supplementary Information; note that carbonate samples were avoided due to the potential for additional uptake of P in the carbonate lattice, which may skew comparisons to average shale compositions). This technique quantifies the proportion of total P (P_{Tot}) associated with Fe (oxyhydr)oxide minerals (P_{Fe}), organic matter (P_{org}), authigenic carbonate fluorapatite, biogenic apatite and $CaCO_3$ (P_{auth}), and detrital apatite (P_{det})[38]. Reactive P ($P_{Fe} + P_{org} + P_{auth}$) defines a pool that may potentially be bioavailable and mobile during deposition and early diagenesis[39], in contrast to detrital P.

Results

In the Kuibis Subgroup (~550 to < 547 Ma), carbonate deposits of the Kanies, Mara and lower Omkyk members have been suggested to record recovery from the Shuram C isotope excursion, however the global nature and geochronology of the Shuram excursion remain uncertain (Fig. 2a; see Methods for details of geochemical techniques and their interpretive framework, and Supplementary Information for all data)[5]. At this time, outer ramp deposits in the Zaris sub-basin have persistently elevated $Fe_{HR}/Fe_T > 0.52$ (Fe/Al = 0.7–7; Fig. 2e)[5], whilst samples deposited above fair weather wave base on the shallow inner ramp near the Osis Arch (Fig. 2b) record a transition from initially high (0.58–1.00), to low (0.13–0.19) Fe_{HR}/Fe_T. Meanwhile, distal inner ramp and mid ramp deposits (Fig. 2c,d) continue to record elevated Fe_{HR}/Fe_T (0.35–1.00) throughout the lower Omkyk Member (and equivalent Mara and Kliphoek members) in both sub-basins. Where Fe_{HR}/Fe_T is > 0.38, ratios of Fe_{py}/Fe_{HR} are ubiquitously <0.3 in samples of the Nama Group, implying anoxic, ferruginous conditions (Figure S11). Mid-ramp shales of the Upper Omkyk Member dominantly yield low Fe_{HR}/Fe_T (<0.22; with mean Fe/Al = 0.58), however, limestone samples of the inner to mid-ramp, and occasional shales of the mid-ramp, show elevated Fe_{HR}/Fe_T and Fe/Al.

Strata correlative to the Upper Omkyk and Hoogland members are absent in the Witputs sub-basin[16], and shales were instead sampled from the mid-ramp Vingerbreek Member of the Nudaus Formation (Schwarzrand Subgroup, <547–> 545 Ma, Fig. 2d). Here, shales with $Fe_{HR}/Fe_T < 0.22$ (Fe/Al = 0.54–0.73) are interbedded with shales characterised by $Fe_{HR}/Fe_T > 0.38$ (Fe/Al = 0.80–1.16) and the occurrence of ironstones (Fe_T up to 29.8 wt%).

In the Zaris sub-basin, samples of the Schwarzrand Subgroup (<547– ~538 Ma) have relatively invariant Fe_{HR}/Fe_T values (Fig. 2b,c), largely confined between the calibrated threshold ratios of 0.22 and 0.38 (Fe/Al = 0.41–0.78, mean = 0.58), challenging an unequivocal palaeoredox interpretation. Superimposed upon the iron speciation record, however, is a notable positive trend in Mn/Al and Mn/Fe, reaching an apex in the Urusis Formation (Figure S11) and culminating in values typical for Phanerozoic shale[40]. More distal deposits of the upper Schwarzrand Subgroup on the mid – outer ramp in the Witputs sub-basin (Fig. 2d,e) are characterised by Fe_{HR}/Fe_T between 0.03 and 0.35 (mean = 0.09, n = 84), with the exception of two carbonate samples that are enriched in Fe_{HR} (Fe_{HR}/Fe_T = 0.51 and 0.61).

The chemical index of alteration falls between 59% and 88%, with the highest values confined to the Kuibis Subgroup and the Nudaus Formation (Fig. 2f). The highest CIA values are observed deeper in the succession, in samples of the Upper Omkyk Member of the Zaris sub-basin and the Vingerbreek Member of the Witputs sub-basin, with a provenance from the Kalahari craton to the present east[12]. These high values give way to a narrower range and lower average value in samples of the Schwarzrand Subgroup of the Zaris sub-basin, which were initially a product of sediment input from the north, followed by supply from the east (upper Schwarzrand Subgroup)[12]. The evolving CIA values from samples derived from the east thus support an overall change in weathering intensity, rather than specific changes in lithology.

All shale samples have TOC < 0.3 wt%, with similar concentrations for samples deposited beneath oxic and anoxic bottom waters (Fig. 3a). While P/Al ratios scatter above and below average shale values for both oxic and anoxic samples (Fig. 3b), there is distinct P phase partitioning between these redox conditions (Fig. 3c,d). Oxic samples have low P_{Fe} (mean = 2.6% of P_{Tot}) and low P_{org} (mean = 1.9% of P_{Tot}), with P_{auth} (mean = 52.3% of P_{Tot}) and P_{det} (mean = 34.3% of P_{Tot}) being the dominant pools. By contrast, ferruginous samples comprise relatively more P_{Fe} (mean = 16.4% of P_{Tot}) and P_{org} (mean = 13.0% of P_{Tot}), whilst the contributions of P_{auth} (mean = 36.9% of P_{Tot}) and P_{det} (mean = 26.8% of P_{Tot}) are relatively diminished (but still significant).

Discussion

Fe-speciation data show pronounced water column redox stratification during deposition of the Kuibis Subgroup[5]. Marine transgression during deposition of the Mara, Kliphoek and lower Omkyk members resulted in basin-wide shoaling of the redoxcline, represented by dominantly anoxic ferruginous deeper and shallower (above fair weather wave base) waters (Fig. 2b,c)[5,6]. The data then show more frequent development of oxygenated conditions through the upper Kuibis Subgroup and the lowermost Schwarzrand Subgroup in both shallower and deeper water. However, short-lived anoxic intervals were a common feature of mid-ramp environments. After this, the inner ramp succession was dominantly deposited under oxic water column conditions, while mid and outer ramp sections were also oxygenated, at least by deposition of the upper Schwarzrand Subgroup. Furthermore, the combination of low and stable Fe_{HR}/Fe_T and increasing Mn/Fe (Figure S11) suggest a progressive increase in oxygenation during deposition of the Urusis Formation, culminating in conditions conducive to widespread Mn oxidation. Fossil evidence for habitation by trace making organisms occurs in all stable oxic settings from the Nudaus Formation onwards (see Supplementary Information).

Phosphorus systematics provide insight into nutrient cycling as the redox state of the water column developed in the Nama Group. In particular, consideration of P speciation and P/Al ratios helps to constrain potential productivity feedbacks arising from changes in redox conditions[41–43]. Upwelling of ferruginous deep waters may promote P drawdown in association with iron minerals, thus potentially resulting in elevated P/Al and a negative productivity feedback[44]. By contrast, P drawdown in association with iron minerals would be expected to be less significant under oxic water column conditions. However, whilst some ferruginous samples do show P enrichment relative to average shale (Fig. 3b), the majority are depleted, and there is no systematic difference in relation to oxic samples.

Low average P/Al in ferruginous samples of the Kuibis Subgroup may be a consequence of either generally low phosphate availability in the water column, or P recycling from sediments back to the water column. The cycling of P in sediments is largely contingent upon the redox state of the porewaters and water column, with sulfidic conditions being particularly conducive to P recycling[41]. Anaerobic organic matter remineralisation results in the preferential release of P, giving high C_{org}/P_{org} ratios relative to the Redfield ratio[45], while reductive dissolution of Fe (oxyhydr)oxide minerals also releases P to solution[46]. The P released by these processes may undergo 'sink switching' to authigenic phases such as carbonate fluorapatite[43] or vivianite[47], or may be re-adsorbed to Fe (oxyhydr)oxide minerals where they persist[48]. However, dissolved P may also be recycled back to the water column, particularly under anoxic conditions, potentially promoting a positive productivity feedback[41].

Our redox data suggest limited sulfide production during diagenesis under both oxic and ferruginous conditions (giving very low Fe_{py}/Fe_{HR} ratios; see Supplementary Information). Such conditions would be expected to limit P recycling from the sediment, particularly under oxic conditions (where anaerobic organic matter degradation and the reductive dissolution of Fe (oxyhydr)oxide minerals are restricted), and this can be tested by considering C_{org}/P_{org} and C_{org}/P_{reac} ratios relative to the Redfield ratio[47]. In oxic samples of the Nama Group, C_{org}/P_{org} ratios (Fig. 3e) cluster around the canonical Redfield ratio (106:1). This suggests little preferential release of P from organic matter, which would be consistent with limited anaerobic organic matter remineralization under these low TOC conditions (Fig. 3a). Relatively low C_{org}/P_{reac} ratios, coupled with a high proportion of authigenic P (Fig. 3c–e), suggests that the P released from oxic organic matter degradation and the reductive dissolution of Fe (oxyhydr)oxides deeper in the sediment was subsequently fixed in the sediment via 'sink-switching', with no evidence for recycling back to the water column. Nevertheless, C_{org}/P_{org} ratios at the Redfield ratio argue against chronically nutrient limited productivity (which may raise primary C_{org}/P_{org} values to as high as ~600[49]), and instead our data suggest that the oxic Nama basin experienced rates of productivity typical of oxic marine settings.

Some ferruginous samples have elevated (above the Redfield ratio) C_{org}/P_{org} ratios, suggesting more effective anaerobic organic matter remineralization relative to oxic samples, as would be expected beneath an anoxic water

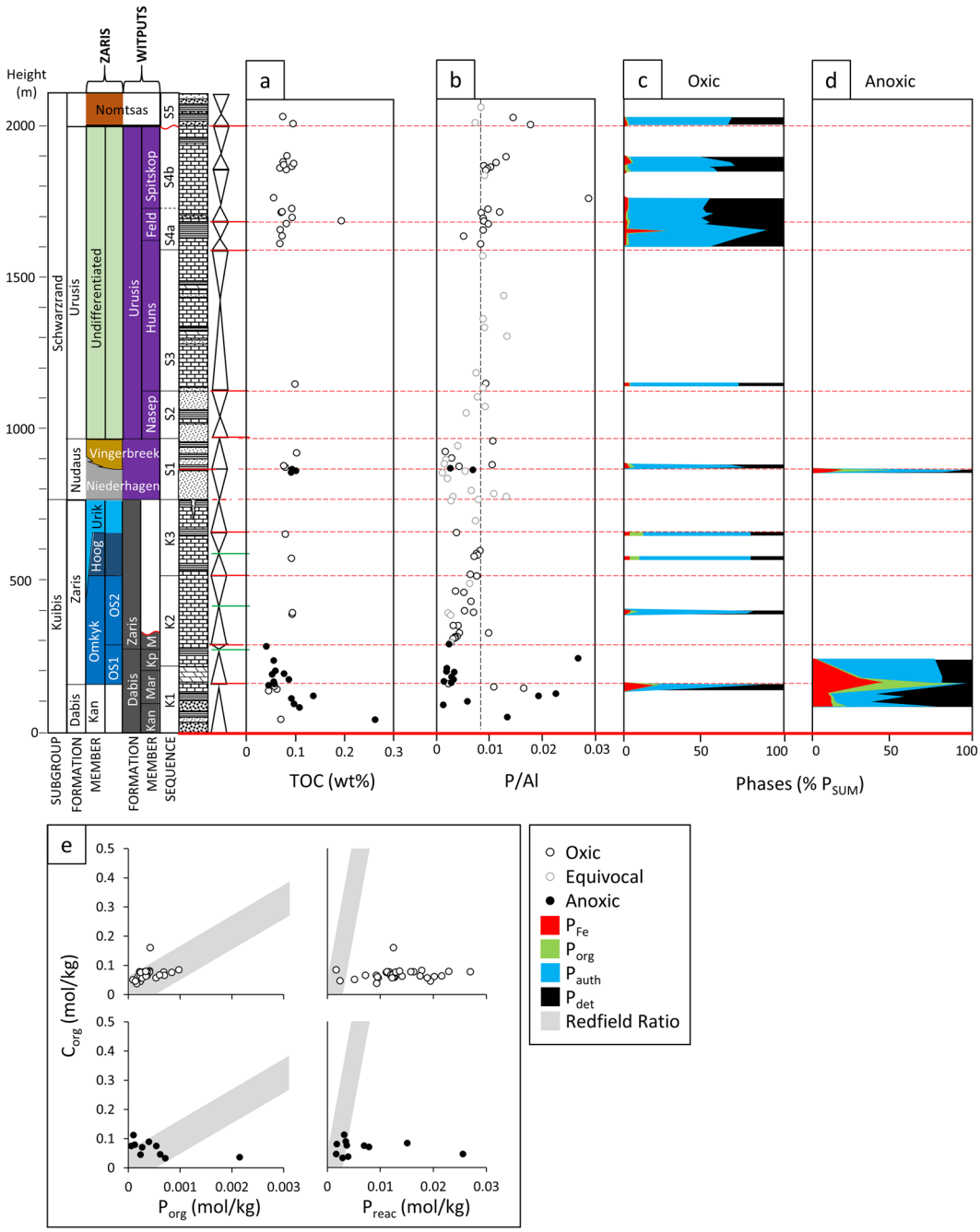

Figure 3. Elemental data of shale samples from the Nama Group, Namibia, differentiated according to redox (based on Fe-speciation). (**a**) TOC, (**b**) The ratio of total phosphorus (P_{Tot}) to aluminium (Al), and P phase proportions in (**c**) oxic and (**d**) anoxic samples. (**e**) Cross-plots show $(C:P)_{org}$ and C_{org}:P_{reac}.

column. C_{org}/P_{reac} ratios are at or below the Redfield ratio, which suggests significant fixation of P in the sediment following draw down with Fe (oxyhydr)oxide minerals. However, despite this enhanced draw down mechanism, the majority of anoxic samples have significantly higher C_{org}/P_{reac} ratios relative to oxic samples, which implies a degree of recycling of P back to the water column under ferruginous conditions, with the potential to stimulate a relative increase in productivity[41].

A specific complication in P speciation analyses of ancient sedimentary rocks involves the post-depositional recrystallisation of authigenic apatite during burial diagenesis[50]. The modified SEDEX protocol employs a sequential chemical extraction which targets P_{auth} (using 1 M Na acetate buffered to pH 4.0) prior to extraction of P_{det} (using 1 M HCl) and as such, any decrease in the solubility of primary P_{auth} as a consequence of burial diagenesis, will be represented by potential transfer of P_{auth} to the P_{det} pool[38]. It has been noted that the detrital P content of modern continental margin sediments is 186 ± 21 ppm[43], whereas modern oligotrophic settings are characterised by P_{det} in the range 62–310 ppm[51]. Samples from the Nama Group have P_{det} concentrations in the

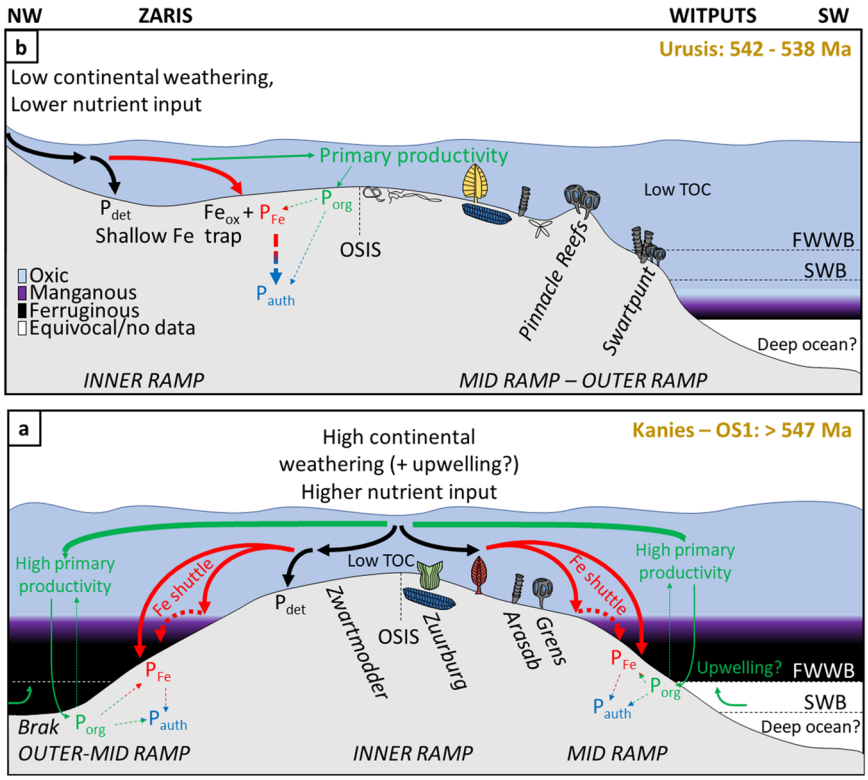

Figure 4. Proposed model for the co-evolution of redox, P burial mechanisms, and evolution of metazoans in the (**a**) lower Kuibis Subgroup (~550–547 Ma), and (**b**) upper Schwarzrand Subgroup (540–538 Ma). Dashed straight arrows denote either sedimentary P diffusion to the water column under ferruginous water column conditions or post-depositional 'sink-switching' of P.

range 4.2–536.4 ppm (mean 208.7 ppm), with maximum values significantly greater than average P_{det} of modern shelf environments. This may suggest that a portion of extracted P_{det} represents burial recrystallisation of initially authigenic P. There is no significant correlation between P_{reac} (as a percentage of P_{Tot}) and Al ($r^2 = 0.077$, Figure S2c), implying negligible contamination of the P_{auth} pool by P_{det}. Consequently, concentrations of P_{auth} (and by extension summed P_{reac}) likely represent minimum values, whilst those of P_{det} represent maximum values (see Supplementary Information for further information).

The combined redox proxy data suggest more oxidising water column conditions in the Nama Group basins (above that required to fully oxidise Fe(II)) in inner to mid ramp environments by the time of deposition of the lower Schwarzrand Subgroup, commencing at ~547 Ma (Fig. 2)[14]. The data also support a further progressive increase in oxygenation of the inner ramp to levels sufficient for Mn oxidation by the upper Urusis Formation at ~542–540 Ma[13,15,52]. Whilst outer ramp sections are sparse in the Nama Group, the available data show that ventilation of the outer ramp occurred, at the latest, by deposition of the Feldschuhhorn Member at ~542 Ma[13,52].

What then, caused the progressive ventilation of the Nama basins at ~547 Ma? Fig. 2f shows available data of the chemical index of alteration through the Nama succession. The extent of chemical weathering is dependent upon factors including tectonics and regional climate, and affects the regional supply of nutrients from the continent and the maturity of terrigenous clays[37]. High average CIA values are a dominant feature of the Kuibis Subgroup, and argue for a high degree of chemical weathering, potentially mediated by hot and humid regional climatic conditions[37]. This is followed by a shift, in the Zaris sub-basin, to lower average values that may record a corresponding transition to cooler and drier conditions. There is a distinct peak in CIA that relates to shales of the Vingerbreek Member from the Witputs sub-basin which were deposited atop a sub-basin scale unconformity attributed to a putative short-lived regional glaciation[53]. This peak reflects sediment transport from a source area to the east on the Kalahari Craton and is coeval with a short-lived return to local water column redox stratification and ironstone deposition (see Supplementary Information, section 3d). The overall decrease in the CIA up-section, coupled with the observed covariation with changes in dominant water column redox conditions, point towards a driving role for changes in continentally derived nutrient influx to the basin through time. In this scenario, initial transgression and a high degree of chemical weathering led to deposition of sediments and delivery of nutrients from the Kalahari Craton to the east of the Nama sub-basins. At this time, nutrient input may have been supplemented by a degree of upwelling from the openly connected Brazilides ocean to the west, leading to elevated regional productivity and anoxia (Figs. 4a, S13). However, gradual closure of the Brazilides[54] ocean likely stifled upwelling in this region, forcing the system to primarily depend upon nutrients supplied from continental weathering. The degree of chemical weathering and associated nutrient input decreased in the Schwarzrand Subgroup, possibly associated with regional climatic

change[53], which would have reduced primary production and hence the extent and maintenance of water column anoxia. The Fe and P speciation data provide insight into the dynamic, regional burial and recycling of the major limiting nutrient P under both ferruginous and oxic conditions[11]. The shallow redoxcline evident during deposition of the lower Kuibis Subgroup readily facilitated the anaerobic degradation of organic matter (and also dissimilatory Fe reduction) in sediments and likely resulted in a small degree of P recycling back to the water column, thus fuelling local productivity (Fig. 4a). However, ferruginous conditions also promoted the removal of reactive P in association with iron minerals, thus limiting the extent of this positive productivity feedback over a timescale of millions of years. By contrast, during deposition of the Schwarzrand Subgroup (547–540 Ma), P was more effectively buried in sediments through sink-switching to authigenic apatite after initial drawdown in association with organic matter and Fe (oxyhydr)oxide minerals (Fig. 4b). The lack of P recycling from oxic sediments of the Schwarzrand Subgoup stabilised oxia in the overlying water column. There is a notable increase in bioturbation intensity recorded in the lowermost Schwarzrand Subgroup[55], however the potential secondary influence of bioirrigation and mixing-induced sedimentary P retention on local water column productivity remains uncertain.

The consistent spatial separation of anoxic deep waters from the distribution of soft-bodied, skeletal and ichnotaxa in the Nama Group may support the contention that oxygen was a metabolic requirement of these organisms. High resolution sub-sampling of fossiliferous beds in the Nama Group has previously revealed the ability of the skeletal *Namacalathus* to opportunistically colonise the substrate during fleeting oxic episodes under a regime of dominantly ferruginous water column conditions[5]. Similarly, palaeoredox studies of fossiliferous shales of the Blueflower Formation, NW Canada, have been interpreted to show the ability of soft-bodied forms including possible *Pteridinium*, *Inkrylovia* and *Windermeria*, to opportunistically colonise environments that were briefly ventilated for shorter durations than those resolvable by bulk Fe proxy capability[56]. Ferruginous conditions that dominated the deeper water column during deposition of the Kuibis Subgroup may have limited habitable space for soft-bodied macrobiota, the majority of which are preserved in the shallowest environments. However, some *in situ Ernietta* and *Rangea* specimens are also suggested to have been able to opportunistically colonise the substrate during short-lived oxic episodes, similar to the Blueflower Formation, or the ability to survive incursions of anoxic bottom waters[57].

Whilst there is no paucity of siliciclastic facies in the Witputs sub-basin throughout the Nama succession, the majority of soft-bodied fossil representatives are known only from shallow, shoreface and inner-ramp, quartz-rich sandstone horizons. Particularly prominent fossiliferous quartzites appear in the Aar, Nasep and Spitskop members (see Supplementary Information Table S1 for references)[23,57]. However, a notable trend of increasing bioturbation intensity is present in the shallow inner to mid-ramp during deposition of the Nudaus Formation[55], within the middle part of the Nama Group succession (Fig. 2g). There is a further increase in bioturbation intensity from the lower Schwarzrand Subgroup to the basal Cambrian unconformity in the Nama Group[26,55]. Indeed, recent quantification of bioturbation intensity in the Nama Group shows an overall increase in the percentage of bedding plane bioturbated from a mean value of 1.94% in the Kliphoek Member to 3.34% in the lower Urusis Formation, and a further increase to 5.61% in the Spitskop Member, immediately beneath the basin-wide unconformity that marks the top of the Urusis Formation (Fig. 2g)[55]. The increase in bioturbation intensity occurs coincident with the stabilisation of oxic conditions in this location (Fig. 2).

The local transition to stable, oxic conditions observed in the Nama succession may have been a prerequisite for the increase in bioturbation intensity in this shallow ramp setting, allowing the efficient exploitation of nutrients held within the sediment and microbial mats. However, the link between oxygenation and increased bioturbation intensity is less clear in broadly contemporaneous successions of South China. Here, sediments of the Dengying Formation contain trace fossils[58] alongside proxy evidence for only punctuated oxic intervals under a regime of dominantly anoxic water column conditions[9,59]. Evidence from nitrogen isotope studies[60] of fossiliferous Ediacaran and early Cambrian strata in South China attest to a regional nutrient regime distinct from that of the Nama Group, with high nutrient delivery to the Yangtze platform and slope, likely (in part) supplied by enhanced upwelling, driving an intense and long-lived OMZ throughout this interval[9]. A comparison of the relative rates of ichnotaxa diversification and their spatial distributions between stratigraphic successions of the Nama Group and South China, is required to test the relationship between palaeoredox of equivalent facies and relative diversification rates between these two potentially differing late Ediacaran palaeoenvironments.

Skeletal macrofossil assemblages of the Ediacaran attain their highest abundance and diversity in the Kuibis Subgroup of the Nama Group, where surface and mid-depths were occasionally well oxygenated but deeper waters were anoxic and nutrient rich[5,6]. Indeed, iron speciation data support the importance of a dominantly oxic local environment for the most diverse skeletal assemblage in the Nama basin (Driedoornvlakte, Figure S7). In the Dengying Formation, the shallowest environments of Shaanxi province and the Baimatuo Member in the Yangtze Gorges host relatively depauperate, microbial mat-related skeletal assemblages (e.g.[61]), where rare earth element profiles suggest continued redox instability with only short-lived oxic intervals[59]. The differing geochemical characteristics observed between palaeoenvironments of the Nama Group and Yangtze Platform may suggest a delicate balance between oxygen demand and nutrient loading as an incentive for the radiation of motile macrobiota, and potentially for ecosystem habitation by skeletal organisms in the late Ediacaran. This may allude to a 'sweet spot' in oxygen and nutrient demand for skeletonising and filter feeding ecologies in the late Ediacaran, however this remains to be tested.

While geochemical evidence from the uranium isotopic composition of carbonates ($\delta^{238}U_{carb}$) points to an increase in the global extent of anoxic ocean waters at ~547 Ma[62,63], the redox data reported here show that, on a local scale, the Nama basins became more stable and oxic at this time. These global and local datasets are not necessarily in conflict, as the uranium proxy data may record an integrated global increase in the spatial extent of productive mid-depth waters at ~547 Ma. In fact, recent compilations of $\delta^{238}U_{carb}$ from globally distributed late

Ediacaran successions do suggest a trend towards an increasingly oxygenated global ocean between 545–540 Ma, in the wake of the highly negative values recorded in the lower Nama Group and Dengying Formation[62–64]. However, these global oxygenation events were transient, and their influence on the pace of animal evolution in shallow shelf ecosystems which were subject to highly heterogeneous local redox conditions demands further investigation.

Conclusions

Soft-bodied macrobiota occupied a predominantly intertidal to shallow sub-tidal setting throughout deposition of the Nama Group, likely at least partly due to the constraint of proximal deep water anoxia[5,6]. Stable and long-lived oxia in shallow marine oases supported the most diverse skeletal communities in mid-ramp settings[5,6]. Both sub-basins exhibit a shift towards widespread oxic stabilisation between ~547 and ~542 Ma that is accompanied by a distinct transition from high average values of CIA in the Kuibis Subgroup to low values in the Schwarzrand Subgroup. The combined trends in redox and weathering proxies may reflect a reduced supply of continentally derived nutrients, potentially linked to a change in regional climate. This, in turn, reduced primary productivity from initial conditions that were conducive to basin wide anoxia during organic matter remineralisation, to normal oxic marine production. Fe and P speciation studies within the context of evolving basin sedimentology provide evidence for distinct P recycling mechanisms between initially redox stratified conditions in the Kuibis Subgroup and stable, oxic conditions of the overlying Schwarzrand Subgroup. During deposition of the Schwarzrand Subgroup, efficient sink-switching of organic and Fe oxide bound P to authigenic phases was promoted under oxic water column conditions, which may have further stabilised oxic conditions through limiting pore water P recycling. Oxic stabilisation of the Nama sub-basins was accompanied by progressive occupation by active, motile trace makers, which thrived first in shallow inner ramp settings, but later in mid-ramp, clastic environments.

Received: 23 September 2019; Accepted: 30 December 2019;
Published online: 10 February 2020

References

1. Pu, J. P. *et al*. Dodging snowballs: Geochronology of the Gaskiers glaciation and the first appearance of the Ediacaran biota. *Geology* **44**, 955–958 (2016).
2. Seilacher, A., Buatois, L. A. & Mángano, M. G. Trace fossils in the Ediacaran-Cambrian transition: Behavioral diversification, ecological turnover and environmental shift. *Palaeogeogr. Palaeoclimatol. Palaeoecol.* **227**, 323–356 (2005).
3. Germs, G. J. B. New shelly fossils from Nama Group, South West Africa. *American Journal of Science* **272**, 752–761 (1972).
4. Sperling, E. A., Knoll, A. H. & Girguis, P. R. The Ecological Physiology of Earth's Second Oxygen Revolution. *Annu. Rev. Ecol. Evol. Syst*. **46**, annurev-ecolsys-110512-135808 (2015).
5. Wood, R. A. *et al*. Dynamic redox conditions control late Ediacaran metazoan ecosystems in the Nama Group, Namibia. *Precambrian Res.* **261**, 252–271 (2015).
6. Tostevin, R. *et al*. Low-oxygen waters limited habitable space for early animals. *Nat. Commun.* **7**, 12818 (2016).
7. Sperling, E. A. *et al*. Statistical analysis of iron geochemical data suggests limited late Proterozoic oxygenation. *Nature* **523**, 451–454 (2015).
8. Och, L. M. *et al*. Palaeoceanographic controls on spatial redox distribution over the Yangtze Platform during the Ediacaran-Cambrian transition. *Sedimentology* **63**, 378–410 (2016).
9. Bowyer, F., Wood, R. A. & Poulton, S. W. Controls on the evolution of Ediacaran metazoan ecosystems: A redox perspective. *Geobiology* **15**, 516–551 (2017).
10. Guilbaud, R. *et al*. Oxygen minimum zones in the early Cambrian ocean. *Geochemical Perspect. Lett*. 33–38. https://doi.org/10.7185/geochemlet.1806 (2018)
11. Tyrrell, T. The relative influences of nitrogen and phosphorus on oceanic primary production. *Nature* **400**, 525–531 (1999).
12. Germs, G. J. B. Implications of a sedimentary facies and depositional environmental analysis of the Nama Group in South West Africa/Namibia. *Spec. Publ. Geol. Soc. South Africa* **11**, 89–114 (1983).
13. Grotzinger, J. P., Bowring, S. A., Saylor, B. Z. & Kaufman, A. J. Biostratigraphic and Geochronologic Constraints on Early Animal Evolution. *Science (80-.).* **270**, 598–604 (1995).
14. Bowring, S. A. *et al*. Geochronologic constraints on the chronostratigraphic framework of the Neoproterozoic Huqf Supergroup, Sultanate of Oman. *Am. J. Sci.* **307**, 1097–1145 (2007).
15. Linnemann, U. *et al*. New high-resolution age data from the Ediacaran-Cambrian boundary indicate rapid, ecologically driven onset of the Cambrian explosion. *Terra Nov*. 0–3, https://doi.org/10.1111/ter.12368 (2018)
16. Saylor, B. Z., Kaufman, A. J., Grotzinger, J. P. & Urban, F. A composite reference section for terminal proterozoic strata of southern Namibia. *J. Sediment. Res.* **68**, 1223–1235 (1998).
17. Kaufman, A. J., Hayes, J. M., Knoll, A. H. & Germs, G. J. B. Isotopic compositions of carbonates and organic carbon from upper Proterozoic successions in Namibia: stratigraphic variation and the effects of diagenesis and metamorphism. *Precambrian Res.* **49**, 301–327 (1991).
18. Saylor, B., Grotzinger, J. P. & Germs, G. Sequence stratigraphy and sedimentology of the Neoproterozoic Kuibis and Schwarzrand Subgroups (Nama Group), southwestern Namibia. *Precambrian Res.* **73**, 153–171 (1995).
19. Saylor, B. Z. Sequence stratigraphy and carbonate-siliciclastic mixing in a terminal Proterozoic foreland basin, Urusis Formation, Nama Group, Namibia. *J. Sediment. Res.* **73**, 264–279 (2003).
20. Kaufman, A. J., Jacobsen, S. B. & Knoll, A. H. The Vendian record of Sr and C isotopic variations in seawater: Implications for tectonics and paleoclimate. *Earth Planet. Sci. Lett.* **120**, 409–430 (1993).
21. Gurich, G. Uber den Kuibisquartzit in Sudwest-afrika. *Zeitschrift Dtsch. Geol. Gesellschaft* **82**, 637 (1930).
22. Germs, G. J. B. A reinterpretation of Rangea schneiderhoehni and the discovery of a related new fossil from the Nama Group, South West Africa. *Lethaia* **6**, 1–9 (1973).
23. Narbonne, G. M., Saylor, B. Z. & Grotzinger, J. P. The youngest Ediacaran fossils from southern Africa. *J. Paleontol.* **71**, 953–967 (1997).
24. Germs, G. J. B., Knoll, A. H. & Vidal, G. Latest proterozoic microfossils from the Nama group, Namibia (south west Africa). *Precambrian Res.* **32**, 45–62 (1986).
25. Wood, R. A., Grotzinger, J. P. & Dickson, J. A. D. Proterozoic Modular Biomineralized Metazoan from the Nama Group, Namibia. *Science (80-.).* **296**, 2383–2386 (2002).

26. Jensen, S. M. & Runnegar, B. N. A complex trace fossil from the Spitskop Member (terminal Ediacaran–? Lower Cambrian) of southern Namibia. *Geol. Mag.* **142**, 561–569 (2005).
27. Buatois, L. A., Almond, J., Mángano, M. G., Jensen, S. & Germs, G. J. B. Sediment disturbance by Ediacaran bulldozers and the roots of the Cambrian explosion. *Sci. Rep.* **8**, 1–9 (2018).
28. Poulton, S. & Canfield, D. Development of a sequential extraction procedure for iron: implications for iron partitioning in continentally derived particulates. *Chem. Geol.* **214**, 209–221 (2005).
29. Poulton, S. W., Krom, M. D. & Raiswell, R. A revised scheme for the reactivity of iron (oxyhydr)oxide minerals towards dissolved sulfide. *Geochim. Cosmochim. Acta* **68**, 3703–3715 (2004).
30. Poulton, S. W., Fralick, P. W. & Canfield, D. E. The transition to a sulphidic ocean, 1.84 billion years ago. *Nature* **431**, 173–177 (2004).
31. Poulton, S. W. & Raiswell, R. The low-temperature geochemical cycle of iron: From continental fluxes to marine sediment deposition. *Am. J. Sci.* **302**, 774–805 (2002).
32. Poulton, S. W. & Canfield, D. E. Ferruginous Conditions: A Dominant Feature of the Ocean through Earth's History. *Elements* **7**, 107–112 (2011).
33. Raiswell, R. *et al*. Turbidite depositional influences on the diagenesis of Beecher's Trilobite Bed and the Hunsrück Slate; sites of soft tissue pyritization. *Am. J. Sci.* **308**, 105–129 (2008).
34. Clarkson, M. O., Poulton, S. W., Guilbaud, R. & Wood, R. a. Assessing the utility of Fe/Al and Fe-speciation to record water column redox conditions in carbonate-rich sediments. *Chem. Geol.* **382**, 111–122 (2014).
35. Saylor, B. Z. & Grotzinger, J. P. Reconstruction of important Proterozoic-Cambrian boundary exposures through the recognition of thrust deformation in the Nama Group of southern Namibia. *Commun. - Geol. Surv. Namibia* **11**, 1–12 (1996).
36. Wood, R., Bowyer, F., Penny, A. & Poulton, S. W. Did anoxia terminate Ediacaran benthic communities? Evidence from early diagenesis. *Precambrian Res.* **313**, 134–147 (2018).
37. Nesbitt, H. W. & Young, G. M. Early Proterozoic climates and plate motions inferred from major element chemistry of lutites. *Nature* **299**, 715–717 (1982).
38. Thompson, J. *et al*. Development of a modified SEDEX phosphorus speciation method for ancient rocks and modern iron-rich sediments. *Chem. Geol.* **524**, 383–393 (2019).
39. Ruttenberg, K. C. Development of a sequential extraction method for different forms of phosphorus in marine sediments. *Limnol. Oceanogr.* **37**, 1460–1482 (1992).
40. Turekian, K. K. & Wedepohl, K. H. Distribution of the Elements in Some Major Units of the Earth's Crust. *Geol. Soc. Am. Bull.* **72**, 175–192 (1961).
41. Ingall, E. & Jahnke, R. Evidence for enhanced phosphorus regeneration from marine sediments overlain by oxygen depleted waters. *Geochim. Cosmochim. Acta* **58**, 2571–2575 (1994).
42. Slomp, C. P., Thomson, J. & De Lange, G. J. Enhanced regeneration of phosphorus during formation of the most recent eastern Mediterranean sapropel (S1). *Geochim. Cosmochim. Acta* **66**, 1171–1184 (2002).
43. Ruttenberg, K. & Berner, R. Authigenic apatite formation and burial in sediments from non-upwelling, continental margin environments. *Geochim. Cosmochim. Acta* **57**, 991–1007 (1993).
44. Reinhard, C. T. *et al*. Evolution of the global phosphorus cycle. *Nature* **541**, 386–389 (2017).
45. Ingall, E. D., Bustin, R. M. & Van Cappellen, P. Influence of water column anoxia on the burial and preservation of carbon and phosphorus in marine shales. *Geochim. Cosmochim. Acta* **57**, 303–316 (1993).
46. Slomp, C. P., Epping, E. H. G., Helder, W. & Van Raaphorst, W. A key role for iron-bound phosphorus in authigenic apatite formation in North Atlantic continental platform sediments. *J. Mar. Res.* **54**, 1179–1205 (1996).
47. Xiong, Y. *et al*. Phosphorus cycling in Lake Cadagno, Switzerland: A low sulfate euxinic ocean analogue. *Geochim. Cosmochim. Acta* **251**, 116–135 (2019).
48. Slomp, C. P., Van Der Gaast, S. J. & Van Raaphorst, W. Phosphorus binding by poorly crystalline iron oxides in North Sea sediments. **52**, 55–73 (1996).
49. White, A. E., Spitz, Y. H., Karl, D. M. & Letelier, R. M. Flexible elemental stoichiometry in Trichodesmium spp. and its ecological implications. *Limnol. Oceanogr.* **51**, 1777–1790 (2006).
50. März, C., Poulton, S. W., Wagner, T., Schnetger, B. & Brumsack, H. J. Phosphorus burial and diagenesis in the central Bering Sea (Bowers Ridge, IODP Site U1341): Perspectives on the marine P cycle. *Chem. Geol.* **363**, 270–282 (2014).
51. Slomp, C. P. *et al*. Coupled Dynamics of Iron and Phosphorus in Sediments of an Oligotrophic Coastal Basin and the Impact of Anaerobic Oxidation of Methane. *PLoS One* **8** (2013).
52. Schmitz, M. D. Radiogenic Isotope Geochronology. in *The Geological Time Scale 2012* (eds Gradstein, F. M., Ogg, J. G., Schmitz, M. D. & Ogg, G. M.) (Elsevier, 2012).
53. Germs, G. J. B. & Gaucher, C. Nature and Extent of a Late Ediacaran (Ca. 547 Ma) Glacigenic Erosion Surface in Southern Africa. *South African J. Geol.* **115**, 91–102 (2012).
54. Gaucher, C., Frimmel, H. E. & Germs, G. J. B. Tectonic Events and Palaeogeographic Evolution of Southwestern Gondwana in the Neoproterozoic and Cambrian. in *Neoproterozoic to Cambrian Tectonics, Global Change and Evolution: a Focus on Southwestern Gondwana. Developments in Precambrian Geology* (eds Gaucher, C., Sial, A. N., Halverson, G. P. & Frimmel, H. E.) **16**, 295–316 (Elsevier, 2009).
55. Cribb, A. T. *et al*. Increase in metazoan ecosystem engineering prior to the Ediacaran–Cambrian boundary in the Nama Group, Namibia. *R. Soc. Open Sci.* **6**, 190548 (2019).
56. Sperling, E. A. *et al*. Oxygen, facies, and secular controls on the appearance of Cryogenian and Ediacaran body and trace fossils in the Mackenzie Mountains of northwestern Canada. *Bull. Geol. Soc. Am.* **128**, 558–575 (2015).
57. Hall, M. *et al*. Stratigraphy, palaeontology and geochemistry of the late Neoproterozoic Aar Member, southwest Namibia: Reflecting environmental controls on Ediacara fossil preservation during the terminal Proterozoic in African Gondwana. *Precambrian Res.* **238**, 214–232 (2013).
58. Meyer, M. *et al*. Interactions between Ediacaran animals and microbial mats: Insights from Lamonte trevallis, a new trace fossil from the Dengying Formation of South China. *Palaeogeogr. Palaeoclimatol. Palaeoecol.* **396**, 62–74 (2014).
59. Ling, H. F. *et al*. Cerium anomaly variations in Ediacaran-earliest Cambrian carbonates from the Yangtze Gorges area, South China: Implications for oxygenation of coeval shallow seawater. *Precambrian Res.* **225**, 110–127 (2013).
60. Cremonese, L., Shields-Zhou, G. A., Struck, U., Ling, H. F. & Och, L. M. Nitrogen and organic carbon isotope stratigraphy of the Yangtze Platform during the Ediacaran-Cambrian transition in South China. *Palaeogeogr. Palaeoclimatol. Palaeoecol.* **398**, 165–186 (2014).
61. Cai, Y., Hua, H., Schiffbauer, J. D., Sun, B. & Yuan, X. Tube growth patterns and microbial mat-related lifestyles in the Ediacaran fossil Cloudina, Gaojiashan Lagerstätte, South China. *Gondwana Res.* **25**, 1008–1018 (2014).
62. Tostevin, R. *et al*. Uranium isotope evidence for an expansion of anoxia in terminal Ediacaran oceans. *Earth Planet. Sci. Lett.* **506**, 104–112 (2019).
63. Zhang, F. *et al*. Extensive marine anoxia during the terminal Ediacaran Period. *Sci. Adv.* **4**, eaan8983 (2018).
64. Zhang, F. *et al*. Global marine redox changes drove the rise and fall of the Ediacara biota. *Geobiology* **17**, 594–610 (2019).

Acknowledgements
FB was funded by a NERC DTP (Grant award code NE/L002558/1), and RW and SWP by the NERC BETR Project (Grant award code NE/P013643/1). AS was funded by the School of GeoSciences, University of Edinburgh, and LA was funded by a Leeds Anniversary Research Scholarship. SWP acknowledges financial support from a Royal Society Wolfson Research Merit Award and a Leverhulme Research Fellowship. FB would like to thank G.J.B. Germs and A. Yu. Zhuravlev for enlightening discussions relating to Nama Group stratigraphy, fossil occurrence and affinity. We are grateful to Helke Mocke and Charlie Hoffmann of the Geological Survey of Namibia and the Ministry of Mines and Energy, Namibia, and to C. Husselman and A. and S. Horn for permission to access localities on farms Driedoornvlakte and Omkyk, respectively, and B. Romer and L. Gessert for permission to access Farm Swartpunt.

Author contributions
F.B., R.W., A.S. and S.P. conceived the work. F.B., R.W., A.P., S.H., A.C. and S.C.-W. collected the sample material. F.B., A.S. and L.A. analysed samples and collected the data, with help from A.T. and I.B. F.B. prepared the figures. All authors wrote the paper.

Competing interests
The authors declare no competing interests.

Additional information
Supplementary information is available for this paper at https://doi.org/10.1038/s41598-020-59335-2.

Correspondence and requests for materials should be addressed to F.T.B.

Reprints and permissions information is available at www.nature.com/reprints.

Publisher's note Springer Nature remains neutral with regard to jurisdictional claims in published maps and institutional affiliations.

Appendix 1.2 Data Tables

1.2.1 Phosphorus speciation data

Blue cells indicate oxic samples and dark grey indicates anoxic samples.

Subasin	Field site	Location	Section Height (m)	Sample i.d.	Sample #	Mass (g)	P_{re1} wt%	P_{auth} wt%	P_{mag} wt%	P_{Fe2} wt%	P_{det} wt%	P_{org} wt%	P_{reac} wt%
Zaris Basin	Brak	23°58'16.98"S, 16°08'06.48"E	60	BRK2/11	23	0.159	0.001	0.008	0	0	0.003	0.001	0.011
			65	BRK2/12	30	0.1603	0.001	0.003	0	0	0.01	0	0.006
	Driedoornvlagte	23°51.429'S 16°39.637'E	460	DV2-19	40	0.1635	0	0.047	0.001	0.001	0.015	0.001	0.05
			470	DV2-20	5	0.1614	0.001	0.031	0.001	0	0.009	0.002	0.035
			555	DV2-21	37	0.1734	0.001	0.03	0.001	0	0.009	0.003	0.034
	Omkyk	24°48'19.02"S, 16°13'45.00"E	3	OMK3/2	9	0.1796	0.001	0.001	0	0.004	0	0.007	0.012
			4.5	OMK3/3	4	0.163	0.002	0	0	0.001	0.001	0.002	0.005
			44	OMK3/14	21	0.165	0.002	0.075	0.001	0	0.024	0.001	0.079
			73	OMK4/1	11	0.1818	0.005	0.001	0	0	0.001	0.002	0.009
	Zwartmodder	24°53'40.98"S, 16°19'31.02"E	3	SWM2/1	29	0.1824	0	0.027	0.001	0	0.048	0.001	0.029
			15.3	SWM2/3	43	0.1756	0.001	0.005	0	0.001	0.001	0	0.007
	D850	Road transect D850	660	S1	39	0.1666	0	0.019	0	0	0.006	0.002	0.022
			865	S5	45	0.1662	0.002	0.017	0.001	0	0.005	0.002	0.021
			1775.45	S12b	42	0.1877	0.002	0.055	0.002	0	0.054	0.001	0.06
	D860/C14	Road transect C14	2022.35	D860-9	32	0.171	0.001	0.051	0.001	0.001	0.022	0.001	0.055
			2045.72	D860-18	27	0.1624	0.002	0.067	0.001	0	0.04	0.001	0.071
				D860-20	44	0.1714	0	0.061	0.001	0	0.031	0.001	0.063
Wiputs Subbasin	Arasab	26°57'48.54"S, 16°27'25.98"E	1.6	ARS4/1	26	0.1712	0.002	0.009	0	0	0.009	0	0.011
			2.6	ARS4/2	16	0.1702	0.002	0.007	0	0	0.015	0	0.01
			22.2	ARS4/6	1	0.1646	0.007	0.015	0.001	0.001	0.006	0.001	0.024
	Nudaus	27°17'05.28"S, 16°46'47.58"E	10	NUD-1	34	0.167	0.008	0.021	0	0	0.003	0.016	0.047
			24	NUD-3	36	0.1725	0.001	0.026	0	0	0.009	0.001	0.029
			31	NUD-4	25	0.1615	0.001	0.051	0.001	0	0.027	0.001	0.054
	Pinnacle Reef	27°26'48.24"S, 16°33'43.62"E	1.5	SK1/1	31	0.1683	0	0.028	0.001	0	0.027	0.001	0.03
			10.15	SK1/3	28	0.1677	0	0.028	0	0	0.012	0.001	0.029
			15.75	SK1l/4	12	0.1608	0.016	0.04	0.001	0	0.008	0.002	0.058
			23.75	SK1/5	41	0.18	0.001	0.034	0.001	0	0.037	0.001	0.037
			34.95	SK1/6	14	0.1658	0.001	0.035	0.001	0	0.034	0.001	0.039
			44.55	SK1/7	33	0.1844	0	0.032	0.001	0	0.038	0.001	0.035
			69.04	SK1/8	35	0.168	0	0.037	0.001	0	0.032	0.001	0.039
			75	SK1/9	24	0.1686	0.001	0.036	0.001	0	0.038	0.001	0.039
			89	SK1/10	47	0.1748	0.001	0.034	0.001	0	0.038	0.001	0.036
	Swartpunt	27°28'25.98"S, 16°41'45.12"E	69.04	SWP2/5	6	0.1694	0.001	0.035	0.001	0	0.028	0.002	0.038
			70.24	SWP2/6	2	0.1604	0	0.036	0.001	0	0.031	0.001	0.038
			72.64	SWP2/7	17	0.1725	0.001	0.038	0.001	0	0.036	0.001	0.04
			74.74	SWP2/8	3	0.1658	0	0.065	0.001	0	0.03	0.001	0.067
			78.44	SWP2/10	19	0.1627	0.001	0.039	0.001	0.003	0.022	0.001	0.044
			87.24	SWP2/12	15	0.1596	0.001	0.034	0.001	0	0.043	0.001	0.037

1.2.2 Bulk element analysis and total organic carbon

Blue cells indicate oxic samples and dark grey indicates anoxic samples.

Subasin	Field site	Location	Section Height	sample	Al	Ca	Fe	K	Mn	Na	P	Ti	TOC	Al	P/Al
			(m)	i.d.	(wt%)	(wt%)	(wt%)	(wt%)	(ppm)	(wt%)	(ppm)	(ppm)	(wt%)	(ppm)	
Zaris Basin	Brak	23°58'16.98"S, 16°08'06.48"E	60	BRK2/11	9.79		5.03		187		116		0.11	97900	0.001185
			65	BRK2/12	2.4		1.48		795		136		0.1	24000	0.005667
	Driedoornvlagte	23°51.429'S 16°39.637'E	460	DV2-19	9.9	0.3	5.7	2.88	427	0.07	681	0.27	0.09	99000	0.006879
			470	DV2-20	9.34	0.26	5.46	2.7	251	0.79	483	0.27	0.09	93400	0.005171
			555	DV2-21	7.13		3.59	1.61	182	0.91	500	0.24	0.09	71300	0.007013
	Omkyk	24°48'19.02"S, 16°13'45.00"E	3	OMK3/2	4.45		0.64		50		121		0.05	44500	0.002719
			4.5	OMK3/3	6.6		1.3		52		87		0.06	66000	0.001318
			44	OMK3/14	4.78		2.03		54		1263		0.06	47800	0.026423
			73	OMK4/1	2.49		0.71		51		57		0.04	24900	0.002289
	Zwartmodder	24°53'40.98"S, 16°19'31.02"E	3	SWM2/1	5.15		2		323		837		0.05	51500	0.016252
			15.3	SWM2/3	4.41		1.86		224		97		0.06	44100	0.0022
	D850	Road transect D850	660	S1	9.22		6.49		352		338		0.08	92200	0.003666
			865	S5	5.86		3.68		205		311		0.09	58600	0.005307
			930	S8	8.28		3.82		260		132		0.1	82800	0.001594
			1775.45	S12b	4.39		3.37		411		1245		0.06	43900	0.02836
	D860/C14	Road transect C14	1157.7	D860-9	9.49	0.25	4.9	2.9	377	1.23	868	0.36	0.1	94900	0.009146
			2022.35	D860-18	6.87	0.38	2.94	1.6	511	1.49	1204	0.26	0.1	68700	0.017525
			2045.72	D860-20	7.36	0.35	3.58	2.05	501	2.02	1051	0.28	0.07	73600	0.01428
Witputs Subbasin	Arasab	26°57'48.54"S, 16°27'25.98"E	1.6	ARS4/1	1.12		1.29		1241		213		0.09	11200	0.019018
			2.6	ARS4/2	1.14		1.2		941		255		0.14	11400	0.022368
			22.2	ARS4/6	11.99		4.93		181		328		0.09	119900	0.002736
	Nudaus	27°17'05.28"S, 16°46'47.58"E	10	NUD-1	9.13	0.14	9.41	2.07	686	1.49	540	0.18	0.1	91300	0.005915
			21	NUD-2	11.15	0.11	8.17	3.07	914	1.04	243	0.31	0.09	111500	0.002179
			24	NUD-3	11.27	0.16	5.07	2.87	912	0.68	397	0.28	0.08	112700	0.003523
			31	NUD-4	10.21	0.23	4.94	2.33	677	0.8	891	0.26	0.08	102100	0.008727
	Pinnacle Reef	27°26'48.24"S, 16°33'43.62"E	1.5	SK1/1	7.76		3.91		743		637		0.07	77600	0.008209
			10.15	SK1/3	9.13		4.81		317		460		0.07	91300	0.005038
			15.75	SK1/4	8.7		4.5		312		758		0.07	87000	0.008713
			23.75	SK1/5	8.33		4.63		1064		803		0.08	83300	0.00964
			34.95	SK1/6	9.05		5.29		705		797		0.19	90500	0.008807
			44.55	SK1/7	9.05		5.37		683		788		0.09	90500	0.008707
			69.04	SK1/8	9.63		5.29		624		799		0.07	96300	0.008297
			75	SK1/9	7.46		4.16		259		877		0.07	74600	0.011756
			89	SK1/10	8.95		5.25		377		858		0.09	89500	0.009587
	Swartpunt	27°28'25.98"S, 16°41'45.12"E	69.04	SWP2/5	7.69				350		704		0.08	76900	0.009155
			70.24	SWP2/6	7.63				502		724		0.07	76300	0.009489
			72.64	SWP2/7	8.18				830		825		0.09	81800	0.010086
			74.74	SWP2/8	8.55				438		750		0.08	85500	0.008772
			78.44	SWP2/10	6.44				857		715		0.07	64400	0.011102
			87.24	SWP2/12	7.1				318		922		0.08	71000	0.012986

Appendix 1.3 Detailed Methods from Bowyer et al. (2020) Supplementary Materials

1.3.1 Analytical Protocols

Sample preparation

Outcrop shale samples were taken with a minimum mass of ~40 g, weathered surfaces were removed and samples were divided in two with a diamond saw, washed and dried at 40°C. Samples with visible signs of alteration and/or veining were rejected at this point. Halved samples were crushed and pulverised to homogeneous powder (<60 µm) using a tungsten carbide jaw crusher and disc mill.

Total digestion

After ashing at 550°C for 8 hours, samples were quantitatively dissolved in trace metal grade HNO_3, HF, and $HClO_4$, heated in open PTFE cups and left to dry fully over a period of 24 hours before addition of H_3BO_3 to prevent the formation of Al complexes. Dry residues were then dissolved in concentrated HNO_3 and diluted with ultrapure 18MΩ H_2O. Resultant solutions were analysed on a Varian Vista-Pro CCD simultaneous ICP-OES at the University of Edinburgh, Grant Institute with replicate analyses yielding a RSD of <3%.

Fe speciation

Iron speciation analyses follow the method of (1). An initial leach targeting iron bound in carbonate phases (Fe_{carb}) employed Na-acetate, buffered to pH 4.5 with acetic acid and agitated at 50°C for 48 hrs. This was followed by a 2hr iron oxide (Fe_{ox}) extraction in Na-dithionite buffered to pH 4.8 and a final extraction of magnetite (Fe_{mag}) with ammonium oxalate for 6 hrs. All steps of the sequential leach were performed at the Cohen Laboratories,

Leeds University, School of Earth and Environment, and resultant solutions were analysed for Fe using a Thermo Scientific iCE-3000 series flame atomic absorption spectrometer with replicate extractions for each step yielding RSDs of <5% (Table S4).

The concentration of pyrite iron (Fe_{py}) was determined through a boiling chromous chloride distillation with a pre-leach in boiling 6 M HCl for quantitative extraction of acid volatile sulfide (AVS) after the method of (2). Weight percent AVS and Fe_{py} were determined gravimetrically after stoichiometric precipitation of Ag_2S.

P speciation

A modified version of the SEDEX method (3), attuned for the analysis of ancient sedimentary rocks (4) was used in the quantitative assessment of P phases. One major advantage of the modified sequential extraction procedure is the ability to target P bound in haematite and magnetite (4) in addition to authigenic, organic and detrital P.

Method

Approximately 0.15 – 0.19 g sample powder was subjected to the modified sequential extraction scheme (4). A graphical representation of the procedural protocol is shown in Figure S1. Following each step in the sequential leach, samples were centrifuged at 4000 rpm for 4 minutes and aliquots of 8 ml were taken from the supernatant solution for analysis. The remaining supernatant in the reaction tube was then decanted to waste and the unreacted sample was subjected to the following extraction step. Some steps in the procedure required additional washes to ensure quantitative extraction of targeted P. The P_{Fe1}, P_{mag} and P_{Fe2} extraction steps were each followed by one wash in $MgCl_2$ and the P_{auth} extraction was followed by one $MgCl_2$ wash and one wash in ultrapure 18MΩ H_2O if the absorbance of undiluted samples was greater than 0.1. The sodium citrate/-dithionite/acetic acid (CDA)

reagent, used for the extraction of P_{Fe2}, and sodium citrate/-bicarbonate/-dithionite (CBD) reagent, used for the extraction of P_{Fe1}, were prepared on the day of use.

For the extraction of P_{org}, samples were transferred to porcelain crucibles using 4-6 ml of MilliQ H_2O, oven dried at 100°C and then ashed for 2 hours at 550°C in a Carbolite furnace. After cooling, samples were quantitatively transferred to the reaction tubes using 10% HCl. The samples were then agitated for 16 hours at 100 rpm.

Multiple stages in the procedure required P measurements via spectrophotometry using molybdate blue, whereby formation of phosphomolybdate in the presence of P was measured at a wavelength of 880 nm. Supernatant solutions from the P_{Fe1}, P_{mag} and P_{Fe2} extractions were measured by ICP-OES in the Cohen Laboratories, School of Earth and Environment, University of Leeds. Solutions were spiked with an internal standard of 100 µl Co (100 ppm). Quality check solutions of 0 and 2 ppm P were run every 10 samples.

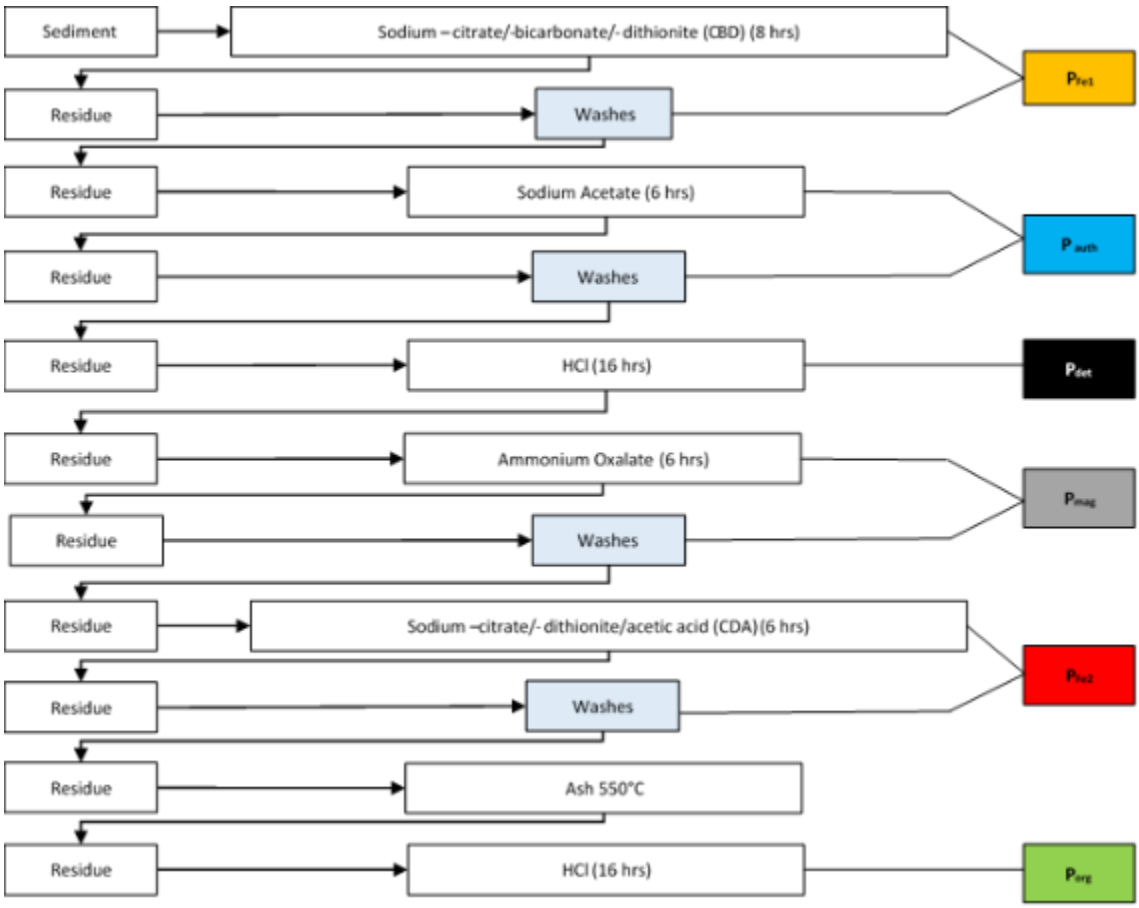

Figure S1. The modified P speciation protocol for ancient sediments utilised in this study.

Critical assessment of P extraction

Of the 47 samples selected for P speciation, 39 show recovery of >70% P_{Tot} (mean = 90.8%) following the sequential P extraction (Figure S2a). The sample with the lowest P recovery (OMK3/8, data not used in this study) also had the highest Al concentration (19 wt%). The negative correlation between P recovery and Al is a recognised complication in P studies of modern sediments (Marz et al., 2014). However, there is no strong correlation between P_{det} (as a percentage of P_{Tot}) and Al (Figure S2b) for samples with P_{SUM}/P_{Tot} >0.7, suggesting that elevated Al was not a compounding issue for P recovery in these samples.

A specific complication in the analysis of ancient sedimentary rocks via the modified SEDEX method involves the potential transfer of P_{auth} to the P_{det} pool as a consequence of the post-depositional recrystallisation of authigenic apatite during burial diagenesis (Marz et al., 2014). It has been noted that the detrital P content of modern continental margin sediments is 186 ± 21 ppm (Ruttenberg et al., 1993), whereas modern oligotrophic settings are characterised by P_{det} in the range 62 – 310 ppm (Slomp et al., 2013). Samples from the Nama Group have P_{det} concentrations in the range 4.2 – 536.4 ppm (mean 208.7 ppm), with maximum values significantly greater than average P_{det} of modern shelf environments. This may suggest that a portion of extracted P_{det} represents burial recrystallisation of initially authigenic P. There is no significant correlation between P_{reac} (as a percentage of P_{Tot}) and Al ($r^2 = 0.077$, Figure S2c), implying negligible contamination of the P_{auth} pool by P_{det}. Consequently, concentrations of P_{auth} (and by extension summed P_{reac}) likely represent minimum values, whilst those of P_{det} represent maximum values, which reinforces our interpretation of elevated authigenic P contribution under oxic conditions in the Nama Group.

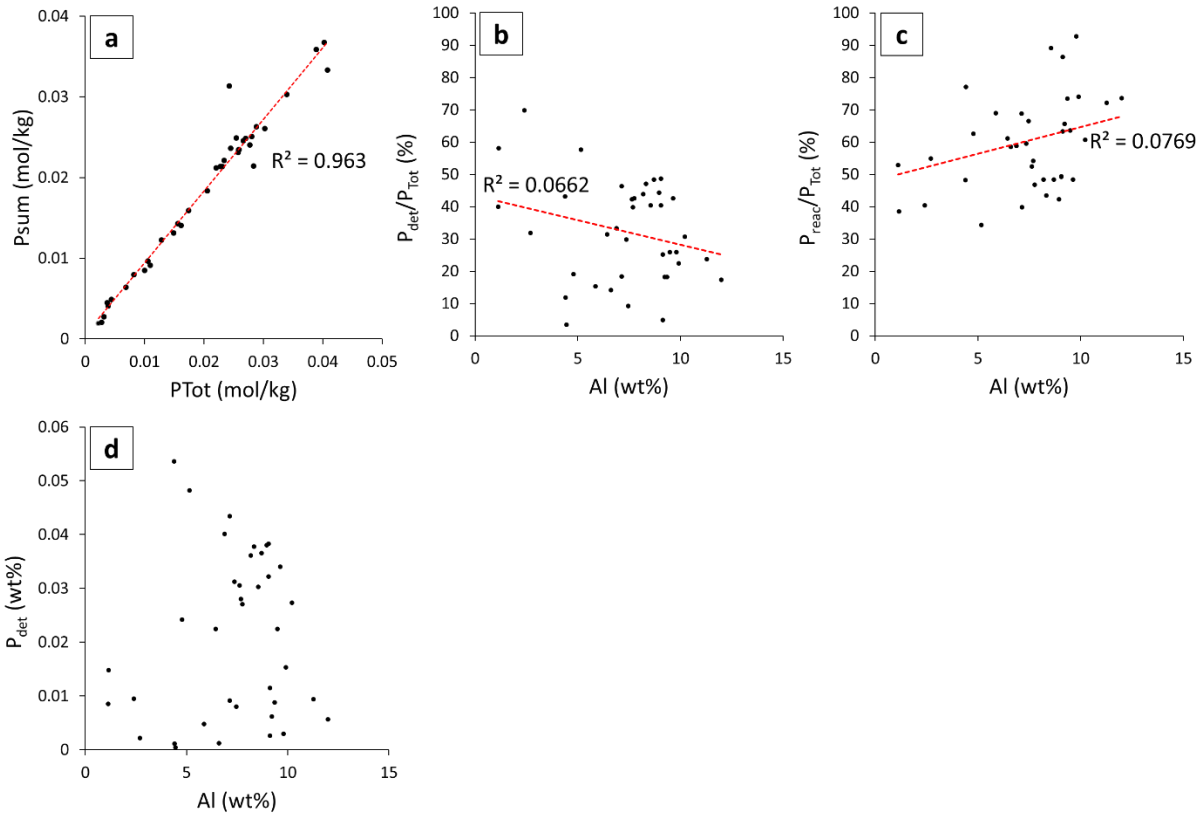

Figure S2. The relationships between extracted P phases and the detrital background (represented by the concentration of Al).

The Chemical Index of Alteration

Chemical weathering plays a major role in controlling the mineralogical composition of fine grained siliciclastic rocks and is therefore a key metric in understanding compositional changes in their major element distribution, particularly in relation to the regional supply of nutrients from the continent and the maturity of terrigenous clay. During chemical weathering, labile elements are preferentially removed, resulting in elevated ratios of immobile elements (Al, Ti) to alkalis (Na, Ca, K) (Nesbitt and Young, 1982). The chemical index of alteration (CIA)[97] has long been used to assess the degree of chemical weathering required for an observed suite of major elements and is derived as:

$$CIA = [Al_2O_3/(Al_2O_3 + CaO^* + Na_2O + K_2O)] \times 100$$

When calculating CIA, the CaO concentration in silicates (CaO*) is evaluated by correcting for Ca contribution in carbonate and apatite (Nesbitt and young, 1982). Available P_2O_5 data was used in order to first correct for Ca in apatite ($CaO_{corr} = CaO - 10/3 \times P_2O_5$, concentrations in mol%) Fedo et al, 1995; Zhai et al., 2018). Where resultant CaO_{corr} in moles was less than Na_2O, CaO_{corr} was used as CaO*. Conversely, where $CaO_{corr} > Na_2O$, the CaO* value was determined through equivalence with the average CaO/Na_2O ratio of the sample set (Zhai et al., 2018; McLennan, 1993).

Additional concern surrounds the diagenetic accumulation of K via potassic metasomatism, which is corrected for by projecting observed K excess onto a theoretical weathering trend in A-CN-K ($Al_2O_3 - [CaO^* + Na_2O] - K_2O$) space (Fedo and Young, 1995; Zhai et al., 2018; Tosca et al, 2010; Johnston et al., 2013; Blanco et al., 2011). Nama Group strata have undergone no greater than zeolite facies metamorphism (thermal alteration in the range 170 - 200°C, [Germ et al., 1986]), therefore deviation from the weathering trend toward the K_2O apex likely reflects K contributed during clay diagenesis. The resulting range of CIA values fall between ~59 – 88% with the highest values confined to the Kuibis and lower Schwarzrand subgroups as previously observed (Figure S14) (Blanco et al., 2011). The overlapping range of CIA values in samples of the Upper Omkyk Member at Farm Driedoornvlakte and the Vingerbreek Member at Farm Kliphoek reflect their provenance from the Kalahari craton to the present east (Germs et al., 1983). By contrast, the narrower range and lower average value of samples of the Schwarzrand Subgroup of the Zaris sub-basin are likely a product of sediment input from the less heavily weathered protolith to the north in addition to that subsequently supplied from the east (upper Schwarzrand Subgroup), consistent with published palaeocurrent and heavy mineral data (Germs et al., 1983; Blanco et al., 2011).

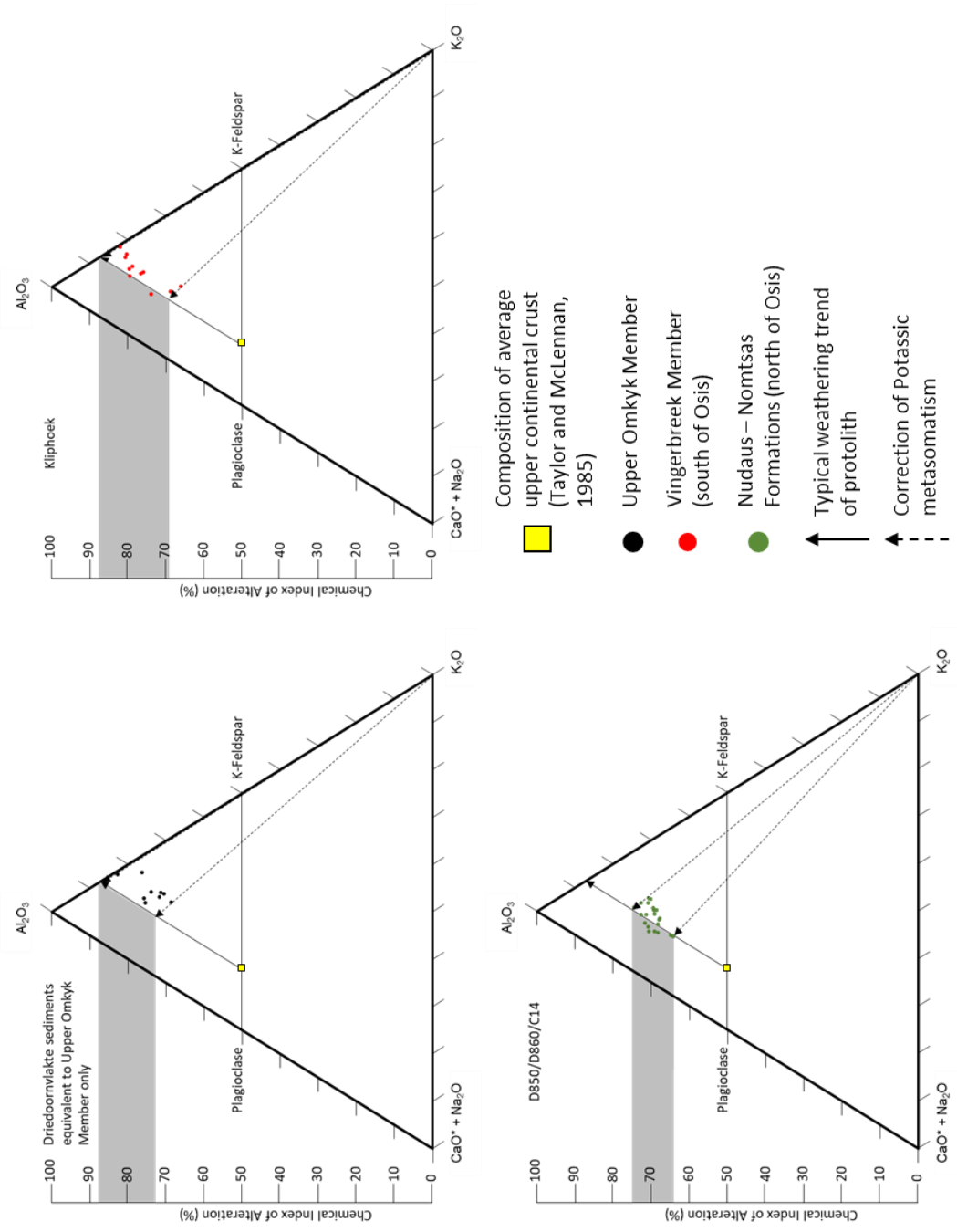

Figure S14. Calculated values of the chemical index of alteration and the relative positions of sampled areas in A-CN-K space.

Blanco, G. et al. Provenance and paleogeography of the Nama Group (Ediacaran to early Palaeozoic, Namibia): Petrography, geochemistry and U-Pb detrital zircon geochronology. Precambrian Res. 187, 15–32 (2011).

Fedo, C. M., Nesbitt, H. W. & Young, G. M. Unraveling the effects of potassium metasomatism in sedimentary rocks and paleosols, with implications for paleoweathering conditions and provenance. *Geology* **23**, 921–924 (1995).

Germs, G. J. B. Implications of a sedimentary facies and depositional environmental analysis of the Nama Group in South West Africa/Namibia. *Spec. Publ. Geol. Soc. South Africa* **11**, 89–114 (1983).

Germs, G. J. B., Knoll, A. H. & Vidal, G. Latest proterozoic microfossils from the Nama group, Namibia (south west Africa). *Precambrian Res.* **32**, 45–62 (1986).

Johnston, D. T. *et al.* Searching for an oxygenation event in the fossiliferous Ediacaran of northwestern Canada. *Chem. Geol.* **362**, 273–286 (2013).

März, C., Poulton, S. W., Wagner, T., Schnetger, B. & Brumsack, H. J. Phosphorus burial and diagenesis in the central Bering Sea (Bowers Ridge, IODP Site U1341): Perspectives on the marine P cycle. *Chem. Geol.* **363**, 270–282 (2014).

McLennan, S. M. Weathering and Global Denudation. *J. Geol.* **101**, 295–303 (1993).

Nesbitt, H. W. & Young, G. M. Early Proterozoic climates and plate motions inferred from major element chemistry of lutites. *Nature* **299**, 715–717 (1982).

Ruttenberg, K. & Berner, R. Authigenic apatite formation and burial in sediments from non-upwelling, continental margin environments. *Geochim. Cosmochim. Acta* **57**, 991–1007 (1993).

Slomp, C. P. *et al.* Coupled Dynamics of Iron and Phosphorus in Sediments of an Oligotrophic Coastal Basin and the Impact of Anaerobic Oxidation of Methane. *PLoS One* **8**, (2013).

Tosca, N. J. *et al.* Clay mineralogy, organic carbon burial, and redox evolution in Proterozoic oceans. *Geochim. Cosmochim. Acta* **74**, 1579–1592 (2010).

Zhai, L., Wu, C., Ye, Y. & Zhang, S. Fluctuations in chemical weathering on the Yangtze Block during the Ediacaran-Cambrian transition: implications for paleoclimatic conditions and the marine carbon cycle. *Palaeogeogr. Palaeoclimatol. Palaeoecol.* **490**, 280–292 (2018).

Appendix 2: Multiple Branching and Attachment Structures in mat-dwelling cloudinomorphs, Nama Group, Namibia

Appendix 2.1 Shore et al. (2020)

Multiple branching and attachment structures in cloudinomorphs, Nama Group, Namibia

GEOLOGY | THE GEOLOGICAL SOCIETY OF AMERICA®

https://doi.org/10.1130/G47447.1

Manuscript received 16 October 2019
Revised manuscript received 26 March 2020
Manuscript accepted 8 April 2020

Published online 29 May 2020

Multiple branching and attachment structures in cloudinomorphs, Nama Group, Namibia

Amy Shore[1]*, Rachel Wood[1], Andrew Curtis[1] and Frederick Bowyer[1,2]
[1]School of GeoSciences, University of Edinburgh, James Hutton Road, Edinburgh EH9 3FE, UK
[2]School of Earth and Environment, University of Leeds, Leeds LS2 9JT, UK

ABSTRACT

The Ediacaran-Cambrian cloudinomorphs, which include *Cloudina*, are the first putative skeletal metazoans. They have a benthic ecology and tubular, organic, or biomineralized stacked funnel morphologies but an unresolved phylogenetic affinity. Rare dichotomous branching has been described in *Cloudina*, but here we demonstrate the presence of multiple (polytomous), dichotomous branching in cloudinomorphs from a microbial mat community from the Nama Group, Namibia, as revealed by three-dimensional models created from serial sections. Branches share an open, central cavity, and branching is achieved via external budding. These cloudinomorphs show attachment and mutual cementation to each other, and also to *Namacalathus*, via extratubular skeletal structures to potentially form a horizontal framework. Polytomous branching excludes a bilaterian affinity as proposed for other cloudinomorphs. This raises the possibility that the Ediacaran tubular, funnel morphology is convergent, and that cloudinomorphs may, in fact, represent taxa of diverse affinity.

INTRODUCTION

Significant evolutionary innovations in metazoans such as biomineralization, reef-building, and motile behavior appeared during the terminal Ediacaran. The most studied Ediacaran skeletal taxa is *Cloudina* (ca. 550–540 Ma), due to its widespread distribution and potential index fossil status (Grant, 1990).

Cloudina and other similar tubular skeletal and organic taxa (informally known as "cloudinids" and "cloudinomorphs") have a sinuous, tube-like morphology formed of eccentrically stacked funnels that lack transverse cross-walls but that can flare to form outer wall flanges (Germs, 1972; Hua et al., 2005; Selly et al., 2020). To date, at least seven genera have been attributed to cloudinomorphs (Yang et al., 2020), and as a group, they are transitional across the Ediacaran-Cambrian boundary. Cloudinomorphs can have a closed or open base, a smooth inner wall, and an aperture (Germs, 1972; Cai et al., 2011; Schiffbauer et al., 2020). The size of *Cloudina* is highly variable globally, cited as ranging from 0.3 to 6.5 mm wide and 1.5 to 150 mm in length; dimensions may be determined by environmental as well as systematic factors (Wood et al., 2017). *Cloudina* communities occupied a range of different carbonate substrates, including microbial mats, thrombolites, and reefs (Cai et al., 2014; Penny et al., 2014; Becker-Kerber et al., 2017; Wood et al., 2017; Álvaro et al., 2020; but see Mehra and Maloof, 2018). Dichotomous branching has been observed in a few cases of *Cloudina* (Hua et al., 2005; Penny et al., 2014) and also budding of daughter tubes between two adjacent tubes (Cortijo et al., 2010), both suggestive of asexual reproduction. Evidence for mutual attachment and cementation of *Cloudina* individuals has been noted in the Nama Group, Namibia, where two forms of attachment are documented: apical terminations serving as attachment sites and "meniscus cements" between adjacent individuals (Penny et al., 2014).

The affinity of cloudinomorphs is problematic, with the group variously attributed to calcareous algae, cnidarians, or annelids (Terleev et al., 2004; e.g., Vinn and Zaton, 2012; Schiffbauer et al., 2020). A cnidarian affinity is supported by the deep-seated division of *Cloudina* tubes within the parent tube (Hua et al., 2005; Cortijo et al., 2014). However, the general nested funnel morphology and skeletal ultrastructure of some cloudinomorphs are similar to modern annelids (Vinn and Zaton, 2012; Yang et al., 2020), and preservation of a central, tubular, pyritized structure in a cloudinomorph inferred to be a gut would support a stem-annelid affinity (Schiffbauer et al., 2020). Indeed, many skeletal features of cloudinomorphs are in fact present in diverse invertebrate groups.

Here, we describe the first recorded instance of multiple (polytomous) branching, and the form of attachment sites, in cloudinomorphs. This informs the debate as to the potential affinities of this global and transitional Ediacaran-Cambrian group.

GEOLOGICAL SETTING

The Nama Group (ca. 550–541 Ma) is a fossiliferous Ediacaran–Cambrian sedimentary ramp succession deposited in two subbasins (Germs, 1983; see also the Supplemental Material[1] and Fig. S1 therein), consisting of the Kuibis Subgroup overlain by the Schwarzrand Subgroup (Germs, 1983; Saylor et al., 1995). Ash bed dates and inferred sedimentation rates suggest the basal Nama unconformity has an age of ca. 550–553 Ma (Saylor et al., 1998), and the top of the Schwarzrand Subgroup is younger than at least 539.64 ± 0.19 Ma (Linnemann et al., 2019).

MATERIAL AND METHODS

Samples from *in situ* bedding planes were collected from near the top of the Upper Omkyk Member of the Kuibis Subgroup, at Omkyk Farm and Driedoornvlagte in the Zaris Subbasin (Table S1; Fig. S1). An ash bed from the overlying Hoogland Member is dated at

*E-mail: amy.shore@ed.ac.uk

[1]Supplemental Material. Geological setting of the study sites within the Nama Group, Namibia; methods used for serial sectioning and 3-D model reconstruction; additional photomicrographs; and cloudinomorph tube measurements. Please visit https://doi.org/10.1130/GEOL.S.12307427 to access the supplemental material, and contact editing@geosociety.org with any questions.

CITATION: Shore, A., Wood, R., Andrew Curtis, A., and Bowyer, F., 2020, Multiple branching and attachment structures in cloudinomorphs, Nama Group, Namibia: Geology, v. 48, p. 877–881, https://doi.org/10.1130/G47447.1

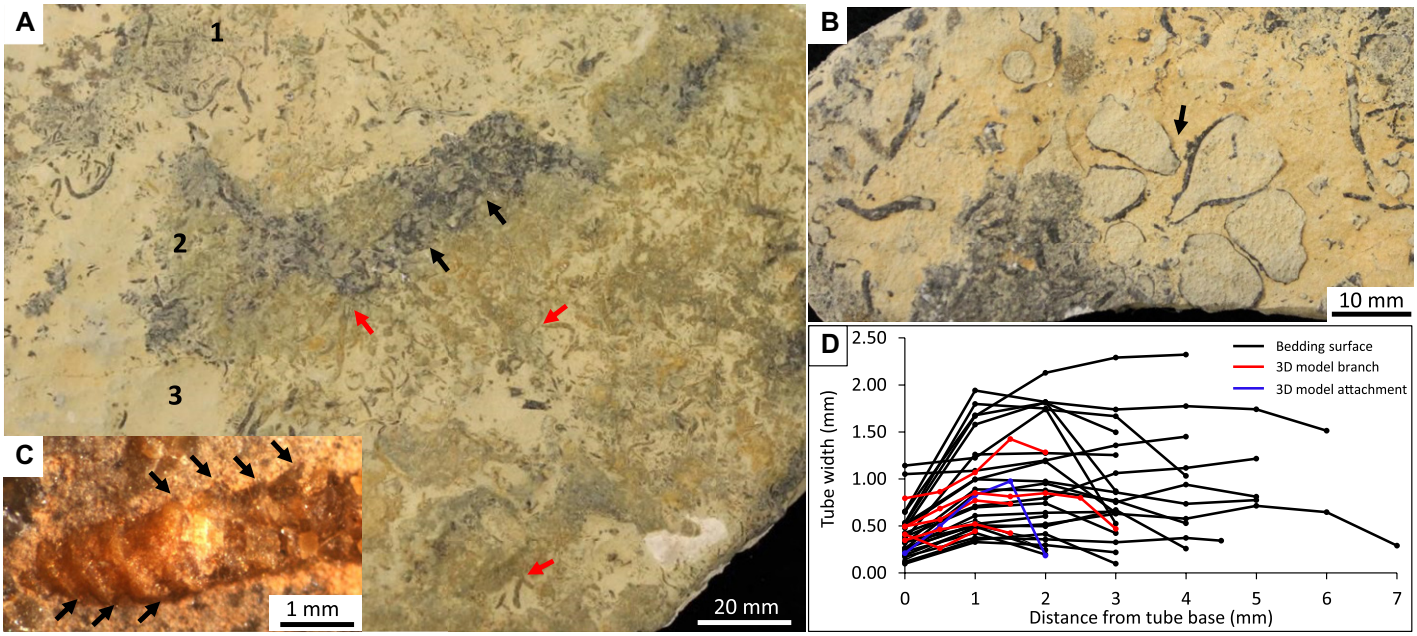

Figure 1. Bedding surfaces from the Upper Omkyk Member, Omkyk Farm, Namibia. (A) *In situ* cloudinomorphs and *Namacalathus* (black arrows) on two generations of microbial mat surfaces (1 and 2) with projecting cloudinomorphs (red arrows), and bioclasts in intermat mudstone (3). (B) Cluster of large *Namacalathus* in intermat area (arrow). (C) Cloudinomorph with annulated morphology (funnels arrowed). (D) Width of cloudinomorph tubes measured from two-dimensional bedding planes and multiple branching three-dimensional (3-D) model.

547.32 ± 0.65 Ma (Grotzinger et al., 1995; Schmitz, 2012). Driedoornvlagte is a shallow reef complex that formed in a midramp setting that contains abundant skeletal taxa, *Cloudina*, *Namacalathus*, and *Namapoikia*. At Omkyk Farm, strata record deposition at an inner-ramp position close to the Osis Arch, into increasingly shallow, very low-energy, lagoonal settings containing *Cloudina* and *Namacalathus* (Wood et al., 2015).

Cloudinomorph specimens were serially ground into increments of either 10 µm (Figs. S2 and S3) or 25 µm (Fig. S4), using a Buehler Petrothin thin-sectioning system, and imaged using a binocular microscope or flatbed scanner. Processed images were imported as a virtual stack into Avizo 9 software to create three-dimensional (3-D) models composed of between 50 and 123 two-dimensional images and smoothed to reduce noise. Cloudinomorph walls and the open cavity were manually segmented separately (Fig. S5). Highly polished thin sections were imaged by standard petrographic and cathodoluminescence microscopy, and ImageJ software (https://imagej.net/) was used for all measurements. See the Supplemental Material for further details of localities and methods.

RESULTS

Microbial Mat Metazoan Communities

Bedding planes of flaggy wackestone to packstone grading into friable, dolomitized wackestone to mudstone from Omkyk Farm, 12–30 mm thick, showed abundant aggregations of sinuous, straight, and apparently branching cloudinomorphs and *Namacalathus* associated with inferred microbial mats (Figs. 1A, 1B, and 2). Inferred microbial mats were dark or covered in iron oxides and had irregular or patchy edges distinct from the yellow, micritic mudstone with skeletal bioclasts. Mats were usually <1 mm thick and undulating, and they occurred parallel to bedding at a spacing of 2–5 mm.

Tubular fossils from Omkyk Farm showed a distinct annulated outer wall structure (Fig. 1C), but recrystallization obscured any internal stacked, funnel organization. They were therefore attributed to cloudinomorphs. Material from Driedoornvlagte can be attributed to *Cloudina* (Grant, 1990).

Cloudinomorph individuals ranged from 1.2 to 21.7 mm in length and from 0.1 to 2.3 mm in width ($n = 604$), as measured on bedding planes, and they were inferred to be attached to mats, because they are most abundant within inferred mats, and some individuals appeared to radiate from the mats (Fig. 1A). *In situ Namacalathus* specimens were present as clusters of small individuals within the mats (Fig. 1A), and as larger individuals outside the mats, which showed close aggregation and radiated from a smaller area of attachment with deformation between individuals (Fig. 1B).

Cloudinomorph Growth Patterns

The diameter of cloudinomorphs measured from bedding surfaces showed an initial fast rate of inflation within the first 1 mm of extensional growth but remained constant thereafter

Figure 2. Cloudinomorphs with multiple attachment sites and branches. (A, C, E) Bedding plane images. (B, D, F) Trace through inferred central axes of tubes. Multiple attachment sites with isopachous cements or sediment infill in E define contact between tubes (single arrows) and inner tube wall (double arrow).

(Fig. 1D). While bedding plane surfaces showed examples of potential attachment sites and/or branching cloudinomorphs (Fig. 2), evidence for bifurcating tubes can only be proven by the presence of a shared cavity.

Polished surfaces revealed that cloudinomorph tubes were infilled first by a cloudy, isopachous cement (21–587 µm thick; mean = 110 µm; Fig. S7) and then by sparry calcite in the remaining internal space (Figs. S2 and S4). Cathodoluminescence revealed an earlier, thin (up to 200 µm) generation of acicular cement (Fig. S6C). The isopachous cement is either patchy or zoned, and sparry calcite cements are distinctly zoned (Figs. 3G, 3H, and 3J). The presence of a shared cavity is evidenced by the absence of a wall or any associated skeletal breakage that might imply postdepositional compaction, and also by the isopachous cement crust that forms a continuous crust connecting both tubes, as well as continuous sparry calcite cement infill (Figs. 3G and 3H).

One 3-D model of the cloudinomorph outer wall, highlighted by the micritic envelope or the outer edge of the cavity-lining isopachous cement, confirmed the presence of multiple branches with differing orientations along one parent tube (Figs. 3A and 3B; Fig. S2). These diverged from the parental tube at angles of 35° to 299° (Table S2; Fig. S8). The plunge angles of the branches and attachment site were consistently shallow, from 1.4° to 7.1°. Models of the cavity as defined by the extent of sparry calcite confirmed this multiple branching structure (Figs. 3C and 3D). The diameter of cloudinomorph branches measured directly from the 3-D models also showed an initial fast rate of inflation within the first 1 mm of growth but constant diameter thereafter (Fig. 1D).

Branches grew from the outer wall of the parent tube, i.e., with no intracalar bifurcation (Figs. 3A–3D). Models also revealed attachment sites of small cloudinomorph individuals, as indicated by the presence of the parental tube outer wall and no shared cavity (Figs. 3A and 3B; Figs. S2D and S2G). The attached tube was often initially more narrow than the width of the tube to which it was attached (Figs. 3A and 3B), but the tube also inflated rapidly to form a cavity (Fig. 1D). Individuals could therefore be reconstructed with both multiple branches and attachment sites (Fig. 3E).

Cloudinomorph Attachment Structures

Cementation was observed as one tube attached either at the base (attachment) or along the length of the shell (mutual cementation). On the bedding surface, potential cemented/attached tubes were indicated by a gap between apparently branching tubes (Fig. 2E). This was inferred to represent either the isopachous cement crust or sediment infill between the parent and inflating daughter tube, or two attached tubes that were differently oriented in 3-D relative to one another.

Mutual cementation was also observed at both Omkyk Farm and Driedoornvlagte between adjacent or near-parallel tubes in close proximity (<0.3 mm; Fig. 4A). At Driedoornvlagte, *Cloudina* walls were composed of brown, inclusion-rich dolomite and dolomitized extratubular structures, with geopetal dolomitized micrite present within the tube (Fig. 4D). Under cathodoluminescence, *Cloudina* walls showed bright luminescence and neomorphosed calcite with the same bright luminescence that was also present between the adjacent tubes, suggesting that the *Cloudina* walls and the extratubular structure shared the same diagenetic signature (Fig. 4E).

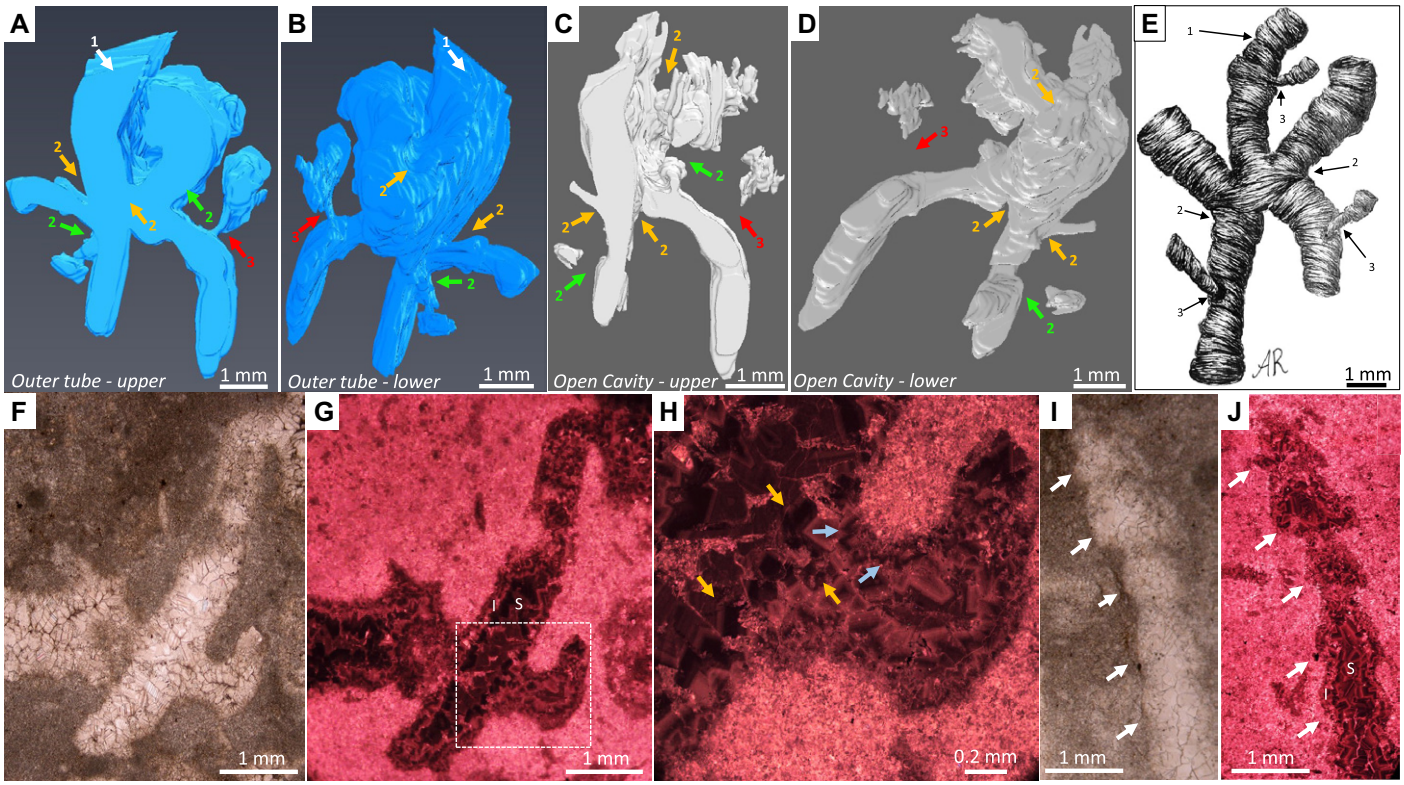

Figure 3. Multiple branching cloudinomorph with parent tube (1, white arrow), branching daughter tube (2, shared cavities, orange arrows), indirect evidence of branching where cavity does not extend to full tube (green arrows), and attachment sites (3, red arrows). (A) Upper, plan view of three-dimensional (3-D) model (from bedding surface) of outer tube with 5% smoothing. (B) Lower, rear view of same model. (C) Upper, plan view of 3-D model (from bedding surface) of open cavity. (D) Lower, plan view of same model. (E) Reconstruction of multiple branching cloudinomorph (artist: Astrid Robertsson). (F) Plane-polarized light (PPL) photomicrograph and (G) cathodoluminescent photomicrograph of branching cloudinomorph, showing continuity of isopachous (I) and sparry calcite (S) cements in parent and daughter tubes. (H) Inset of G, showing continuity of isopachous cement between two tubes (blue arrows) and later sparry cement infilling both tubes (orange arrows). (I) PPL photomicrograph and (J) cathodoluminescent photomicrograph of cloudinomorph tube where arrows mark successive funnels, with isopachous (I) and sparry calcite (S) cement infill.

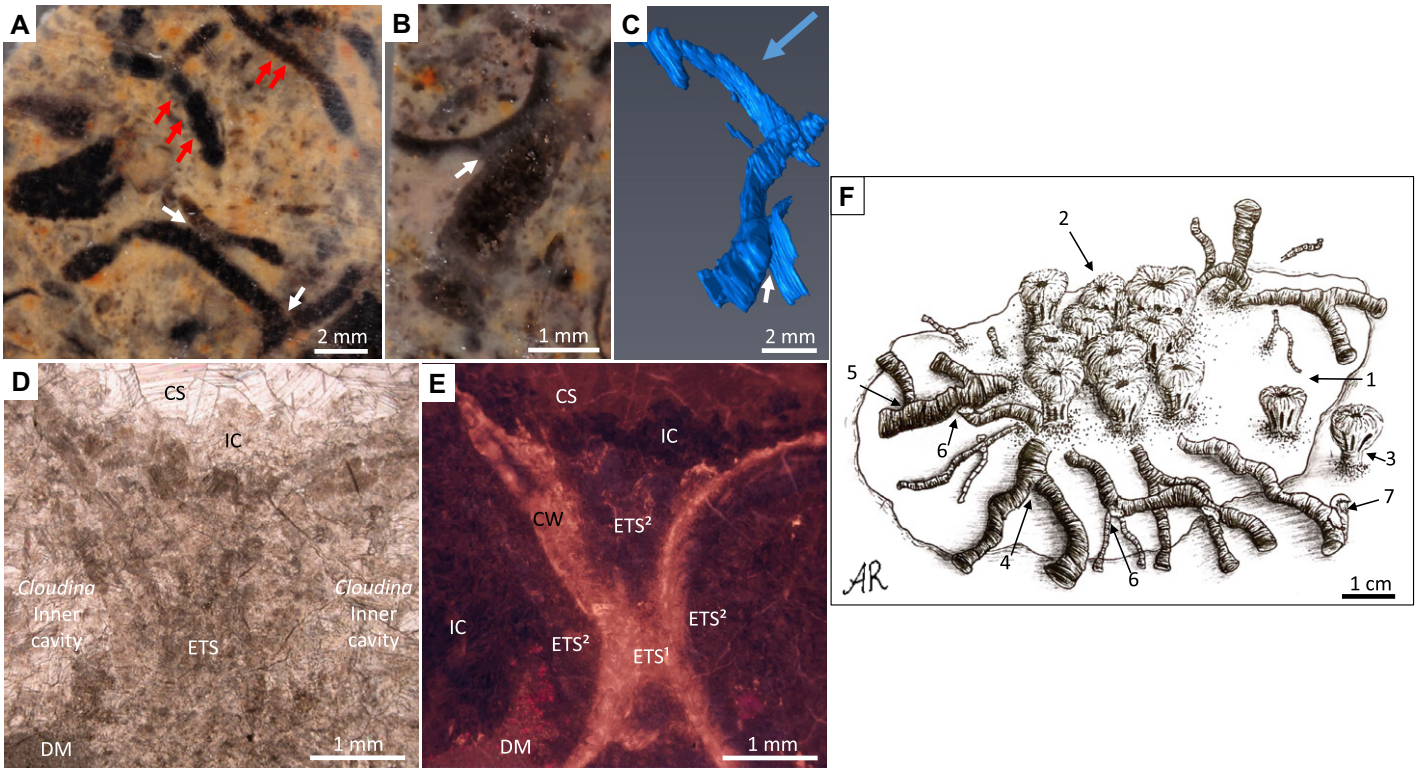

Figure 4. Cloudinomorph attachment. (A) Plan view of attached parallel cloudinomorph tubes (white arrows) with stacked funnel morphology (red arrows indicate funnels). (B) Plan view of extratubular structure between cloudinomorph tube and *Namacalathus* (white arrow). (C) Three-dimensional (3-D) model showing cementation between *Namacalathus* and cloudinomorph (white arrow), where blue arrow indicates way up. (D) Plane-polarized light (PPL) photomicrograph of two *Cloudina* tubes from Driedoornvlagte, with inclusion-rich extratubular structure (ETS) between tubes, geopetal dolomitic micrite (DM), inclusion-rich cement (IC), and calcitic spar infill (CS). (E) Cathodoluminescence image of same area as D, showing two generations within ETS: bright luminescence (ETS¹) and then dull luminescence with patches of bright luminescence (ETS²). Both predate inclusion-rich cement (IC) and latest sparry cements (CS). (F) Reconstruction of inferred microbial mat community with *in situ* skeletal metazoans: (1) microbial mat; (2) *Namacalathus* cluster; (3) isolated *Namacalathus* outside microbial mat; (4) branching cloudinomorph with horizontal habit; (5) multiple branching cloudinomorph; (6) mutual attachment of cloudinomorph by extratubular structures; (7) attachment between cloudinomorph and *Namacalathus* (artist: Astrid Robertsson).

This structure predated the formation of a further distinctive, slightly bluish, dully luminescent neomorphosed calcite with patchy areas of brighter luminescence, which formed both adjacent to *Cloudina* walls and within the inner tube adjacent to the contact structure (Fig. 4E). An inclusion-rich, nonluminescent sparry calcitic cement and a later clear sparry calcite postdate these cements (Fig. 4E).

Similar mutual cementation was also noted between cloudinomorphs and the outer wall of a fragment of *Namacalathus* (Fig. 4B; Fig. S4), reaching 0.4 mm thickness. Attachment was further confirmed via serial sectioning and 3-D modeling (Fig. 4C).

DISCUSSION

The low-energy, inner-ramp environment of the Upper Omkyk Member at Omkyk Farm allowed for the preservation of an inferred microbial mat community of delicate, *in situ*, branching or cemented cloudinomorphs and *Namacalathus*.

The presence of a shared cavity in these cloudinomorphs shows that the parent and daughter branches shared the same living space. The continuation of early cement between the parent and daughter tubes and the lack of evidence for breakage of the tube walls suggest that this is a growth feature. This style of branching is unlike that previously recorded, where the tube splits into two half cylinders within the parent tube, i.e., intraparietal budding, or dichotomous branching (Hua et al., 2005; Cortijo et al., 2010). We saw no evidence of a dividing wall along the midline within the parent tube, suggesting a different form of reproduction, here conforming to external budding.

We found multiple examples of apical and longitudinal attachment accompanied by a neomorphosed calcite extratubular structure, which aided mutual cloudinomorph attachment. We further observed the occurrence of attachment between cloudinomorph and *Namacalathus*. These structures predated all inorganic cements, including pseudomorphed aragonitic cement botryoids, where present (Penny et al., 2014). Given that these structures were only found associated with cloudinomorphs, and they also showed multiple positions relative to the tubular growth form, it is likely that they have a biological origin. These structures may have formed by extratubular secretion, perhaps via extracellular polymeric substances (EPS) or an organic template, which became calcified. The close proximity of individuals appears to have encouraged mutual cementation, allowing for the formation of a horizontal, multicomponent, rigid structure associated with microbial mat surfaces (Fig. 4F). This confirms that the ability to gain secure, mutual attachment was present by the terminal Ediacaran.

The observation of multiple branching in cloudinomorphs suggests a non-bilaterian affinity for these representatives. Modern cnidarians, in particular hydrozoans, show various forms of asexual reproduction, including longitudinal fission and external budding, rapid daughter branch diameter increase after branching, similar diameters of parent and daughter tubes, and multiple branching (Vinn and Zaton, 2012; Han et al., 2017; Yang et al., 2020).

Such a non-bilaterian affinity would be counter to that implied by the presence of an inferred gut in cloudinomorphs from Nevada (Schiffbauer et al., 2020), as well as the organized, lamellar microstructure of organic-walled cloudinomorphs from Mongolia (Yang et al., 2020).

This apparent contradiction therefore raises the possibility that the common Ediacaran-Cambrian tubular and stacked, funnel morphology is convergent, and that cloudinomorphs may, in fact, represent taxa of diverse affinity.

ACKNOWLEDGMENTS

Shore acknowledges support from the University of Edinburgh (UK), and Wood acknowledges support from a Natural Environment Research Council grant (NE/P013651/1). We thank Helke Mocke and Charlie Hoffmann of the Geological Survey of Namibia, and the Ministry of Mines and Energy, Namibia. We thank Andre and Susan Horn of Omkyk Farm, and Mike Hall for technical support. We thank Astrid Robertsson for her fine artwork. We also thank Jim Schiffbauer and two anonymous reviewers for their valuable comments.

REFERENCES CITED

Álvaro, J.J., Cortijo, I., Jensen, S., Mus, M.M., and Palacios, T., 2020, *Cloudina*-microbial reef resilience to substrate instability in a Cadomian retro-arc basin of the Iberian Peninsula: Precambrian Research, v. 336, p. 105479, https://doi.org/10.1016/j.precamres.2019.105479.

Becker-Kerber, B., Pacheco, M.L.A.F., Rudnitzki, I.D., Galante, D., Rodrigues, F., and de Moraes Leme, J., 2017, Ecological interactions in *Cloudina* from the Ediacaran of Brazil: Implications for the rise of animal biomineralization: Scientific Reports, v. 7, p. 5482–5488, https://doi.org/10.1038/s41598-017-05753-8.

Cai, Y., Schiffbauer, J.D., Hua, H., and Xiao, S., 2011, Morphology and paleoecology of the late Ediacaran tubular fossil *Conotubus hemiannulatus* from the Gaojiashan Lagerstätte of southern Shaanxi Province, South China: Precambrian Research, v. 191, p. 46–57, https://doi.org/10.1016/j.precamres.2011.09.002.

Cai, Y., Hua, H., Schiffbauer, J.D., Sun, B., and Yuan, X., 2014, Tube growth patterns and microbial mat–related lifestyles in the Ediacaran fossil *Cloudina*, Gaojiashan Lagerstätte, South China: Gondwana Research, v. 25, p. 1008–1018, https://doi.org/10.1016/j.gr.2012.12.027.

Cortijo, I., Mus, M.M., Jensen, S., and Palacios, T., 2010, A new species of *Cloudina* from the terminal Ediacaran of Spain: Precambrian Research, v. 176, p. 1–10, https://doi.org/10.1016/j.precamres.2009.10.010.

Cortijo, I., Cai, Y., Hua, H., Schiffbauer, J.D., and Xiao, S., 2014, Life history and autecology of an Ediacaran index fossil: Development and dispersal of *Cloudina*: Gondwana Research, v. 28, p. 419–424, https://doi.org/10.1016/j.gr.2014.05.001.

Germs, G.J.B., 1972, New shelly fossils from Nama Group, south west Africa: American Journal of Science, v. 272, p. 752–761, https://doi.org/10.2475/ajs.272.8.752.

Germs, G.J.B., 1983, Implications of a sedimentary facies and depositional environmental analysis of the Nama Group in South West Africa/Namibia, *in* Miller, R.Mc., ed., Evolution of the Damara Orogen of South West Africa/Namibia: Geological Society of South Africa Special Publication 11, p. 89–114.

Grant, S., 1990, Shell structure and distribution of *Cloudina*, a potential index fossil for the terminal Proterozoic: American Journal of Science, v. 290, p. 261–294.

Grotzinger, J.P., Bowring, S.A., Saylor, B.Z., and Kaufman, A.J., 1995, Biostratigraphic and geochronologic constraints on early animal evolution: Science, v. 270, p. 598–604, https://doi.org/10.1126/science.270.5236.598.

Han, J., Cai, Y., Schiffbauer, J.D., Hua, H., Wang, X., Yang, X., Uesugi, K., Komiya, T., and Sun, J., 2017, A *Cloudina*-like fossil with evidence of asexual reproduction from the lowest Cambrian, South China: Geological Magazine, v. 154, p. 1294–1305, https://doi.org/10.1017/S0016756816001187.

Hua, H., Chen, Z., Yuan, X., Zhang, L., and Xiao, S., 2005, Skeletogenesis and asexual reproduction in the earliest biomineralizing animal, *Cloudina*: Geology, v. 33, p. 277–280, https://doi.org/10.1130/G21198.1.

Linnemann, U., Ovtcharova, M., Schaltegger, U., Gärtner, A., Hautmann, M., Geyer, G., Vickers-Rich, P., Rich, T., Plessen, B., and Hofmann, M., 2019, New high-resolution age data from the Ediacaran-Cambrian boundary indicate rapid, ecologically driven onset of the Cambrian explosion: Terra Nova, v. 31, p. 49–58, https://doi.org/10.1111/ter.12368.

Mehra, A., and Maloof, A., 2018, Multiscale approach reveals that *Cloudina* aggregates are detritus and not in situ reef constructions: Proceedings of the National Academy of Sciences of the United States of America, v. 115, p. E2519–E2527, https://doi.org/10.1073/pnas.1719911115.

Penny, A.M., Wood, R., Curtis, A., Bowyer, F., Tostevin, R., and Hoffman, K.-H., 2014, Ediacaran metazoan reefs from the Nama Group, Namibia: Science, v. 344, p. 1504–1506, https://doi.org/10.1126/science.1253393.

Saylor, B.Z., Grotzinger, J.P., and Germs, G.J., 1995, Sequence stratigraphy and sedimentology of the Neoproterozoic Kuibis and Schwarzrand Subgroups (Nama Group), southwestern Namibia: Precambrian Research, v. 73, p. 153–171, https://doi.org/10.1016/0301-9268(94)00076-4.

Saylor, B.Z., Kaufman, A.J., Grotzinger, J.P., and Urban, F., 1998, A composite reference section for terminal Proterozoic strata of southern Namibia: Journal of Sedimentary Research, v. 68, p. 1223–1235, https://doi.org/10.2110/jsr.68.1223.

Schiffbauer, J.D., Selly, T., Jacquet, S.M., Nelson, L.L., Strange, M.A., Cai, Y., and Smith, E.F., 2020, Discovery of bilaterian-type through-guts in cloudinomorphs from the terminal Ediacaran Period: Nature Communications, v. 11, p. 205, https://doi.org/10.1038/s41467-019-13882-z.

Schmitz, M., 2012, Radiogenic isotope geochronology, *in* Gradstein, F., et al., eds., The Geologic Time Scale 2012: Amsterdam, Elsevier, p. 115–126, https://doi.org/10.1016/B978-0-444-59425-9.00006-8.

Selly, T., Schiffbauer, J.D., Jacquet, S.M., Smith, E.F., Nelson, L.L., Andreasen, B.D., Huntley, J.W., Strange, M.A., O'Neil, G.R., Thater, C.A., Bykova, N., Steiner, M., Yang, B., and Cai, Y., 2020, A new cloudinid fossil assemblage from the terminal Ediacaran of Nevada, USA: Journal of Systematic Palaeontology, v. 18, p. 357–379, https://doi.org/10.1080/14772019.2019.1623333.

Terleev, A., Luchinina, V., Sosnovskaya, O., and Bagmet, G., 2004, Calcareous algae and lower boundary of the Cambrian in the western Altai-Sayan folded area: Geologiya i Geofizika, v. 45, p. 485–491.

Vinn, O., and Zaton, M., 2012, Inconsistencies in proposed annelid affinities of early biomineralized organism *Cloudina* (Ediacaran): Structural and ontogenetic evidences: Carnets de Géologie, v. 3, p. 39–47, https://doi.org/10.4267/2042/46095.

Wood, R., Poulton, S., Prave, A., Hoffmann, K.-H., Clarkson, M., Guilbaud, R., Lyne, J., Tostevin, R., Bowyer, F., and Penny, A., 2015, Dynamic redox conditions control late Ediacaran metazoan ecosystems in the Nama Group, Namibia: Precambrian Research, v. 261, p. 252–271, https://doi.org/10.1016/j.precamres.2015.02.004.

Wood, R., Curtis, A., Penny, A., Zhuravlev, A.Y., Curtis-Walcott, S., Iipinge, S., and Bowyer, F., 2017, Flexible and responsive growth strategy of the Ediacaran skeletal *Cloudina* from the Nama Group, Namibia: Geology, v. 45, p. 259–262, https://doi.org/10.1130/G38807.1.

Yang, B., Steiner, M., Schiffbauer, J.D., Selly, T., Wu, X., Zhang, C., and Liu, P., 2020, Ultrastructure of Ediacaran cloudinids suggests diverse taphonomic histories and affinities with non-biomineralized annelids: Scientific Reports, v. 10, p. 1–12, https://doi.org/10.1038/s41598-019-56317-x.

Printed in USA

Appendix 2.2 Data Tables

2.2.1 Cloudinomorph width at Omkyk Farm

Sample Picture	Cloudinomorph No.	Width (mm)
OMK/18/1.2	1	0.7
	2	1.0
OMK/18/1.4	1	1.3
	2	0.5
	3	0.5
	4	0.6
	5	0.6
	6	0.6
	7	0.4
	8	0.6
	9	0.5
	10	0.6
	11	0.3
	12	0.4
	13	0.4
	14	0.2
OMK/18/1.6	2	1.7
	3	0.6
	4	0.5
	5	0.7
	6	0.7
	7	0.7
	8	0.7
	9	0.5
	10	0.2
OMK/18/1.8	1	0.7
	2	0.4
	3	0.7
	4	0.6
	5	1.1
	6	0.4
	7	0.9
	8	0.4
	9	0.4
OMK/18/1.9	1	1.0
	2	0.5
	3	0.5
	4	0.3
	5	0.5

OMK/18/1.10	1	0.5
	2	0.3
	3	0.5
	4	0.3
	5	0.3
	6	0.4
	7	0.3
	8	0.5
	9	0.3
	10	0.5
	11	0.4
	12	0.4
	13	0.3
OMK/18/1.17	1	2.1
	2	0.6
	3	1.3
	4	1.3
	5	0.5
	6	0.4
	7	0.4
	8	0.3
	9	0.4
	10	0.4
	11	0.8
	12	0.2
	13	0.2
	14	0.2
	15	0.3
OMK/18/1.20	1	1.7
	2	2.0
	3	1.7
	4	1.0
	5	0.4
	6	0.3
	7	0.7
	8	0.2
	9	0.1
OMK/18/1.23	1	0.2
	2	2.3
	3	0.3
	4	0.6
	5	1.2
	6	0.5
	7	0.7
	8	0.2

	9	0.4
	10	0.3
	11	0.2
	12	0.2
	13	0.5
	14	0.4
OMK/18/1.28	1	1.6
	2	0.8
	3	0.6
	4	0.4
OMK/18/1.46	1	1.7
	2	1.1
	3	1.0
	4	0.9
OMK/18/1.47	1	1.3
	2	1.2
	3	0.8
	4	1.1
	5	0.8
	6	0.7
	7	0.3
	8	0.5
	9	1.0
	10	0.7
	11	0.3
OMK/18/3.1	1	0.9
	2	0.6
	3	0.4
	4	0.5
	5	1.3
	6	0.5
	7	0.3
	8	0.2
	9	0.2
	10	0.4
	11	0.1
	12	0.4
	13	0.2
	14	0.4
	15	0.2
OMK/18/3.3	1	1.2
	2	0.9
	3	0.5
	4	0.4
	5	0.5

	6	0.2
OMK/18/3.4	1	0.9
	2	0.6
	3	1.1
	4	0.8
	5	1.1
	6	0.9
	7	0.5
	8	1.0
	9	0.6
OMK/18/3.8	1	0.7
	2	0.5
	3	0.7
	4	0.6
	5	0.7
	6	0.6
	7	0.8
	8	0.5
	9	0.4
	10	0.7
	11	0.6
	12	0.9
	13	0.7
	14	0.6
	15	0.8
	16	0.9
	17	1.1
	18	0.2
	19	0.2
	20	0.6
OMK/18/5.1	1	1.6
	2	1.0
	3	0.8
	4	0.6
	5	1.7
	6	1.0
	7	0.6
OMK/18/5.3	1	1.6
	2	0.8
	3	0.4
OMK/18/5.5	1	1.5
	2	1.0
	3	1.1
	4	0.7
	5	0.6

OMK/18/5.9	1	0.8
	2	0.7
	3	0.6
	4	0.4
	5	0.3
	6	0.5
	7	0.5
	8	0.3
OMK/18/5.13	1	1.6
	2	0.8
	3	0.8
	4	0.6
	5	0.8
	6	1.1
	7	1.0
	8	0.8
	9	0.9
	10	1.8
	11	1.0
	12	0.6
	13	0.7
	14	0.6
	15	0.6
	16	0.3
	17	0.6
	18	0.7
	19	1.1
	20	0.6
OMK/18/5.18	1	1.1
	2	0.3
	3	0.4
	4	0.6
	5	0.4
	6	0.7
	7	0.4
	8	0.2
	9	0.2
	10	0.4
	11	0.4
	12	1.0
	13	0.4
OMK/18/5.22	1	1.9
	2	0.6
	3	1.3
	4	0.9

	5	0.4
	6	0.6
	7	0.6
	8	0.7
	9	0.7
	10	0.5
OMK/18/5.25	1	1.1
	2	1.5
	3	0.6
	4	1.5
	5	1.0
	6	1.0
	7	0.9
	8	0.7
	9	0.5
	10	0.9
	11	1.3
	12	0.5
OMK/18/5.27	1	1.1
	2	0.6
	3	0.6
	4	1.0
	5	1.1
	6	0.5
	7	0.7
	8	0.7
	9	0.8
	10	0.7
	11	0.7
	12	0.4
	13	0.2
	14	0.3
	15	0.6
	16	0.7
	17	0.5
OMK/18/5.34	1	1.3
	2	1.1
	3	1.0
	4	0.9
	5	0.8
	6	1.0
	7	0.5
	8	0.8
	9	1.0
	10	0.2

	11	0.6
	12	0.5
	13	1.2
OMK/18/5.38	1	1.5
	2	0.8
	3	0.4
	4	0.6
	5	0.2
	6	0.2
	7	0.5
	8	0.7
OMK/18/5.39	1	0.6
	2	1.5
	3	0.6
	4	0.4
	5	0.5
	6	0.5
	7	0.2
	8	0.5
	9	0.4
	10	0.7
	11	0.2
OMK/18/5.40	1	0.7
	2	0.3
	3	0.3
	4	0.5
	5	0.5
	6	1.0
	7	0.5
	8	0.7
	9	0.4
	10	0.3
	11	0.4
OMK/18/7.1	1	0.8
	2	0.5
	3	0.4
	4	0.6
	5	0.4
	6	0.4
	7	0.9
	8	0.4
	9	0.3
	10	0.3
	11	0.4
	12	0.8

	13	0.5
	14	0.5
	15	0.2
	16	0.2
	17	0.2
	18	0.3
	19	0.2
	20	0.3
	21	0.4
	22	0.7
	23	0.4
OMK/18/7.2	1	1.9
	2	0.7
	3	0.4
	4	0.7
	5	0.4
	6	0.5
	7	0.4
	8	0.4
	9	0.4
	10	0.5
	11	0.6
	12	0.3
	13	0.5
	14	0.2
	15	0.1
	16	0.2
	17	0.5
	18	0.3
	19	0.5
	20	0.4
	21	0.4
	22	0.6
	23	0.6
	24	0.2
OMK/18/7.6	1	1.9
	2	0.8
	3	0.6
	4	1.3
	5	0.3
	6	1.6
	7	0.4
	8	0.4
	9	0.5
	10	0.4

	11	0.4
	12	0.5
	13	0.5
	14	0.7
	15	0.6
	16	0.6
	17	0.6
OMK/18/7.8	1	0.9
	2	0.8
	3	0.5
	4	0.3
	5	0.5
	6	0.5
	7	0.5
	8	0.5
	9	0.5
	10	0.7
	11	0.5
	12	0.4
	13	0.2
	14	0.5
	15	0.4
	16	0.4
	17	0.2
	18	0.3
	19	0.3
	20	0.5
	21	0.2
OMK/18/10.1	1	0.7
	2	0.3
	3	0.6
	4	0.5
	5	0.6
	6	0.4
	7	0.4
	8	0.6
	9	0.6
	10	0.3
	11	0.6
OMK/18/11.1	1	0.7
	2	0.9
	3	0.6
	4	1.0
	5	0.8
OMK/18/11.16	1	1.1

	2	0.7
	3	1.2
	4	0.9
	5	2.0
	6	0.6
	7	0.7
	8	0.4
	9	0.9
OMK/18/11.15	1	1.8
	2	1.1
	3	0.8
	4	0.8
	5	0.5
	6	0.4
	7	1.5
	8	0.2
	9	0.6
	10	0.4
	11	1.2
	12	0.5
	13	0.6
	14	0.5
	15	0.7
	16	0.6
	17	0.3
	18	0.4
	19	0.5
	20	1.0
OMK/18/11.22	1	0.6
	2	0.6
	3	0.7
	4	0.4
	5	0.5
	6	0.9
	7	0.8
	8	0.5
	9	1.0
	10	0.7
	11	0.3
OMK/18/11.23	1	1.5
	2	0.7
	3	0.7
	4	1.1
	5	1.0
	6	0.7

	7	1.6
	8	0.6
	9	0.5
	10	0.4
	11	0.7
	12	0.7
	13	0.5
	14	0.8
	15	0.7
	16	0.2
OMK/18/11.27	1	1.7
	2	0.7
	3	0.6
	4	1.2
	5	0.7
	6	0.7
	7	0.5
	8	0.8
	9	0.2
	10	1.1
	11	0.2
	12	0.8
	13	0.8
	14	0.4
	15	0.5
	16	0.2
	17	0.2
	18	0.2
	19	0.2
	20	0.4
OMK/18/13.1	1	0.8
	2	0.8
	3	0.9
	4	0.5
	5	0.6
	6	0.5
	7	0.4
	8	0.6
	9	0.8
	10	0.6
	11	1.7
	12	1.0
	13	0.6
	14	0.3
	15	0.4

	16	0.3
	17	0.5
	18	1.0
	19	1.4
OMK/18/13.4	1	0.5
	2	0.6
	3	0.5
	4	0.4
	5	0.6
	6	0.6
	7	0.3
	8	0.6
	9	1.0
	10	0.5
	11	0.4
	12	0.5
	13	0.7
	14	0.3
	15	0.7
OMK/18/13.8	1	1.4
	2	0.6
	3	0.6
	4	0.5
	5	0.7
	6	0.5
	7	0.3
	8	0.5
	9	0.6
	10	0.4
	11	0.3
	12	0.8
	13	0.8
	14	0.8
	15	0.8
OMK/18/13.13	1	0.8
	2	0.7
	3	0.4
	4	0.9
	5	0.3
	6	0.3
	7	0.8
	8	0.5
OMK/18/13.9	1	0.8
	2	0.6
	3	0.8

	4	1.4
	5	0.7
	6	0.9
	7	1.4
	8	0.7
	9	0.3
	10	1.4
	11	0.6
	12	0.1
	13	0.4
	14	0.2
OMK/18/13.12	1	0.7
	2	0.5
	3	0.2
	4	0.7
	5	0.9
	6	0.5
	7	0.2
	8	0.7
	9	0.7
	10	0.7
	11	0.3
OMK/18/13.19	1	0.5
	2	0.6
	3	0.8
	4	0.9
	5	0.7
	6	1.0
	7	0.5
	8	0.2
	9	1.0
	10	0.6
	11	0.5
	12	0.7
	13	0.7
	14	0.6
	15	0.7
	16	0.2
	17	0.7
	18	0.3
	19	0.3
	20	0.9
	21	0.7
	22	0.3
	23	0.2

	24	0.7
OMK/18/16.2	1	1.0
	2	1.3
	3	0.9
	4	0.7
	5	0.9
	6	0.3
	7	0.3
	8	0.2
OMK/18/20.1	1	0.3
	2	0.3
	3	0.3
	4	0.1
	5	0.4
	6	0.5
	7	0.3
	8	0.1
	9	0.5
	10	0.3
	11	0.2
	12	0.6
	13	0.4
	14	1.0
	15	0.6
	16	0.1

2.2.2 Data of the width of cloudinomorph tubes measured from 2D bedding planes

Sample Picture	mm from base	Width (mm)	Growth rate between last Increment	Average Growth rate
OMK/18/1.23 (1)	0	0.17	0.00	
	1	0.38	1.18	
	2	0.36	-0.05	
	3	0.33	-0.08	
	4	0.37	0.14	-0.01
OMK/18/1.23 (2)	0	0.14		
	1	0.50	2.63	
	2	0.35	-0.30	-0.30
OMK/18/3.4 (1)	0	0.26		
	1	0.84	2.24	
	2	0.95	0.13	
	3	0.75	-0.21	
	4	0.94	0.25	
	5	0.81	-0.14	1.15
OMK/18/3.4 (2)	0	0.43		
	1	0.71	0.67	
	2	0.80	0.12	
	3	1.06	0.33	
	4	1.12	0.05	
	5	1.22	0.09	0.71
OMK/18/3.4 (3)	0	0.32		
	1	0.89	1.80	
	2	0.88	-0.01	
	3	0.77	-0.12	
	4	0.53	-0.31	-0.41
OMK/18/3.4 (4)	0	0.26		
	1	0.61	1.37	
	2	0.64	0.05	
	3	0.65	0.02	0.07
OMK/18/3.4 (5)	0	0.25		
	1	0.52	1.04	
	2	0.60	0.16	0.16
OMK/18/3.8 (1)	0	1.05		
	1	1.09	0.04	
	2	1.20	0.10	
	3	1.36	0.14	
	4	1.45	0.07	0.33
OMK/18/3.8 (2)	0	0.53		
	1	1.80	2.36	

	2	1.75	-0.03	
	3	0.52	-0.70	-0.71
OMK/18/3.8 (3)	0	0.48		
	1	1.58	2.30	
	2	1.82	0.15	
	3	0.87	-0.52	-0.45
OMK/18/3.8 (4)	0	1.14		
	1	1.22	0.07	
	2	1.74	0.42	
	3	1.67	-0.04	
	4	1.03	-0.38	-0.16
OMK/18/3.8 (5)	0	0.65		
	1	1.68	1.60	
	2	1.81	0.08	
	3	1.50	-0.17	-0.11
OMK/18/5.22 (1)	0	0.19		
	1	0.48	1.47	
	2	0.52	0.09	
	3	0.63	0.22	
	4	0.58	-0.08	
	5	0.71	0.23	
	6	0.65	-0.09	
	7	0.29	-0.55	-0.39
OMK/18/5.22 (2)	0	0.36		
	1	1.26	2.51	
	2	1.27	0.01	
	3	1.26	-0.01	-0.004
OMK/18/5.22 (3)	0	0.33		
	1	0.49	0.50	
	2	0.24	-0.51	-0.51
OMK/18/5.22 (4)	0	0.27		
	1	0.50	0.91	
	2	0.50	-0.02	
	3	0.67	0.35	
	4	0.26	-0.61	-0.49
OMK/18/5.22 (5)	0	0.32		
	1	0.56	0.75	
	2	0.25	-0.56	-0.56
OMK/18/5.23 (1)	0	0.52		
	1	1.67	2.20	
	2	2.13	0.28	
	3	2.29	0.08	
	4	2.32	0.01	0.39
OMK/18/5.23 (2)	0	0.65		
	1	1.94	1.96	

	2	1.82	-0.06	
	3	1.74	-0.04	
	4	1.77	0.02	
	5	1.74	-0.02	
	6	1.51	-0.13	-0.22
OMK/18/5.23 (3)	0	0.39		
	1	0.70	0.81	
	2	0.74	0.06	
	3	0.42	-0.43	-0.39
OMK/18/5.23 (4)	0	0.50		
	1	0.99	1.00	
	2	1.19	0.20	
	3	0.64	-0.46	-0.36
OMK/18/7.1 (1)	0	0.23		
	1	0.43	0.88	
	2	0.20	-0.54	-0.54
OMK/18/7.1 (2)	0	0.12		
	1	0.35	1.97	
	2	0.42	0.18	
	3	0.10	-0.76	-0.72
OMK/18/7.1 (3)	0	0.52		
	1	1.00	0.91	
	2	0.97	-0.02	
	3	0.86	-0.12	
	4	0.74	-0.14	
	5	0.78	0.06	-0.22
OMK/18/7.1 (4)	0	0.10		
	1	0.33	2.35	
	2	0.30	-0.10	
	3	0.22	-0.26	-0.33

Appendix 3: Environmental and diagenetic controls on the morphology and calcification in *Cloudina* of the Nama Group, Namibia

Appendix 3.1 Shore et al. (2021)

Environmental and diagenetic controls on the morphology and calcification in of the Ediacaran metazoan *Cloudina*

scientific reports

Check for updates

OPEN

Environmental and diagenetic controls on the morphology and calcification of the Ediacaran metazoan *Cloudina*

Amy Shore✉ & Rachel Wood

Cloudina **is a globally distributed Ediacaran metazoan, with a tubular, funnel-in-funnel form built of thin laminae (ca. 1–10 µm). To what degree local environmental controlled morphology, and whether early diagenesis controlled the degree of calcification of *Cloudina*, is debated. Here we test these hypotheses by considering assemblages from four, coeval localities from the Upper Omkyk Member, Nama Group, Namibia, from inner ramp to mid-ramp reef across the Zaris Subbasin. We show that sinuosity of the *Cloudina* tube is variable between sites, as is the relative thickness of the tube wall, suggesting these features were environmentally controlled. Walls are thickest in high-energy reef settings, and thinnest in the low-energy, inner ramp. While local diagenesis controls preservation, all diagenetic expressions are consistent with the presence of weakly calcified, organic-rich laminae, and lamina thicknesses are broadly constant. Finally, internal 'cements' within *Cloudina* are found in all sites, and pre-date skeletal breakage, transport, as well as syn-sedimentary botryoidal cement precipitation. Best preservation shows these to be formed by fine, pseudomorphed aragonitic acicular crystals. Sr concentrations and Mg/Ca show no statistically significant differences between internal *Cloudina* cements and botryoidal cements, but we infer all internal cements to have precipitated when *Cloudina* was still *in-situ* and added considerable mechanical strength, but may have formed post-mortem or in abandoned parts of the skeleton.**

The terminal Ediacaran saw the appearance of evolutionary innovations such as the first appearance of supposed metazoans with motile behaviour and biomineralised skeletons[1,2]. *Cloudina,* and cloudinomorphs (or cloudinids)—a term defining a group of similar tubular fossils including *Conotubus, Saarina, Multiconotubus, Costatubus, Zuunia,* and *Rajatubulus*—were globally distributed between ca. 550-ca. 522 million years ago (Ma)[1,3,4]. Cloudinomorphs share a similar, funnel-in-funnel organisation without transverse structures, with a straight or sinuous morphology[1,5]. They can be organic-only or preserved as calcite, phosphate, limonite/pyrite, or silica. Both organic and calcified skeletons may be phosphatised.

Cloudinomorph affinity is unresolved. Recent findings of a pyritised central tubular structure within cloudinomorph tubes from Nevada, inferred to be a gut which, together with the nested-funnel morphology and laminar ultrastructure, suggest an annelid affinity. However, the presence of deep-seated branching within the parent *Cloudina* tube as well as polytomous branching in cloudinomorphs, might indicate a cnidarian affinity[5–7]. Cloudinomorphs may in fact represent a group of diverse taxa with a convergent morphology[7].

Cloudina is a generalist taxa found in multiple carbonate settings, including attached to microbial mats and thrombolites, and capable of reef-framework formation[5,8–10]. Tube size varies inter-specifically and is also environmentally-controlled. For example, in the Nama Group, Namibia, *Cloudina* which grew associated with shallow, hydrodynamically-energetic reefs shows the largest tube diameters recorded, but individuals with smaller tube diameters were dominant in low-energy, microbial mat settings[10].

Cloudina is considered to have either aragonite or high-Mg calcite original mineralogy[1,3,11,12], and is thought to have biomineralised during life. *Cloudina* may have biomineralised via calcification of pre-existing organic laminae as revealed by Raman spectroscopy, which are 1–10 µm in thickness. These are often paired, with up to eight laminae within a wall[14,15]. The walls of *Cloudina* show a granular, micritic microstructure (crystal size ca.1 µm), even in phosphatised specimens[13]. This calcification may have proceeded via growth of initial amorphous calcium carbonate (ACC) nanoparticles, comparable to that found in modern echinoderms, molluscs and cnidarians[16].

School of GeoSciences, University of Edinburgh, James Hutton Road, Edinburgh EH9 3FE, UK. ✉email: amy.shore@ed.ac.uk

Cloudina are observed to show both brittle fracturing of the tube walls, suggesting early, probable in-vivo and potentially strong calcification, as well as ductile deformation suggesting weaker calcification of organic-rich laminae[3,13]. It has been argued that delamination structures (where laminae peel apart from one another) in *Zuunia*, and widespread plastic deformation in cloudinomorphs generally, suggests a skeleton of primarily organic composition, where calcification was post-mortem and diagenetically-mediated[15]. Large sparry calcite crystals that incorporate multiple laminae and infill *Cloudina* tubes from the Mooifontein Member in the Witputs Basin of the Nama Group, have been noted, which has been used to further support the notion that *Cloudina* tube walls consist of diagenetic, rather than biotic, calcite[15]. But it has long been known that acicular, pseudomorphed aragonitic cements are present between the laminae of *Cloudina*, which are often neomorphosed to a fibrous or sparry calcite[3], and these areas have been found to be organic-rich in specimens from Brazil[14].

Identifying biologically controlled vs. biologically induced calcification[17] can be problematic, as the degree of biological control can vary. Indeed, limited or considerable biological control can still be demonstrated even where most aspects of calcification vary with environmental parameters[18,19]. Conversely, apparently organised microstructures may not result from biological control per se but may reflect interactions among otherwise disorganised crystals[20].

Here we test the hypothesis that the type and extent of calcification and morphology in *Cloudina* was controlled environmentally, by considering coeval assemblages from the Upper Omkyk Member of the Nama Group, Namibia, from diverse water depth and hydrodynamic settings along an inner shelf to reef transect from the Zaris Subbasin. We seek to quantify the ecophenotypic response of *Cloudina* tube construction to the environmental conditions of growth, by comparing whole tube sinuosity (the degree of curvature), as well as individual lamina thickness and overall tube wall thickness to test whether these are variable and hence subject to environmental control, or invariant and therefore under strong biological control. The sinuosity of *Cloudina* tubes, for example, is noticeably variable throughout the Nama Group, and this may reflect some aspect of ambient hydrodynamics or feeding efficiency. We also consider the control of differing early diagenetic style on the preservation of *Cloudina* skeletal material, as the inner ramp settings are prone to meteoric diagenesis but the more energetic mid-ramp reef settings to high carbonate supersaturation and marine phreatic diagenesis. Features found consistently across all diagenetic settings might be considered more likely to have a biological, rather than diagenetic, origin. We use descriptive and quantitative data derived from reef surfaces, and bedding planes, using petrographic and cathodoluminescence (CL) microscopy, and electron microprobe analysis (EMPA) of Sr concentrations, which can indicate differences in original carbonate mineralogy, and Mg/Ca which may also vary according to diagenetic phase or with biological fractionation.

Geological setting

The Nama Group, Namibia (ca. 550–539 Ma), is a late Ediacaran fossiliferous carbonate-siliciclastic succession deposited in supratidal to outer ramp settings[21] (Fig. 1). The Zaris and Witputs Subbasins are separated by the tectonic Osis Arch, and are correlated using sequence stratigraphy and chemostratigraphy[22–24]. We consider *Cloudina* assemblages attributed to both *Cloudina riemkeae* and *Cloudina hartmannae* from four localities that provide a transect of the Upper Omkyk Member, Kuibis Subgroup across the Zaris Subbasin (Fig. 1B,C), from Driedoornvlakte (mid-ramp, high-energy reef), Zebra River (inner mid-ramp, thrombolitic-stromatolitic reefs), Omkyk (inner-ramp, low-energy), to Zwartmodder (proximal inner-ramp, very low-energy)[25]. These record coeval communities that grew at different water depths, with differing host lithologies, hydrodynamic energies, and early diagenetic settings (Fig. 1C; summarised in Table S1 and Supplementary Information). Ash bed U/Pb data collected from the overlying Hoogland Member has been dated at 547.32 ± 0.65 Ma[26].

Results

Sinuosity of *Cloudina*. The four localities show a varying degree of sinuosity of *Cloudina* tubes (Figs. 1D–G, 2B,C). At Driedoornvlakte, sinuosity ranges between 1.00 and 1.70 (mean = 1.04, n = 156, standard deviation = 0.07), with the percentage shortening (the amount of shortening as a percentage in relation to the length along the midline) ranging between 0.00 and 41.29% (mean = 3.23%, standard deviation = 4.42). Zebra River and Omkyk both show greater tube sinuosity, from 1.00 to 2.98 (mean = 1.21, n = 98, standard deviation = 0.38) and 1.00–2.42 (mean = 1.07, n = 144, standard deviation = 0.15), respectively. Zebra River *Cloudina* show shortening from 0.00 to 66.69% (mean = 13.01%, standard deviation = 15.8), greater than the percentage found at Omkyk, where the shortening ranges between 0.00 and 58.67% (mean = 5.22%, standard deviation = 7.86). Zwartmodder *Cloudina* shows the lowest range of sinuosity, from 1.00 to 1.36 (mean = 1.04, n = 99, standard deviation = 0.06), and shortening between 0.00 and 26.25% (mean = 3.27, standard deviation = 4.57). Comparing the percentage of different ranges of sinuosity values at each locality, *Cloudina* at Zebra River show the greatest sinuosity, accounting for 100% of these values (Fig. 2C). These also have the lowest percentage of low sinuosity values (12%), whereas *Cloudina* from Driedoornvlakte show the highest percentage of low sinuosity values (37%) (Fig. 2C).

Using the Kruskal–Wallis Test, the H-value for these data is 14.96, with a *P*-value of 0.002, indicating that the sinuosity of the *Cloudina* tubes varies significantly between localities. Z-tests also confirm that the sinuosity varies between all localities except between Driedoornvlakte and Zwartmodder.

Diagenetic preservation of *Cloudina*. The form of preservation of *Cloudina* varies across the Zaris subbasin transect (Table S2).

At Driedoornvlakte, *Cloudina hartmannae* are often surrounded by pseudomorphed aragonitic botryoids[3,7,27] (Fig. 1D). Individuals show brittle deformation. *Cloudina* walls are preserved as light grey calcite, or light brown to yellow crusts indicating partial dolomitisation (Fig. 1D). This inclusion-rich dolomite is brightly luminescent varying between bright yellow to red under CL (Fig. 3). Laminae are often found as pairs, where abundant

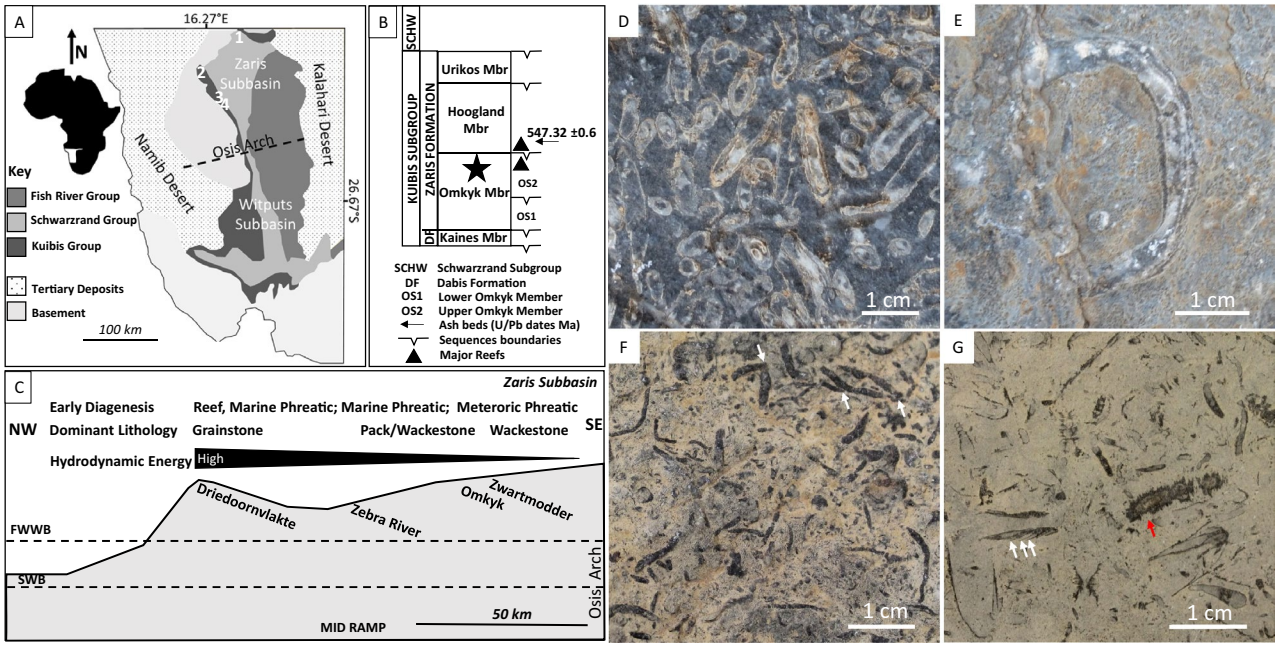

Figure 1. Geological map and study site locations (1: Driedoornvlakte; 2: Zebra River; 3: Omkyk Farm; 4: Zwartmodder) within the Nama Group, Namibia, with bedding surface images of *Cloudina* from different coeval communities from the Upper Omkyk Member (drawn in Microsoft PowerPoint 2016). (**A**) Localities, modified from Grotzinger and Miller 2008[21]. (**B**) Stratigraphy of the Nama Group with the Upper Omkyk Member highlighted by a star, modified from Wood et al.[25] (drawn in Microsoft PowerPoint 2016). (**C**) Schematic of the Zaris Subbasin with relative position of localities, and dominant hydrodynamic regime and lithologies, and early diagenetic setting. Modified from Wood et al.[25] (drawn in PowerPoint 2016). (**D**) Driedoornvlakte, preserved as white or grey calcite cement surrounded by darker calcite cements, predominantly pseudomorphed aragonitic botryoids. (**E**) Zebra River, infilled with light sparry calcite cement surrounded by dolomitised micrite. (**F**) Omkyk Farm, cloudinomorphs, probably *Cloudina*, including potential branching individuals (arrowed) as branching can only be proven through the presence of a shared cavity, preserved as black sparry calcite surrounded by dolomitised wackestone[7]. (**G**) Zwartmodder, preserved as black sparry calcite surrounded by dolomitised micrite which preserves the fine annulated structure and phlanges (white arrowed). Possible fragments of *Corumbella* may also be present (red arrow). Figure created in PowerPoint 2016.

non-luminescent fine acicular cements with blunt terminations (4.2–17.6 µm in length, mean = 11.2 µm; and 2.1–7 µm in width, mean = 4.5 µm, n = 17) that nucleate from the laminae (Fig. 3D). This is here termed *inter-lamina cement* (Fig. 2A). Between separate paired laminae is a patchily luminescent cement (Fig. 3I)—here termed *inter-funnel cement* (Fig. 2A). The paired laminae with inter-lamina cement, and inter-funnel cements constitute the *Cloudina* wall extending from the outer wall to inner wall that forms the central cavity (Fig. 2A).

A further dull, patchily luminescent cement is present, which formed from the innermost laminae and grew upon the inner wall of the tube—here termed *intra-cloudinomorph cement* (Figs. 2A, 3B,C;). A cement with similar cathodoluminescence is found between the tubes themselves—here termed *inter-cloudinomorph cement* (Figs. 2A, 3B,C,K,L), as noted by Penny, et al[27]. Dolomitised geopetal micrite with red luminescence infills *Cloudina*, and postdates the intra-cloudinomorph cement (Fig. 3A–C). Pseudomorphed aragonitic botryoids, with blunt crystal terminations, nucleate from both the intra- and inter-cloudinomorph cements, and are also covered by geopetal sediment (Fig. 3B). Breakage of laminae is evident, with associated breakage of the inter-funnel cement (Fig. 3D,F–I).

Cloudina from Zebra River are preserved as calcite surrounded by wackestone (Fig. 1E). The ornamental features of the tube are not preserved and the tube cavity is infilled with sparry calcite. Individuals show brittle and ductile deformation. Paired laminae (Figs. 4K-L) are present, and the inter-lamina space is infilled by acicular crystals (Fig. 4D,G,N) ranging from 9.4 to 15.5 µm in length (mean = 11.7 µm, n = 6) and 2.1 to 4 µm in width (mean = 3.1 µm), forming the inter-lamina cement. In some areas the laminae are undulating, with a prominent inter-funnel cement infill (Fig. 4C–G,J–L).

Patchily luminescent inter-funnel cement is also present, formed by abundant clusters of acicular cements with blunt terminations which nucleate from the laminae (Fig. 4B,D,E,G). A dull luminescent, pore-lining patchy cement (Fig. 4C–G) overlies inter-funnel cements. Later tube cavity infill consists of calcite spar with duller luminescence (Fig. 4B). In *Cloudina riemkeae*, the acicular cements are finer and pore-lining cements are not observed, but inter-funnel cements with dull luminescence are present, followed by more luminescent pseudomorphosed aragonitic botryoids which nucleate from the outer tube walls (Fig. 4H–I). There is variation in the preservation of this inter-funnel cement, which varies even within a single *Cloudina* tube: inter-funnel cements

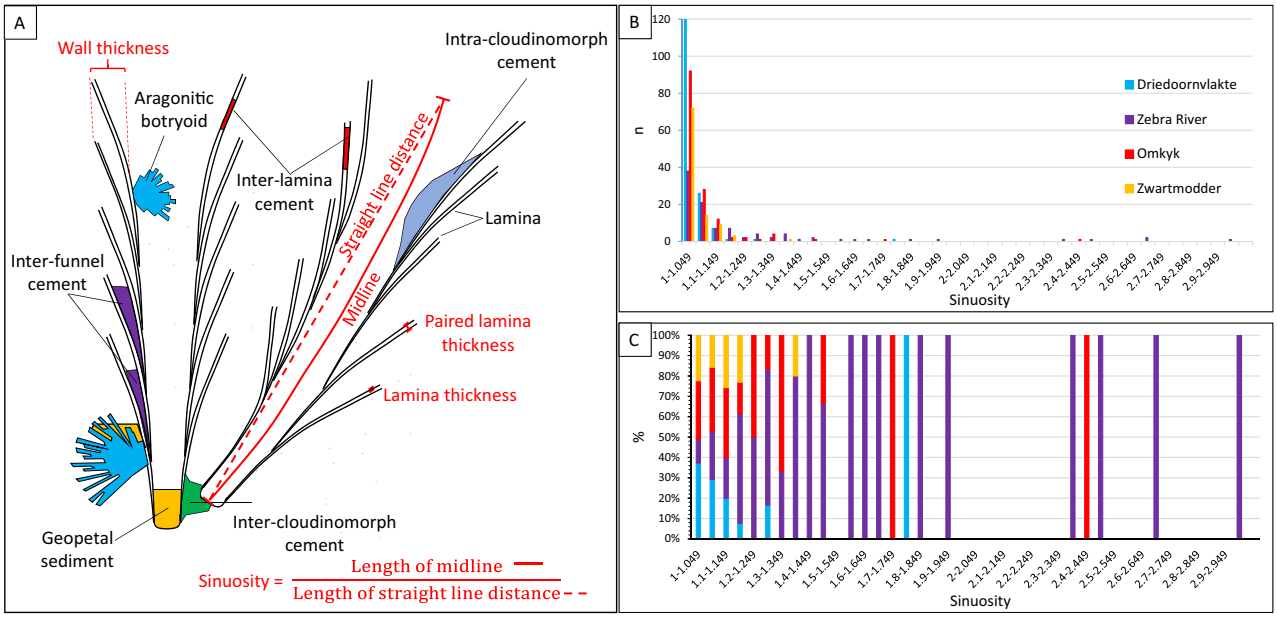

Figure 2. *Cloudina* terminology and sinuosity data. (**A**) Schematic of two *Cloudina* tubes with terminology (black text) and measurements (red text) used in this paper derived from 2D surfaces (drawn in Microsoft PowerPoint 2016). Sinuosity is defined as the length of the midline over the straight line distance between the two ends of the tube in longitudinal section. *Lamina thickness* is the thickness of an individual lamina and *paired laminae thickness* the thickness of two laminae including the area between. *Wall thickness* is the sum of all components that form the complete tube wall in transverse section from outer wall to inner wall defining the central cavity. Cements formed between paired laminae are termed *inter-lamina cement*, between sets of paired laminae *inter-funnel cement,* between different tubes *inter-cloudinomorph cement,* and that which forms within the central cavity is termed *intra-cloudinomorph cement*. Inorganic pseudomorphed aragonitic botryoidal cements and sediment have also been labelled in the figure. (**B**) Sinuosity distribution (created in Microsoft Excel 2016). (**C**) Percentage of *Cloudina* with different sinuosities, based on 2D bedding plane measurements. Figure created in PowerPoint 2016, graphs created in Microsoft Excel 2016.

close to the exterior of the *Cloudina* tubes are mostly preserved as clear, dull or non-luminescent neomorphic calcite spar, but inter-lamina cements within the central areas of the tubes preserve acicular crystals (Fig. 4C,D).

The inter-funnel cements in *Cloudina riemkeae* show breakage, with fractured crystal boundaries where sediment has entered the tube (Fig. 4J–L). Individual or paired laminae also show spalling as a result of breakage of the outer wall (Fig. 4G).

The cloudinomorphs of Omkyk are dark in colour and composed of large (0.1–1 mm) calcite spar crystals (Fig. 1F). These also lack ornamentation, but some retain the stacked funnel-in-funnel structure[7]. Individuals show brittle and ductile deformation. CL highlights three generations of cements within the cloudinomorph tube (Fig. 5A,B,D). First a thin (200 µm) acicular cement generation, which is not continuous throughout the tube cavity, followed by an isopachous cement with patchy or dull-luminescence with limited zonation (Fig. 5D). The tube cavity is infilled by zoned sparry cement, which nucleates from the isopachous cement (Fig. 5D).

Zwartmodder *Cloudina* are also preserved wholly as coarse calcite spar (Figs. 1G, 6A,C). Fine external features, including external phlanges and the annulated outer wall, are well preserved (Fig. 1G), and *Cloudina* shows evidence of brittle deformation (Fig. 6C). The *Cloudina* skeleton is preserved a mould, infilled by a centripetal, sparry calcite cement with dull luminescence that becomes brighter towards the centre of the moulds (Fig. 6A,B). Individual laminae cannot be detected, but inter-lamina and inter-funnel cement are present as sparry calcite (Fig. 6F). Individual or paired laminae are evident through the spalling of the tube walls in areas where inter-funnel cement is not present and are instead separated by micrite infill (Fig. 6F). Under CL, the micrite shows three zones of cement growth, dull-luminescent followed by bright luminescent, and a final non-luminescent zone (Fig. 6B,E,F). These cement zones protrude into the sparry calcite infill, which can also be seen under SEM along with small, cube shaped holes (Fig. 6G).

Elemental distribution. Strontium (Sr) concentrations and the Mg/Ca ratios were sampled from *Cloudina* and associated early cements from Driedoornvlakte and Zebra River using EMPA (See Methods, Supplementary Information; Fig. 7; S1; Tables S3–S6).

The Kruskal–Wallis test shows a statistical difference between the Sr concentration of different cements at Zebra River, between the inter-laminae cements and both laminae ($P = 0.016$) and inter-funnel cements ($P = 0.014$), and between the micritic matrix and both inter-laminae cement ($P = 0.001$) and inter-funnel cement ($P = 0.030$) (Table S7). There are no statistical differences in Mg/Ca contents of any measured features (Table S8).

Cloudina riemkeae from Driedoornvlakte also shows statistical differences in Sr concentration between the inter-laminae and the inter-funnel cements ($P = 0.041$) (Table S9), and between inter-laminae and the inter-funnel

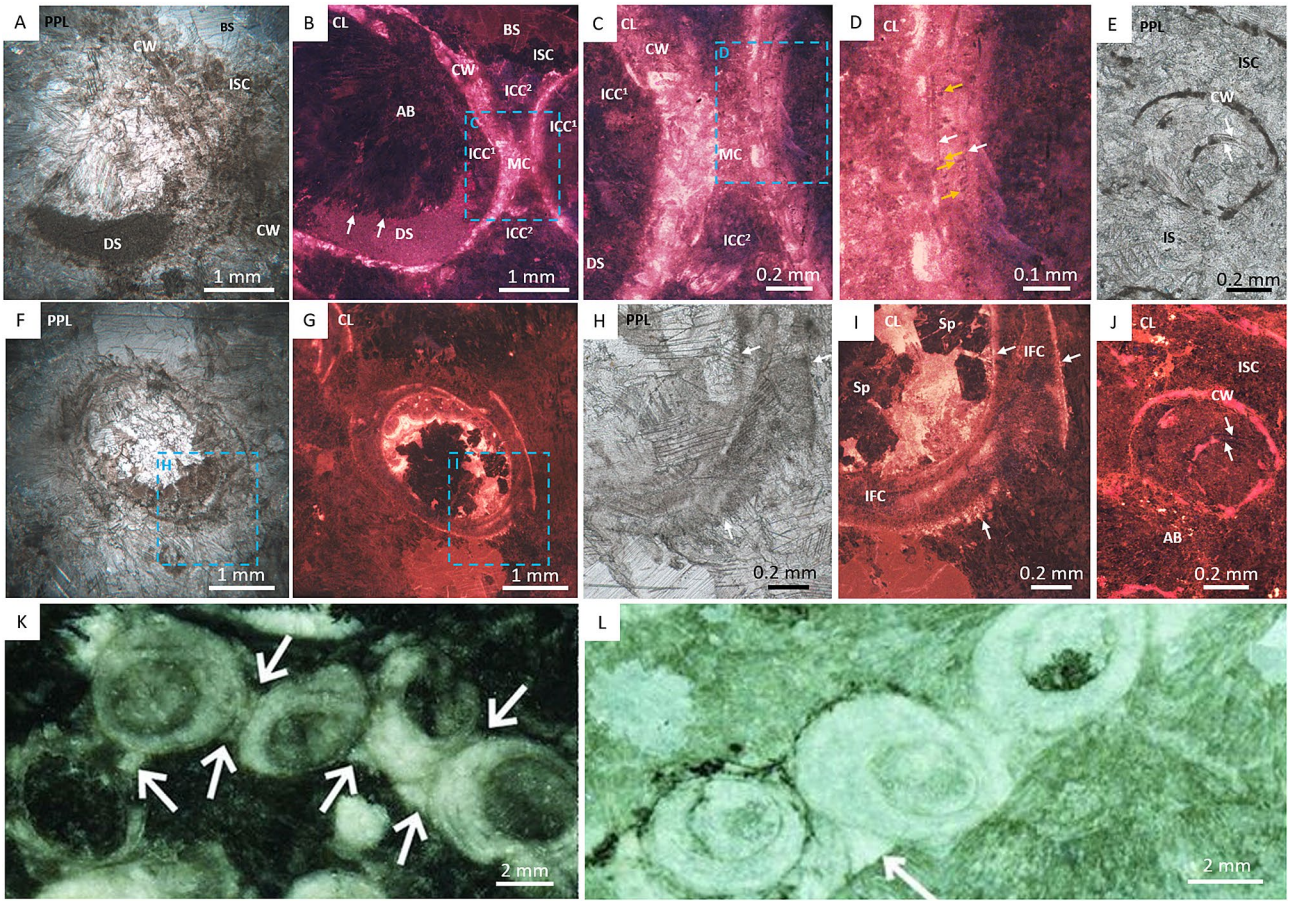

Figure 3. Photomicrographs of *Cloudina hartmannae* and *Cloudina riemkeae* from Driedoornvlakte, Upper Omkyk Member, Nama Group. (**A**) PPL of attached *Cloudina* with a dolomitised wall (CW) and filled with dolomitised sediment (DS), followed by an inclusion-rich sparry calcite (ISC) and a later clear burial spar (BS). (**B**) CL image of A, intra-cloudinomorph cement (ICC^1) nucleated from the inner *Cloudina* wall and inter-cloudinomorph cement (ICC^2) formed between the *Cloudina* tubes and nucleated from the outer wall and including the mutual cement (MC) which has the same luminescence as CW. Non-luminescent pseudomorphed aragonitic botryoids (AB) nucleate from ICC^1. These are proceeded by ISC and BS. (**C**) Inset of B, showing ICC^1 and ICC^2 -cements with same luminescence. (**D**) Inset of C, showing bright luminescent CW with multiple non-luminescent laminae (white arrows) with small aragonitic needles (orange arrows) nucleating from laminae. (**E**) PPL of *Cloudina* with a dolomitised wall (CW) composed of laminae (arrowed) with thin sparry calcite infill between the two laminae, surrounded by inclusion-rich sparry calcite (ISC). (**F**) Transverse PPL of dolomitised individual. (**G**) CL of C. (**H**) Inset of F, of broken, dolomitised *Cloudina* wall (arrowed). (**I**) Inset of G in CL, of broken bright luminescent *Cloudina* wall (arrowed) exposing the inter-funnel cement (IFC). The rest of the tube is infilled with non-luminescent spar (Sp). (**J**) CL of E, with dull luminescent cements (arrowed) highlighting cements between the laminae and is surrounded by ISC. AB nucleate from the CW. (**K**) from Penny et al.[27]. Polished slab highlighting inter-cloudinomorph cements (arrowed) between multiple *Cloudina* individuals. (**L**) From Penny et al.[27]. PPL image of inter-cloudinomorph cements (arrowed) situated between *Cloudina* individuals from which botryoids nucleate. Figure created in PowerPoint, 2016.

cements compared to the *Cloudina* wall ($P = 0.009$ and $P = 0.002$, respectfully) (Table S9). Sr content of the inter-laminae cement and *Cloudina* wall are statistically different to the inclusion-rich spar ($P = 0.023$ and $P = 0.011$, respectfully), but this is not the case for the inter-funnel cement ($P = 0.291$) which is recrystallised as an inclusion-rich spar (Fig. 3E,J; Table S9). There is a significant difference between the *Cloudina* wall at Driedoornvlakte and the other *Cloudina*-associated cements, probably as a result of the dolomitisation. Sr content within internal cements associated with *Cloudina hartmannae* show no statistical differences, but there is a significant difference between the inter-cloudinomorph cement and botryoidal cements ($P = 0.043$) (Table S10).

There are no statistical differences in Mg/Ca contents of any measured features at Driedoornvlakte apart from the *Cloudina* wall of the *Cloudina riemkeae*, due to selective dolomitisation (Tables S11, S12).

Lamina thickness. Organic laminae have not been preserved at the studied sites. Laminae are preserved as moulds at Zebra River and Zwartmodder (Figs. 4, 6), at Driedoornvlakte they have been dolomitised (Fig. 3),

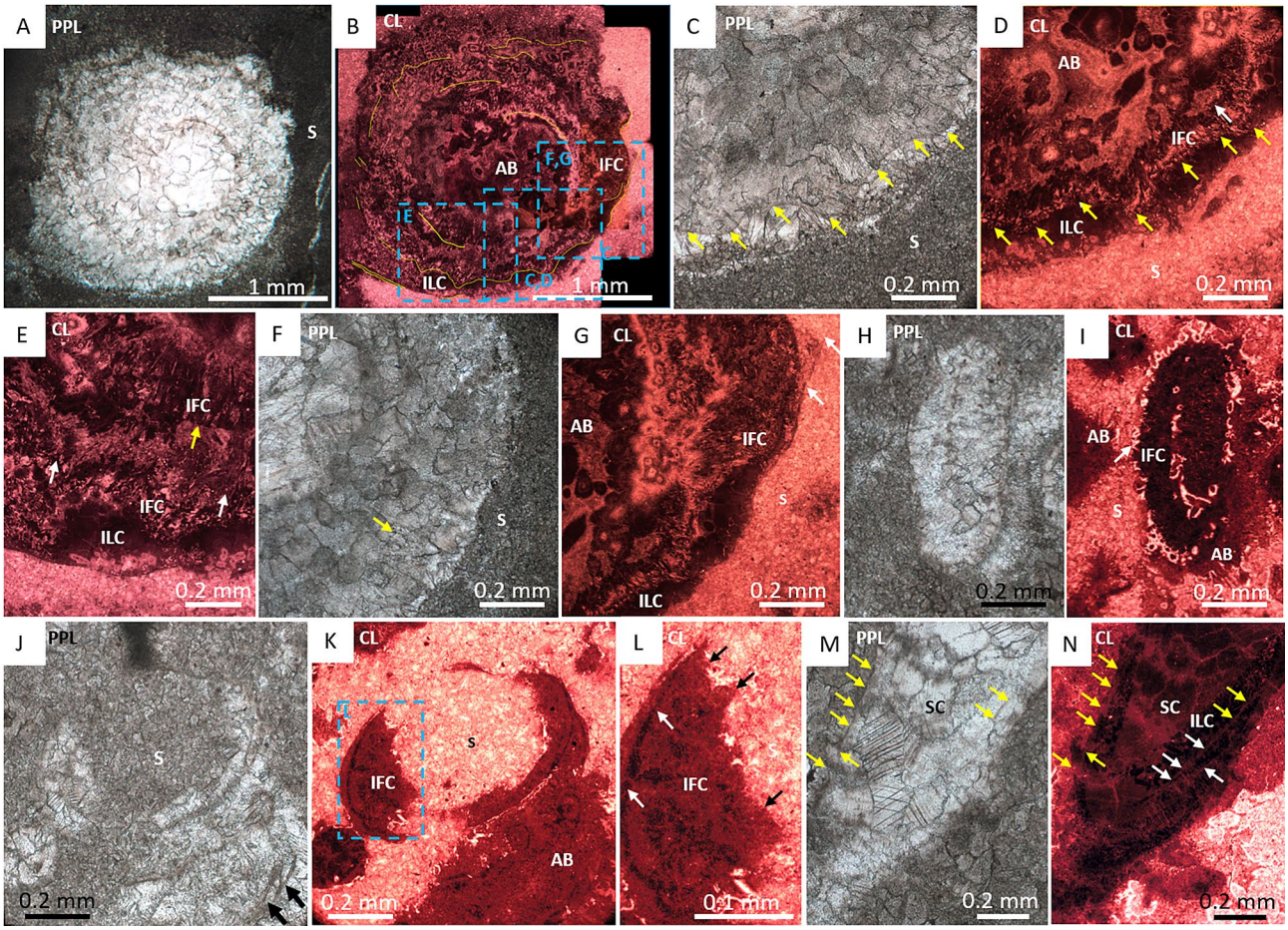

Figure 4. Photomicrographs of *Cloudina* from Zebra River, Upper Omkyk Member, Nama Group. (**A**) PPL of *Cloudina* infilled with sparry calcite surrounded by micritic sediment (S). (**B**) CL image of A, with inter-lamina cements (ILC) forming between outer laminae (highlighted in yellow). Pseudomorphed aragonitic botryoids (AB) grow from the laminae, and the inter-funnel cements (IFC) pre-date dull luminescent burial cements with ILC forming between paired laminae. AB infilled the *Cloudina* tube and S surrounds the tube. (**C**) Inset of B \, PPL showing laminae with a wavy form (yellow arrows). (**D**) CL image of E, laminae highlighted by yellow arrows with same form as PPL image. Nucleation of IFC indicates location of laminae. (**E**) Inset of B, ILC located between two outer laminae (white arrows). IFC nucleate from inner laminae (yellow arrow). (**F**) Inset of B in PPL with lamina visible (arrowed). (**G**) CL of F, where outer laminae shows evidence of 'spalling' (arrowed) and infilled by S. ILC situated between laminae and areas of patchy bright luminescence indicate IFC. AB infills the rest of the tube. (**H**) PPL of *Cloudina*. (**I**) Pseudomorphed aragonitic botryoids (AB) outside *Cloudina* tube. Botryoids grow from the outer tube wall into the surrounding sediment (S), and have a different luminescence to those inside the tube. Early IFC grows from the inner *Cloudina* laminae (arrowed). (**J**) PPL of a transverse section of a *Cloudina*, which is infilled by dolomitised sediment (S), and have a different luminescence to those inside the tube. Early IFC grows from the inner *Cloudina* laminae (arrowed). (**J**) PPL of a transverse section of a *Cloudina*, which is infilled by dolomitised sediment (S) and two sets of broken paired laminae (arrowed) (**K**) CL of J, bright luminescent dolomitised sediment infills the central area of the broken tube. Dull luminescent botryoids (AB) outside the tube. Dull luminescent IFC forms the *Cloudina* skeleton. (**L**) Inset of K, with evidence of breakage of the non-luminescent ILC (white arrows) and IFC (black arrows). (**M**) PPL of *Cloudina* tube infilled with sparry calcite (SC) with preserved laminae (yellow arrowed). (**N**) CL of M, with laminae observed in PPL (yellow arrows), laminae shown in CL (white arrows). Laminae are preserved with the same luminescence as the SC infill with a dull cement ILC between the laminae. Figure created in PowerPoint 2016.

whilst at Omkyk laminae are not detectable at all (Fig. 5). Laminae thickness at Zebra River and Driedoornvlakte were measured using both CL and PPL images and using CL at Zwartmodder.

Cloudina of Driedoornvlakte and Zebra River have laminae of similar thicknesses, with Driedoornvlakte laminae thicknesses ranging from 2.1 to 9.6 µm (mean = 5 µm, n = 23) and Zebra River *Cloudina* laminae ranging from 3.3 to 10.8 µm in thickness (mean = 6.5 µm, n = 23), with a T = 1.872, and *P*-value = 0.034 (Fig. 8A).

Paired laminae thickness, however, varies between sites. At Driedoornvlakte from 10.6 to 55.3 µm (mean = 34.3 µm, n = 14), Zebra River from 5.9 to 40.3 µm (mean = 19.3 µm, n = 10), and Zwartmodder from 11 to 23.7 µm (mean = 15.4 µm, n = 10) (Fig. 8B). The spalled features of the *Cloudina* from Zwartmodder are now

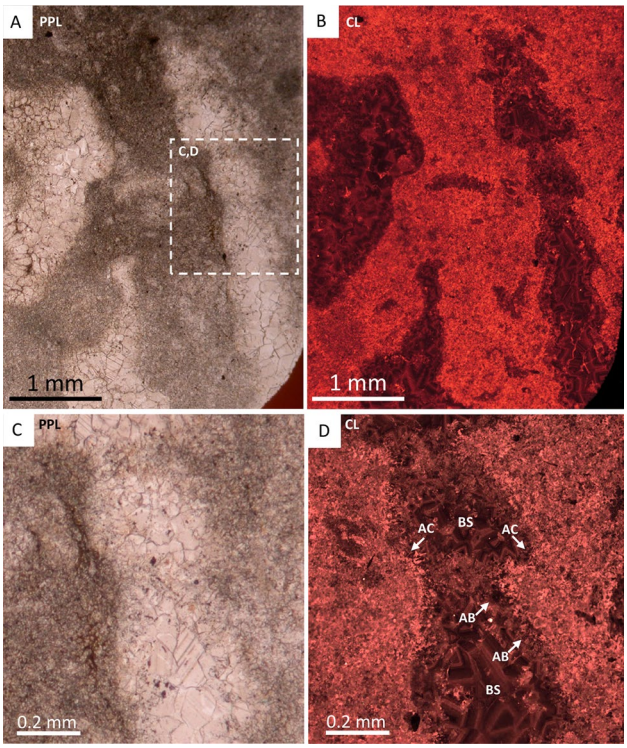

Figure 5. Photomicrographs of cloudinomorphs, probably *Cloudina,* from Omkyk Farm, Upper Omkyk Member, Nama Group. (**A**) PPL image of cloudinomorph tube. (**B**) CL image of A. (**C**) Inset of A. (**D**) CL image of A, with early acicular cements (AC) which vary between bright and non-luminescence. AC is followed by poorly-zoned acicular bladed calcite (AB). A well zoned blocky calcite (BS) infills the remaining tube cavity. Figure created in PowerPoint 2016.

preserved as centripetal calcite cement (Fig. 6F) and consist of the inter-lamina cement and two laminae; the thickness of these features is similar to that of the paired laminae at Driedoornvlakte and Zebra River.

These differences are statistically significant (T = 2.32, *P*-value = 0.040). The Kruskal–Wallis Test shows that paired laminae thickness from Driedoornvlakte, Zebra River and Zwartmodder, are significantly different (H-value = 7.65, *P*-value = 0.022).

Wall thickness. *Cloudina* wall thickness is defined as the width between the outer tube wall and the inner tube wall forming the internal cavity (Fig. 2A). Measurements of wall thickness were taken from bedding surfaces at Driedoornvlakte, Zebra River and Zwartmodder. At Driedoornvlakte, maximum wall thickness for any individual *Cloudina* tube ranges from 0.25 to 1.88 mm (mean = 0.93 mm, n = 147) (Fig. 8C). Ranges were lower at Zebra River and Zwartmodder, from 0.16 to 1.43 mm (mean = 0.51 mm, n = 79) and 0.12–1.38 mm (mean = 0.42 mm, n = 87), respectively (Fig. 8C).

When comparing maximum wall width: maximum tube width, *Cloudina* at Driedoornvlakte show the greatest ratios ranging from 0.077 to 0.505 (mean = 0.235), with Zwartmodder ranging from 0.079 to 0.434 (mean = 0.190), and Zebra River showing the smallest range from 0.065 to 0.375 (mean = 0.235) (Fig. 8C). All localities show a weak positive correlation between the thickness of the tube and the maximum wall thickness (Fig. 8D). Ratios are statistically different between Driedoornvlakte and both Zebra River and Zwartmodder ($P = 0.031$ and $P = 5.77^{-5}$, respectively), but not between Zebra River and Zwartmodder ($P = 0.060$).

Discussion

Sinuosity of *Cloudina*. *Cloudina* at Driedoornvlakte and Zwartmodder show the lowest sinuosity, and Zebra River the highest (Fig. 2B,C). This systematic variation (Table S2; Fig. 8E) suggests that this feature is in some way environmentally dictated, and that mineralisation of *Cloudina* occurred via a flexible organic templates that allowed adaptation to local conditions. Very little is known as to the controls on sinuosity in modern benthos, but orientation to maximise feeding efficiency in ambient currents and local sedimentation regime is thought to be a major control in calcareous tubed polychaetes (serpulids)[28,29]. Creating hypotheses as to what advantage might be conferred by increased sinuosity is therefore problematic, but sinuosity may be governed by diverse factors such as substrate type and morphology, vertical or horizontal growth, competition for space, nutrient regime, water depth, and response to hydrodynamic energy and water flow.

We note that sinuosity measurements are based on 2D bedding plane measurements, and further insight might be gained by 3D analysis for both more accurate sinuosity quantification, as well as information about curvature in the third dimension.

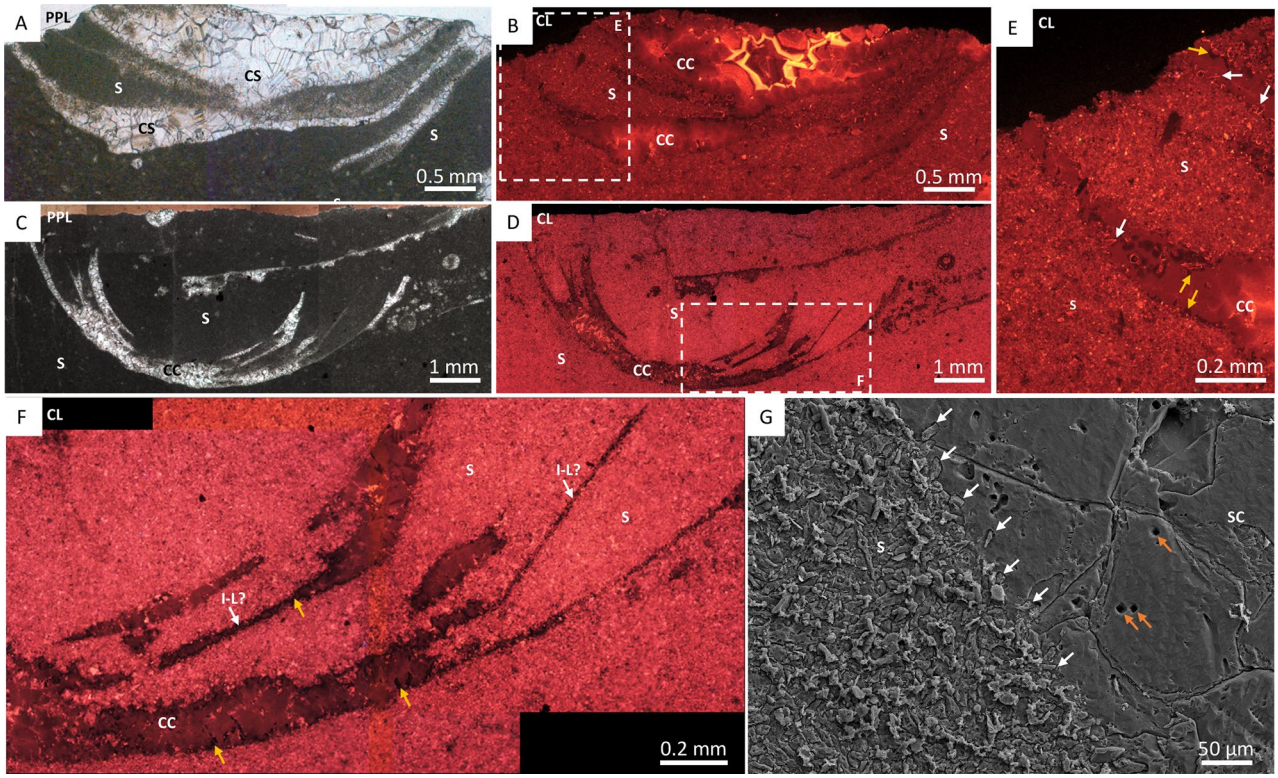

Figure 6. Photomicrographs of *Cloudina* from Zwartmodder, Upper Omkyk Member, Nama Group. (**A**) PPL of compacted *Cloudina* skeleton (CS) surrounded by dolomitised micritic sediment (S). (**B**) CL of A, featuring dull cement which becomes well-zoned with bright luminescence during later growth. The cement infill is centripetal cement (CC) which nucleates from the wall and grows into the mould formed through dissolution. (**C**) PPL of broken and spalled laminae. (**D**) CL of C, the skeletal tube consists of a dull luminescent CC, which in thicker areas is brightly luminescent. Dolomitised micritic sediment surrounds the `spalling' skeleton. (**E**) Inset of B, brightly luminescent cement nucleates from sediment grains, which protrude into the *Cloudina* mould (white arrows) and are overgrown by a non-luminescent cement (yellow arrows) that formed before CC. (**F**) Inset of D, sediment infills areas between spalling potential inter-laminae (I-L?), spalling occurs where CC has not formed between the laminae. Bright luminescent cements on micritic sediment grains which protrude into the *Cloudina* mould which is overgrown by a non-luminescent cement (yellow arrows). (**G**) Sparry calcite (SC) infill of the *Cloudina* skeleton, where cement crystals protrude from surrounding sediment (white arrows). Cube-shaped holes in the SC may represent plucked micro-dolomite or pyrite crystals. Figure created in PowerPoint 2016.

Diagenesis of *Cloudina* and associated cements. While local diagenesis controls the expression of laminae, ranging from dolomite replacement of another carbonate phase, to moldic preservation, i.e. dissolution of an unstable carbonate phase, individual lamina thickness is always consistent (Table S2). We have not observed the micritic microstructure described for the walls of *Cloudina*, but these modes of preservation are consistent with laminae being organic-rich but calcified.

Moldic preservation at Omkyk and Zwartmodder has resulted in the absence of preserved skeletal walls. Early acicular isopachous cement generations are present at Omkyk, which grew from the cloudinomorph walls, followed by an infilling well-zoned clear sparry burial calcite[7] (Fig. 5). *Cloudina* are preserved only via a sparry infill of moulds at Zwartmodder, which represent dissolved paired laminae together with inter-lamina cement and inter-funnel cement (Fig. 6). Dissolution pre-dated cement growth around the grains of the surrounding sediment as this cement grew into *Cloudina* moulds (Fig. 6E).

The extent of dissolution at these shallow, inner ramp localities suggest the influence of freshwater via early meteoric diagenesis, perhaps associated with the degradation of the organic material, which would preferentially remove aragonite. By contrast, the mid-ramp sites Driedoornvlakte and Zebra River, preserve very early botryoidal pseudomorphed aragonitic cements formed in cavities and pores within the marine phreatic zone.

Zebra River *Cloudina* show undulose laminae, with some evidence of both brittle fracturing and ductile deformation (Fig. 4G), in contrast to Driedoornvlakte where there is only evidence of brittle deformation (Table S2). Compaction also caused breakage of *Cloudina* tubes at Zebra River and Zwartmodder, similar to that of a spalling ooid, where the resultant area was infilled by sediment (Figs. 4G, 6F). Inter-lamina and inter-funnel cements formed prior to the breakage of the *Cloudina* tubes, and that of the laminae, where moulds were later filled by a burial cement (Fig. 4M,N). The formation of the dull luminescent inter-funnel cement, seen most clearly at Zebra River, occurred before compaction and lithification of the surrounding dolomitised sediment as evidenced by

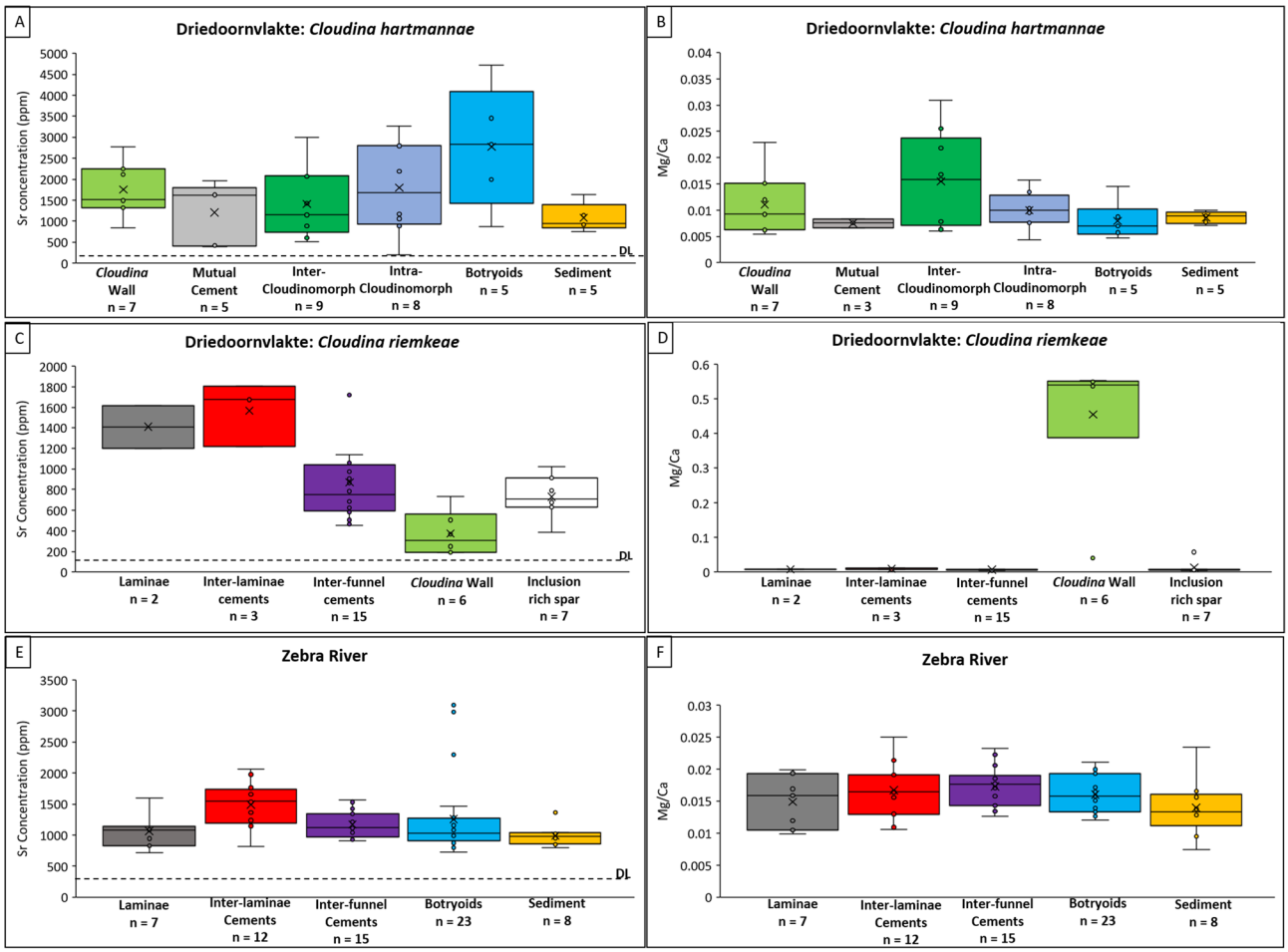

Figure 7. EMPA data from *Cloudina* and associated cements from Driedoornvlakte and Zebra River, Upper Omkyk Member, Nama Group. (**A**) Strontium concentration (ppm). (**B**) Mg/Ca ratio of *Cloudina riemkeae* from Zebra River. (**C**) Strontium concentration (ppm) of *Cloudina hartmannae* from Driedoornvlakte. (**D**) Mg/Ca ratio of *Cloudina hartmannae* from Driedoornvlakte. E: Strontium concentration (ppm) of *Cloudina riemkeae* from Zebra River. (**F**) Mg/Ca ratio of *Cloudina riemkeae* from Zebra River. Detection limits for elements are shown as horizontal dashed lines (DL). Figure created in PowerPoint 2016, graphs created in Excel 2016.

the sharp fracture of the inter-funnel cement where sediment has encroached into the tube (Fig. 4J–L). All these cements also formed prior to the precipitation of pseudomorphed aragonitic botryoidal cements both inside and outside the tubes (Figs. 3B, 4B). Botryoids external to *Cloudina* tube have brighter luminescence than those within the tube, suggesting some degree of diagenetic compartmentalisation. At Zebra River, the pseudomorphed aragonitic acicular crystals are not preserved in the outermost inter-lamina cements, but rather were replaced by the non-luminescent neomorphic cements later in diagenesis.

Inter-lamina, inter-funnel, intra-cloudinomorph, and inter-cloudinomorph cements are all composed of fine, acicular crystal bundles (mean width = ca. 3–5 µm, length = ca. 11 µm) that nucleated on both *Cloudina* laminae and from the outer wall of the tube. Crystal terminations are blunt and are inferred to be pseudomorphed aragonite. All precipitated prior to transport and breakage of the tubes, and also pre-dated the cement botryoids, so can be inferred to be very early syn-sedimentary. The sparry calcite noted previously[15] is either neomorphic or burial spar that formed after the replacement or dissolution of these original cements.

Inter-funnel cements, first described by Grant[3] have also been documented in *Cloudina* from Brazil[14,30], Paraguay[9], and Spain[31], suggesting that such cements are a widespread feature of *Cloudina* present irrespective of early diagenetic setting, mineralogy, or palaeogeographic region. These cements probably formed when *Cloudina* was in-situ and provided mechanical strength and rigidity to the tube.

These cements are similar to those described from the skeleton in the extant sphinctozoan sponge *Vaceletia*, suggested to have a basal mode of biomineralisation[32]. Here, the skeleton is secreted upon a non-collagenous organic template, which becomes substituted by crystalline aragonite deposited as tangled crystal bundles of aragonite. The organic framework consists of proteins and polysaccharides rich in galactose, glucose and fucose, the latter suggesting that bacterial EPS (exopolymeric substances) may be involved in calcification[33]. In most cases, the basal parts of the skeleton, which is free from living tissue, is infilled by a micritic granular secondary deposit. The presence of organic matter has led to the suggestion of biofilm or microbial involvement in such cement precipitation for *Cloudina*[14]. Similar secondary deposition can occur where aragonite crystals continue

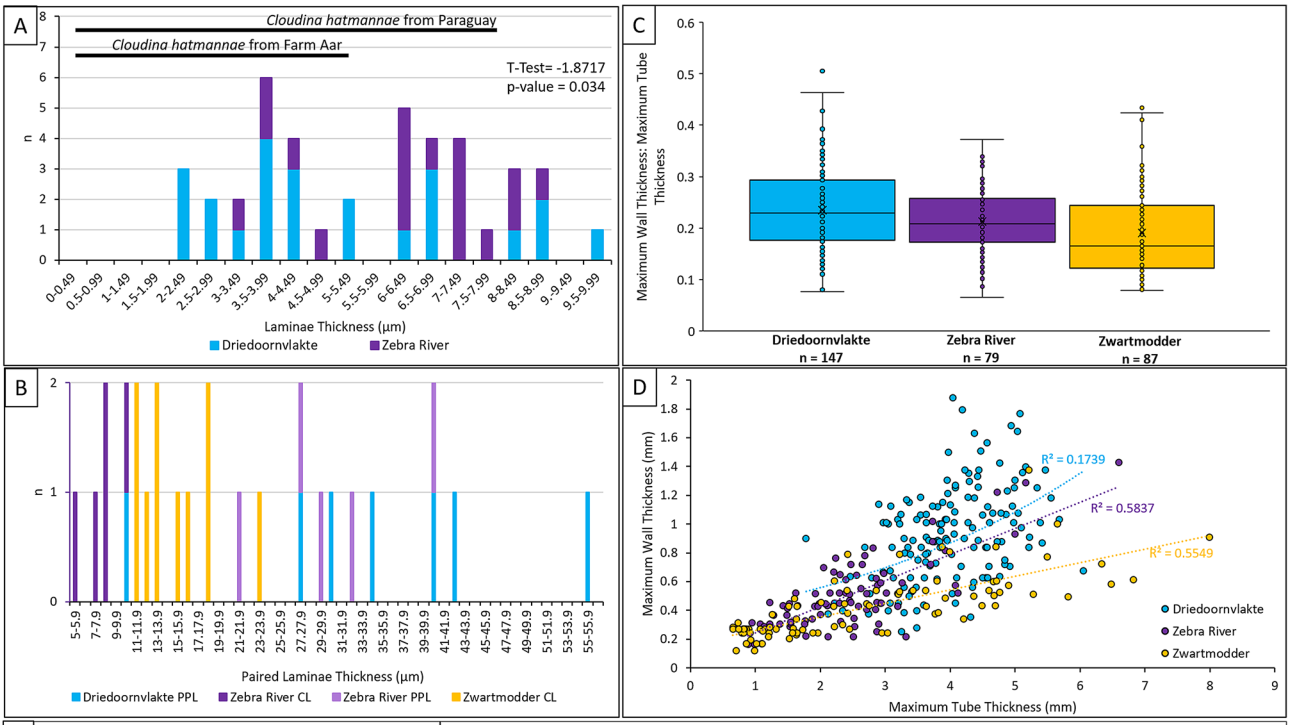

E

Cloudina	Localities			
	Driedoornvlakte	Zebra River	Omkyk	Zwartmodder
Average Sinuosity	1.04	1.21	1.07	1.04
Mean Lamina Thickness	5 µm	6.5 µm	N/A	N/A
Mean Paired Lamina Thickness	30 µm	19.3 µm	N/A	15.4 µm
Mean Wall Thickness: Tube Width	0.235	0.213	N/A	0.19

Figure 8. Features of *Cloudina* walls, including laminae thickness, paired laminae thickness and ratio between the maximum *Cloudina* wall width and maximum tube width of *Cloudina* of the Upper Omkyk Member, Zaris Subbasin, Namibia. (**A**) Lamina thickness, with thicknesses reported from Yang et al.[15]. (**B**) Paired laminae thickness. (**C**) Distribution of ratios of wall thickness: tube thickness. (**D**) Relationship between wall thickness: tube thickness. (**E**) Summary of quantitative features of *Cloudina* at the four coeval sites of the Upper Omkyk Member. Figure created in PowerPoint 2016, graphs created in Microsoft Excel 2016.

to grow after soft tissue has vacated a region of the skeleton. This is known in taxa as diverse as scleractinian corals[18] and the algae *Halimeda*[19]. So it is not clear if these cements in *Cloudina* formed during life, or in-situ but post-mortem, or in parts of the *Cloudina* skeleton abandoned by soft-tissue.

Elemental signatures. Elemental signatures of similar cements cannot be compared directly between localities because of differing diagenetic histories, but statistically significant differences between phases can be determined for each locality. First, we note statistical differences in Sr concentration between various *Cloudina*-associated cements and botryoidal cements. This potentially indicates that the *Cloudina*-associated cements were of a different origin. However, the botryoidal cement used for this comparison is located within *Cloudina* tubes, adjacent to intra-cloudinomorph cements and here there is no significant difference in Sr values ($P = 0.197$) (Table S10). When comparing the Sr content of inter-cloudinomorph cement to those measured from botryoids outside *Cloudina* tube[34], no significant difference is found between these cements. This suggests that all cements found within the *Cloudina* tube irrespective of type retain a higher concentration of Sr compared to those cements situated outside tubes, where leaching was more extensive. This is supported by the higher mean Sr concentration of the intra-cloudinomorph cement compared to the inter-cloudinomorph cement. We find no statistical differences between the *Cloudina*-associated cements, the inorganic botryoids and dolomitised sediment, which suggests that they cannot be distinguished using this criterion.

A similar conclusion was reached from study of Sr content of *Cloudina* from the Tamengo Formation of the Corumbá Group, Brazil[14]. On the basis of their timing of precipitation and the acicular, but non-botryoidal, texture, we conclude that all internal cements associated with *Cloudina* precipitated very early, but lack any distinctive Sr or Mg/Ca signature that might indicate either a diagenetic origin from a different pore fluid or biological fractionation.

Lamina thickness. The variation of paired lamina thicknesses noted could be due to deformation between the laminae, especially at Zebra River, as laminae are observed to be flexible at this site. However, these differences are more likely due to the different methods used to measure paired laminae thickness: laminae at Zebra River and Driedoornvlakte were measured using both CL and PPL images, but the CL images show thinner

laminae compared to their PPL counterparts (Fig. 8B). When comparing data of laminae thickness collected from PPL images only, the data sets are not statistically different (T = 0.57) and so the null hypothesis that the paired laminae thickness at Zebra River and Driedoornvlakte is the same is supported, but due to the small sample size this is not significant (*P*-value = 0.58). This is not the case, however, when comparing the CL data, as T-Test values indicate the paired laminae thickness varies (T = 2.54, *P*-value = 0.029), especially when spalled laminae are not included with the calculations (T = 4.75, *P*-value = 0.002). When comparing the thickness of the moldic-paired laminae seen at Zwartmodder, the values fall in the range of paired laminae at other sites. This suggests that the assumed moldic laminae are paired laminae combined with inter-lamina cements, as observed at Driedoornvlakte and Zebra River.

Presumed *Cloudina* laminae at Zwartmodder also occupy a narrower range of paired laminae thicknesses than those from Driedoornvlakte and Zebra River (mean = 15.4 μm). These laminae are expressed as sparry-calcite infilled moulds formed by the dissolution of both the paired laminae and the inter-lamina cement, and so this dissolution may account for the increased range of laminae thickness at Zwartmodder.

Cloudina laminae from the Mooifontein Member have a thickness of 0.5–5 μm, and samples from Paraguay range between 0.5 and 8 μm[15], so falling within the overall range found in this study (Fig. 8A). Although we note greater lamina thicknesses, we consider these to be likely artefactual due to thickening by dolomitisation at Driedoornvlakte.

Variability of wall thickness. The maximum thickness of the *Cloudina* wall and the thickness of the wall as a ratio of tube diameter is variable across the Zaris Subbasin (Fig. 8D,E). The weak positive correlation between the thickness of the tube and the maximum wall thickness at all localities suggests that the wall thickness was not a function of tube width. These data show that for a given tube width, the thickness of the wall is greatest at Driedoornvlakte, which is significantly and statistically greater than those at other sites.

This implies that wall thickness is environmentally-controlled, determining the distance between paired laminae sets and also potentially the volumetric extent of inter-lamina and inter-funnel cement formation. Driedoornvlakte was the most hydrodynamically energetic of those localities analysed, where rates of carbonate precipitation may have been higher, as shown by the abundant, volumetrically-significant syn-sedimentary botryoidal cements[27]. Such a regime may have promoted more rapid precipitation, and increased volumes, of internal cements. This is consistent with the observation that only brittle fracture is noted at Driedoornvlakte. Many other environmental parameters might have been important to produce a robust, more heavily calcified, and strong skeletal wall in this setting, however, such as enhanced food availability or as a response to currents.

Conclusions

The consistent lamina thickness of *Cloudina* along the Zaris Subbasin shelf suggest that lamina formation was under biological control (Fig. 8E). The moldic or replacive dolomitised preservation of lamina indicate calcification of an organic-rich structure, potentially during life, from which early, acicular pseudomorphed aragonitic cements could nucleate. The precipitation of these cements pre-dates breakage prior to sediment infill, transport, and pseudomorphed aragonitic botryoid precipitation. The presence of such internal cements is a widespread feature of *Cloudina,* although diagenetic expression varies. Geochemical analysis (Mg/Ca; Sr concentrations), however, shows no statistically significant differences between these cements and the surrounding sedimentary matrix, and so no signature of biological fractionation is detected. We conclude that these cements associated with *Cloudina* formed rapidly, but it is not clear if they formed during life, post-mortem, or in parts of the *Cloudina* skeleton that were abandoned by soft-tissue as the animal grew to occupy younger parts of the skeleton. But the formation of these cements, particularly the inter-lamina and inter-funnel cements, would impart rigidity to the *Cloudina* tube, and the inter-cloudinomorph cements would create attachment between adjacent tubes.

The variation of sinuosity in *Cloudina* in different populations across the ramp of the Zaris Subbasin (Fig. 8E) implies that the curvature of the tube is environmentally-controlled, perhaps to maximise feeding efficiency in any given setting. This complements the findings that *Cloudina* tube diameter is also environmentally variable within the Nama Basin[10]. Variability in the cloudinomorph wall thickness is not a function of tube width and also differs between localities (Fig. 8E), further suggesting the influence of environmental factors in determining the distance between paired laminae sets and the volumetric extent of inter-lamina and inter-funnel cement formation. This may have been controlled by factors such as carbonate supersaturation or hydrodynamic energy, as thicker walls and only brittle fracture are noted in high-energy reef settings.

Material and methods

ImageJ (Fiji) software (https://imagej.net) was used to quantify the size of features from photographs, hand specimens, and thin sections. Sinuosity, the degree of curvature, of the cloudinomorph tubes and wall thickness from bedding surface images was determined using ImageJ. Sinuosity, a term mostly associated with river morphology, is defined by dividing the length of an object by the length of the straight-line distance from bedding plane surfaces (see Fig. 2A). Values of < 1.1 indicate straight linear objects with higher values indicating increasing sinuosity. Percentage shortening is the amount of shortening of the tube in comparison to the original and assumed straight *Cloudina* tube and is calculated as a percentage ((straight line distance/ midline distance)*100/ midline distance). A large number of measurements were obtained to overcome any systematic bias due to use of 2D measurements.

Highly-polished thin sections were used for plane polarised light (PPL) and cathodoluminescent (CL) petrography on a cathodoluminescence Cold Cathode CITL 8200 MK3A attached to a Nikon optiphot microscope at the University of Edinburgh. Samples from Zwartmodder were imaged using a Carl Zeiss SIGMA HD VP Field Emission scanning electron microscope (SEM) at the University of Edinburgh. Sections from Driedoornvlakte

and Zebra River were used to quantify major element concentrations (Ca, Mg, Sr) of *Cloudina* and associated diagenetic components via Electron Microprobe analysis (EMPA) following CL images to test for differences in original mineralogy, diagenetic phase, or evidence of vital fractionation. EMPA was undertaken on a Cameca SX100 Electron Microprobe at the University of Edinburgh using a 80 s count time, a beam diameter of 3 µm, an accelerating voltage of 15 kV, and a beam current of 35 nA.

All data were statistically analysed using the Kruskal–Wallis Test, after data normalisation, using MS Excel 2016. Z-Tests were used on sample sizes where $n > 50$, such as sinuosity, and T-Tests were undertaken where sample sizes were $n < 50$ to provide a statistical comparison of each site using MS Excel 2016, variance was tested to determine which T-Test function to use, i.e. whether data sets had equal or unequal variance.

Received: 24 February 2021; Accepted: 11 May 2021
Published online: 11 June 2021

References

1. Germs, G. J. New shelly fossils from Nama Group, south west Africa. *Am. J. Sci.* **272**, 752–761 (1972).
2. Wilson, J. P. *et al.* Deep-water incised valley deposits at the ediacaran-cambrian boundary in southern namibia contain abundant treptichnus pedum. *Palaios* **27**, 252–273 (2012).
3. Grant, S. Shell structure and distribution of Cloudina, a potential index fossil for the terminal Proterozoic. *Am. J. Sci.* **290**, 261–294 (1990).
4. Selly, T. *et al.* A new cloudinid fossil assemblage from the terminal Ediacaran of Nevada, USA. *J. Syst. Paleontol.* **18**, 357–379 (2020).
5. Hua, H., Chen, Z., Yuan, X., Zhang, L. & Xiao, S. Skeletogenesis and asexual reproduction in the earliest biomineralizing animal Cloudina. *Geology* **33**, 277–280 (2005).
6. Cortijo, I., Cai, Y., Hua, H., Schiffbauer, J. D. & Xiao, S. Life history and autecology of an Ediacaran index fossil: development and dispersal of Cloudina. *Gondwana Res.* **28**, 419–424 (2015).
7. Shore, A., Wood, R., Curtis, A. & Bowyer, F. Multiple branching and attachment structures in cloudinomorphs, Nama Group, Namibia. *Geology* https://doi.org/10.1130/G47447.1 (2020).
8. Grotzinger, J. P., Watters, W. A. & Knoll, A. H. Calcified metazoans in thrombolite-stromatolite reefs of the terminal Proterozoic Nama Group, Namibia. *Palaeobiology* **26**, 334–359 (2000).
9. Warren, L. V. *et al.* Corumbella and in situ Cloudina in association with thrombolites in the Ediacaran Itapucumi Group, Paraguay. *Terra Nova* **23**, 382–389 (2011).
10. Wood, R. *et al.* Flexible and responsive growth strategy of the Ediacaran skeletal Cloudina from the Nama Group, Namibia. *Geology* **45**, 259–262 (2017).
11. Tucker, M. E. & Wright, V. P. *Carbonate sedimentology* (Wiley, 2009).
12. Pruss, S. B., Blättler, C. L., Macdonald, F. A. & Higgins, J. A. Calcium isotope evidence that the earliest metazoan biomineralizers formed aragonite shells. *Geology* **46**, 763–766 (2018).
13. Feng, W. M., Chen, Z. & Sun, W. G. Diversification of skeletal microstructures of organisms through the interval from the latest Precambrian to the Early Cambrian. *Sci. China Ser. D-Earth Sci.* **46**, 977–985. https://doi.org/10.1360/03yd0534 (2003).
14. Becker-Kerber, B. *et al.* Ecological interactions in Cloudina from the Ediacaran of Brazil: implications for the rise of animal biomineralization. *Sci. Rep.* **7**, 1–11 (2017).
15. Yang, B. *et al.* Ultrastructure of Ediacaran cloudinids suggests diverse taphonomic histories and affinities with non-biomineralized annelids. *Sci. Rep.* **10**, 1–12 (2020).
16. Gilbert, P. U. *et al.* Biomineralization by particle attachment in early animals. *Proc. Natl. Acad. Sci.* **116**, 17659–17665 (2019).
17. Lowenstam, H. A. Minerals formed by organisms. *Science* **15**, 1126–1131 (1981).
18. Enmar, R. *et al.* Diagenesis in live corals from the Gulf of Aqaba. I. The effect on paleo-oceanography tracers. *Geochimica et Cosmochimica Acta* **64**, 3123–3132 (2000).
19. Wizemann, A., Meyer, F. W. & Westphal, H. A new model for the calcification of the green macro-alga Halimeda opuntia (Lamouroux). *Coral Reefs* **33**, 951–964 (2014).
20. Cartwright, J. H. & Checa, A. G. The dynamics of nacre self-assembly. *J. R. Soc. Interface* **4**, 491–504 (2007).
21. Grotzinger, J. & Miller, R. The Nama Group. *Geol. Namibia Geol. Soc. Namibia* **2**, 13229–13272 (2008).
22. Germs, G. Implications of a sedimentary facies and depositional environmental analysis of the Nama Group in South West Africa/Namibia. *Spec. Publ. Geol. Soc. South Africa* **11**, 89–114 (1983).
23. Kaufman, A. J., Hayes, J., Knoll, A. H. & Germs, G. J. Isotopic compositions of carbonates and organic carbon from upper Proterozoic successions in Namibia: stratigraphic variation and the effects of diagenesis and metamorphism. *Precambr. Res.* **49**, 301–327 (1991).
24. Saylor, B. Z., Grotzinger, J. P. & Germs, G. J. Sequence stratigraphy and sedimentology of the Neoproterozoic Kuibis and Schwarzrand subgroups (Nama Group), southwestern Namibia. *Precambr. Res.* **73**, 153–171 (1995).
25. Wood, R. & Curtis, A. Extensive metazoan reefs from the Ediacaran Nama Group, Namibia: the rise of benthic suspension feeding. *Geobiology* **13**, 112–122. https://doi.org/10.1111/gbi.12122 (2015).
26. Schmitz, M. *The geologic time scale* 115–126 (Elsevier, 2012).
27. Penny, A. M. *et al.* Ediacaran metazoan reefs from the Nama Group, Namibia. *Science* **344**, 1504–1506 (2014).
28. Bosence, D. Recent serpulid reefs, Connemara, Eire. *Nature* **242**, 40–41 (1973).
29. Sanfilippo, R. Systematics and life habit in Serpula israelitica Amoureux, 1977 (Polychaeta Serpulidae) from the Mediterranean with remarks on other soft-bottom serpulids. *J. Nat. Hist.* **43**, 2009–2025 (2009).
30. Beurlen, K. & Sommer, F. W. *Observações estratigráficas e paleontológicas sôbre o calcário Corumbá.* (DNPM, 1957).
31. Cortijo, I., Mus, M. M., Jensen, S. & Palacios, T. A new species of Cloudina from the terminal Ediacaran of Spain. *Precambr. Res.* **176**, 1–10 (2010).
32. Vacelet, J., Willenz, P. & Hartman, W. Treatise Online, no. 1, Part E, Revised, Volume 4, Chapter 1: Living hypercalcified sponges. *Treatise Online* **4** (2010).
33. Germer, J., Mann, K., Wörheide, G. & Jackson, D. J. The Skeleton forming proteome of an early branching metazoan: a molecular survey of the biomineralization components employed by the coralline sponge vaceletia sp.. *PLoS ONE* **10**, e0140100 (2015).
34. Wood, R., Bowyer, F., Penny, A. & Poulton, S. W. Did anoxia terminate Ediacaran benthic communities? evidence from early diagenesis. *Precambrian Research* **313**, 134–147 (2018).

Acknowledgements

AS acknowledges support from the University of Edinburgh and the International Centre for Carbonate Reservoirs, and RW from NERC Grant (NE/T008458/1). We thank Mike Hall, Nicola Cayzer, Chris Haywood and

John Craven for technical support. We are grateful for permission to access localities on many farms, and we thank A. and S. Horn of Omkyk Farm, L. and G. Fourie of Zebra River and C. Husselman of Rocky Mountain Farm, Driedoornvlakte.

Author contributions

R.W. conceived the study. R.W. collected field photographic images. A.S. conducted research. A.S. wrote the first draft of the manuscript, with R.W. editing and contributing to the final document.

Competing interests

The authors declare no competing interests.

Additional information

Supplementary Information The online version contains supplementary material available at https://doi.org/10.1038/s41598-021-90768-5.

Correspondence and requests for materials should be addressed to A.S.

Reprints and permissions information is available at www.nature.com/reprints.

Publisher's note Springer Nature remains neutral with regard to jurisdictional claims in published maps and institutional affiliations.

Appendix 3.2 Data Tables

3.2.1 *Cloudina* sinuosity within Zaris Basin, Namibia.

Sinuosity of *Cloudina*				
No.	Driedoornvlakte	Zebra River	Omkyk	Zwartmodder
1	1.00	1.04	1.72	1.02
2	1.05	1.04	1.00	1.05
3	1.00	1.18	1.13	1.01
4	1.00	1.11	1.00	1.15
5	1.00	1.02	1.03	1.00
6	1.03	2.68	1.18	1.00
7	1.09	1.03	1.00	1.03
8	1.01	1.01	1.00	1.03
9	1.12	1.06	1.06	1.01
10	1.03	1.11	1.01	1.02
11	1.02	1.02	1.02	1.00
12	1.06	1.03	1.00	1.00
13	1.04	1.24	1.13	1.00
14	1.01	1.05	1.09	1.02
15	1.00	1.05	1.03	1.03
16	1.00	1.62	1.02	1.09
17	1.02	1.07	1.02	1.05
18	1.02	1.05	1.06	1.00
19	1.01	1.03	1.02	1.01
20	1.06	1.04	1.07	1.01
21	1.01	1.25	1.02	1.05
22	1.03	1.40	1.13	1.19
23	1.00	1.23	1.02	1.05
24	1.03	2.46	1.00	1.04
25	1.00	1.03	1.04	1.12
26	1.02	1.34	1.02	1.06
27	1.01	1.09	1.08	1.19
28	1.11	1.01	1.01	1.03
29	1.04	1.35	1.05	1.06
30	1.02	1.01	1.05	1.00
31	1.03	1.06	1.14	1.02
32	1.01	2.65	1.34	1.00
33	1.00	1.39	1.04	1.00
34	1.12	1.00	1.00	1.06
35	1.00	1.68	1.34	1.03
36	1.10	1.17	1.01	1.00

37	1.00	1.19	1.04	1.00
38	1.05	1.15	1.01	1.00
39	1.04	1.04	1.04	1.00
40	1.07	1.07	1.02	1.05
41	1.03	1.04	1.00	1.05
42	1.03	2.36	1.04	1.00
43	1.02	1.01	1.06	1.04
44	1.00	1.01	1.00	1.00
45	1.04	1.00	1.02	1.12
46	1.02	1.04	1.05	1.13
47	1.01	1.00	1.00	1.00
48	1.00	1.16	1.05	1.00
49	1.02	1.07	1.07	1.00
50	1.00	1.09	1.08	1.00
51	1.02	1.02	1.20	1.03
52	1.11	1.82	1.00	1.14
53	1.02	1.32	1.01	1.07
54	1.04	1.07	1.02	1.12
55	1.00	1.25	1.02	1.00
56	1.06	1.10	1.02	1.07
57	1.03	1.06	1.02	1.02
58	1.01	1.46	1.20	1.00
59	1.02	1.03	1.30	1.00
60	1.00	1.01	1.04	1.01
61	1.05	1.10	1.01	1.00
62	1.01	1.10	1.01	1.00
63	1.10	1.06	1.00	1.00
64	1.00	1.46	1.17	1.00
65	1.01	1.03	1.10	1.01
66	1.02	1.01	1.00	1.03
67	1.00	1.10	1.03	1.04
68	1.03	1.00	1.00	1.04
69	1.06	1.05	1.04	1.03
70	1.05	1.17	1.03	1.03
71	1.00	1.07	1.01	1.00
72	1.08	1.06	1.04	1.00
73	1.03	1.05	1.00	1.03
74	1.00	1.04	1.03	1.12
75	1.04	1.02	1.03	1.00
76	1.09	1.05	1.01	1.00
77	1.09	2.98	2.42	1.01
78	1.00	1.39	1.06	1.11
79	1.00	1.17	1.31	1.00

80	1.03	1.06	1.04	1.00
81	1.10	1.00	1.07	1.36
82	1.08	1.07	1.01	1.00
83	1.03	1.00	1.00	1.00
84	1.00	1.00	1.13	1.00
85	1.03	1.05	1.12	1.00
86	1.00	1.01	1.03	1.00
87	1.02	1.58	1.01	1.01
88	1.02	1.04	1.01	1.08
89	1.00	1.01	1.02	1.08
90	1.02	1.26	1.47	1.01
91	1.03	1.26	1.02	1.00
92	1.03	1.00	1.03	1.04
93	1.06	1.01	1.28	1.01
94	1.00	1.10	1.00	1.11
95	1.00	1.01	1.09	1.01
96	1.00	1.90	1.10	1.00
97	1.03	1.03	1.06	1.13
98	1.04	1.35	1.03	1.01
99	1.04		1.03	1.00
100	1.08		1.03	
101	1.00		1.03	
102	1.05		1.01	
103	1.07		1.11	
104	1.02		1.02	
105	1.01		1.06	
106	1.09		1.00	
107	1.03		1.01	
108	1.01		1.07	
109	1.04		1.05	
110	1.03		1.02	
111	1.28		1.06	
112	1.03		1.00	
113	1.03		1.00	
114	1.01		1.06	
115	1.02		1.00	
116	1.03		1.01	
117	1.03		1.06	
118	1.02		1.01	
119	1.00		1.03	
120	1.04		1.01	
121	1.00		1.04	
122	1.00		1.06	

123	1.09		1.03	
124	1.01		1.03	
125	1.04		1.07	
126	1.00		1.00	
127	1.01		1.10	
128	1.00		1.00	
129	1.07		1.01	
130	1.03		1.05	
131	1.17		1.00	
132	1.07		1.01	
133	1.09		1.11	
134	1.00		1.00	
135	1.02		1.00	
136	1.05		1.00	
137	1.01		1.00	
138	1.06		1.07	
139	1.01		1.02	
140	1.02		1.07	
141	1.04		1.10	
142	1.01		1.04	
143	1.02		1.06	
144	1.01		1.04	
145	1.05			
146	1.03			
147	1.00			
148	1.01			
149	1.03			
150	1.04			
151	1.70			
152	1.02			
153	1.00			
154	1.03			
155	1.06			
156	1.00			
Mean	1.04	1.21	1.07	1.04
Min	1.00	1.00	1.00	1.00
Max	1.70	2.98	2.42	1.36
Range	0.70	1.98	1.42	0.36
StDev	0.07	0.38	0.15	0.06

3.2.2 Electron microprobe analysis (EMPA) data table of *Cloudina hartmannae* of Driedoornvlakte with corresponding cathodoluminescence image.

Data Point	Ca (ppm)	Mg (ppm)	Mn (ppm)	Fe (ppm)	Sr (ppm)	O (ppm)	Total (ppm)	Mg/Ca
1	396128	2791	37	-4	3453	160612	563017	0.007
2	395455	5333	48	109	889	161584	563418	0.013
3	398106	3008	138	22	195	160986	562454	0.008
4	398446	3331	71	557	1427	161694	565526	0.008
5	397317	6266	-32	72	1173	162959	567756	0.016
6	399777	3028	178	1156	1654	162269	568061	0.008
7	395100	12192	13	161	914	165967	574346	0.031
8	399563	2401	13	171	2067	161516	565731	0.006
9	401933	2675	-19	35	3748	162902	571273	0.007
10	393154	3688	60	1567	1144	160051	559664	0.009
11	400075	2158	161	258	1492	161524	565669	0.005
12	397409	2630	121	-34	2111	160788	563026	0.007
13	297455	109172	23	290	777	190844	598560	0.367
14	400059	3489	2	-27	1595	162285	567402	0.009
15	398544	2277	13	-16	4723	161459	566999	0.006
16	398113	2765	104	18	2834	161300	565133	0.007
17	396249	1872	32	113	1998	159822	560086	0.005
18	393220	5726	20	56	869	160923	560815	0.015
19	397249	4100	80	-25	2193	161697	565294	0.010
20	394665	3762	39	559	2811	160712	562549	0.010
21	397929	1717	95	319	3267	160699	564026	0.004
22	398544	3267	64	306	2794	161866	566842	0.008
23	392693	8579	-84	92	1150	162623	565053	0.022
24	391175	6178	-7	121	521	160352	558339	0.016
25	182307	113192	129	14175	427	151468	461698	0.621
25	224211	112917	118	9348	393	166623	513611	0.504
26	399618	2664	117	470	1628	161747	566244	0.007
27	377438	9652	76	122	888	157246	545422	0.026
28	378584	6374	24	62	598	155461	541103	0.017
29	400792	2534	104	44	3003	162256	568733	0.006
30	398237	3128	46	184	2116	161487	565196	0.008
31	395214	3267	116	255	1958	160385	561195	0.008
32	336024	2608	20	892	955	136293	476791	0.008
32	392290	3503	42	251	755	159130	555971	0.009
33	396467	3939	139	506	1637	161347	564035	0.010
34	396026	2821	76	1190	921	160482	561515	0.007
35	381743	4118	108	-42	1060	155316	542303	0.011

36	399596	2680	61	36	2496	161767	566636	0.007
37	395778	2263	30	40	2724	160002	560836	0.006
38	390875	6990	14	121	820	160828	559648	0.018
39	399224	4766	167	245	2249	163038	569689	0.012
40	219344	1364	-4	355	840	88714	310614	0.006
40	392624	3612	17	236	2773	159692	558953	0.009
41	398503	6009	87	400	1323	163420	569743	0.015
42	393565	9003	61	4825	1523	164716	573692	0.023

Key

- Sediment
- Intra-cloudinomorph
- Botryoids
- Inter-cloudinomorph
- Mutual Cement
- *Cloudina* Wall
- Laminae

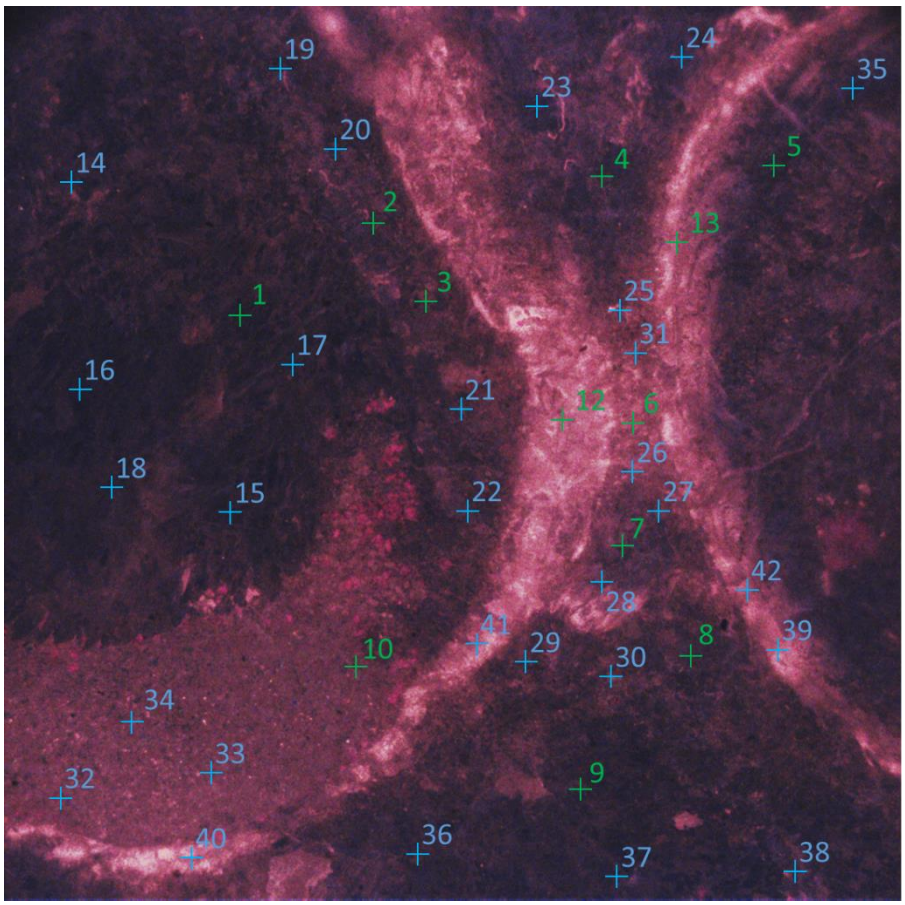

3.2.3 Electron microprobe analysis (EMPA) data table of *Cloudina riemkae* of Driedoornvlakte with corresponding plane polarised light image.

Data Point	Ca (ppm)	Mg (ppm)	Mn (ppm)	Fe (ppm)	Sr (ppm)	O (ppm)	Mg/Ca
1	398495	2999	80	109	784	161251	0.008
2	398908	3201	16	-92	906	161495	0.008
3	395791	2222	47	105	973	159684	0.006
4	399277	2381	28	103	864	161154	0.006
5	396510	3241	10	-47	1202	160629	0.008
6	396075	3270	8	134	1221	160530	0.008
7	397727	4686	82	-56	1674	162171	0.012
8	396745	2996	-13	-56	1804	160663	0.008
9	392936	2915	100	17	1617	159108	0.007
10	396265	1760	-79	78	663	159468	0.004
11	389155	4827	-22	94	1747	158868	0.012
12	392177	3194	-8	28	626	158779	0.008
13	394054	2648	16	149	1061	159291	0.007
14	399696	2482	67	120	467	161332	0.006
15	398630	2613	-16	151	583	160998	0.007
16	398114	1858	-18	118	457	160263	0.005
17	396412	2813	41	104	720	160273	0.007
18	396615	2448	55	165	1142	160212	0.006
19	396352	2595	36	-30	685	160059	0.007
20	404815	1524	2	170	507	162748	0.004
21	401037	2811	-62	153	1721	162285	0.007
22	233503	117310	1	1635	189	170943	0.502
23	226587	121481	50	959	250	170759	0.536
24	224038	123825	50	729	369	171240	0.553
25	225554	123917	-57	822	192	171869	0.549
26	225949	123310	-10	356	507	171566	0.546
27	361314	14722	-6	192	736	154116	0.041
28	397853	1805	-42	155	678	160167	0.005
29	396840	2557	-39	180	791	160287	0.006
30	397318	2221	-15	179	712	160248	0.006
31	399259	2804	5	124	911	161433	0.007
32	374968	2439	-44	111	632	151427	0.007
33	386411	22203	-25	249	385	169006	0.057
34	398570	2278	-32	123	1022	160822	0.006

Key

- Inter-laminae cement
- Laminae
- Inter-funnel
- Cloudina Wall
- Inclusion rich spar

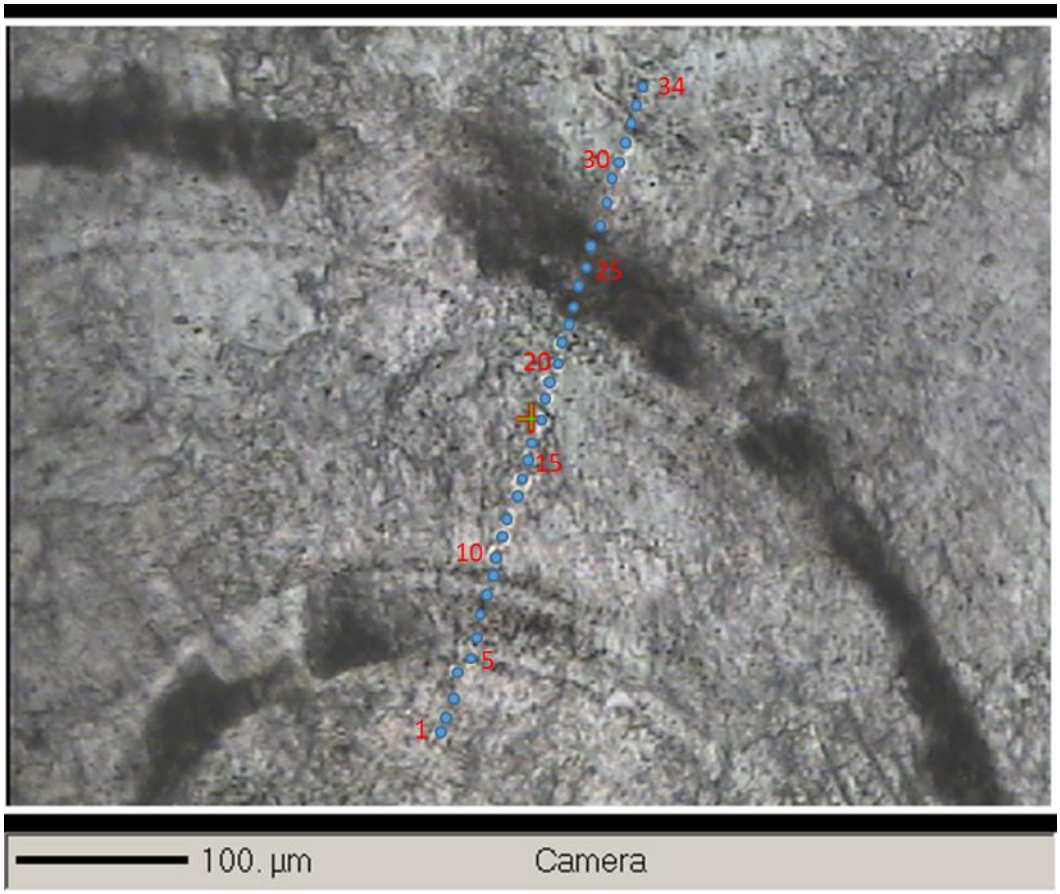

3.2.4 Electron microprobe analysis (EMPA) data table of *Cloudina hartmannae* of Zebra River with corresponding cathodoluminescence and plane polarised light images.

Data Point	Ca (ppm)	Mg (ppm)	Mn (ppm)	Fe (ppm)	Sr (ppm)	O (ppm)	Mg/Ca
1	389840	5876	175	1260	2983	2E+05	0.015
2	386016	5433	204	3765	908	2E+05	0.014
3	392111	4949	162	1399	3098	2E+05	0.013
4	377350	6661	209	5339	796	2E+05	0.018
5	383669	6598	93	2852	1277	2E+05	0.017
6	388775	6634	215	1353	826	2E+05	0.017
7	394277	5362	112	1255	904	2E+05	0.014
8	392219	5073	83	1098	1030	2E+05	0.013
9	389016	5690	182	1130	1209	2E+05	0.015
10	387604	5215	193	1723	1530	2E+05	0.013
11	386229	8616	1437	1545	1345	2E+05	0.022
12	386830	7977	204	360	1567	2E+05	0.021
13	383661	4879	45	1665	1326	2E+05	0.013
14	391089	6921	103	302	926	2E+05	0.018
15	386817	7171	143	1340	1140	2E+05	0.019
16	382975	7270	710	2078	1111	2E+05	0.019
17	390783	5385	305	1937	1363	2E+05	0.014
18	389268	4661	243	3727	719	2E+05	0.012
19	385916	7628	48	2706	724	2E+05	0.020
20	399270	5318	103	774	985	2E+05	0.013
21	383012	5987	252	3302	862	2E+05	0.016
22	391484	3714	497	2092	1038	2E+05	0.009
23	391739	6177	47	835	1463	2E+05	0.016
24	393628	5491	197	658	998	2E+05	0.014

Key

- Sediment
- Intra-funnel
- Botryoids
- Laminae

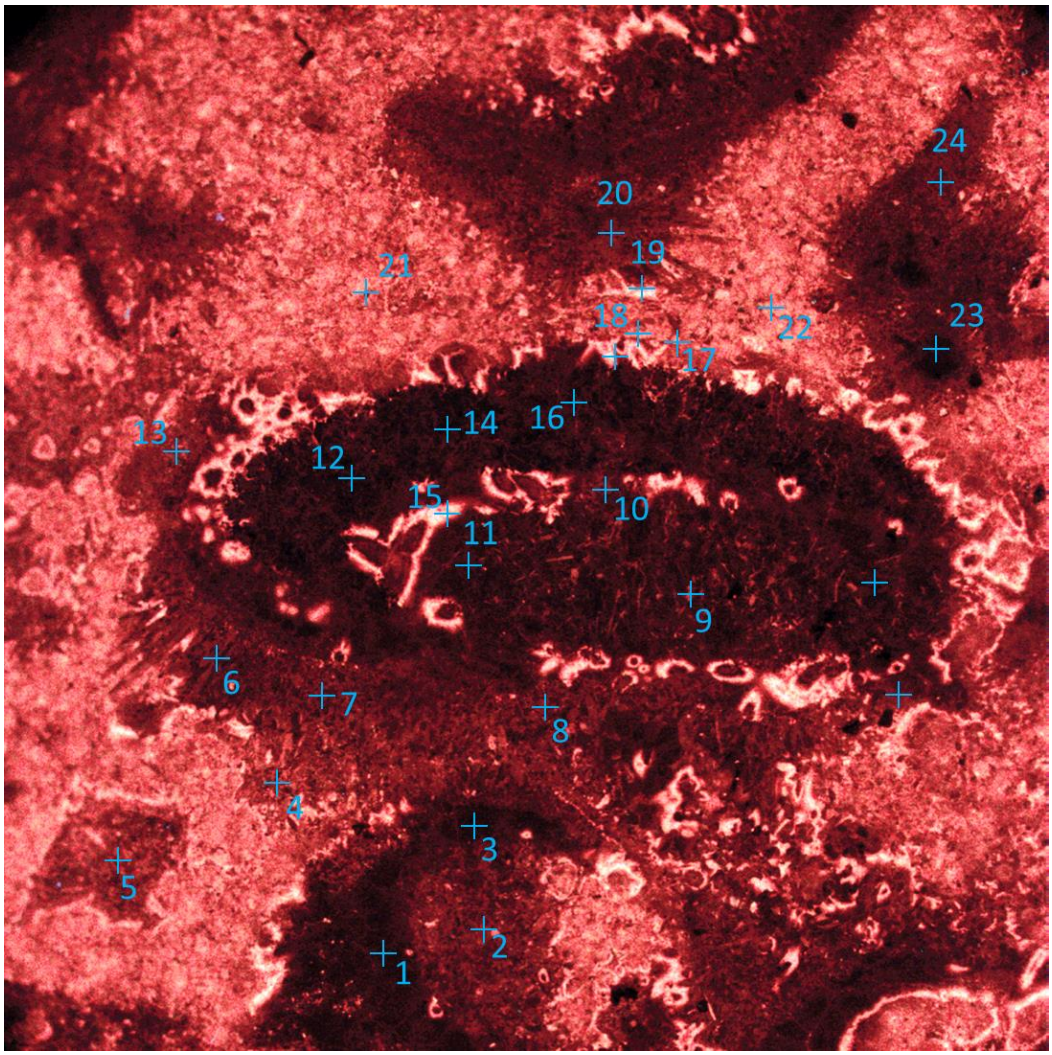
24
20
19
21
18
22
23
17
16
14
13
12
15
10
11
9
6
7
8
4
3
5
2
1

Data Point	Ca (ppm)	Mg (ppm)	Mn (ppm)	Fe (ppm)	Sr (ppm)	O (ppm)	Mg/Ca
1	388128	6062	26	977	1361	159467	0.016
2	383815	7657	167	1283	1145	158885	0.020
3	383370	7425	-5	1610	1084	158587	0.019
4	391892	6545	61	1579	1567	161508	0.017
5	386799	6545	98	955	1137	159228	0.017
6	392183	6239	116	1803	1596	161508	0.016
7	391171	4092	23	938	823	159275	0.010
8	388257	7425	-60	1647	1147	160544	0.019
9	395835	3915	61	945	944	161055	0.010
10	390978	4700	171	1375	871	159775	0.012
11	393054	7724	201	717	1155	162467	0.020
12	388314	7751	248	920	1130	160660	0.020
13	389451	7518	186	1057	1011	160960	0.019
14	389228	6459	160	1026	913	160139	0.017
15	383458	7520	65	1823	996	158750	0.020
16	391873	6465	185	637	1036	161117	0.016
17	392279	5114	105	815	2295	160648	0.013
18	386388	6011	47	1144	1125	158750	0.016
19	394350	6237	121	940	1421	162094	0.016
20	391868	7489	209	1095	1181	161954	0.019
21	391554	5083	27	1162	1656	160298	0.013
22	393422	5622	126	821	904	161192	0.014
23	388004	4120	58	1559	1976	158428	0.011
24	389210	6461	374	2314	951	160571	0.017
25	387015	8499	116	1250	1530	160762	0.022
26	392203	4963	37	1161	972	160355	0.013
27	392639	5042	437	1802	796	160850	0.013
28	387709	6619	78	1310	1242	159756	0.017
28	387284	9013	163	906	1075	161040	0.023
29	390525	7229	93	1200	1119	161232	0.019
30	387857	6181	60	748	1584	159423	0.016
31	390586	6417	140	1489	819	160763	0.016
32	389735	4259	155	2859	2064	159628	0.011
33	388303	6959	86	993	944	160074	0.018
34	367137	4900	382	6655	1016	151990	0.013
35	376359	9436	-71	1404	1238	157062	0.025
36	390866	5391	49	1068	1038	160092	0.014
37	389207	8201	87	1477	1081	161416	0.021
38	387666	9104	428	2794	844	161829	0.023

39	389513	5118	563	2285	979	159860	0.013
42	384624	2870	354	3047	1031	156596	0.007

Key

Sediment

Inter-laminae cement

Inter-funnel

Botryoids

Laminae

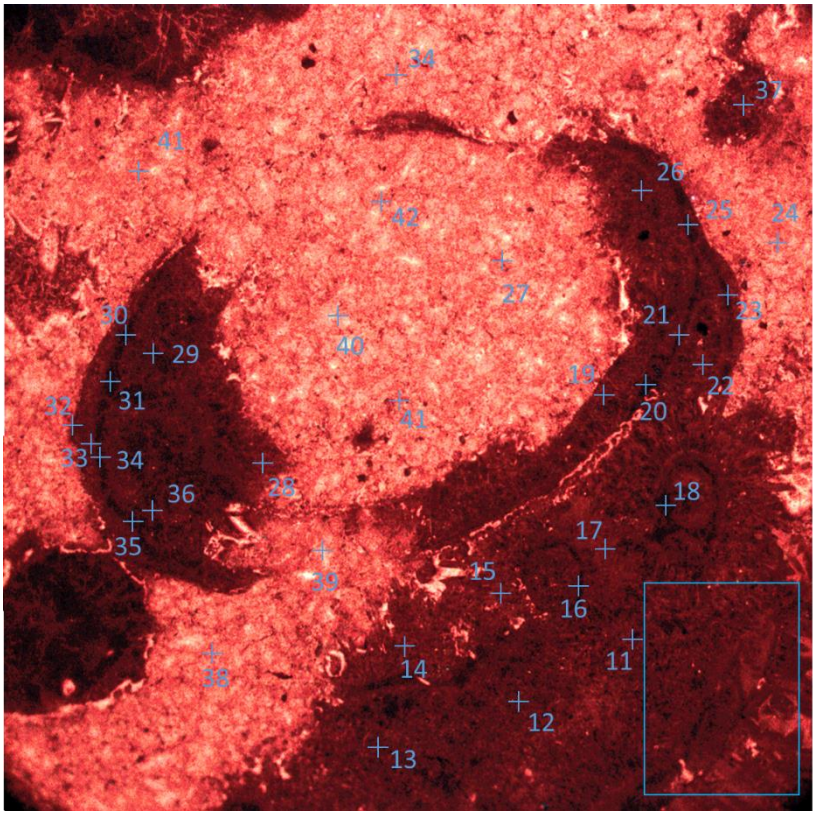

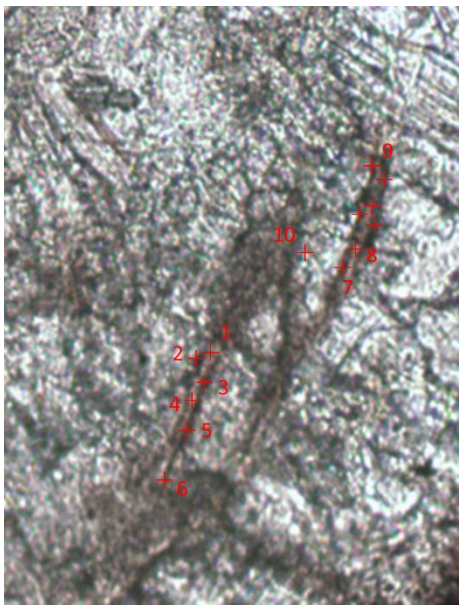

3.2.5 Lamina thickness of *Cloudina* of Driedoornvlakte and Zebra River

Cloudina lamina thickness (µm)	
Driedoornvlakte	Zebra River
8.4	7.3
8.5	6.2
3.7	6.8
8.8	4.6
9.6	3.9
3.7	8.3
6.4	8.6
6.9	7.2
5.2	6.2
5.2	7.3
4.4	6.2
4.2	3.3
2.1	8.1
2.4	3.5
2.1	7.1
2.7	6.0
3.5	7.8
2.8	4.0
4.0	
3.1	
6.8	
6.9	
3.8	

3.2.6 *Cloudina* wall: inner tube diameter ratio of *Cloudina* at Driedoornvlakte, Zebra River and Zwartmodder.

Cloudina wall: inner tube diameter		
Driedoornvlakte	Zebra River	Zwartmodder
0.208	0.230	0.156
0.147	0.475	0.151
0.285	0.341	0.125
0.608	0.575	0.246
0.275	0.196	0.166
0.949	0.229	0.140
0.148	0.219	0.121

0.195	0.165	0.168
0.339	0.481	0.225
0.098	0.319	0.192
0.378	0.459	0.165
0.226	0.127	0.277
0.416	0.262	0.101
0.306	0.114	0.134
0.485	0.075	0.136
0.263	0.346	0.630
0.342	0.218	0.526
0.187	0.251	0.377
0.397	0.102	0.270
0.286	0.217	0.220
0.541	0.456	0.126
0.403	0.374	0.328
0.575	0.176	0.489
0.194	0.240	0.547
0.173	0.883	0.353
0.312	0.272	0.262
0.277	0.342	0.395
0.166	0.316	0.148
0.521	0.406	0.226
0.446	0.382	0.119
0.292	0.247	0.295
0.164	0.280	0.227
0.577	0.405	0.151
0.533	0.155	0.246
0.305	0.200	0.133
0.484	0.179	0.229
0.440	0.232	0.340
0.164	0.351	0.281
0.988	0.445	0.460
0.296	0.425	0.574
0.540	0.251	0.181
0.755	0.536	0.237
0.482	0.410	0.418
0.496	0.296	0.312
0.760	0.224	0.299
0.385	0.269	0.090
0.409	0.318	0.107
0.571	0.254	0.334
0.338	0.374	0.180
0.612	0.380	0.256

0.289	0.179	0.194
0.312	0.259	0.136
0.158	0.203	0.132
0.426	0.153	0.102
0.254	0.235	0.245
0.507	0.228	0.178
0.384	0.566	0.190
0.449	0.451	0.294
0.523	0.276	0.566
0.228	0.255	0.474
0.329	2.885	0.238
0.588	0.403	0.185
0.270	0.472	0.143
0.587	0.466	0.089
0.598	0.502	0.092
0.472	0.241	0.135
0.520	0.178	0.308
0.199	0.362	0.182
0.484	0.332	0.182
0.431	0.334	0.141
0.484	0.534	0.363
0.215	0.515	0.205
0.318	0.323	0.089
0.860	0.214	0.130
0.539	0.547	0.456
0.197	0.331	0.263
0.205	0.205	0.427
0.304	0.118	0.169
0.612	0.352	0.148
0.250		0.255
0.397		0.357
0.208		0.454
0.426		0.386
0.102		0.419
0.467		0.555
0.199		0.692
0.275		0.371
0.635		
0.426		
0.669		
0.375		
0.261		
0.131		

0.372		
0.617		
0.623		
0.372		
0.342		
0.667		
0.294		
0.360		
0.189		
0.326		
0.288		
0.651		
0.397		
0.249		
0.587		
0.196		
0.381		
0.228		
0.380		
0.168		
0.684		
0.296		
0.393		
0.187		
0.228		
0.101		
0.188		
0.275		
0.164		
0.573		
0.358		
0.391		
0.184		
0.260		
0.207		
0.287		
0.693		
0.283		
0.372		
0.326		
0.357		
0.443		
0.233		

0.268		
0.549		
0.447		
0.394		
0.326		
0.609		
0.458		
0.736		
0.337		
0.650		
0.459		

Appendix 4: Exceptional Preservation of Ediacaran Skeletal Metazoan *Namacalathus*, Nama Group, Namibia

Appendix 4.1 Shore et al. (2021)

Ediacaran metazoan reveals lophotrochozoan affinity and deepens the root of the Cambrian Explosion

EVOLUTIONARY BIOLOGY

Ediacaran metazoan reveals lophotrochozoan affinity and deepens root of Cambrian Explosion

A. J. Shore[1]*, R. A. Wood[1], I. B. Butler[1], A. Yu. Zhuravlev[2], S. McMahon[1,3], A. Curtis[1], F. T. Bowyer[1†]

Through exceptional preservation, we establish a phylogenetic connection between Ediacaran and Cambrian metazoans. We describe the first three-dimensional, pyritized soft tissue in *Namacalathus* from the Ediacaran Nama Group, Namibia, which follows the underlying form of a stalked, cup-shaped, calcitic skeleton, with six radially arranged lobes projecting into an apical opening and lateral lumens. A thick body wall and probable J-shaped gut are present within the cup, and the middle layer of the often-spinose skeleton and skeletal pores are selectively pyritized, supporting an organic-rich composition and tripartite construction with possible sensory punctae. These features suggest a total group lophotrochozoan affinity. These morphological data support molecular phylogenies and demonstrates that the origin of modern lophotrochozoan phyla, and their ability to biomineralize, had deep roots in the Ediacaran.

INTRODUCTION

Exceptional preservation of fossils from the Ediacaran-Cambrian, ca. 570 to 500 million years (Ma) ago, provides great insight into the first radiation of metazoans. While the oldest putative skeletal metazoans known are from the terminal Ediacaran, the general absence of both definitive skeletal characteristics and soft-tissue preservation has precluded clear assignment of affinity and, hence, an understanding of the origin of major metazoan groups. Here, we describe the first, three-dimensional, pyritized preservation of soft tissue in the Ediacaran skeletal metazoan *Namacalathus hermanastes*, from the Nama Group, Namibia, where new features support a bilaterian, lophotrochozoan affinity. In so doing, we also establish a strong evolutionary link between terminal Ediacaran and early Cambrian taxa.

Namacalathus is a sessile, benthic skeletal organism with a widespread distribution known from diverse carbonate settings, including thrombolite reefs and shallow lagoons, ca. 550 to 540 Ma ago. *Namacalathus* has a goblet-like skeletal morphology formed by a hollow stalk expanding into a calyx from ca. 3 to 35 mm in diameter with an apical central opening and five to seven, but generally six, lateral lumens (*1*–*3*). Spines are present on the outer surface of the stem and cup in some individuals (*2*), and adjacent individuals have been found with shared cavities, interpreted as representing potential bilateral, asexual, external budding (*3*). Present skeletal mineralogy is generally low-Mg calcite, but the original mineralogy may have been either Mg calcite or aragonite (*1*,*4*). Preserved plastic deformation implies that skeletal walls were flexible and, therefore, organic rich (*1*). Skeletal microstructure has been described as a diagenetic, tufa-like cement (*5*), but well-preserved specimens display foliated outer and inner skeletal layers, with a middle layer inferred to have been organic rich (*3*).

Namacalathus has been proposed to be a cnidarian because of its hexaradial symmetry and a goblet-like morphology, as found in some hydrozoan polyps, scyphozoan scyphistomae, and stauromedusae (*1*). Others have suggested a protozoan affinity because of the absence of accretionary growth (*6*) or a total group lophophorate based on foliated skeletal microstructure and bilateral budding (*3*). Recently, a stem group ctenophore affinity has been proposed on the basis of phylogenetic analyses and a general morphological similarity to sessile, Cambrian skeletonized "dinomischids" and scleroctenophores (*7*).

RESULTS

Here, we report exceptionally preserved *Namacalathus* individuals found within the uppermost Upper Omkyk Member of the Nama Group, Namibia, from a low-energy, very shallow, dominantly carbonate, inner ramp setting, just below an ash bed dated at 547.32 ± 0.65 Ma old (see fig. S1) (*8*). *Namacalathus* individuals range from 4 to 12 mm in diameter, although many are partially covered with sediment and are preserved as reddish brown to yellow (oxyhydr) oxide minerals, FeOx ["FeOx" here denotes unspecified iron (oxyhydr) oxide] resulting from oxidation of pyrite (FeS_2), or as raised gray limestone casts that sometimes reveal weathered sections through the calcified skeleton (Fig. 1 and figs. S2A and S3). Seventy-three individuals (numbered 1 to 73) are found on a bedding plane sample, some with stalks (fig. S2, A and D), with 29% preserved upright in inferred growth position, 48% slightly toppled, and 23% of undetermined orientation (fig. S3). The host lithology is finely laminated micrite that grades from a mud-rich packstone with some silt-grade quartz and recrystallized bioclasts, often with a stylolitic contact (fig. S2C). *Namacalathus* individuals are immediately overlain by a thin (<1 mm) micritic carbonate with silt-grade, angular lithic fragments of quartz, albite, clays, and phosphatic minerals (figs. S4 and S5).

The best-preserved individuals show a raised pin cushion–like form, which surrounds the central, apical, opening. The central apical opening ranges from 1.3 to 12.3 mm (n = 37, mean = 3.6 mm) in diameter and can either be circular (Fig. 1, E and F, and fig. S3, K to N) or show five to seven, but generally six, isoclinal folds that radiate outward (Fig. 1, A to D and F, and fig. S3, A to J, P, and Q). Fold height ranges from 0.18 to 2.78 mm and width ranges from 0.43 to 4.66 mm (table S1). Both types of opening are preserved either as an FeOx crust (Fig. 1, A to D and F, and fig. S3, A to G and M to Q) or as casts of limestone (Fig. 1, E and I, and fig. S3, H to L and W to X). In cups where the central opening and lumens are visible, central opening folds oppose folds across the lumens (Fig. 1D). Full lumens are

[1]School of GeoSciences, University of Edinburgh, James Hutton Road, Edinburgh EH9 3FE, UK. [2]Department of Biological Evolution, Faculty of Biology, Lomonosov Moscow State University, Leninskie Gory, Moscow 119991, Russia. [3]UK Centre for Astrobiology, School of Physics and Astronomy, University of Edinburgh, James Clerk Maxwell Building, Peter Guthrie Tait Road, Edinburgh EH9 3FD, UK.
*Corresponding author. Email: amy.shore@ed.ac.uk
†Present address: School of Earth and Environment, University of Leeds, Leeds LS2 9JT, UK.

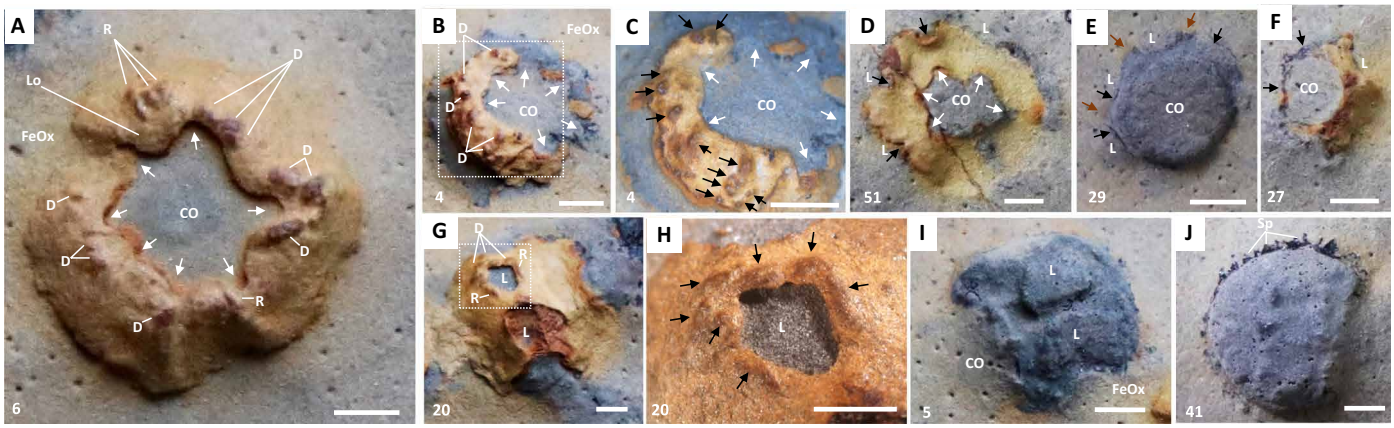

Fig. 1. *N. hermanastes*, Nama Group, Namibia. Museum No. F1547, Museum of the Geological Survey of Namibia. For numbered individuals, see fig. S2A. Scale bars, 2 mm. (**A** to **D**) Upright *Namacalathus* cup showing the central opening (CO) with folds (white arrows). Ridges (R) and domes (D) are present around the CO, with intervening pillow-like lobes (Lo), and iron (oxyhydr)oxide staining (FeOx) of sediment around fossil. (B) Folds (arrowed) around the CO and associated D. (C) Inset of (B), showing radiating D (black arrows) and folds (white arrows) around the CO. (D) Upright view showing folds (white arrows) around the central CO and lumens (L) with opposing folds (black arrows). (**E**) Cast preservation, with the CO and top of three L with calcite skeleton (black arrows). Sediments between lumens stained with FeOx (brown arrows). (**F**) CO and L preserved in FeOx, with calcite skeleton beneath (black arrows). (**G**) Toppled *Namacalathus* cup with R and D around L. (**H**) Inset of (G), showing domes and ridges (black arrows) around L. (**I**) Cast of toppled *Namacalathus* with L and CO. (**J**) Toppled *Namacalathus* with spines (Sp).

similarly observed either as FeOx crusts (Fig. 1, G and H, and fig. S3, P to U) or as casts (Fig. 1I and fig. S3, V to Y). Lumen height is smaller when preserved by FeOx (mean = 1.59 mm) compared to limestone casts (mean = 2.34 mm), but preservation style does not notably influence lumen width (mean = 1.8 mm; fig. S6B). Small (0.33 to 1.27 mm; table S2), domal, or elongate ridge-like swellings are present around the edges of the central opening and lumens (Fig. 1, A to C, G, and H, and fig. S7), concentrated at the apex of folds around the apical opening (Fig. 1A and figs. S3, A and C, and S8, A and B) or parallel to the edges of the lumen in one specimen (Fig. 1, G and H, and figs. S3R and S7, C and D), or as pairs that radiate from the apical opening to the lumens (Fig. 1, B and C, and fig. S3, C, D, and P). The calcitic skeleton is also preserved (Fig. 1, E, F, and J, and fig. S3, Q, Z, and A*ii* to A*v*), revealing robust, radiating spines of up to 0.4 mm in length and width where the FeOx crust has not been preserved (Fig. 1J and fig. S3, Z to A*v*).

X-ray micro–computed tomographic (μCT) imaging of two individuals (nos. 4 and 32) shows that pyritization reveals the presence of soft tissue as well as a cup-shaped calcite skeleton without a stalk below the bedding plane surface (Fig. 2 and fig. S8). Both visual inspection of the fossils (Fig. 1) and μCT images reveal the uppermost soft tissue to be present as six radially arranged lobes separated by the folds that project into the central opening and into the top of the lumens (Fig. 2). A cluster of helically coiled large bacteria, possibly *Obruchevella*, known mostly from Neoproterozoic and Cambrian successions (*9*), is also selectively pyritized outside the *Namacalathus* cup (Fig. 2, C, F to H, and K to M).

Polished serial sections through *Namacalathus* (no. 32) confirm the presence of an internal calcite skeleton with selective pyritization, with the overlying soft-tissue lobes preserved by framboidal pyrite, the vast majority of which is oxidized to FeOx and is thus referred to here as FeOx framboids that are pseudomorphs after pyrite (Figs. 2, D, I, and N, and 3, and figs. S9 and S10). Backscatter scanning electron microscopy (SEM) images also distinguish between the selectively pyritized calcitic skeleton and lobes preserved wholly via pyritization (Fig. 3A and figs. S11 and S12). Horizontal calcitic skeletal flanges are present that extend outward up to 950 μm from the central opening (Figs. 2N, 3A, and 4C), which abut with straight edges against the pyritized lobes as revealed by cathodoluminescence (CL) imaging (Fig. 4D). FeOx staining of up to 0.5 mm thick is also apparent within the cup adjacent to the inner wall (Figs. 2, D, I, and N; 3A; and 4B), which extends into the lumens (Fig. 2N and fig. S10, B and C), and also in patches of up to 0.1 mm thick on the outer wall (Fig. 2I). Thin, FeOx-rich channels 50 to 300 μm wide are present that extend orthogonally through the entire wall thickness, often passing through the central parts of spines (Figs. 3, A, E, and F, and 4, E and F). Slits also appear parallel to the skeletal wall (Fig. 4H), or between spines (Fig. 4I), and may bifurcate (Fig. 4I). These slits extend to at least 450 μm in depth (figs. S10 and S13). FeOx staining is notable on both the outer and inner walls where the channels terminate (Figs. 2, D, I, and N; 3, E and F; and 4, E and G to I). CL imaging shows the skeleton to be composed of poorly zoned, dominantly dull luminescent, blocky neomorphic sparry calcite (Fig. 4, F and R), where crystals differing in orientation are present on either side of the pyritized pores (Fig. 4F).

A tube-like structure, often defined by a central area of framboidal FeOx and an outer area of nonzoned, dark dull luminescent, sparry calcite (also present as a later-stage cement infill within the carbonate sediment), is found within three of four *Namacalathus* cups analyzed and can be distinguished in polished serial sections, as well as imaging via CL and backscatter SEM (Figs. 2, D, I, and N; 3, A and D; and 4, L and M; and figs. S4, S9, S13, and S14) and μCT (Fig. 2, E, G, H, J to M, and O). This structure has an elliptical cross section of up to 400 μm in diameter and may connect with a thin layer of FeOx 100 to 400 μm thick draped across the central opening of the cup (Figs. 2, D, I, and N; 3D; and 4, N and O). The tube then descends into the cup moving toward the inner wall, inflating to a circular section up to 600 μm, and then curves to form a J-shaped structure within the cup (Fig. 2, E, J, and O), sometimes decreasing in width to lastly disappear without attachment (fig. S12).

FeOx framboids are abundant in both the soft tissue (Fig. 3C and figs. S11 and S12) and skeleton (Fig. 3J and figs. S5 and S12). There

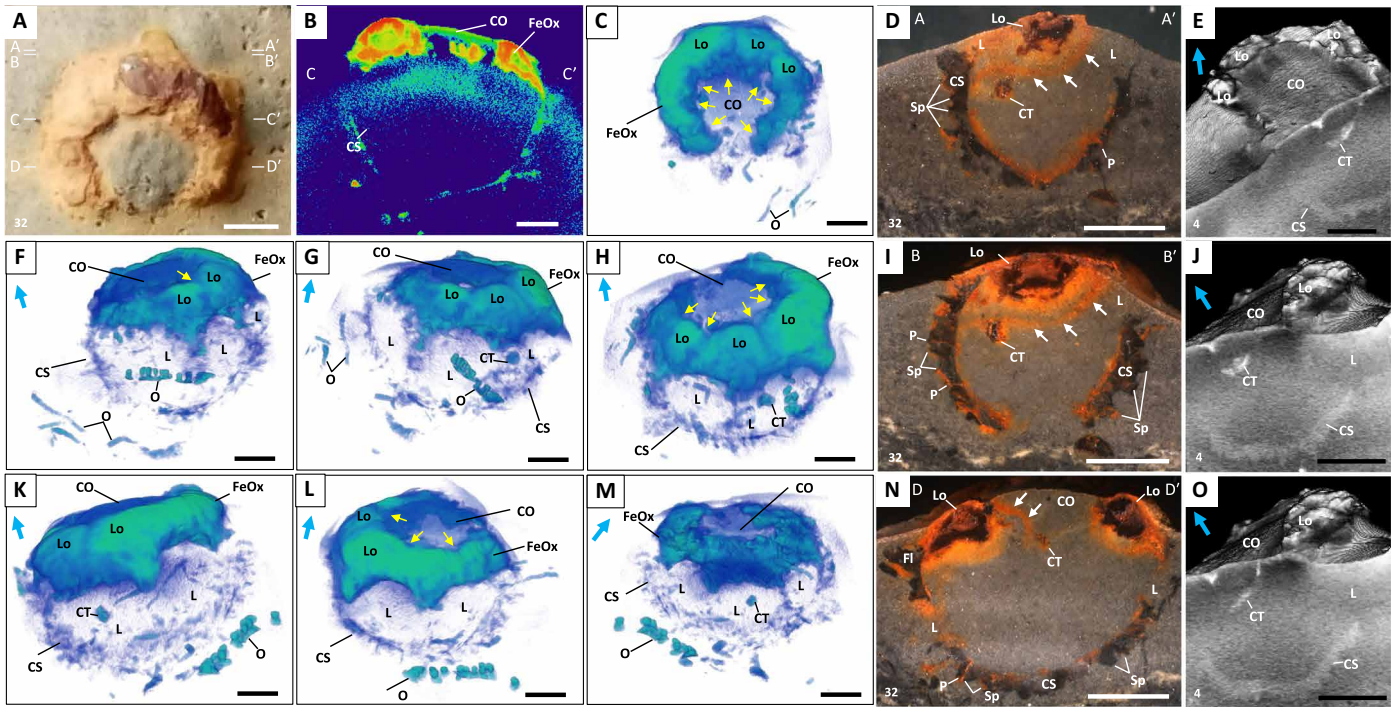

Fig. 2. X-ray μCT reconstruction of *N. hermanastes*. Museum No. F1547, Museum of the Geological Survey of Namibia. (A) to (D), (F) to (I), and (K) to (N), no. 32, and (E), (J), and (O), no. 4 showing the CO surrounded by FeOx (green-blue), showing Lo, L, and folds (yellow arrows). The calcite skeleton (CS; blue) is preserved below the bedding surface and outlines the L. CT, central tube; scale bars, 2 mm. (**A**) Plain view of *Namacalathus* cup. (**B**) False-color μCT slice of core (C to C′ of A). (**C**, **F** to **H**, and **K** to **M**) Reconstruction of *Namacalathus* cup rotated from the central axis. O, large bacterium, possible *Obruchevella*. (**D**, **I**, and **N**) Photomicrographs of successive longitudinal surfaces during serial sectioning (A and A′, B and B′, and D and D′ of A), with arrows tracing the membrane across the CO. (**E**, **J**, and **O**) Rendered three-dimensional model with grayscale CT sections, highlighting Lo, CS, and CT. Sp, spine; P, pore; CT, central structure; Fl, flange; white arrows, iron oxide concentration within the cup; blue arrows, way up.

are no framboids in the wider sediment. The neomorphic sparry calcite skeleton of *Namacalathus* also contains extensive FeOx framboids. These often occur within a well-defined, straight-edged middle layer (Fig. 3G), where pyritization extends to almost the full width of the skeleton in the uppermost parts of the cup, thinning toward the base of the cup where the calcitized outer and inner skeletal layers thicken (Fig. 3, G and H). Thin accumulations of FeOx framboids also occur in patches along the inner and outer skeletal surfaces and additionally pick out inverted V-shapes within the calcitic parts of the skeleton (Fig. 3, G and J). CL imaging shows zoned calcite cements growing around uncompacted sediment, which project into the neomorphic calcite skeleton of *Namacalathus* and other neomorphosed bioclastic grains (Fig. 4F). The dominant bright CL zone of the zoned calcite cements growing around uncompacted sediment coincides with visible FeOx staining near the upper parts of the cup (Fig. 4, C and D) and also with the thin layer of FeOx across the central opening (Figs. 2, D, I, and N, and 4, N and O). SEM images of this area confirm the presence of a line of framboidal FeOx (Fig. 3D).

Peloids are abundant in the area with visible iron staining, where the peloids are partially replaced by pyrite/FeOx (Fig. 3H). Likewise, sediment grains in the bed surface overlying the *Namacalathus* individuals are coated by pyrite/FeOx cements (Fig. 3I). Thus, CL imaging reveals three carbonate sediment types associated with the *Namacalathus* cups (Fig. 3C)—a bioclast-rich sediment infilling the bottom of cups (S1), a peloid-rich sediment with partial pyrite/FeOx replacement in the upper part of cups (S2), and an overlying lithic-rich sediment with pyrite/FeOx cements (S3) (Figs. 3, H and I, and 4R).

DISCUSSION

We therefore infer that early precipitation of both pyrite and calcite cements is responsible for this exceptional, three-dimensional preservation (*10*). This type of preservation occurs in sulfate-reducing environments with high concentrations of highly reactive iron but low or very localized availability of organic carbon available during early diagenesis, where pyrite precipitation is only associated with labile tissues and cellular structure is destroyed (*10*) and where the form of pyrite may reflect the relative susceptibility to decay of the original material (*11*,*12*). Pyrite framboid formation can occur within hours to days on organic matter under these conditions (*13*). We infer that framboidal pyrite formed very early and replaced both soft tissue and the inferred organic-rich parts of the skeleton. The occurrence of pyritized bacteria, here found alongside *Namacalathus*, is highly unusual in the fossil record and confirms that pyritization was rapid enough to replicate soft tissue.

The bright CL zone of early calcite cements associated with sediment within the upper part of cups (S2) is indicative of high-Mn and low-Fe pore water conditions (fig. S4). The sediment of S2 is also characterized by FeOx staining, which is inferred to derive from the oxidation of pyrite. This confirms the coincidence of both early

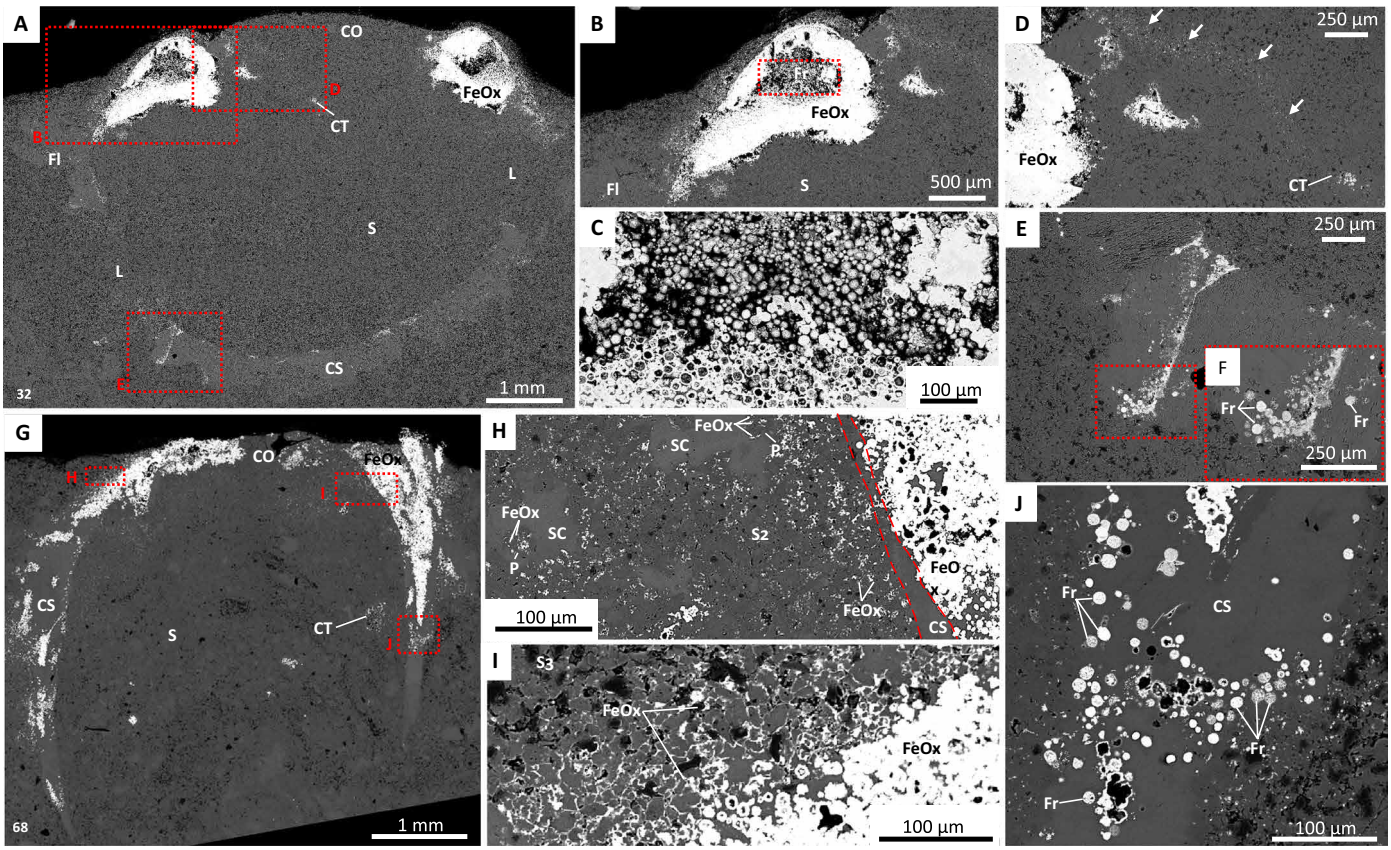

Fig. 3. Backscatter SEM images of *N. hermanastes*. Museum No. F1547, Museum of the Geological Survey of Namibia. (A) to (F), no. 32, slices D and D′ (Fig. 2N). (G) to (J), no. 68. (**A**) Scanning electron microscopy (SEM) image showing CS and Fl with L, pyritized/FeOx soft tissue of lobes (FeOx) and CT, with S. (**B**) Inset of (A), soft-tissue lobe of *Namacalathus* at the bedding surface infilled by FeOx framboids (Fr). (**C**) Inset of (B), showing FeOx Fr. (**D**) Inset of (A), showing line of FeOx Fr (arrowed) across the CO, which attach to CT. (**E**) Inset of (A), spine with perpendicular pore infilled with FeOx Fr. (**F**) Inset of (E), showing FeOx Fr. (**G**) FeOx Fr within the central area of the skeleton and CT. (**H**) Inset of (G), showing the middle layer of FeOx Fr (FeOx) in CS widening toward the bedding surface, and S2 peloidal sediment with FeOx (arrowed) partially replacing peloids (P). SC, burial sparry calcite. (**I**) Inset of (G), FeOx cement around angular calcitic and lithic grains of S3. (**J**) Inset of (G), FeOx Fr within the CS.

pyrite and early calcite cementation. Early carbonate cement formation is known to be facilitated by cell walls, extracellular polymeric substances, organic matter degradation, and other metabolic or microbial processes where peloids may form [e.g., (*14*)]. Local dissolution around pyritized soft tissue, perhaps induced by limited oxidation of pyrite, led to the formation of molds that later became infilled with a burial calcite spar cement.

Similar three-dimensional preservation of soft tissues in pyrite is found in the terminal Ediacaran Gaojiashan Member of the Dengying Formation, China (*15*), the Early Cambrian Chengjiang and Guanshan Lagerstätten from China (*11*), the Lower Ordovician Fenxiang Formation (*16*), and the Lower Cretaceous Santana Formation (*12*), often created by rapid entombment via storms. In the Nama Group, the proximal, very shallow, low-energy environment provided both a fine-grained medium and sufficient calcium carbonate saturation to facilitate early cementation. The *Namacalathus* individuals may also have been rapidly buried, in life, by a thin incursion of terrestrially derived lithic-rich sediment, and the folds of the central apical opening may represent a contracted state. The folding is unlikely to be taphonomic as the number of folds appears to correlate with lumen number (Fig. 1D). Cloudinids in siliciclastic-dominated beds of the Wood Canyon Formation, Nevada, show more spatially restricted framboidal pyritization that preserves cylindrical internal structures recently interpreted as possible digestive tracts (*17*). Internal digestive tissue is otherwise completely unknown from the Ediacaran record although common in Cambrian Lagerstätten (*17*). In sum, the processes operating in this preservational setting have created a taphonomically unique Lagerstätte.

The pyrite-rich middle layer within the *Namacalathus* skeleton confirms the presence of a tripartite skeleton with an organic-rich central portion (*3*). FeOx framboids in thin layers within other parts of the skeleton also suggest the presence of thinner organic-rich layers, parallel to potential accretionary growth lines. The additional presence of framboids that traverse the wall, as well as neomorphic calcite of differing orientations on either side of the pores, suggests that these are primary biological features, such as pores piercing the walls and the longer channels penetrating the spines. The thickness of the pyritized middle layer increases toward the upper part of the skeletal cup, suggesting that this may have been the area of initial skeletogenesis in contact with other soft tissue. This middle layer may have formed an organic template upon which the outer and inner calcareous layers formed and, as such, was the area of active skeletal growth, as observed in modern corals and lophophorates [e.g., (*18*)]. The FeOx staining noted extensively within the cup and lumens, and in

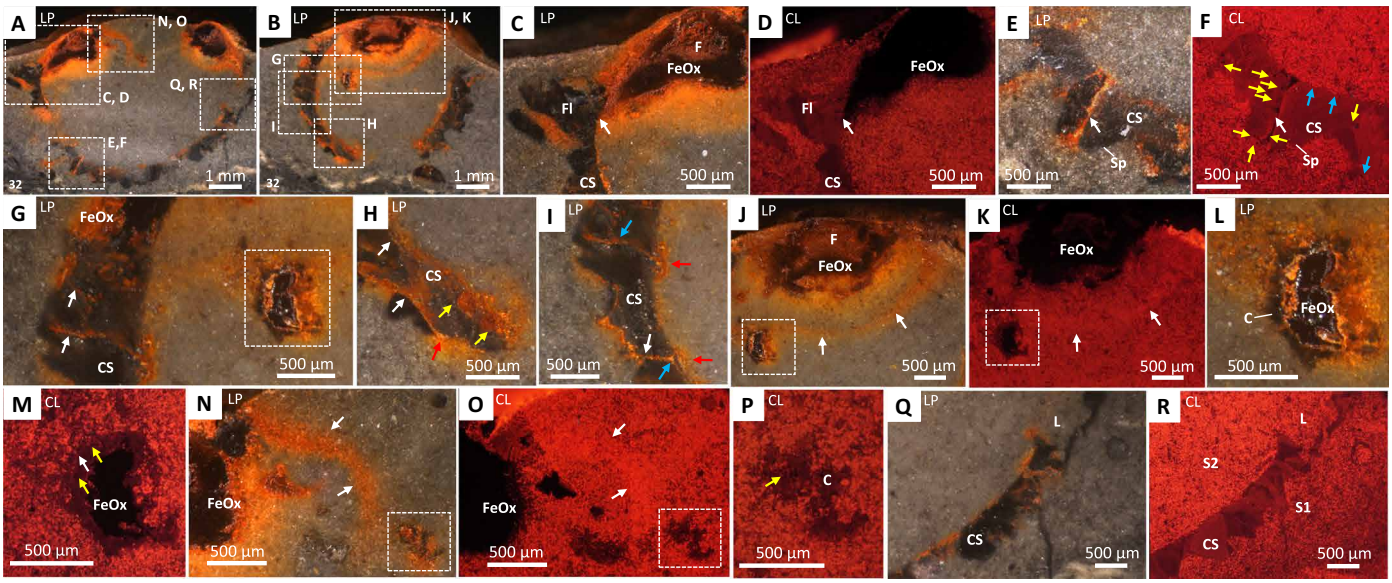

Fig. 4. Photomicrographs (LP) and CL images of *N. hermanastes*. Museum No. F1547, Museum of the Geological Survey of Namibia, no. 32. Longitudinal section highlighting features of the CS and FeOx. (**A**) Sections D and D′ (Fig. 2N) and (**B**) sections B and B′ (Fig. 2I) showing highlighted areas. (**C** and **D**) CS with a Fl overlain by FeOx (contact arrowed). (**E**) Pore (arrowed) along an Sp. (**F**) FeOx framboid-lined pore (F) (yellow arrow), forming a crystal boundary (white arrows). (**G**) Pores infilled with FeOx framboids (arrowed) and section of a central tubular structure (CT, boxed). (**H**) CS with FeOx staining parallel to (white arrows) and on the outer skeletal wall (yellow arrows). FeOx is concentrated where channels penetrate the outer wall of the cup (red arrow). (**I**) Channels with bifurcation (blue arrows) and with FeOx in areas between spines (white arrow). Concentrated FeOx located on the outer wall and where channels penetrate the inner wall of the cup (red arrows). (**J**) Lobe surrounded by FeOx staining (arrowed) connecting to CT (boxed). (**K**) FeOx staining coincident with bright luminescent calcite. (**L** and **M**) Section of CTS in (G) and (J), with sparry calcite (white arrow) surrounding F (yellow arrows). (**N** and **O**) FeOx staining of membrane (arrowed) coincident with brighter luminescence (arrowed), connecting to the CT. (**P**) Inset of (O), CT with calcite (C) with central F (yellow arrow). (**Q** and **R**) CS; lumen (L), with S1 and S2 sediments outside and inside the cup, respectively.

thinner patches inside and outside the cup, suggests the presence of soft tissue.

In sum, *Namacalathus* has a goblet-shaped calcareous skeleton with a hollow stalk and central opening, generally hexaradial symmetry with lateral facets bearing large lumens, a foliate microstructure with concordant columnar inflections and a middle organic-rich layer, and asexual reproduction expressed by bilateral budding (*1*,*3*). Soft tissue faithfully follows the internal skeleton, and the lumens do not have a localized, diagenetic, dissolution origin as previously suggested (*1*). In addition, we note the presence of folds formed between radially arranged lobes that extend from the central apical opening to lateral lumens, organic-rich pores, and channels within the skeletal wall; an internal, asymmetric, J-shaped tube-like structure, soft tissue adhering to the inner skeletal wall; an internal membrane abutting the central opening; and a thin organic-rich external covering. The tube-like structure is present in multiple specimens and has an apparent connection to the membrane across the aboral opening, suggesting a feeding function. Alternatively, this may represent a retractor muscle band but is more likely a gut or body cavity extension, potentially a partially preserved U-shaped gut. We note that the framboidal pyritic preservation of this putative gut is like that of the soft-tissue structure recently interpreted as a gut in cloudinids of the Wood Canyon Formation, Nevada (*17*). The small ridges and domes associated with the central opening and lumens could represent the base of tentacles; alternatively, they may have formed by the pyrite weathering process.

The pores or punctae may be homologous to those of similar size in brachiopods, extinct tommotiids, and microconchids, and to pseudopunctae in bryozoans, which house setae and other sensory structures (*19*–*21*). Punctae and channels connect the thin external and thick internal FeOx-rich layers, allowing interpretation as a mucopolysaccharide-protein periostracum and the body wall, respectively. The periostracum has a lobate pattern around the central opening, and these lobes could represent grooves where the tentacles were retracted. The variable constriction and scalloping of the central opening infers the presence of radially arranged, parietal diaphragm dilatator muscles. In some bryozoan groups, contraction of these muscles pulls the frontal membrane of the polyp inward with protrusion of the tentacle collar (*19*). The thin organic structure that traverses the apical opening of *Namacalathus* (Fig. 2, D, I, and N) can be interpreted as a frontal membrane, and so the position of the presumed gut below would correspond to the coelomic cavity following a lophophorate model. A retraction mechanism can also be inferred in *Namacalathus*, where muscle bundles may connect the frontal membrane and body wall (Fig. 2, D, I, and N).

This set of features, together with those seen in other specimens [bilateral budding and columnal inflections in the skeletal laminae (*3*)], excludes assignment of *Namacalathus* to protists, coralline algae, poriferans, cnidarians, and ctenophores (table S3). While hexaradial symmetry might favor an affinity within the Cnidaria, and some extinct Paleozoic corals have a foliated microstructure (*22*), the presence of skeletal columnar punctae, channels, a J- or U-shaped inferred gut, and a frontal membrane rather than a large, central, pharynx, as well as an absence of mesentery-like structures, does not support a cnidarian affinity.

Skeletal representatives of the Lophophorata, including stem and crown group brachiopods, bryozoans, and extinct microconchids, have very similar foliated microstructures with columnar inflections

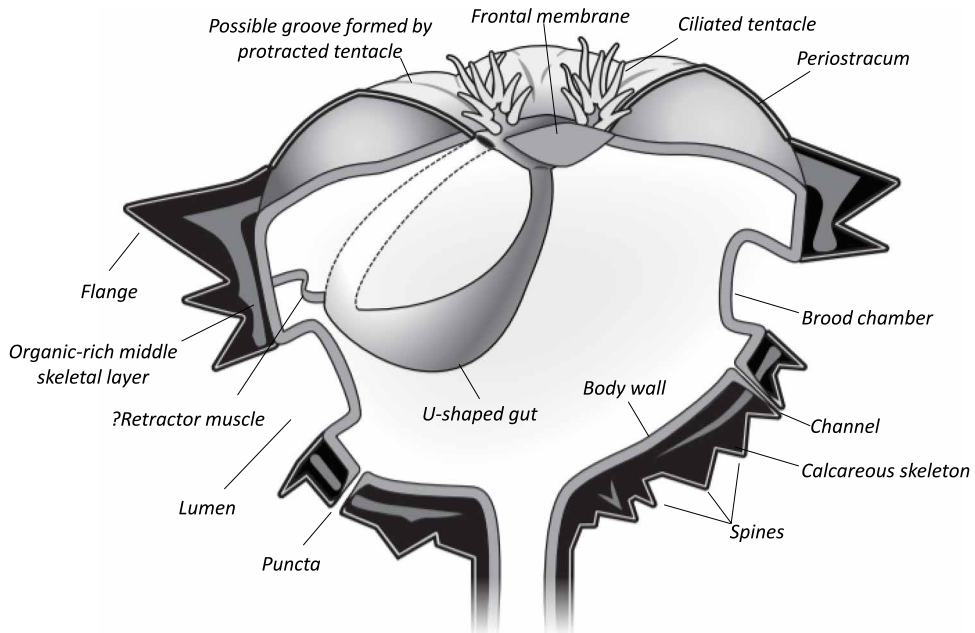

Fig. 5. Reconstruction of *N. hermanastes* as a total group lophotrochozoan.

in places extending into spines. A consensus tree for 54 lophotrochozoan taxa where *Namacalathus* occupies a basal position reveals that such "canaliculate" microstructure and "punctae" have multiple origins across the brachiozoan total group (*23*). The absence of any traces of a gastral cavity and the discovery of possible organic-rich punctae and channels within the skeletal walls further emphasize a similarity with the sensory porosity observed in lophophorates (brachiopods, tommotiids, and microconchids) (*21*,*24*), as does the presence of a possible J- or U-shaped gut. The generally six, large lateral lumens point to either a colonial organization for *Namacalathus* or a solitary organism in which lumens might correspond to brood chambers formed by external body wall invaginations, as found in bryozoans (*19*). Invaginations of the body wall are observed within the lumens in *Namacalathus* (fig. S10, B and C).

The confirmation of total group lophotrochozoans in the Ediacaran is supported by molecular phylogenies (*25*) and has implications for the earliest evolution of lophotrochozoans. The fossil record of biomineralized stem group lophotrochozoans is abundant from the early Cambrian onward where the possession of a calcareous skeleton or external sclerites likely represents the independent acquisition of skeletons of variable mineralogy in sessile, attached benthic fossil taxa, which have features shared with *Namacalathus*. These include tommotiids (*26*) and hyoliths, which were pedunculate and tentaculate organisms lacking a lophophore (*23*). Some goblet-shaped Cambrian forms that resemble *Namacalathus*, such as *Cotyledion tylodes* from the Chengjiang deposits, may represent stem lophophorates and also show an upper calyx and elongate stalk, with a central canal interpreted as an extension of the calycal cavity, a U-shaped gut with a mouth and aboral anus ringed by retractable marginal tentacles, and an outer surface covered by external sclerites, which may have been mineralized (*27*).

Cotyledion and some other Cambrian stalked fossils, namely, *Dinomischus* and *Siphusauctum*, have been compared with entoprocts (*27*–*29*). These fossils are relatively large (over 15 mm in height), while extant entoprocts are extremely small (less than 1 mm) and nonbiomineralized.

The Entoprocta are an enigmatic monophyletic acoelomate group that occupies a phylogenetically basal position among lophotrochozoans, close to molluscs (*30*). *Namacalathus* displays some notable similarities with the entoprocts, including the goblet-shaped overall morphology (a body divided into distinct stalk and calyx), hexaradial symmetry, the position of both mouth and anus within the presumable tentacle collar, and bilateral buds emerging from frontal area of the parental individual. Hence, we are now able to reconstruct *Namacalathus* as a total group lophotrochozoan, capable of asexual budding with an organic-rich, foliated calcareous skeleton and an open, apical J- or U-shaped gastric cavity within the apical opening potentially accommodating a retractable collar of tentacles and with brood chambers around the lumens (Fig. 5).

Sessile extant lophotrochozoan phyla such as annelids, molluscs, brachiopods, and phoronids have been suggested to have their origins in the earliest Cambrian small skeletal fauna [e.g., (*26*)], which are iconic representatives of the Cambrian Explosion. However, now, we can extend the origin of these modern lophotrochozoan phyla further back still into the terminal Ediacaran. In so doing, we establish a phylogenetic connection between Ediacaran and early Cambrian taxa, faunas that were previously thought distinct. We hence extend the roots of the Cambrian Explosion itself into the Ediacaran, where total group lophotrochozoans such as *Namacalathus* show a combination of features that became typical of both later lophophorates and representatives of the entoproctan-molluscan-annelidan branch.

MATERIALS AND METHODS

One float sample (237 mm by 194 mm by 33 mm) was collected from Zwartmodder Farm. A single-lens reflex camera and a binocular microscope were used to photograph and document each *Namacalathus*,

with ImageJ software used for the quantification of dimensions, such as lumen width and height.

The float sample was radiographed to determine whether individual *Namacalathus* cups had a density contrast with the surrounding sediment. Because of a high contrast, *Namacalathus* no. 32 was cored and underwent μCT scanning. Scanning was at 120 kV and 1500 projections (2 × 2 s exposure averaged) were collected and reconstructed by filtered back projection to 824 tomographic slices. The contrast was enhanced by applying the stretch histogram option in ImageJ, while not affecting the original data. Three-dimensional models of the scans were rendered using Avizo 9 software. Voxel size of reconstructions equates to 20.7 μm. The predefined color map "physics.icol" was applied to the model to aid in the visualization of the features of the fossil, but the false colors are not quantitatively correlated to any property of the object. The color thresholds of the color map were altered in Avizo (255-65535) to remove the background of the surrounding calcium carbonate sediment to produce a model of the whole individual. Scanning of *Namacalathus* cup no. 4 was also at 120 kV, using the same data acquisition parameters, and 633 tomographic slices were reconstructed. The model was rendered using Avizo 9, with a voxel size of 23 μm, using the predefined color map "greyscale.icol" as the low contrast of the scan did not lend itself to be rendered in false color.

Namacalathus no. 32 was then cut into three sections to observe the internal structure of the *Namacalathus* cup (fig. S9). These sections were finely polished and imaged using binocular microscopy and CL (fig. S10). One of the slices underwent serial sectioning at 26-μm increments, which were also imaged through binocular microscopy and CL.

Two highly polished thin sections were made of the slab to describe the lithology using petrographic microscopy. Three highly polished, uncovered thick sections (200 to 2000 μm) were cut from transverse sections of *Namacalathus* no. 68 for backscatter electron imaging and EDX analysis.

Two samples (nos. 66 and 68) were serially sectioned and highly polished at 1-mm and 500-μm increments, respectively, to understand the distribution of iron oxide and its relationship to the calcitic skeleton using light microscopy and CL imaging. Serial sectioning at 1 mm of a core plug containing *Namacalathus* no. 66 allowed us to observe the relationship between the iron oxide and the calcite skeleton. A CanoScan LiDE 210 flatbed scanner was used to scan each section (4000 dots per inch for both sections).

SUPPLEMENTARY MATERIALS

Supplementary material for this article is available at http://advances.sciencemag.org/cgi/content/full/7/1/eabf2933/DC1

REFERENCES AND NOTES

1. J. P. Grotzinger, W. A. Watters, A. H. Knoll, Calcified metazoans in thrombolite-stromatolite reefs of the terminal Proterozoic Nama Group, Namibia. *Paleobiology* **26**, 334–359 (2000).
2. H. J. Hofmann, E. W. Mountjoy, *Namacalathus-Cloudina* assemblage in Neoproterozoic Miette Group (Byng Formation), British Columbia: Canada's oldest shelly fossils. *Geology* **29**, 1091–1094 (2001).
3. A. Y. Zhuravlev, R. A. Wood, A. M. Penny, Ediacaran skeletal metazoan interpreted as a lophophorate. *Proc. R. Soc. B Biol. Sci.* **282**, 20151860 (2015).
4. S. B. Pruss, C. L. Blättler, F. A. Macdonald, J. A. Higgins, Calcium isotope evidence that the earliest metazoan biomineralizers formed aragonite shells. *Geology* **46**, 763–766 (2018).
5. M. D. Brasier, J. B. Antcliffe, R. H. T. Callow, in *Taphonomy: Process and Bias Through Time*, P. A. Allison, D. J. Bottjer, Eds. (Topics in Geobiology, 2011), vol. 32, pp. 519–567.
6. A. Seilacher, D. Grazhdankin, A. Legouta, Ediacaran biota: The dawn of animal life in the shadow of giant protists. *Paleont. Res.* **7**, 43–54 (2003).
7. Y. Zhao, J. Vinther, L. A. Parry, F. Wei, E. Green, D. Pisani, X. Hou, G. D. Edgecombe, P. Cong, Cambrian sessile, suspension feeding stem-group ctenophores and evolution of the comb jelly body plan. *Current Biol.* **29**, 1112–1125.e2 (2019).
8. S. A. Bowring, J. P. Grotzinger, D. J. Condon, J. Ramezani, M. J. Newall, P. A. Allen, Geochronologic constraints on the chronostratigraphic framework of the Neoproterozoic Huqf Supergroup, Sultanate of Oman. *Am. J. Sci.* **307**, 1097–1145 (2007).
9. A. H. Knoll, The early evolution of eukaryotes: A geological perspective. *Science* **256**, 622–627 (1992).
10. N. J. Butterfield, Exceptional fossil preservation and the Cambrian explosion. *Integr. Compar. Biol.* **43**, 166–177 (2003).
11. S. E. Gabbott, H. Xian-Guang, M. J. Norry, D. J. Siveter, Preservation of Early Cambrian animals of the Chengjiang biota. *Geology* **32**, 901–904 (2004).
12. G. L. Osés, S. Petri, C. G. Voltani, G. M. E. M. Prado, D. Galante, M. A. Rizzutto, I. D. Rudnitzki, E. P. da Silva, F. Rodrigues, E. C. Rangel, P. A. Sucerquia, M. L. A. F. Pacheco, Deciphering pyritization-kerogenization gradient for fish soft-tissue preservation. *Sci. Rep.* **7**, 1468 (2017).
13. D. Rickard, How long does it take a pyrite framboid to form? *Earth Planet. Sci. Lett.* **513**, 64–68 (2019).
14. M. Obst, J. J. Dynes, J. R. Lawrence, G. D. W. Swerhone, K. Benzerara, C. Karunakaran, K. Kaznatcheev, T. Tyliszczak, A. P. Hitchcock, Precipitation of amorphous $CaCO_3$ (aragonite-like) by cyanobacteria: A STXM study of the influence of EPS on the nucleation process. *Geochim. Cosmochim. Acta* **73**, 4180–4198 (2009).
15. J. D. Schiffbauer, S. Xiao, Y. Cai, A. F. Wallace, H. Hua, J. Hunter, H. Xu, Y. Peng, A. J. Kaufman, A unifying model for Neoproterozoic–Palaeozoic exceptional fossil preservation through pyritization and carbonaceous compression. *Nat. Commun.* **5**, 5754 (2014).
16. A. Baliński, Y. Sun, Preservation of soft tissue in an Ordovician linguloid brachiopod from China. *Acta Palaeont. Polon.* **58**, 115–120 (2013).
17. J. D. Schiffbauer, T. Selly, S. M. Jacquet, R. A. Merz, L. L. Nelson, M. A. Strange, Y. Cai, E. F. Smith, Discovery of bilaterian-type through-guts in cloudinomorphs from the terminal Ediacaran Period. *Nat. Commun.* **11**, 205 (2020).
18. A. Williams, L. E. Holmer, M. Cusack, Chemico-structure of the organophosphatic shells of siphonotretide brachiopods. *Palaeontology* **47**, 1313–1337 (2004).
19. H. Mukai, K. Terakado, C. G. Reed, in *Microscopic Anatomy of Invertebrates*, F. W. Harrison, R. M. Woollacott, Eds. (Wiley-Liss, 1997), vol. 13, pp. 45–206.
20. A. Williams, in *Microscopic Anatomy of Invertebrates,* F. W. Harrison, R. M. Woollacott, Eds. (Wiley-Liss, 1997), vol. 13, pp. 237–296.
21. C. Garbelli, Shell microstructures in Lopingian brachiopods: Implications for fabric evolution and calcification. *Riv. It. Paleont. Strat.* **123**, 541–560 (2017).
22. M. Jakubowicz, B. Berkowski, M. L. Correa, E. Jarochowska, M. Joachimski, Z. Belka, Stable isotope signatures of middle Palaeozoic ahermatypic rugose corals—Deciphering secondary alteration, vital fractionation effects, and palaeoecological implications. *PLOS ONE* **10**, e0136289 (2015).
23. H. Sun, M. R. Smith, H. Zeng, F. Zhao, G. Li, M. Zhu, Hyoliths with pedicles illuminate the origin of the brachiopod body plan. *Proc. R. Soc. B: Biol. Sci.* **285**, 20181780 (2018).
24. P. D. Taylor, O. Vinn, M. A. Wilson, Evolution of biomineralisation in 'lophophorates'. *Spec. Pap. Palaeont.* **84**, 317–333 (2010).
25. J. A. Cunningham, A. G. Liu, S. Bengtson, P. C. J. Donoghue, The origin of animals: Can molecular clocks and the fossil record be reconciled? *Bioessays* **39**, 1600120 (2017).
26. C. B. Skovsted, G. A. Brock, J. R. Paterson, L. E. Holmer, G. E. Budd, The scleritome of *Eccentrotheca* from the Lower Cambrian of South Australia: Lophophorate affinities and implications for tommotiid phylogeny. *Geology* **36**, 171–174 (2008).
27. Z. Zhang, L. E. Holmer, C. B. Skovsted, G. A. Brock, G. E. Budd, D. Fu, X. Zhang, D. Shu, J. Han, J. Liu, H. Wang, A. Butler, G. Li, A sclerite-bearing stem group entoproct from the early Cambrian and its implications. *Sci. Rep.* **3**, 1066 (2013).
28. S. Conway Morris, A new entoproct-like organism from the Burgess Shale of British Columbia. *Palaeontology* **20**, 833–845 (1977).
29. J. Kimmig, L. C. Strotz, B. S. Liberman, The stalked filter feeder *Siphusauctus lloydguntheri* n. sp. from the middle Cambrian (Series 3, Stage 5) Spence Shale of Utah: Its biological affinities and taphonomy. *J. Paleont* **91**, 902–910 (2018).
30. F. Marlétaz, K. T. C. A. Peijnenburg, T. Goto, N. Satoh, D. S. Rokhsar, A new spiralian phylogeny places the enigmatic arrow worms among gnathiferans. *Curr. Biol.* **29**, 312–318 (2019).
31. G. J. B. Germs, Implications of a sedimentary facies and depositional environmental analysis of the Nama Group in South West Africa/Namibia, in *Evolution of the Damara Orogen of South West Africa/Namibia*, R. M. Miller, Ed. (Geological Society of South Africa Special Publication, 1983), vol. 11, pp. 89–114.
32. R. Wood, S. W. Poulton, A. R. Prave, K.-H. Hoffmann, M. O. Clarkson, R. Guilbaud, J. W. Lyne, R. Tostevin, F. Bowyer, A. M. Penny, A. Curtis, S. A. Kasemann, Dynamic redox

conditions control late Ediacaran metazoan ecosystems in the Nama Group, Namibia. *Precambrian Res.* **261**, 252–271 (2015).
33. J. B. Antcliffe, R. H. T. Calloway, M. D. Brasier, Giving the early fossil record of sponges a squeeze. *Biol. Rev.* **89**, 972–1004 (2014).
34. A. H. Knoll, Biomineralization and evolutionary history. *Rev. Mineral. Geochem.* **54**, 329–356 (2003).
35. H. A. Armstrong, M. D. Brasier, *Microfossils* (Blackwell, ed. 2, 2005).
36. T. N. Taylor, E. L. Taylor, M. Krings, *Paleobotany, The Biology and Evolution of Fossil Plants* (Academic Press/Elsevier, ed. 2, 2009).
37. J. N. A. Hooper, R. W. M. Van Soest, Eds., *Systema Porifera: A Guide to the Classification of Sponges* (Kluwer Academic/Plenum Publishers, 2002).
38. T.-y. Park, J. Woo, D.-J. Lee, D.-C. Lee, S.-b. Lee, Z. Han, S. K. Chough, D. K. Choi, A stem-group cnidarian described from the mid-Cambrian of China and its significance for cnidarian evolution. *Nat. Commun.* **2**, 442 (2011).
39. I. Coronado, A. Pérez-Huerta, S. Rodríguez, Primary biogenic skeletal structures in Multithecopora (Tabulata, Pennsylvanian). *Palaeogeogr. Palaeoclimatol. Palaeoecol.* **386**, 286–299 (2013).
40. T. S. Bagaeva, D. M. Kupaeva, A. A. Vetrova, I. A. Kosevich, Y. A. Kraus, S. V. Kremnyov, cWnt signaling modulation results in a change of the colony architecture in a hydrozoan. *Dev. Biol.* **456**, 145–153 (2019).
41. N. V. Whelan, K. M. Kocot, T. P. Moroz, K. Mukherjee, P. Williams, G. Paulay, L. L. Moroz, K. M. Halanych, Ctenophore relationships and their placement as the sister group to all other animals. *Nat. Ecol. Evol.* **1**, 1737–1746 (2017).
42. A. Williams, C. H. C. Brunton, S. J. Carlson, F. Alvarez, A. D. Ansell, P. G. Baker, M. G. Bassett, R. B. Blodgett, A. J. Boucot, J. L. Carter, L. R. M. Cocks, B. L. Cohen, P. Copper, G. B. Curry, M. Cusack, A. S. Dagys, C. C. Emig, A. B. Gawthrop, R. Gourvennec, R. E. Grant, D. A. T. Harper, L. E. Holmer, H. Hong-fei, M. A. James, J. Yu-gan, J. G. Johnson, J. R. Laurie, S. Lazarev, D. E. Lee, C. Lüter, S. Mackay, D. I. Mac Kinnon, M. O. Manceñido, M. Mergl, E. F. Owen, L. S. Peck, L. E. Popov, P. R. Racheboeuf, M. C. Rhodes, J. R. Richardson, R. Jia-yu, M. Rubel, N. M. Savage, T. N. Smirnova, S. Dong-li, D. Walton, B. Wardlaw, A. D. Wright, *Treatise on Invertebrate Paleontology, Pt H (Revised), Brachiopoda, v. 1* (University of Kansas, Geological Society of America, 1997).
43. A. Kouchinsky, L. E. Holmer, M. Steiner, G. T. Ushatinskaya, The new stem-group brachiopod *Oymurania* from the lower Cambrian of Siberia. *Acta Palaeontol. Polon.* **60**, 963–980 (2014).
44. J. Merkel, B. Lieb, A. Wanniger, Muscular anatomy of an entoproct creeping-type larva reveals extraordinary high complexity and potential shared characters with mollusks. *BMC Evol. Biol.* **15**, 130 (2015).
45. P. D. Taylor, C. Lombardi, S. Cocito, Biomineralization in bryozoans: Present, past and future. *Biol. Rev.* **90**, 1118–1150 (2015).
46. A. O. Borisanova, A new species of solitary Entoprocta, *Loxosomella angusta* sp.n., from the White Sea. *Invertebrate Zoology* **13**, 43–50 (2016).

Acknowledgments: We thank H. Mocke and C. Hoffmann of the Geological Survey of Namibia and the Ministry of Mines and Energy, Namibia. We thank A. Horn and S. Horn of the Omkyk Farm; M. Hall, N. Cayzer, and J. Craven for technical support; and R. Anderson and D. Erwin for useful discussion. **Funding:** A.J.S. acknowledges support from the University of Edinburgh and the International Centre for Carbonate Reservoirs, and R.A.W. acknowledges support from NERC grant (NE/P013651/1). **Author contributions:** A.J.S. conducted the research. R.A.W., A.C., and F.T.B. undertook fieldwork. I.B.B. and A.J.S. conducted the μCT imaging. A.J.S. wrote the first draft of the manuscript, with all authors contributing to the final document. **Competing interests:** The authors declare that they have no competing interests. **Data and materials availability:** All data needed to evaluate the conclusions in the paper are present in the paper and/or the Supplementary Materials. Additional data related to this paper may be requested from the authors.

Submitted 16 October 2020
Accepted 9 November 2020
Published 1 January 2021
10.1126/sciadv.abf2933

Citation: A. J. Shore, R. A. Wood, I. B. Butler, A. Yu. Zhuravlev, S. McMahon, A. Curtis, F. T. Bowyer, Ediacaran metazoan reveals lophotrochozoan affinity and deepens root of Cambrian Explosion. *Sci. Adv.* **7**, eabf2933 (2021).

Ediacaran metazoan reveals lophotrochozoan affinity and deepens root of Cambrian Explosion

A. J. Shore, R. A. Wood, I. B. Butler, A. Yu. Zhuravlev, S. McMahon, A. Curtis and F. T. Bowyer

Sci Adv **7** (1), eabf2933.
DOI: 10.1126/sciadv.abf2933

Appendix 4.2 Data Tables

4.2.1 Features of *Namacalathus hermanastes* collected from the Upper Omkyk Member at Zwartmodder, key for numbered specimens in Chapter 5 section 5.2

No.	Diameter (mm)	Top opening (longest) (mm)	Top opening (shortest) (mm)	Lumen Width (mm)	Lumen Height (mm)	Iron oxide coating present	Ridges	Spines	Number of Crenulations
1	9.1					N	N/A	Y	
2	6.6			2.3	1.5	Y	N	N	Broken up
3	7.5			2.8	1.7	Y	N	N	
4	7.5	3.7	2.9			Y	Y	N	6
5	8.3			2.2 2.7	3.2 3.1	N	N	N N	
6	6.1	4.7	3.2			Y	Y	N	7
7	7.3	5.3		2.7		N	N	N	
8						N	N/A	N	
9	3.5	3.1	2.2	1.8		Y	Y	N	6
10	3.3							N	
11						Y	N	N	
12	4.9					N	N/A	Y	
13	6.9					N	N/A	Y	
14	6.0					Y	N/A	N	6
15	4.8					Y	N	Y	
16	2.7					N	N/A	N	Broken up
17	3.0	3.5	2.6			N	N/A	Y	
18	3.7			1.9 1.5	1.8 1.4	Y	N	N	
19	4.5					Y	N	N	
20	6.1			0.8 1.3	0.8 0.7	Y	N	N	
21	6.3	2.9	2.4			Y	N/A	Y	
22				1.9	1.8	N	N/A	N	
23	8.9					Y	N	Y	
24						N	N/A	Y	
25						Y	N/A	N	
26	9.5					N	N/A	N	
27						N	N/A	N	
28		5.1	4.7			N	N/A	N	
29	8.0			3.1	3.0	Y	N	N	
30	6.2					N	N/A	N	
31	4.7	4.3	3.7			Y	N/A	N	
32	7.9	4.0	3.3			Y	N	N	7
33	5.4					Y	N	N	
34	2.4			1.2	2.0	N	N/A	N	

				1.7	2.0				
35	4.5			1.6 1.4	2.1 2.1	N	N/A	N	
36	7.7					N	N/A	N	
37	2.9	2.2	1.8			Y	N	N	
38	5.7					N	N/A	N	
39						N	N/A	N	
40	3.7	1.5	1.3			Y	N	N	5
41	3.5			0.9 0.6	1.7 1.6	Y	N	N	
42	4.2					N	N/A	Y	
43	6.5					N	N/A	Y	
44	13.7	12.3	6.3			N	N/A	Y	6
45	3.3					Y	Y	N	
46						Y	Y	N	
47	4.6					N	N/A	Y	
48	3.8					N	N/A		
49	11.3	3.8	2.3			Y	N	N	
50	3.7	1.5	1.4			N	N/A	Y	
51	8.0	3.5	2.9			Y	N	N	5
52	7.4					N	N/A	Y	
53	1.9					N	N/A	N	
54	5.8					N	N/A	Y	
55	2.5					N	N/A	Y	
56	3.2					N	N/A	Y	
57	3.9	3.7	2.7			N	N/A	N	5
58	3.5					N	N/A	N	
59	4.6	4.3	3.3			Y	N	N	6
60						Y	N	N	
61	3.5					N	N/A	Y	
62						N	N/A	N	
63						N	N/A	Y	
64						Y	N	N	
65	5.7					Y	N	N	
66		5.1	4.1			Y	N	N	6
67	8.4					Y	N	N	
68						Y	N	N	
69	7.6	4.2	3.2			N	N	N	6
70	6.2			2.6	1.6	Y	Y	N	
71						N	N	N	
72						N	N	N	
73						N	N	N	